Sensitivity of DARWIN to Rare Events and the Purity Monitor for Xenoscope

Dissertation

zur
Erlangung der naturwissenschaftlichen Doktorwürde
(Dr. sc. nat.)

vorgelegt der
Mathematisch-naturwissenschaftlichen Fakultät
der
Universität Zürich

von
Yanina Biondi
aus
Argentinien

Promotionskommission
Prof. Dr. Laura Baudis (Vorsitz)
Prof. Dr. Florencia Canelli
Dr. Michelle Galloway

Zürich, 2022

Abstract

The standard model (SM) of particle physics has been a successful paradigm for the explanation of processes at the most fundamental scales of Nature. However, there is vast evidence of this model being incomplete, as it only explains 15% of the matter content in the Universe. The nature of the remaining 'dark matter' content, from which only the gravitational interaction with normal matter has been observed, has not been resolved to the present day. Moreover, with the discovery of neutrino oscillations, the question of how neutrinos acquired mass was introduced, with no known answer within the SM. Other fundamental properties and mechanisms, such as the exceedingly small upper limit on the neutron electric dipole moment or the mass generation mechanism for neutrinos, cannot be explained, and the necessity of theories beyond the SM is unquestionable.

This work was developed in the context of the design and physics reach studies of the future DARWIN observatory, a dual-phase time projection chamber (TPC) able to detect the light and charge yield from incident particles scattering off the liquid xenon target. DARWIN can search for dark matter candidates, such as weakly interacting massive particles and axions, as well as put constraints on the neutrino properties, among others.

This thesis focuses on the projected sensitivity of DARWIN to rare processes, such as the detection of axions produced in the Sun and the neutrinoless double beta decay process of ^{136}Xe, that can provide evidence of the mechanism that gives mass to neutrinos.

One of the challenges of future LXe detectors resides in the purification of the xenon target in order to prevent charge signal degradation. To that end, a TPC that will serve as a demonstrator in the vertical dimension of $2.6\,\mathrm{m}$ long was designed and will be constructed at the University of Zurich. Its mechanical and electrical design for the Xenoscope project is described in this work. At the first stage of this project, a purity monitor of $53\,\mathrm{cm}$, corresponding to a section of the $2.6\,\mathrm{m}$ TPC, was designed and operated in Xenoscope, yielding promising results on the achievable LXe purity and electron transport properties.

Author's contribution

My main contributions to the work described in this thesis are summarised:

- For Chapter 3, the background and signal modelling in order to derive the sensitivity to the $0\nu\beta\beta$-decay from ^{136}Xe was done in a collaboration with other people. In particular, I contributed to the implementation of the baseline DARWIN geometry in the Geant4 simulation toolkit, in order to estimate the expected radiogenic background from detector materials. I used this information and other calculations for the expected intrinsic and cosmogenic background sources to perform the inference of the sensitivity and discovery potential of $0\nu\beta\beta$ signatures in DARWIN. This work is published in Ref. [1].

- In Chapter 4, I calculated the expected electron recoil rate in DARWIN induced by the hypothetical flux of solar axions via the axioelectric and inverse Primakoff effects with the LXe target. I calculated as well the expected background rate from different sources, by using diverse theoretical estimates and projected targets, to derive the sensitivity of DARWIN to solar axions. In particular, I included the theoretical estimates of the inverse Primakoff interaction of axions with the xenon target, which adds a novel channel for its search. I followed a novel statistical analysis for the inference of upper limits on the axion couplings to normal matter by performing simultaneous minimisation on three independent yield parameters, in order to construct a confidence volume. A publication of this work is in progress.

- Chapter 5 is exclusively my work. I designed the field cage in close collaboration with the Mechanical Workshop at the University of Zürich, produced 3D models and the 2D technical drawings in close contact with the component manufacturers. In particular, I focused on the design of a purity monitor (PM), including the optical system and the electronic readout. The assembly of the Xenoscope facility was conducted together with other group members, while the design of the electronic circuit done together in collaboration with the Electronics Workshop of the Department of Physics at the University of Zurich. I have performed electric field

and current signal simulations for a $2.6\,\mathrm{m}$ field cage. I fabricated thin films for photocathodes immersed in LXe in the laboratory of Condensed Matter in the University of Zürich, and performed quality assessment of this photocathodes in the Center for Microscopy and Image Analysis.

Table of Contents

List of Tables

List of Figures

List of Abbreviations

For the unavoidable words in our field, this appendix defines jargon terms in a table of acronyms and their meaning.

Table 1: Acronyms

Acronym	Meaning
CEνNS	Coherent elastic neutrino-nucleus scattering
CMB	Cosmic microwave background
GN	Gas nitrogen
FSR	Field shaping rings
GXe	Gase xenon
LNGS	Laboratori Nazionali del Gran Sasso
DAQ	Data acquisition
ER	Electronic Recoil
LHC	Large hadron collider
LN	Liquid nitrogen
LXe	Liquid xenon
HV	High voltage
MC	Monte Carlo
NR	Nuclear recoil
pdf	Probability density function
PM	Purity monitor
PMT	Photomultiplier tube
PTFE	Polytetrafluorethylene
QE	Quantum efficiency
RGB	Red-giant branch
ROI	Region of interest
SS	Stainless steel
toyMC	Toy Monte Carlo
TPC	Time projection chamber
VUV	Ultraviolet light with wavelengths in the 100–200 nm range
UHV	Ultra high vacuum
WIMP	Weakly interacting massive particle

Chapter 1

What Lies Beyond the Standard Model?

The 20th century has witnessed the accelerated development of the current understanding of elementary particles in Nature. Since the pivotal understanding of matter as composed of fundamental particles, more particles were added to the elementary particle landscape, with the last addition being the discovery of the Higgs boson in 2012 by ATLAS and CMS at the Large Hadron Collider (LHC) [2]. This is not a closed ending in the efforts to describe particles at the most fundamental scales in Nature. By the end of this chapter, the reader should be convinced that several open problems cannot be explained inside the SM.

1.1 Standard model and open questions

The Standard Model (SM) of Particle Physics is based in Gauge groups, and consists of twelve fermions, which interact via two fundamental forces mediated by exchange bosons. The fundamental fermions consist of six quarks and six leptons [3], with different electrical charges: $\pm 2/3$ or $\pm 1/3$ charges for the quarks, and ± 1 for the charged leptons. Bosons have integer spin, while elementary fermions have a spin of half a unit[1]. The mediators consist of eight gluons for the strong interaction and photons, and $W^{\pm}$, Z^0 for the electroweak interaction. Lastly, the Higgs field introduces the Higgs boson of charge and spin-zero and provides the mechanism from which the bosons Z, $W^{\pm}$ and the charged fermions acquire mass. While the Higgs mechanism breaks the weak isospin symmetry of the electroweak interaction, part of the gauge field remains unaffected, which translates into massless photons. When assembling all these components, the theory has a $SU(3)_C \times SU(2)_L \times U(1)_Y$ gauge structure, where $SU(3)_C$ is the group of strong interactions, and $SU(2)_L \times U(1)_Y$ represents

[1] We will use now natural units unless stated otherwise.

the electroweak interactions, where $SU(2)_L$ are gauge transformations applied only to left-handed particles.

Although the SM successfully predicted phenomena that were time after time corroborated by experimental data, there are some open questions that it does not address. We will set aside the questions about the naturalness of the theory, which inquire about the origin from first principles for the 19 parameters of the model [4], the Higgs mass correction terms [5], or the anomalous magnetic moment of the muon [6, 7]. We will focus, instead, on three open questions: charge conjugation parity (CP) violating processes, the overwhelming evidence of *dark matter* in the universe, and lastly, neutrino flavour oscillation and, consequently, neutrino mass.

1.2 Charge-parity violation and axions

CP-symmetry refers to the invariance of equations in particle physics when exchanging the particle for its antiparticle (charge conjugation operator, C) and mirroring the spatial coordinates (parity, P-operator). P-symmetry (parity symmetry) has been considered a fundamentally conserved quantity, along with energy and momentum. The discovery of K-meson decays to either two or three π-mesons in the 1950s pointed toward a possible P-violation, since the final CP state could be $P = \mathbf{1}$, for 2 π-mesons, or $P =$**-1** with 3 π-mesons, making the final state of the decay not an eigenstate of the CP operator [8]. When the two decay modes of the K-meson were discovered, the community started to design experiments that could test P-conservation in weak interactions [9].

The proposed idea to test parity violation in β-decays was by measuring the angular distribution of the electrons coming from the β-decays of polarised nuclei. The reasoning was the following: if the pseudoscalar term $\langle(\sigma \cdot p)\rangle$, which is the expectation value, where σ is the spin of the nucleus and p is the momentum of the electron, changes sign under space inversion, then there is a CP violation. Therefore, the distribution of the electrons emitted from a polarized nucleus is asymmetrical, and the term $\langle(\sigma \cdot p)\rangle \neq 0$. In mathematical terms:

$$\langle(\sigma \cdot p)\rangle \equiv \int dr \psi^*(r)[\sigma \cdot p]\psi(r). \tag{1.1}$$

If parity invariance is valid, then a **P**-operation gives:

$$\mathbf{P}\psi(r) = \psi(-(r) = \pm\psi(r), \tag{1.2}$$

and the expected value must be zero if parity invariance is valid. The experiments of C. S. Wu, where she studied the decay of ^{60}Co, demonstrated an asymmetry in the β-emission, as shown in Figure

1.1.

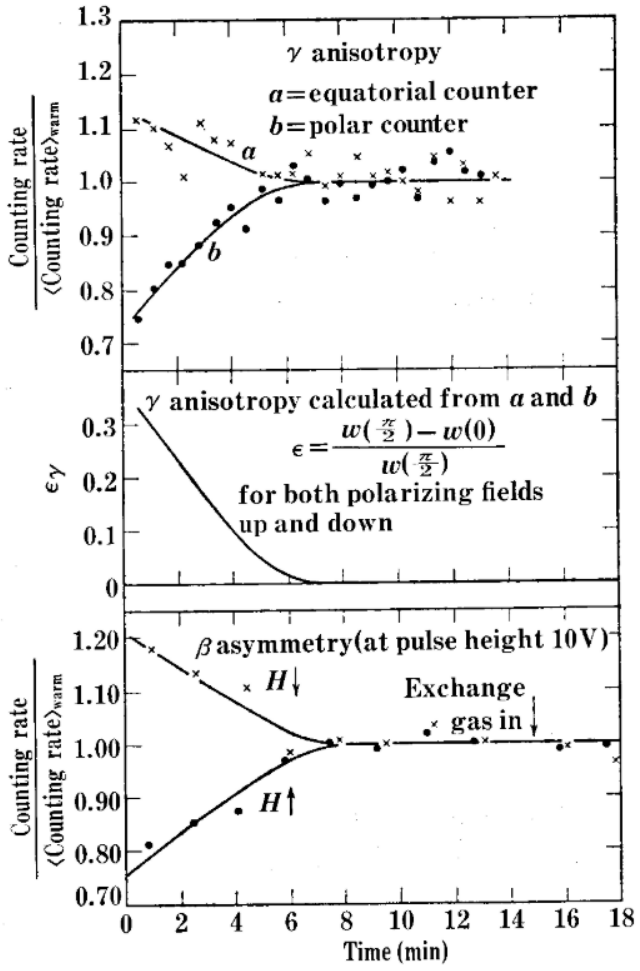

Figure 1.1: Results of the β asymmetry and γ anisotropy from polarized ^{60}Co experiment. The counting rate of the directional counters (a) and (b) in the top plot, indicates an asymmetry in the emission of electrons from the polarized nucleus. The middle plot indicates the anisotropy term γ, where values greater than zero indicates asymmetry in the direction emission of the electrons. Figure from Ref. [10].

The discovery of the parity violation in weak interactions posed the following problem: Why is CP conserved with such a high level of precision in strong interactions? Quantum Chromodynamics (QCD) introduces in the Lagrangian a CP-violating term that arises due to its complex structure in vacuum, given as

$$\mathcal{L}_\theta = \frac{\theta}{32\pi^2} F^a_{\mu\nu} \widetilde{F}^{a\mu\nu}, \tag{1.3}$$

where θ is a QCD phase and $F^a_{\mu\nu}$ and $\widetilde{F}^{a\mu\nu}$ are gluon related tensor and its dual. The CP-violating term in QCD could produce a electric dipolar moment (EDM) of the neutron d_n[11],

$$d_n \simeq 2.9 \times 10^{-17}\theta\ [e\ \mathrm{cm}] + 0.32 d_d - 0.08 d_u + e\left(+0.12\tilde{d}_d - 0.12\tilde{d}_u - 0.006\tilde{d}_s\right), \tag{1.4}$$

where d_q and $\tilde{d}_q$ are the EDM and chromoelectric dipole moments of quarks, respectively. However, current values constrain are $(0.0 \pm 1.1) \times 10^{-26}\ \mathrm{e \cdot cm}$ [12], meaning that CP is a highly conserved value in strong interactions. Why QCD seems to preserve CP is called the strong CP problem.
Peccei and Quinn [13, 14] showed that the problem could be solved by the introduction of a global $U(1)_{\mathrm{PQ}}$ symmetry, by adding the field a

$$\mathcal{L}_\theta = \frac{a}{f_a}\frac{1}{32\pi^2}F^a_{\mu\nu}\widetilde{F}^{a\mu\nu} + \frac{\theta}{32\pi^2}F^a_{\mu\nu}\widetilde{F}^{a\mu\nu}, \tag{1.5}$$

with f_a a decay scale term. Performing the transformation $U(1)_{\mathrm{PQ}} : a \to a - f_a\theta$ allows to absorb the CP-violating phase θ term in QCD in a single coupled field, and the CP-violating term disappears. Weinberg and Wilczek [15, 16] showed that the spontaneous symmetry breaking of the Peccei-Quinn-symmetry leads to the existence of a neutral spin-zero pseudoscalar particle (Nambu-Goldstone boson) with a non-zero mass. Weinberg and Wilczek proposed the simplest realization of the Peccei-Quinn solution, where the decay term f_a is proportional to the electroweak scale. A Nambu-Goldstone boson of the Peccei-Quinn symmetry has a mass and an interaction strength that is given in terms of π^0, scaled with f_π/f_a where $f_\pi = 92\,\mathrm{MeV}$ is the pion decay constant and f_a is a constant related to the axion mass,

$$m_a = \frac{\sqrt{m_u m_d}}{m_u + m_d} m_\pi f_\pi \frac{1}{f_a} \approx 6\ \mu\mathrm{eV}\left(\frac{10^{12}\mathrm{GeV}}{f_a}\right). \tag{1.6}$$

Axions can interact with photons, electrons and nucleons with couplings $g_{a\gamma\gamma}$, g_{ae} and g_{an}, respectively. These couplings are constrained by several accelerator and astrophysical measurements, and the original solution from Weinberg and Wilczek is excluded [17, 18]. Nonetheless, models for 'invisible' axions remain viable, and two well-motivated models are the hadronic axion from the Kim-Shifman-Vainshtein-Zakharov (KSVZ) [19, 20] and Dine-Fischler-Srednicki-Zhitnitsky (DFSZ) models [21, 22]. The interactions of axions (a) with photons through the coupling $g_{a\gamma\gamma}$ can be written in terms of the electric $\mathbf{E}$ and magnetic $\mathbf{B}$ fields [23]

$$\mathcal{L}_{a\gamma\gamma} = -g_{a\gamma\gamma}\, a\, \mathbf{E}\cdot\mathbf{B}, \tag{1.7}$$

where the coupling $g_{a\gamma\gamma}$ can be written as

$$g_{a\gamma\gamma} = \frac{\alpha}{2\pi f_a}\left(\frac{E}{N} - 1.92\right). \tag{1.8}$$

The coefficients E and N are from model-dependent electromagnetic and QCD anomalies, and α is the fine structure constant. The KSVZ model assumes $E/N = 0$, while the DFSZ model assumes $E/N = 8/3$. These two models are commonly used as benchmarks in searches due to their simplicity. Additionally, in the KSVZ model, the axion does not interact with leptons and ordinary quarks at the tree level, which results in a suppression of g_{ae}. An axion-like-particle (ALP) could also interact with other particles similarly to axions, but their mass m_a is not constrained by the scale parameter f_a. Invisible axions could be a candidate for dark matter, as it will be seen in the next section.

1.3 Dark matter

An overwhelming number of observations in the universe indicate the existence of an invisible form of matter that can be detected due to its gravitational effect. This *dark matter* (DM) holds the explanation of what keeps galaxies together and is a fundamental participant in the evolution of large-scale structures in the universe itself. Dark matter candidates that do not couple to photons, have neutral charge, 'weakly' interact with other particles and have a non-zero mass have been proposed [24]. We proceed by listing a selection of the available evidence of its existence and outline how terrestrial detectors could detect particle DM.

1.3.1 The ΛCDM model

The ΛCDM model stands for the Standard Model of cosmology, given cosmological and astrophysical observations. This model holds the current understanding of the evolution of the universe from hot a Big Bang, from which the universe has been continuously expanding in an accelerated manner. This expansion ended up in a universe that is uniform in large scales. The smooth energy density in the early universe makes adequate the use of hydrodynamics equations to describe its expansion as a perfect fluid. The expansion rate is related to the energy content of the universe and can be expressed by the Einstein field equations as [25]

$$R_{\mu\nu} - \frac{1}{2}g_{\mu\nu}R = -8\pi G T_{\mu\nu} + \Lambda g_{\mu\nu}, \tag{1.9}$$

where $R_{\mu\nu}$ is the *Ricci tensor*, associated with the curvature of the space, R is Ricci scalar, and $T_{\mu\nu}$ is the energy-momentum tensor, Λ is the cosmological constant, which accounts for the accelerated expansion of the universe, G is the Newtonian constant of gravitation, and $g_{\mu\nu}$ is the space-time metric.

The Robertson-Walker metric states that there is a comoving frame where we can write [26]

$$ds^2 = dt^2 - a^2(t)\left[\frac{dr^2}{1-Kr^2} + a^2 d\Omega^2\right]. \tag{1.10}$$

Here, $a(t)$ is a scale factor representing the expansion of the universe, and the spatial part dependent on (r, Ω) is a set of coordinates that make the space spherically symmetric (homogeneous and isotropic), and K is a curvature term that arises from the spatial coordinates chosen to represent the isotropy and homogeneity.

If we insert this metric into Equation 1.9 and write the momentum-energy tensor with terms of energy density ρ, we can find the solution given by Friedmann [27]

$$\begin{aligned} H^2 = \left(\frac{\dot{a}}{a}\right)^2 &= \frac{8\pi G\rho}{3} - \frac{K}{a^2} + \frac{\Lambda}{3} \\ \frac{\ddot{a}}{a} &= \frac{\Lambda}{3} - \frac{4\pi G}{3}(\rho + 3p), \end{aligned} \tag{1.11}$$

where the isotopic pressure p, Λ represents a constant in the universe that drives the continuous expansion, the energy density ρ arises when writing the tensor momentum for a perfect fluid: $T_{\mu\nu} = -pg_{\mu\nu} + (p+\rho)u_\mu u_\nu$, where u is the velocity vector for the isotropic fluid in comoving coordinates. This solution provides insight into how the universe expansion is governed. The scale $a(t)$ governs the universe expansion. We can split the density of the universe into three parts

$$\begin{aligned} \rho(t) &= \frac{3H_0^2}{8\pi G}\left(\Omega_{R,0}a^{-4} + \Omega_{M,0}a^{-3} + \Omega_{\Lambda,0}\right) \\ &= \rho_{cr}^0\left(\Omega_{R,0}a^{-4} + \Omega_{M,0}a^{-3} + \Omega_{\Lambda,0}\right), \end{aligned} \tag{1.12}$$

where ρ_{cr}^0 stands for the current value of the critical density parameters, $\rho_{cr} = 3H_0^2/8\pi G$ and the three terms stand for the density of radiation $\Omega_{R,0}$, matter $\Omega_{M,0}$ and dark energy $\Omega_{\Lambda,0}$ present values in terms of the critical density. Therefore, the scale factor in Equation 1.11 depends on relativistic ($\Omega_{R,0}$) and non-relativistic parts ($\Omega_{M,0}$). These can give us different timescales related to which type of matter dominated at different times [15]. We have assumed that $K = 0$, which is the case when the universe is flat, and which is supported by current measurements [28]. The ΛCDM model uses a set of parameters, including the density of baryons and DM, for the prediction of the universe

evolution.

1.3.2 Cosmic microwave background

The Cosmic Microwave Background (CMB) was discovered by Penzias & Wilson [29]. It is the remnant of an earlier universe, approximately 38×10^4 years old (or around 3000 K) [28, 30]. As the universe expanded and experienced adiabatic cooling, it transitioned from a hot plasma of ionised nuclei and free electrons to stable atoms. Without charged particles, the universe became transparent for freely travelling photons [31]. Photons originating from hotter, denser regions had higher energy, in contrast with those from cooler, less dense regions, with lower energies. The pattern of hot and cold fluctuations is embodied in the CMB. The CMB was found to have a very accurate blackbody spectrum, with an average temperature of T = (2.725 $\pm$ 0.001)K [28, 30]. The CMB is isotropic, indicating that the universe was mostly homogeneous at the time of the transition. Nonetheless, the richness of information is contained in the anisotropies of the CMB.

The power spectrum of the CMB temperature anisotropies can be analysed by making a decomposition in spherical harmonics, shown in Figure 1.2. The multipole l represents large angular scales when small, and vice-versa. The power spectrum features a series of peaks, where the first peak corresponds mainly to the density of matter and the third peak to the density of DM. The position of the first peak of the power spectrum is influenced by the curvature of the universe K. The relative heights of the odd and even peaks in the power spectrum are affected by a process on which increasing the fraction of baryons in the universe leads higher odd peaks relative to the heights of the even peaks, called baryon loading. If the density of DM is decreased, the effects of baryon loading are reduced, as denser regions of DM that pull in baryons and photons by gravitational attraction. By considering the first three peaks the different effects and break degeneracies between the effects of baryonic and DM can be disentangled.

The matter density is well constrained by the observations first by WMAP [30] and later by the Planck collaborations [28]:

$$\Omega_{\mathrm{M}} h^2 = 0.1430 \pm 0.0011, \tag{1.13}$$

with h The baryonic density only represents a fraction of Ω_{M}

$$\Omega_{\mathrm{b}} h^2 = 0.02237 \pm 0.00015, \tag{1.14}$$

and leads to conclude that there is a DM component inside the matter density Ω_{M}, which is placed

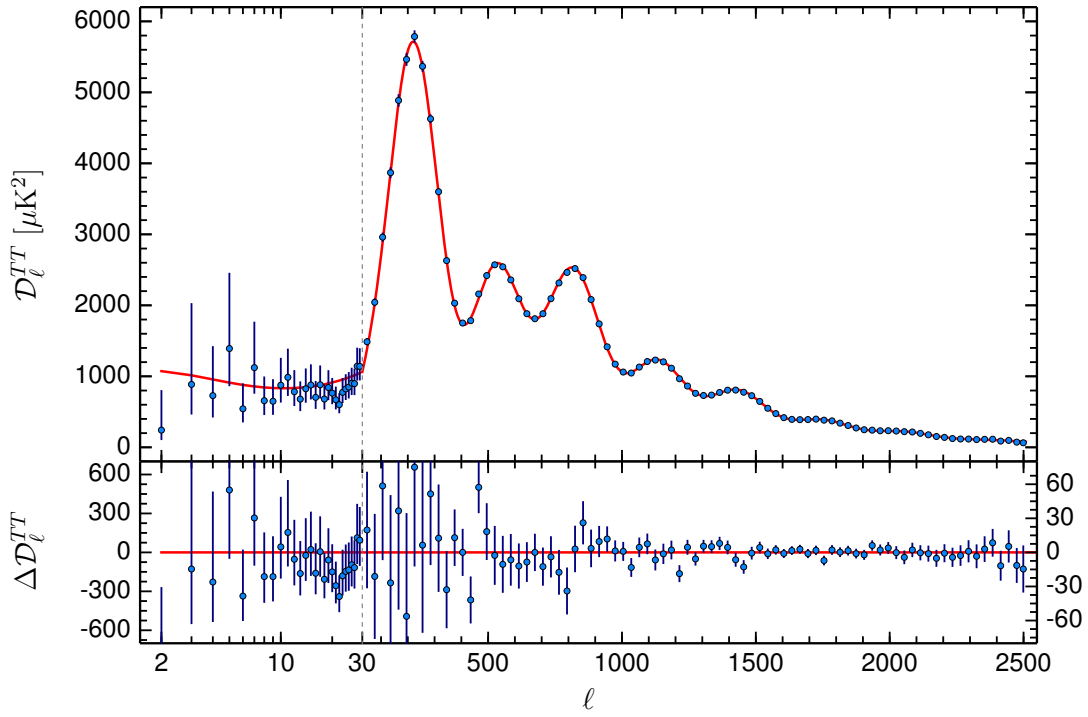

Figure 1.2: Top: The power spectrum of the cosmic microwave background radiation temperature anisotropy in terms of the angular scale (or multipole moment), where the first peak corresponds mainly to the density of matter and the third peak to the density of DM. Bottom: Residuals from the fit of Planck results from 2015. From Ref. [32].

at

$$\Omega_{\rm c}h^2 = 0.1200 \pm 0.0012. \tag{1.15}$$

This value constitutes approximately 85% of the matter content contained in the universe (27% of the total mass-energy). The densities are given in terms of the reduced Hubble constant

$$h = H/\left(100\ \mathrm{km\ s^{-1}Mpc^{-1}}\right). \tag{1.16}$$

1.3.3 Evidence for dark matter in galaxy clusters

One of the primary pieces of evidence of DM existence and total matter distribution is gravitational lensing, which refers to the bending of light due to the curvature of space-time produced by massive bodies [33]. Weak lensing uses the subtle gravitational lensing effects of many galaxies to infer

statistically the large-scale matter distribution in the universe. The measurement is based on small, per cent-level 'shears' or distortions of galaxy shapes due to lensing and conventional weak lensing analysis involves calculating the N-point statistics of the shear field. The weak lensing effect also introduces distortions in the observed cosmic microwave background (CMB) maps [34]. One of the most known images of gravitational lensing due to DM was captured by the Chandra Observatory, where the collision of two large clusters of galaxies was observed, shown in Figure 1.3 and known as the Bullet Cluster. From the gravitational lensing observed in the background of the image, the density of mass in the clusters can be inferred. Most of the mass cannot be observed from the detected light, and its in the form of DM, coloured as blue in the image. The hot gas, made of normal matter in the cluster and coloured in the image as pink, is slowed down in the collision due to the interaction with other particles. The smaller sub-cluster acquires a 'bullet' shape in the collision. The DM part do not interact with itself or other particles and in consequence, is not slowed down in the collision. It effects are only seen by the gravitational interaction, and in contrast with the hot gas, its distribution remains unchanged due to the absence of interactions.

1.3.4 Coma cluster evidence

From an astrophysical point of view, the hints of DM comes from our galactic neighborhood. In the early 1930s, the Fritz Zwicky estimated the total mass of large structures, particularly from the Comma Cluster. From the calculation of the virial theorem and measured the variance of peculiar velocities of the visible matter via redshift, information about the mass in the cluster can be inferred. The virial formula for the M can be written as

$$M = \frac{2\left\langle v^2 \right\rangle}{G\left\langle 1/r \right\rangle}. \tag{1.17}$$

This equation only applies to regular cluster of galaxies, where a statistical equilibrium is reached. Following the assumption of statistical equilibrium, the RMS velocity dispersion is expected to be equal to the velocity dispersion of the visible galaxies in the cluster. This can be measured from the spread of the Doppler shifts, via the X-ray spectrum of the gas. Zwicky found large velocity dispersions, indicating that the cluster density was much higher than the one derived from luminous matter alone.

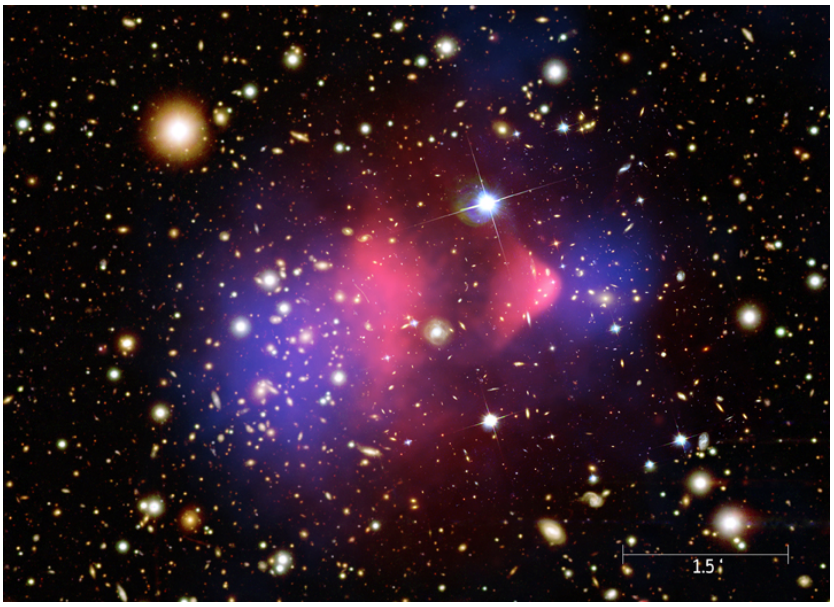

Figure 1.3: Collision of two large clusters of galaxies, as observed by NASA Chandra X-ray Observatory. The hot gas contains most of the normal matter in the cluster. Most of the mass in the cluster, shown in blue, is measured by gravitational lensing from the distortion of background images by mass in the clusters, and is dominated by DM. During the collision, the hot gas in each cluster is slowed and distorted by a drag force. A bullet-shaped cloud of gas forms in one of the clusters. In contrast, the DM shows no distortion from the impact as it cannot interact directly with itself or the gas except through gravity. Therefore, the DM parts from the two clusters can continue, ahead from the hot gas clouds, and produce the separation of the two species as observed in the image. Credit: X-ray: NASA/CXC/CfA.

1.3.5 Rotational curves in spiral galaxies

The circular velocity of an object within a spiral galaxy v_c can be related to its radial distance from the Galactic Centre by Newtonian mechanics as [35]

$$\frac{v_c^2}{r} = \frac{GM(r)}{r^2}, \tag{1.18}$$

where r is the radial distance of that object to the galaxy centre. This equation, valid for a perfectly symmetric distribution of matter, where the velocity should vary with the radius. Taking $M(r)$ equal to the mass in the centre of the galaxy as $M(r) \propto r^3$ (spherical distribution), it follows from this assumption that $v_c(r)$ is proportional to r in a central region of the galaxy. From an outer region, one can confine the total mass M_{total} in an inner core where the density remains constant, the velocity

should fall as

$$v_c(r) = \sqrt{\frac{GM_{total}}{r}}. \tag{1.19}$$

Therefore, v_c should increase as r near the centre of the galaxy and vary as $v_c \propto r^{-1/2}$ in the outer regions. It was observed that the rotational curves from galaxies become flat as the radius increases, as shown in Figure 1.4. The measured rotational curves for galaxies differed from the theoretical expectation [36].

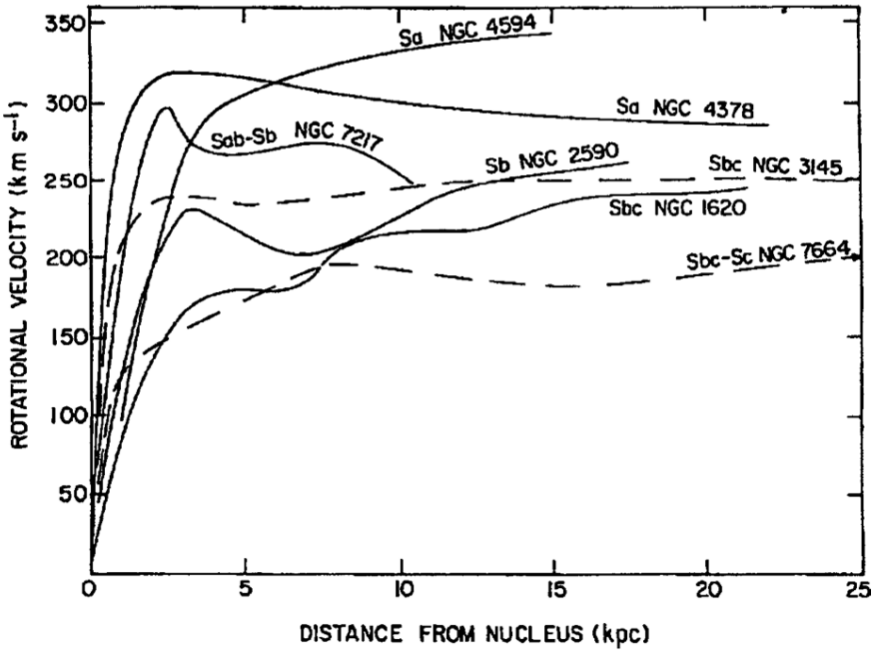

Figure 1.4: Rotational velocities for seven galaxies as a function of distance from the nucleus [36].

In the flat region, v_c depends on the mass of the spiral galaxy. The total mass corresponding to these curves is a few times the mass of the visible stars, and a massive galaxy is expected to emit more light. From rotation curves, the DM mass density distribution is inferred to scale as [37]

$$\rho(r) \propto \frac{M(r)}{r^3} \sim \frac{1}{r^2}, \tag{1.20}$$

which implies that the DM is distributed in a spherically symmetric halo around the centre of the galaxy, in contrast to baryons which are concentrated in the disk. The concentration of baryons in the disk is due to the interaction between baryons, allowing them to dissipate energy and collapse into a disk. The self-interaction of DM is highly constrained by the energy density calculated from cosmological observations, and without a mechanism to radiate energy, the gravitational collapse of

DM into compact objects is suppressed.

1.3.6 Particle candidates to dark matter

Together, the observations mentioned above provide overwhelming evidence for DM in the universe. Within the context of ΛCDM, the galaxies are formed within the DM halos. These halos are the result of a sequence of lower mass halo mergers, with a smooth accretion onto the halo. Therefore, DM acts as a regulator for the formation of large-scale structures, and its identity is one of the most important missing pieces in the cosmological, astrophysical and Particle Physics puzzles. The potential candidate to explain these observations has to be appropriately motivated by cosmology and particle physics models. Moreover, no SM particle can be a good candidate for DM, and the evidence for DM requires a Beyond Standard Model (BSM) explanation [38].

Some model-independent general statements can be derived about the nature of this particle. For example, a DM particle candidate to explain these phenomena must be either a boson or a fermion. Assuming a DM particle that is a scalar boson and using the fact that DM forms halos, there is no limit on the number of bosons that can be packed in the halo, as bosons can occupy a single volume in the phase space without restrictions. Therefore, the stability of the halo is set by the uncertainty principle. Considering a halo of radius R_{halo}, and a DM particle of mass m_χ and velocity v, the uncertainty principle is $\Delta x \Delta p \sim 1$, where $\Delta p \sim m_\chi v$ and $\Delta x \sim 2R_{\text{halo}}$. The halos surrounding dwarf galaxies provide the lowest bounds [39]

$$m_{\text{scalar}} \geq 10^{-22}\text{eV},$$

with m_{scalar} the mass of the scalar boson.
In the case the particle is a fermion, the Pauli exclusion limit sets a limit to the occupation of each volume of phase space,

$$M_{\text{halo}} = m_{\text{ferm}}\, V \int f(p) d^3p \lesssim m_{\text{ferm}}\, V \int d^3p \sim m_{\text{ferm}}\, R_{\text{halo}}^3\, \left(m_{\text{ferm}}\, v\right)^3,$$

where $V = \frac{4}{3}\pi R^3$ is the volume of a spherical halo of radius R, $f(p)$ is the phase-space distribution, m_{ferm} is the mass of the fermionic particle, and $\lesssim$ arises from the maximum in an average of one fermionic particle per unit cell. The phase space of dwarf galaxies set [40]

$$m_{\text{ferm}} \geq 0.7 \text{ keV}.$$

These restrictions can be improved by observing the DM density in the early universe: Initially, the early universe was hot and dense, and all particles were in thermal equilibrium. The annihilation and creation of DM particles was equally in equilibrium (i.e $\chi\chi \rightleftharpoons XX$, where X is a SM particle and χ a DM particle) [41]. As the universe expanded, the probability of a DM particle finding a DM antiparticle to annihilate decreased until this reaction stopped, and the DM density remained constant in time. When this 'freeze-out' occurred, the DM particle could have either relativistic or non-relativistic velocities, referred to as *hot* or *cold* DM, respectively. This difference has consequences in the formation of structures in the universe, as the *hot* DM cannot form clusters without cooling down to non-relativistic velocities. Current observations favour the cold DM (CDM) hypothesis, given the evolution of the universe and the formation of structures [42].

The WIMP miracle

In the case of CDM, the Boltzmann equation provides a way to calculate quantitatively the evolution of the number density given the annihilation process before the freeze-out of a particle in thermal equilibrium in the primordial plasma

$$\frac{dn_\chi}{dt} + 3Hn_\chi = -\langle\sigma_A v\rangle\,[(n_\chi^2 - (n_\chi^{eq})], \tag{1.21}$$

where the DM number density n_χ decreases with the expansion of the universe and H is the expansion rate of the universe. The term $\langle\sigma_A v\rangle$ represents the thermally averaged cross section for the annihilation, and n_χ^{eq} indicates the number density in the equilibrium of the annihilation process. The thermal relic density can be determined by solving numerically Equation 1.21. However, a simple approximation can be obtained. Defining the freeze-out at time T_f when $n_\chi\langle\sigma_A v\rangle = H$,

$$n_f \sim (m_\chi T_f)^{3/2}\exp(-m_\chi/T_f) \sim \frac{T_f^2}{M_{Pl}\langle\sigma_A v\rangle^{-1}}, \tag{1.22}$$

where the subscripts f denote the quantities at the freeze-out, $M_{Pl} = \sqrt{\frac{\hbar c}{G}}$ is the Planck mass, and m_χ is the DM particle mass. The thermal relic density can then be written as

$$\Omega_X = \frac{m_X n_0}{\rho_c} = \frac{m_X T_0^3}{\rho_c}\frac{n_0}{T_0^3} \sim \frac{m_X T_0^3}{\rho_c}\frac{n_f}{T_f^3} \sim \frac{x_f T_0^3}{\rho_c M_{\rm Pl}}\langle\sigma_A v\rangle^{-1} \sim 0.1\left(\frac{0.01}{\alpha}\right)^2\left(\frac{m_\chi}{100{\rm GeV}}\right)^2, \tag{1.23}$$

where ρ_c is the critical density and the subscript 0 denotes the present day quantities, and $\alpha^2/m_\chi^2 \sim \langle\sigma_A v\rangle$. Assuming a weakly interacting DM particle with $\alpha \sim 0.01$ and mass $m_\chi = 100$ GeV gives

the correct abundance measured by Planck and WMAP collaborations. The finding that a weak-scale ($\sigma \sim G_F^2 T^2$, with G_F the Fermi constant) DM particle (or Weakly Interacting Massive Particles, WIMPs) can reconstruct the observed energy density is known as *The WIMP miracle*. WIMPs have been the dominating paradigm in DM detection and are well motivated by supersymmetry theories such as Minimal Supersymmetric Standard Model (MSSM) [43], Phenomenological Minimal Supersymmetric Models (pMSSM) [44] or pseudo-Goldstone Boson DM models [45]. More details on the WIMP paradigm can be found in Refs. [46, 47]. The mass range for a WIMP is typically taken from $\mathcal{O}\left(2\ \mathrm{GeV/c^2}\right)$ to $\mathcal{O}\left(100\ \mathrm{TeV/c^2}\right)$ [38].

Axions

Axions could make up the DM content or part of it [48]. The favoured region of axion mass parameter space, given the production mechanism that would recreate the relic density in which axions may be all of the DM, can be taken as $1\ \mu\mathrm{eV} \lesssim m_a \lesssim 100\ \mu\mathrm{eV}$ [43].

1.3.7 Dark matter searches

The detection of DM is divided into three categories that are complementary to each other:

- **Production**: The particle is created through the high-energy collisions of particles in accelerators, such as the LHC. The DM particle escapes the detector, and the observables are the missing energy and momentum in the collision. The DM particle mass must be smaller than the centre of mass energy for particle creation. The search for the production of DM particles in the LHC is extensively documented in literature [49, 50, 51, 52].

- **Indirect**: The detection is aimed at the products of the DM particle-antiparticle annihilation, such as γ-rays, neutrinos or positrons. The annihilation rate depends on the density of both particle species unless the DM particle is its own antiparticle, and stronger signals are expected in high-density regions, such as the Galactic Centre. Reviews on results from indirect searches can be found in Refs. [53, 54].

- **Direct**: The detection is aimed at the interaction of the flux of DM particles that traverse the Earth with detectors. The interaction can occur in the form of scattering with an SM particle or the interaction with electromagnetic fields. The first is used to search for WIMP and axions, while the latter is used to detect axions, and both will be discussed in the following sections.

Dark matter flux on Earth and scattering with targets

Direct detection relies on the flux of DM particles reaching Earth and interacting with detectors. The terrestrial flux of DM particles bounded to the galactic halo is called galactic DM. The flux depends on the local DM density, which determines the number of particles, and velocity distribution, which determines the energy available in the interaction. The DM velocity with respect to the Galactic Centre is assumed is assumed to follow a Maxwellian distribution $f(\mathbf{v}, t)$ in all directions[2]. The upper limit of this distribution is given by the galactic escape velocity, v_{max}. The spherical symmetry of the DM particle velocity distribution is broken for the observed lab-frame distribution on Earth. This flux is sometimes called the 'WIMP wind' [55].

The expected scattering rate of DM particles of mass m_χ with the nucleus of a target material, given the motion of Earth in the Galaxy is

$$\frac{dR}{dE_R} = \frac{\rho_\chi}{m_\chi m_N} \int_{v_{\text{min}}}^{v_{\text{max}}} d^3v v \tilde{f}(\mathbf{v}, t) \frac{d\sigma}{dE_R}, \tag{1.24}$$

where $\tilde{f}(\mathbf{v}, t)$ is the velocity distribution of the DM particles with velocity $\mathbf{v}$ in the lab frame, $\frac{d\sigma}{dE_R}$ is the differential cross section, v_{max} is the escape velocity, v_{min} the minimum velocity required to produce a scatter with the nuclei of mass m_N with a cross section σ. The local DM density ρ_χ was measured as $0.3\,\text{GeV/cm}^3$ [56, 57] and v_{max} is taken as $544\,\text{km/s}$ [58] in the galactic rest frame. The minimum velocity to produce a recoil is given by

$$v_{\text{min}} = \sqrt{m_N E/(2\mu^2)}, \tag{1.25}$$

where $\mu = m_\chi m_N/(m_\chi + m_N)$ is the DM particle-nucleus reduced mass. The scatter of the DM particle will produce a recoil of energy [59]

$$E_R = E_\chi \frac{4 m_N m_\chi}{(m_N + m_\chi)^2} cos^2(\theta_R), \tag{1.26}$$

where E_χ is the kinetic energy of the DM particle, m_χ its mass, m_N the mass of the recoiling nucleus and θ_R is the angle of the nuclear recoil relative to the direction given by the DM particle. As an example, the kinetic energy of an incident DM particle with a mass of $100\,\text{GeV}$ is $10\,\text{keV}$, which is much smaller than the nuclear binding energy of an atomic target (in the MeV scale). The scatter can be considered with the nucleus coherently, neglecting its constituents.

[2] If they are in thermodynamic equilibrium.

For WIMP particle, the differential cross section can be written as

$$\frac{d\sigma}{dE_R} = \left(\frac{d\sigma}{dE_R}\right)_{SI} + \left(\frac{d\sigma}{dE_R}\right)_{SD} = \frac{m_N}{2\mu^2 v^2}\left(\sigma_{SI}F^2(q) + \sigma_{SD}S(q)\right), \tag{1.27}$$

where $F^2(q)$ (σ_{SI}) and $S(q)$ (σ_{SD}) are the spin-independent (SI) and spin-dependent (SD) form factors (cross sections), respectively. The spin-independent term for the cross section is given by

$$\sigma_{\mathrm{SI}} = \frac{4}{\pi}\mu^2\left(Z\mathcal{F}_P + (A-Z)\mathcal{F}_N\right)^2, \tag{1.28}$$

where Z and A are the atomic and atomic mass numbers, and $\mathcal{F}_P$ and $\mathcal{F}_N$ are the couplings to protons and neutrons, respectively. It is clear from this expression that increasing cross sections can be find for heavier atoms. When considering only the spin-dependent cross section and assuming independent scattering with protons or neutrons, the total differential cross section can be written as [60]

$$\frac{\mathrm{d}\sigma_{\mathrm{SD}}}{\mathrm{d}E_{\mathrm{R}}} = \frac{E_{\mathrm{R}}}{3\mu_P v^2}\frac{4\pi}{2J+1}S_P\left(E_{\mathrm{R}}\right)\sigma_P, \tag{1.29}$$

where the subscript P stands for protons, S_P is a structure function and σ_P is the cross section of the scattering with a single nucleon. An identical expression can be found with the assumption that the scattering with protons is equal to the scattering with neutrons. Direct detection measurements are located in underground laboratories to shield from the constant flux of cosmic particles. Many types of direct search detectors exist using diverse materials and methods to reject backgrounds. The energy transfer to the nucleus recoil can be detected as heat, scintillation, and charge, depending on the target. For example, as experiments that searched using scintillators we can list DAMA/LIBRA [61], DEAP-3600 [62], XMASS [63]. Current experiments are COSINE [64] and ANAIS [65]. The experiments searching the generated charge by the recoil are DAMIC [66], SENSEI [67], PICO [68]. Another set of experiments search in both heat and charge, such as SuperCDMS [69], or heat and light, such as CRESST [70]. Noble liquid dual-phase TPCs aim to detect DM using light and charge signals, and these will be treated in this work.

Noble liquids

For spin-independent couplings, the expected rate of WIMP scattering with target atoms increases by the square of the atomic mass due to the coherent summation over all the scattering centres in the nucleus. Consequently, this process is enhanced on heavy target nuclei and more pronounced when WIMP mass is comparable to the atomic mass of the target nuclei, as shown in Figure 1.5.

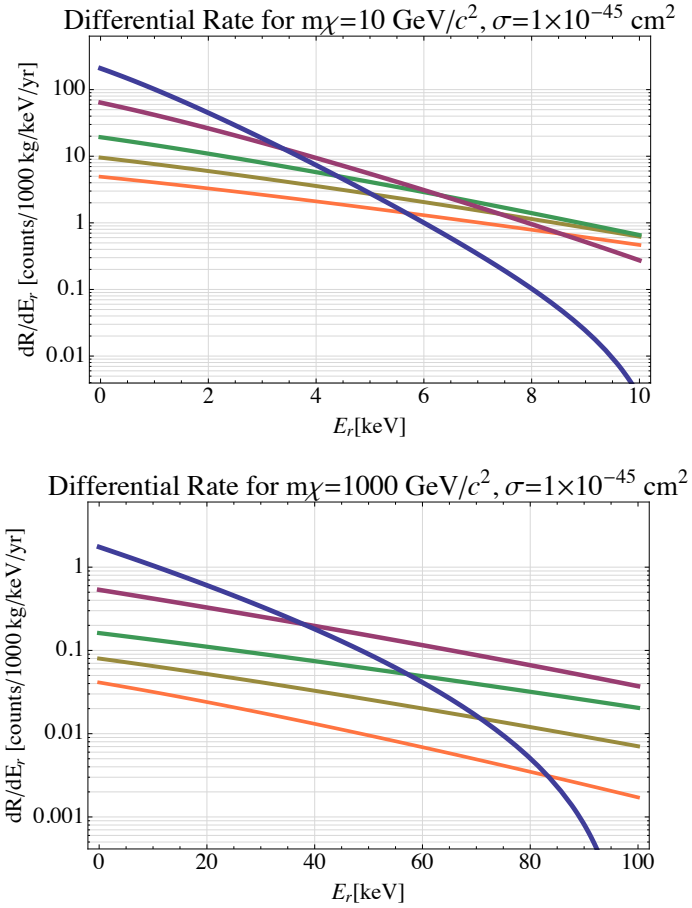

Figure 1.5: Differential rate versus nuclear recoil energy for 10 GeV and 1000 GeV WIMP masses assuming a spin-independent WIMP-nucleon cross section of 10^{-45} cm^2, shown for xenon (blue), germanium (purple), argon (green), silicon (brown) and neon (orange) target. Figure adapted from Ref. [71].

Noble liquids such as Xe and Ar are excellent scintillators [72], which make them very attractive target materials in astroparticle and neutrino physics. Liquid argon (LAr) and liquid Xenon (LXe) provide both a high light yield and an ionisation potential [73, 74], and they are an example of target materials that can be used to detect both charge and scintillation. These target materials are used in Time Projection Chambers (TPCs), where the interaction of an incident particle produces scintillation and ionisation-proportional scintillation, which are detected by photomultipliers (PMTs) [75]. The high density of LXe and atomic number mean that gamma rays have a short interaction length, and LXe acts as a self-shield for external radiation. The previous LXe experiments XENON1T [76], LUX [77], PandaX-4T [78], and the LAr TPCs DarkSide-50 [79] and DEAP-3600 [62] placed the most stringent limits in the SI and SD WIMP-nucleon couplings at different mass scales (mainly from

1–1000 GeV). These exclusion limits are based on the lack of signals assigned to a WIMP or WIMP-like particle. The next generation experiments, XENONnT [80] and LZ [81] are currently acquiring data and aim to improve the current limits further.

Considering the ever-improving sensitivity of DM direct searches over the last decades, it will become unavoidable to measure not only possible WIMP interactions with the target material but also the neutrino flux from several astrophysical sources [82]. The coherent elastic neutrino-nucleus scattering (CEνNS) was observed by the COHERENT experiment [83]. The implication for LXe TPCs is that astrophysical neutrinos, particularly solar ^{8}B neutrinos, interacting coherently with the xenon nucleus will be observed. At this stage, a DM particle and an astrophysical neutrino would leave similar signatures in the detector. The rate of this process in LXe is covered in the Refs.[84, 85, 86, 87, 82, 88, 89, 90]. Recent works [89, 90] have emphasised that these neutrino backgrounds do not impose a hard limit on physics reach by running statistical analyses and deriving a discovery limit for WIMPs in different regions of the parameter space.
The DARWIN (DARk matter WImp search with liquid xenoN) observatory will be a next-generation detector containing 50 tonnes (40 tonnes active) of xenon for DM searches, aiming to reach the neutrino region in the Spin-Independent WIMP parameter space but also with a very broad neutrino and rare interaction program [91]. Figure 1.6 shows the exclusion limits in the SI WIMP-nucleon cross section given by past and current detectors, as well as the projected median sensitivity of the DARWIN experiment.
DARWIN will also be sensitive to signals from axions produced in the Sun when blackbody photons are converted to axions due to the presence of strong electromagnetic fields in the plasma [98]. This process is called the Primakoff effect, and the expected flux from this production channel is referred to as the Primakoff flux. Similarly, axions may be produced from their coupling to electrons and nucleons. These axions are called *solar axions*, and will be treated later in this work in Chapter 4 when estimating the sensitivity of DARWIN.

1.4 Solar and galactic axions

Axions may be produced in the interior of starts, and their production provides another mechanism for stars to lose energy, leading to potentially observable modifications in the properties of stars or stellar populations. Two particular sensitive observables are the stars in the Horizontal Branch (HB) and Red-Giant Branch (RGB), which provide strict constraints on the coupling parameters [99]. The energy loss during the RGB phase leads to a larger core mass in simulations [100, 101]. To

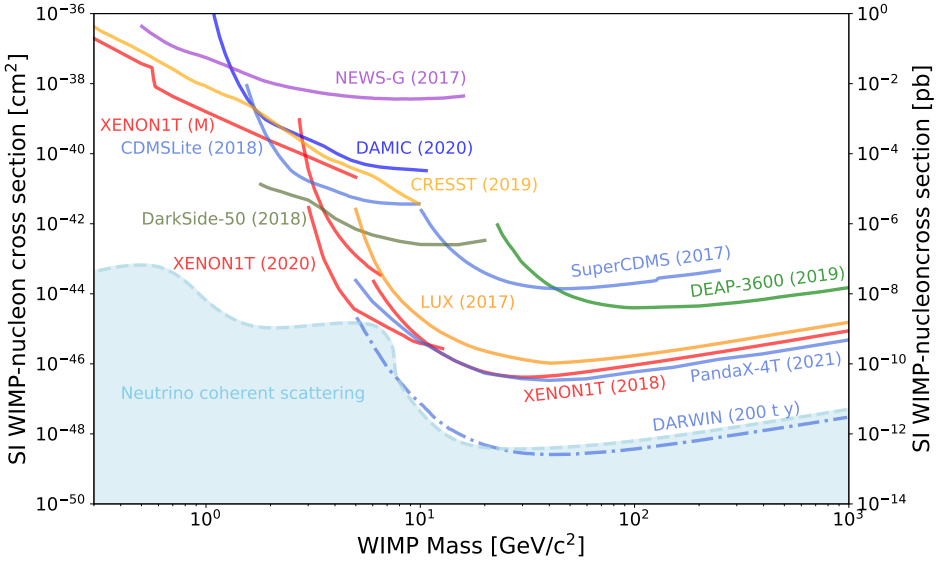

Figure 1.6: Spin-independent WIMP-nucleon scattering results: Existing upper limits from the CRESST-II [92], DAMIC [66], NEWS-G[93], CDMSLite [94] SuperCDMS [69], PandaX-4T [78], DarkSide-50 [79], XENON100 [80], DEAP3600[62], LUX [95], XENON1T [76], and the projections for DARWIN [91] and neutrino coherent scattering [96]. Figure from Ref. [97].

quantify the cooling of stars, the R-parameter is used, taken as $R = N_{\mathrm{HB}}/N_{\mathrm{RGB}}$, which compares the numbers of stars in the HB, N_{HB}, to the number of stars in the upper portion of the RGB, N_{RGB}, which results on a favoured region in the parameter space in the couplings of axions to photons and electrons. Moreover, if axions decay by $a \to 2\gamma$, the lifetime drops below the age of the universe for $m_a \gtrsim 20$ eV [102].

Solar axions could be detected in LXe TPCs by signals that arise in the detector from the induced recoil, which will be covered in more detail in the following chapters. The recoil of a hypothetical axion with the LXe target is via the interaction of axions with atoms, and it can be used to place limits in the g_{ae} and $g_{a\gamma\gamma}$ couplings. Moreover, the excess reported by XENON1T in 2020 [103] could be explained by solar axions. The future experiments LZ [104], XENONnT [104] and PandaX-4T [78] aim to probe further the region with the reported excess and confirm or exclude a signal. Figure 1.7 shows the limits in the axion coupling to electrons, g_{ae}, from underground detectors and astrophysical sources. The region inside the orange band is usually referred as QCD axions, where the scale parameter f is related to the axion mass. Outside this region, solar axions are referred as ALPs and their mass is unconstrained by the scale parameter, but do not provide a solution for the CP-strong problem. Underground detectors, particularly LXe TPCs, provide a complimentary direct detection to the astrophysical bounds.

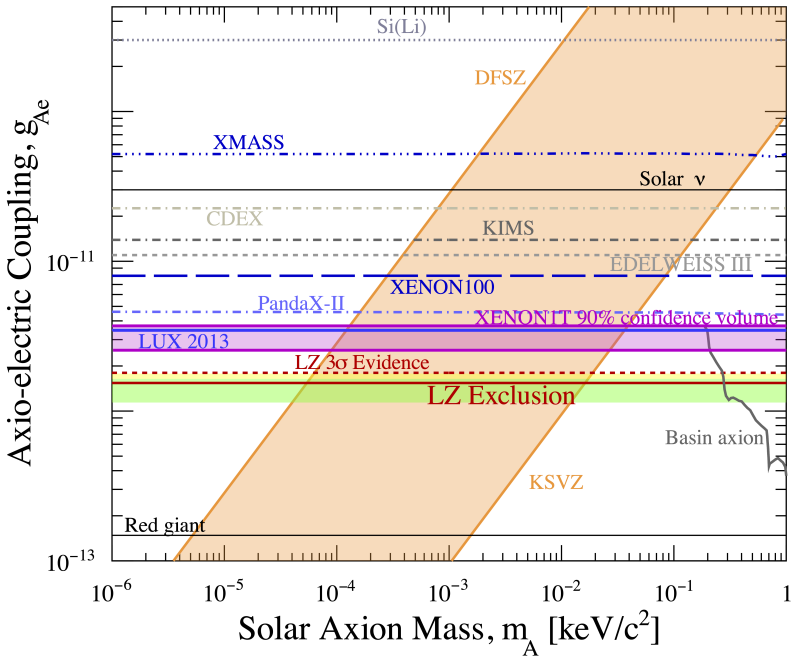

Figure 1.7: Limits in the axion coupling to electrons from XENON100 [105], EDELWEISS [106], XENON1T [103], LUX [107], and XMASS [108]. The figure contains as well limits from indirect constraint from the solar neutrino flux [109] and experimental constraints from solid state experiments [110, 111, 112]. Also shown in the figure is the constraint from a model that includes a 'stellar basin' of gravitationally bound axions [113]. Figure from Ref. [104].

Solar axions could be detected in a very different type of detector, called helioscopes. Helioscopes aim to detect the back-conversion of axions to X-ray photons using a powerful transverse magnetic field [114]. An example of this detector is the CERN Axion Solar Telescope (CAST), which placed strong limits in the $g_{a\gamma\gamma} < 8.8 \times 10^{-11}$ GeV^{-1} coupling for masses below $m_a < 0.02$ keV [115]. In the future, the IAXO experiment has been proposed to improve the sensitivity toward lower couplings in a larger mass range [116].

For the detection of galactic axions (i.e. axions from the DM in the galactic halo), haloscopes have been proposed and built, with the advantage of detecting lower axion masses [98], as the mass range for DM axions is 1 μeV $\lesssim m_a \lesssim$ 100 μeV, mentioned in previous sections. Haloscopes typically use a resonant microwave cavity in the centre of a strong solenoid magnet. The axion can convert its rest mass to a photon in the presence of a static magnetic field. This process can be enhanced by tuning the resonant frequency of the cavity and matching the mass of the axion. Example of this

type of detector are ADMX [117], ABRA [118], and SHAFT [119]. Limits on the coupling of DM axions to photons from haloscopes, helioscopes, and astrophysical sources are shown in Figure 1.8.

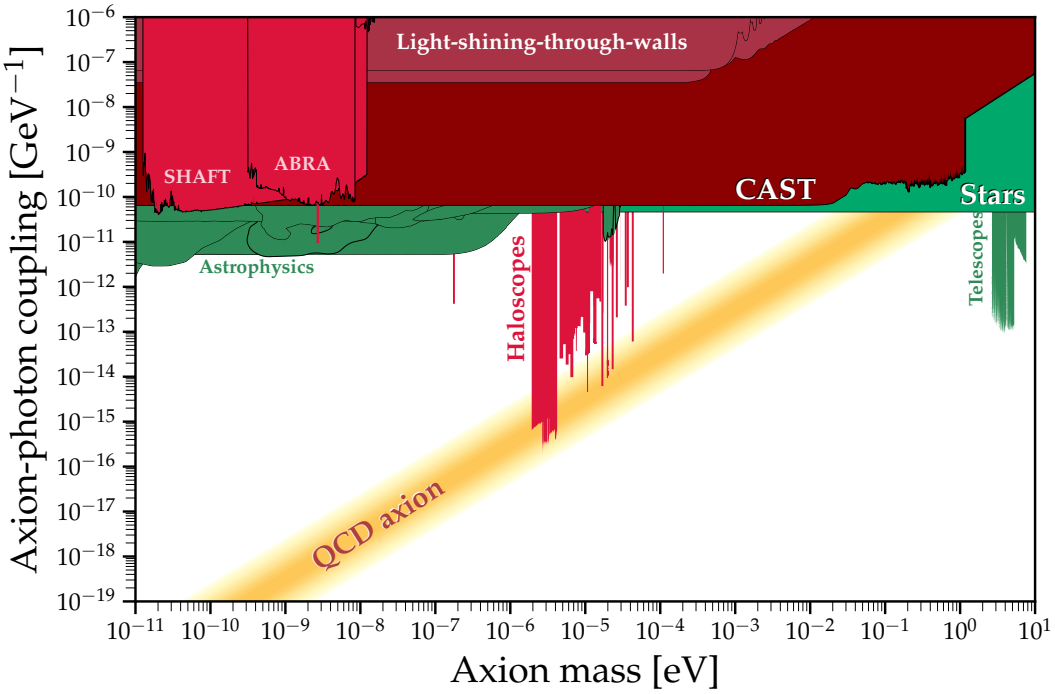

Figure 1.8: Limits in the axion coupling to photons from CAST [115], and haloscopes: ADMX [117], ABRA [118], SHAFT [119], Telescopes [120], and light-shining-through-walls [121, 122, 123]. Plotting scripts and data available in Ref. [124].

1.5 Massive neutrinos and neutrinoless double beta decay

LXe DM detectors, like the ones described above, can search for neutrino signals due to their low backgrounds. The neutrino induced signals in the TPC can provide information about their properties, such as the mass generation mechanism. Given the natural abundance of ^{136}Xe in xenon, it is possible to look for the neutrinoless double beta decay ($0\nu\beta\beta$) of ^{136}Xe in LXe TPCs such as XENON1T [125], and in the future, XENONnT [125] and DARWIN [126]. The calculation of the sensitivity for DARWIN is part of this work.

1.5.1 Neutrino oscillations and mass mechanism

In the SM, neutrinos are fermions that do not have strong or electromagnetic interactions. In the SM, the masses of the fermions are generated via Yukawa couplings to the Higgs boson, with a fermion right-handed and left-handed component. Nevertheless, no right-handed neutrinos were observed so far [127], and the Yukawa interaction term cannot be constructed. Therefore, inside the SM, the neutrinos are massless. Pontecorvo proposed in 1957 a mechanism in which neutrinos would oscillate to antineutrinos, and later Maki, Nakagawa and Sakata proposed the neutrino flavour mixing and flavour oscillations [128, 129]. The flavour oscillation of neutrinos implies that they have mass and that the SM is incomplete.

Davis, Harmer and Hoffman were the first to observe a deficit from the expected flux of neutrinos coming from the Sun [130]. The Kamiokande experiment made the first directional counting observation and confirmed the deficit [131], later joined by SAGE [132] and GALLEX [133], validating what is known now as the 'solar neutrino problem'. In 1998, the Super-Kamiokande experiment observed oscillations in atmospheric neutrinos and provided the first evidence of neutrino oscillation [134]. Both searches were performed by looking for charge-current inverse beta decay interactions. Shortly after, in 2002, the SNO experiment observed neutral current neutrino-nucleon interactions from solar neutrinos, along with charged current neutrino-nucleon interactions and elastic scatters on electrons, providing further evidence that neutrino oscillations were the cause of the solar neutrino problem [135]. The mechanism of neutrino oscillation is described by assuming that the weak eigenstate of neutrinos, ν_α are produced by a linear combination of the mass eigenstates ν_i [136]

$$|\nu_\alpha\rangle = \sum_{i=1}^{n} U^*_{\alpha i} |\nu_i\rangle \,, \tag{1.30}$$

where n is the number of light neutrino species, and U is the Pontecorvo-Maki-Nakagawa-Sakata (PMNS) mixing matrix, given by

$$U = \begin{pmatrix} c_{12}c_{13} & s_{12}c_{13} & s_{13}e^{-i\delta} \\ -s_{12}c_{23} - c_{12}s_{13}s_{23}e^{i\delta} & c_{12}c_{23} - s_{12}s_{13}s_{23}e^{i\delta} & c_{13}s_{23} \\ s_{12}s_{23} - c_{12}s_{13}c_{23}e^{i\delta} & -c_{12}s_{23} - s_{12}s_{13}c_{23}e^{i\delta} & c_{13}c_{23} \end{pmatrix} \tag{1.31}$$

where $c_{ij} \equiv \cos\theta_{ij}$ and $s_{ij} \equiv \sin\theta_{ij}$, $\theta_{ij} \in [0, \pi/2]$ and the phase δ accounts for CP-violation.

We can reduce the problem in order to obtain a simplified probability of the neutrino oscillating in flavour. We consider a ultra-relativistic neutrino of mass and momentum m_i and p_i, respectively.

The energy E_i can be written as

$$E_i = \sqrt{p^2 + m_i^2} \simeq p + \frac{m_i^2}{2p} \simeq p + \frac{m_i^2}{2E}. \tag{1.32}$$

By considering only two flavours e, μ, in which the U mixing matrix is 2×2, we can write the probability of transition from ν_e flavour to ν_μ, after covering a distance L, as [137]

$$P\left(\nu_e \to \nu_\mu; L\right) = \sin^2 2\theta_0 \sin^2\left(\pi \frac{L}{l_{osc}}\right). \tag{1.33}$$

Here, θ_0 stands for the mixing angles in the 2×2 matrix, and

$$l_{osc} = \frac{4\pi E}{\Delta m^2} \simeq 2.48 m \frac{E(\mathrm{MeV})}{\Delta m^2\left(\mathrm{eV}^2\right)} = 2.48 \text{ km} \frac{E(\mathrm{GeV})}{\Delta m^2\left(\mathrm{eV}^2\right)}, \tag{1.34}$$

where $\Delta m^2 = m_2^2 - m_1^2$ and E is the neutrino energy.
In the case of three neutrino mixing, there are two independent mass-squared differences. From the analysis of experimental data, it follows that one mass-squared difference is about 30 times smaller than the other one [138]. The small solar and large atmospheric mass-squared differences are referred to by the origins of the neutrino species in which they can be observed experimentally. They are denoted by Δm_S^2 and Δm_A^2, respectively.
The solar and atmospheric mass-squared differences are given by

$$\Delta m_S^2 \equiv \Delta m_{12}^2, \tag{1.35}$$

$$\Delta m_A^2 \equiv \Delta m_{31}^2, \tag{1.36}$$

respectively, assuming the definition $\Delta m_{ki}^2 = m_i^2 - m_k^2$. From measurements of the energy dependence of the oscillation probability for different solar neutrino species it follows that [139]

$$\Delta m_{12}^2 > 0. \tag{1.37}$$

For the mass of the third neutrino m_3 there are two possibilities:

1. Normal ordering (NO)

$$m_3 > m_2 > m_1 \tag{1.38}$$

2. Inverted ordering (IO)

$$m_2 > m_1 > m_3. \tag{1.39}$$

The atmospheric mass-squared difference Δm^2_A can be determined as follows

$$\Delta m^2_A = \Delta m^2_{23} \text{ (NO)}, \quad \Delta m^2_A = |\Delta m^2_{13}| \text{ (IO)}. \tag{1.40}$$

In NO case for the neutrino masses m_2 and m_3 we obviously have

$$m_2 = \sqrt{m_1^2 + \Delta m^2_S}, \;\; m_3 = \sqrt{m_1^2 + \Delta m^2_S + \Delta m^2_A}. \tag{1.41}$$

In the case of IO we find

$$m_1 = \sqrt{m_3^2 + \Delta m^2_A}, \quad m_2 = \sqrt{m_3^2 + \Delta m^2_A + \Delta m^2_S}. \tag{1.42}$$

Values of Δm^2_S and Δm^2_A, the δ CP phase, and the neutrino mixing angles are shown in Table 1.1.

Table 1.1: Values of neutrino oscillation parameters, obtained from the global fit of the data from Ref. [140].

Parameter	Normal Ordering	Inverted Ordering
$\sin^2\theta_{12}$	$0.310^{+0.013}_{-0.012}$	$0.310^{+0.013}_{-0.012}$
$\sin^2\theta_{23}$	$0.582^{+0.015}_{-0.019}$	$0.582^{+0.015}_{-0.018}$
$\sin^2\theta_{13}$	$0.02240^{+0.00065}_{-0.00066}$	$0.02263^{+0.00065}_{-0.00066}$
δ/π	$1.20^{+0.23}_{-0.14}$	1.54 ± 0.13
Δm^2_S	$(7.39^{+0.21}_{-0.20}) \times 10^{-5}$ eV^2	$(7.39^{+0.21}_{-0.20}) \times 10^{-5}$ eV^2
Δm^2_A	$(2.525^{+0.033}_{-0.031}) \times 10^{-3}$ eV^2	$(-2.512^{+0.034}_{-0.031}) \times 10^{-3}$ eV^2

1.5.2 Mass generation mechanism for neutrinos

The reconstruction of mass terms in the Lagrangian requires adjusting the SM. By extending the SM with m number of right-handed 'sterile' neutrinos ν_s, we can build two types of mass terms [141]

$$-\mathcal{L}_{M_\nu} = M_{Dij}\bar{\nu}_{si}\nu_{Lj} + \frac{1}{2}M_{Nij}\bar{\nu}_{si}\nu^c_{sj} + \text{ h.c. }, \tag{1.43}$$

with ν^c a neutrino charge conjugated field (charge conjugation operator C), ν_L are left-handed neutrinos, M_D a complex matrix of dimension $m \times 3$ and M_N a symmetric $m \times m$ matrix. Similar to the charged fermions, the first term in Equation 1.43 comes from the spontaneous electroweak symmetry breaking from Yukawa interactions, and it is called the Dirac mass term. Including this

term in the neutrino minimal standard model (νMSM) implies that the Yukawa coupling related to the neutrino mass term has to be ten orders of magnitude smaller than the ones from quarks and charged leptons. The second term is called a Majorana mass term and as opposed to the Dirac term, involves two neutrinos fields, breaking the lepton number conservation by two units [142]. Both terms can contribute to the mass generation, and they appear summed in the Lagrangian. One can rewrite Equation 1.43 as

$$-\mathcal{L}_{M_\nu} = \frac{1}{2}\left(\overline{\vec{\nu}_L^{\,c}}, \overline{\vec{\nu}_s}\right)\begin{pmatrix} 0 & M_D^T \\ M_D & M_N \end{pmatrix}\begin{pmatrix} \vec{\nu}_L \\ \vec{\nu}_s^{\,c} \end{pmatrix} + \text{ h.c. } \equiv \overline{\vec{\nu}^c} M_\nu \vec{\nu} + \text{ h.c.} \tag{1.44}$$

where the matrix M_ν is complex and symmetric, and $\vec{\nu} = (\vec{\nu}_L, \vec{\nu}_s^{\,c})^T$ is a $(3+m)$-dimensional vector. By diagonalising M_ν with a unitary matrix V^ν of dimension $(3+m)$, one obtains

$$(V^\nu)^T M_\nu V^\nu = \text{diag}\,(m_1, m_2, \ldots, m_{3+m})\,. \tag{1.45}$$

The weak eigenstates can be then expressed in term of $3+m$ mass eigenstates, $\vec{\nu}_{\text{mass}} = (V^\nu)^\dagger \vec{\nu}$. Equation 1.44 can be written as

$$\begin{aligned} -\mathcal{L}_{M_\nu} &= \frac{1}{2}\sum_{k=1}^{3+m} m_k \left(\bar{\nu}^c_{\text{mass},k}\nu_{\text{mass},k} + \bar{\nu}_{\text{mass},k}\nu^c_{\text{mass},k}\right) \\ &= \frac{1}{2}\sum_{k=1}^{3+m} m_k \bar{\nu}_{Mk}\nu_{Mk}, \end{aligned} \tag{1.46}$$

where

$$\nu_{Mk} = \nu_{\text{mass},k} + \nu^c_{\text{mass},k} = \left(V^{\nu\dagger}\vec{\nu}\right)_k + \left(V^{\nu\dagger}\vec{\nu}\right)^c_k. \tag{1.47}$$

When a charge conjugation operator is applied to Equation 1.47, one obtains $\nu_M = \nu_M^c$, which is necessary for the mass production mechanism to work, and it is referred to as the Majorana condition. The Majorana condition can be described as only one field for both neutrino and antineutrino states, unlike the case where two different fields describe particle and antiparticle. In summary, it is described by a two-component spinor, unlike charged Dirac particles, represented by four-component spinors. If ν_i are Majorana particles, the mixing matrix is characterized by three angles and three phases and has the form

$$U^M = U\ S^M(\alpha), \tag{1.48}$$

where

$$S^M(\alpha) = \begin{pmatrix} e^{i\alpha_1/2} & 0 & 0 \\ 0 & e^{i\alpha_2/2} & 0 \\ 0 & 0 & 1 \end{pmatrix}, \tag{1.49}$$

with U the PMNS matrix and α_1 and α_2 the unknown Majorana phases.
If one imposes $M_N = 0$ in Equation 1.43, only the Dirac component is allowed. This scenario would not explain why neutrinos are much lighter than the charged fermions, as they would acquire mass with the same mechanism.

Shedding light on the mass generation mechanism with neutrinoless double beta decay

Certain even-even nuclei (Z, A) can transform into lighter stable nuclei by the conversion of two neutrons into protons under the emission of two electrons and two electron anti-neutrinos, a double beta ($2\nu\beta\beta$) decay, in which the nuclear charge changes by two units,

$$(Z, A) \rightarrow (Z + 2, A) + 2e^- + 2\bar{\nu}_e. \tag{1.50}$$

This process is possible when the binding energy of the final nucleus has a higher binding energy that undergoing a simple β-decay [143]. The half-life in the case of a two neutrino double beta decay can be factorised to

$$\left[T^{2\nu}_{1/2}\right]^{-1} = G_{2\nu} \left|M_{2\nu}\right|^2, \tag{1.51}$$

where $G_{2\nu}$ is a phase space factor and $M_{2\nu}$ the nuclear matrix element. Since its prediction by Maria Göppert-Mayer in 1935 [144], the probability of this process is known to be small, as it implies a second-order weak transition. Göppert-Mayer estimated a half-life of $\approx 1 \times 10^{17}$ y for the decay with the emission of two electrons and two antineutrinos carrying 10 MeV in total. Later in the 20th century, several experiments observed this process. A selection of measured half-lives is given in Table 1.2.
If neutrinos are their own antiparticles, the lepton number that is an accidental symmetry in the SM would be violated [138]. If neutrinos are Majorana particles and massive (due to the required change of helicity for one of the neutrinos) as outlined above, a double-beta decay could occur without neutrino emission,

$$(Z, A) \rightarrow (Z + 2, A) + 2e^-. \tag{1.52}$$

Table 1.2: Selection of nuclides with observed double beta decays. The statistical and systematic errors are separated.

Nuclide	Half-life [10^{21}y]	Experiment
^{48}Ca	$0.064^{+0.007}_{0.006}\pm^{+0.012}_{0.009}$	NEMO-3 [145]
^{76}Ge	1.926 ± 0.094	GERDA [146]
^{130}Te	$0.82 \pm 0.02 \pm 0.06$	CUORE-0 [147]
^{136}Xe	$2.165 \pm 0.016 \pm 0.059$	EXO-200 [148]

In the simplest decay process, called light neutrino exchange, two electrons are emitted, and the emitted right-handed antineutrino from a nucleon is absorbed as a left-handed neutrino by another nucleon. A simplified schematic spectrum of the sum of the kinetic energy of the two electrons emitted is shown in Figure 1.9. The electrons share the total energy of the nuclear transition, called $Q_{\beta\beta}$, which is the difference in the energy between the final and the initial states.

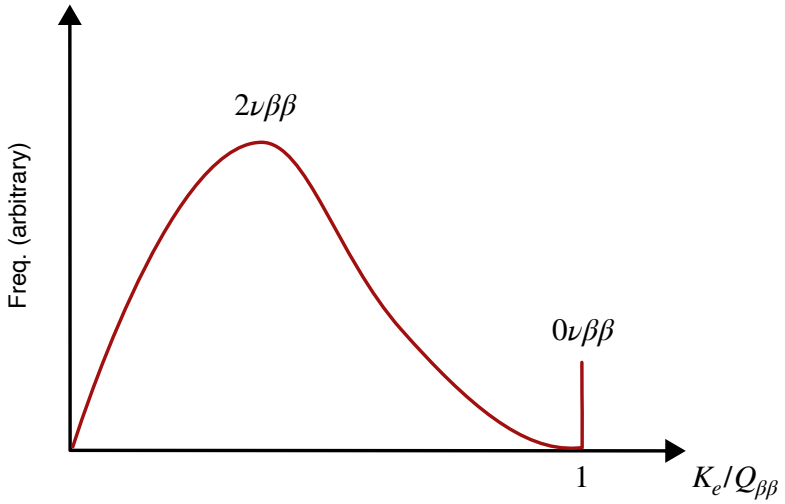

Figure 1.9: Simplified schematic of the spectra of the sum of the kinetic energy of the two electrons emitted divided by the Q-value ($Q_{\beta\beta}$) of the process. In the $0\nu\beta\beta$, the electrons share the energy $Q_{\beta\beta}$. The absolute scale of the plot and the relative scalings of the $2\nu\beta\beta$ and $0\nu\beta\beta$ signals are unknown in the absence of $0\nu\beta\beta$ detection.

The half-life for the process that exchanges neutrinos and produces two electrons that carry together the total energy available $Q_{\beta\beta}$ is [149]

$$\left(T^{0\nu}_{1/2}\right)^{-1} = G^{0\nu}\left(Q_{\beta\beta}, Z\right)\left|M^{0\nu}\right|^2 \frac{\left|\langle m_{\beta\beta}\rangle\right|^2}{m_e^2}, \tag{1.53}$$

where $M^{0\nu}$ is the nuclear matrix element (NME), the term $G^{0\nu}(Q_{\beta\beta}, Z)$ is a two-body phase-space factor which includes effects of the Coulomb interaction of electrons and daughter nucleus, and m_e is the electron mass. The term

$$\langle m_{\beta\beta} \rangle = \sum_{i=1}^{3} U_{ek}^2 \, m_k, \tag{1.54}$$

is *the effective Majorana mass*, where m_k are well-defined mass eigenstates of the neutrinos, and the matrix U is the PMNS matrix. Equation 1.53 gives the rate for exchange of light Majorana. Light neutrino exchange is regarded as the minimal mechanism for $0\nu\beta\beta$ (also called Mass Mechanism). Other mechanisms are possible, but further assumptions in new mediators and interactions must be added to the requirement that neutrinos are Majorana particles. The Left-Right symmetric model [150], for example, incorporates left-handed and right-handed currents (RHC) under the exchange of light and heavy neutrinos, which predicts new gauge bosons as well. Figure 1.10 shows the Feynman diagrams of both processes.

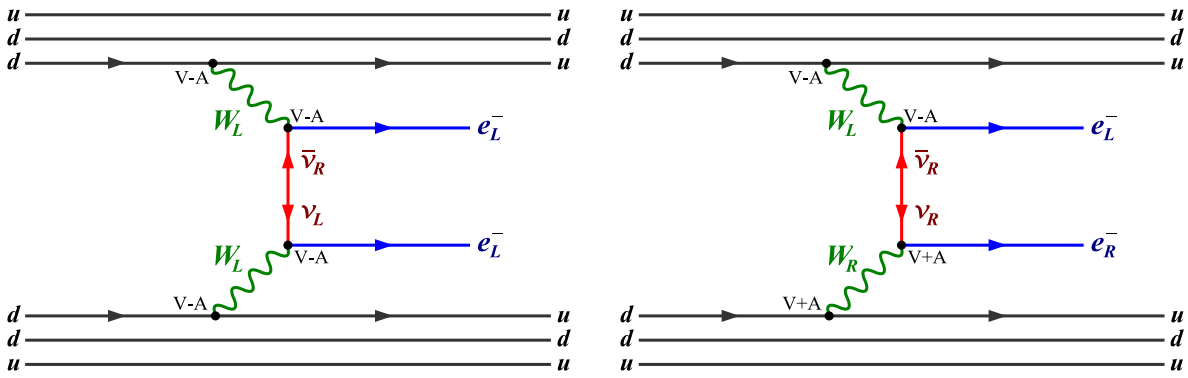

Figure 1.10: Diagrams illustrating $0\nu\beta\beta$ decay through (a) the mass mechanism and (b) the right-handed current. From Ref. [151].

The matrix element $M^{0\nu}$ describes the nuclear part of the decay process. In the case of xenon, a combined range of $1.68 < M^{0\nu} < 4.773$ is found in theoretical calculations for NME [152, 153]. The value adopted for the phase-space factor is $G^{0\nu} = 14.58 \times 10^{-15} y$ [154]. The spread in the NME introduces a source of uncertainty to the effective Majorana mass. Equation 1.53 can be written as

$$|\langle m_{\beta\beta} \rangle|^2 = \frac{\left(T_{1/2}^{0\nu}\right)^{-1} m_e^2}{G^{0\nu}\left(Q_{\beta\beta}, Z\right) |M^{0\nu}|^2}, \tag{1.55}$$

and it can be used to calculate the effective Majorana mass from the experimental searches of the

decay rate, when compared to the Equation 1.54, which it can be expanded as

$$\langle m_{\beta\beta} \rangle = \left| c_{12}^2 c_{13}^2 m_1 + s_{12}^2 c_{13}^2 m_2 e^{i\alpha_1} + s_{13}^2 m_3 e^{i\alpha_2} \right|, \tag{1.56}$$

where m_1, m_2, m_3 depend on the NO and IO.

1.5.3 Experimental sensitivity of neutrinoless double beta decay

In order to compare different experiments, it is helpful to derive a metric for their sensitivity to the $0\nu\beta\beta$-decay. The metric is referred to as the figure-of-merit (FOM) for the comparison of a $0\nu\beta\beta$ experiment, and will be used in the following chapters. We can take the expected background events B, as

$$B = bMt\Delta E, \tag{1.57}$$

where b is the background rate in (keV kg y)$^{-1}$, M is the target mass in kg, t is the experiment lifetime of the experiment, in years, and δE is the energy window of the $0\nu\beta\beta$ decays in keV, called the region of interest (ROI), which depends on the resolution of the detector. The number of $0\nu\beta\beta$-decay events $S_{0\nu\beta\beta}$ can be expressed in terms of the decay rate $\lambda_{0\nu\beta\beta}$ [155, 156]

$$S_{0\nu\beta\beta} = \lambda_{0\nu\beta\beta} N t \epsilon = \lambda_{0\nu\beta\beta} \left(\frac{A_0}{W} \right) \alpha \epsilon M t, \tag{1.58}$$

where N is the number of parent nuclei undergoing $0\nu\beta\beta$ decay, A_0 is the Avogadro number, W molar mass of the source material, α the isotopic abundance of the parent nuclide, and ϵ the detection efficiency to the $0\nu\beta\beta$-decay events. Different experiments can be compared in terms of their signal-to-background ratio. For example, if $S_{0\nu\beta\beta}/B \approx 1$, the choice of $S_{0\nu\beta\beta} = \gamma\sqrt{B}$ can be taken, in which $\gamma = S_1\sqrt{(2)}$, where S_1 is the confidence level (CL) expressed in units of the standard deviation σ of a Poisson distribution. Using this relation, we obtain

$$\lambda_{0\nu\beta\beta} A_0 \left(\frac{\alpha\epsilon}{W} \right) Mt = \sqrt{bMt\Delta E}. \tag{1.59}$$

Combining Equations 1.58 and 1.57, and assuming 1σ level, a figure-of-merit (FoM) for the half-life sensitivity of a given experiment can be written as

$$\text{FoM} = \ln(2)\varepsilon \frac{\alpha A_0}{W} \sqrt{\frac{M \cdot t}{\Delta E \cdot b}}. \tag{1.60}$$

In the limit where the expected background counts are low, the experimental sensitivity increases

as FoM $\propto M \cdot t$, referred to 'background-free'. The FoM can be used to exemplify the different approaches that an experiment can use in order to increase the sensitivity of an experiment:

- Utilising a source where the $0\nu\beta\beta$ candidate has a high isotopic abundance α, or by enriching the source,
- High detector mass and/or long livetime to maximise the exposure $M \cdot t$,
- Low background rate in the ROI b, that can be achieved using passive or active shields and background rejection techniques. A high detector resolution can discriminate more efficiently the $2\nu\beta\beta$ events in the ROI,
- High detection efficiency ε of the hypothetical signal.

Past and current $0\nu\beta\beta$ experiments use different sources and techniques. For example, cryogenic bolometers are employed by the CUORE [157] experiment, to search for the $0\nu\beta\beta$ decay of ^{130}Te. GERDA [158] and MAJORANA [159] used solid-state germanium diodes enriched in ^{76}Ge. GERDA achieved a 'background-free' level in the ROI, while the MAJORANA demonstrator achieved an excellent energy resolution in the ROI. These collaborations merged into a common one, LEGEND [160], in order to reach a sensitivity of $\sim 10^{27}$ y and $\sim 10^{28}$ y with its two phases LEGEND-200 and LEGEND-1000, respectively. A LXe single phase TPC was used in order to search for the $0\nu\beta\beta$ decay of ^{136}Xe by EXO-200 [161]. An next generation of this experiment is planned in the future, nEXO [162], and aims to observe decays from $5000\,\mathrm{kg}$ of isotopically enriched xenon and reach a sensitivity of $\sim 10^{28}$ y. The current lower limit on the half-life of ^{136}Xe is set by KamLAND-Zen, $T^{0\nu}_{1/2} > 1.07 \times 10^{26}$y at 90% CL [163], which consists of a large scale ^{136}Xe-loaded liquid scintillator. The experiment is now running with an increased mass of $745\,\mathrm{kg}$ of xenon, aiming to reach a sensitivity of $T^{0\nu}_{1/2} > 4.6 \times 10^{26}$y [164]. The XENON1T experiment has recently set limits in the search of $0\nu\beta\beta$ from its previous run, due to the presence of ^{136}Xe in its target. The present limits of XENON1T and projected for XENONnT [125], as well as the comparison to other dedicated searches with different isotopes, are shown in Figure 1.11.

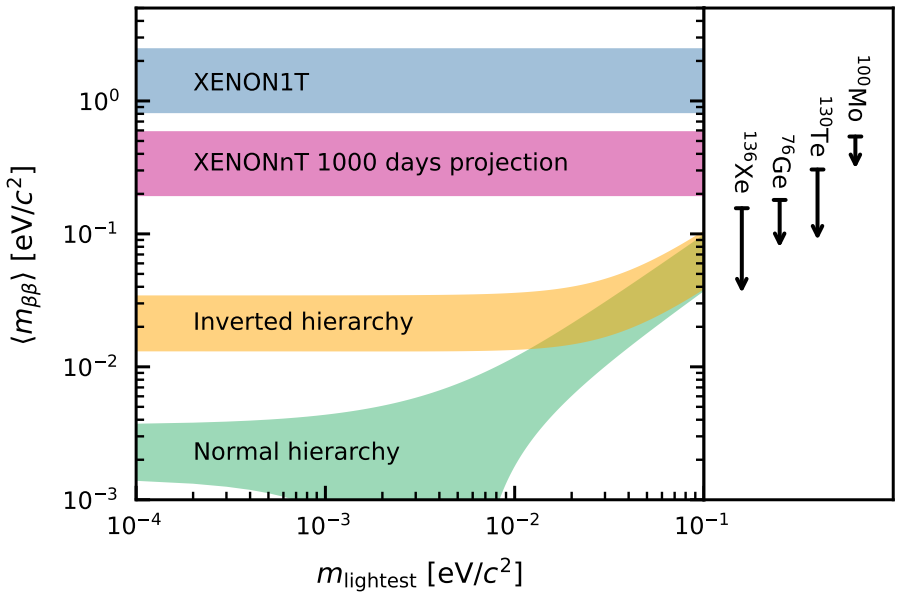

Figure 1.11: Effective Majorana neutrino mass $\langle m_{\beta\beta} \rangle$ calculated from the XENON1T $0\nu\beta\beta$ search (blue), the projection for XENONnT after 1000 days (violet), and neutrino mass ordering depending on the mass of the lightest neutrino m_{lightest}. In the right panel, the current best experimental limits 90% CL from the searches using different isotopes is shown, with the values extracted from Ref. [149]. The value for ^{136}Xe is taken from [165]. Figure from Ref. [125].

Chapter 2

Liquid xenon time projection chambers and the DARWIN observatory

> *The information contained in nature allows us a partial reconstruction of the past. The development of the meanders in a river, the increasing complexity of the earth's crust, are information-storing devices in the same manner that genetic systems are. Storing information means increasing the complexity of the mechanism.*
>
> **— Ramon Margalef**

While the previous chapter gave an overview of the missing pieces in our current understanding of particle physics and different BSM models, this chapter focuses on the principle of particle detection in LXe TPCs and motivates the use of LXe as detection target. We will start in Section 2.1 with the description of the properties of LXe that makes it a good choice for dark matter detection. The section continues by describing the microphysics of how particles interact with LXe. Once having a picture of the detection principle, Section 2.2 describes the implementation of the essential technological systems in current LXe TPCs. The section proceeds by introducing the next generation of LXe TPCs, DARWIN. Section 2.4 focuses on the background sources that impact the sensitivity of the DARWIN detector to several physics channels of interest. The background sources and the models used to estimate their rate will serve as input to the next chapter for the characterisation of the sensitivity of DARWIN to rare processes.

2.1 Xenon as a medium for particle detection

As hinted in the previous chapter, LXe is an attractive target for particle detection due to a significant number of properties, shown in Table 2.1. Xenon is a noble gas with no intrinsic radioactivity, as it contains no medium-lived radioactive isotopes[1]. This is an advantage compared with argon, which has trace amounts of the medium-lived ^{39}Ar, with a half-life of $T_{1/2} = 269\,\mathrm{y}$ [166, 167]. The isotopes ^{129}Xe and ^{131}Xe, which make up 26.4% and 21.2% of natural xenon, have non-zero intrinsic angular momenta, which can be used for spin-dependent dark matter searches [168], while argon contains only zero intrinsic angular momenta naturally abundant isotopes[2].

Table 2.1: Properties of xenon relevant for particle detection.

Property	Value
Atomic number, Z	54
Molar mass	$131.29\ \mathrm{g\ mol^{-1}}$ [169]
Isotopic abundances	^{124}Xe(0.095%), ^{126}Xe(0.089%), ^{128}Xe(1.91%) [169] ^{129}Xe(26.4%), ^{130}Xe(4.07%), ^{131}Xe(21.2%) ^{132}Xe(26.9%), ^{134}Xe(10.4%), ^{136}Xe(8.86%)
Gas density (273 K, 1 atm)	$5.8971\ \mathrm{g\ L^{-1}}$ [169]
Liquid density (165.05 K, 1 atm)	$3.057\ \mathrm{g\ cm^{-3}}$ [169]
Melting point (1 atm)	161.4 K [169]
Boiling point (1 atm)	163.05 K [169]
Triple point	$161.31\ \mathrm{K}, 0.805\ \mathrm{atm}, 3.08\ \mathrm{g\ cm^{-3}}$ [169]
Critical point	$289.74\ \mathrm{K}, 57.65\ \mathrm{atm}, 1.155\ \mathrm{g\ cm^{-3}}$ [169]
Latent heat of fusion	17.29 kJ kg [169]
Maximum yield	73 photons/keV [170]
Path length 100 keV γ	0.18 cm [171]
Path length 100 MeV γ	5.9 cm [171]
Path length 1 MeV neutron	10.6 cm [172]
Path length 10 MeV neutron	15.9 cm [172]

As a particle detection medium, xenon has excellent scintillation properties: compared to other noble gases, it is very effective in converting the kinetic energy of particles into detectable light [72], with a maximum yield of 73 photons/keV, the highest compared to other noble gases [170]. Another good quality of xenon as a scintillator is its transparency to its own light, of (178 ± 1) nm [173][3].

[1] ^{124}Xe and ^{136}Xe have half-lives of the order 10^{22} and 10^{21} years, respectively.

[2] A non-zero nuclear spin requires odd number of protons and/or neutrons, and argon contains ^{36}Ar, ^{38}Ar, ^{42}Ar, and trace amounts of ^{39}Ar which is a potential background in their signal region.

[3] The first ionisation energy of xenon is at ~ 12 eV, while 178 nm ~ 7 ev [174].

Additionally, xenon has a high density of $2.8574\,\mathrm{g/ml}$ at $177.5\,\mathrm{K}$, resulting in a high mass energy-absorption coefficient. As a consequence, xenon is a scintillator that can shield electromagnetic radiation, as X-rays and γ-rays that interact through photoelectric absorption, Compton scattering, or pair production are highly attenuated. Figure 2.1 shows the total photoelectric absorption, Compton scattering, and pair production attenuation coefficients in xenon as a function of energy.

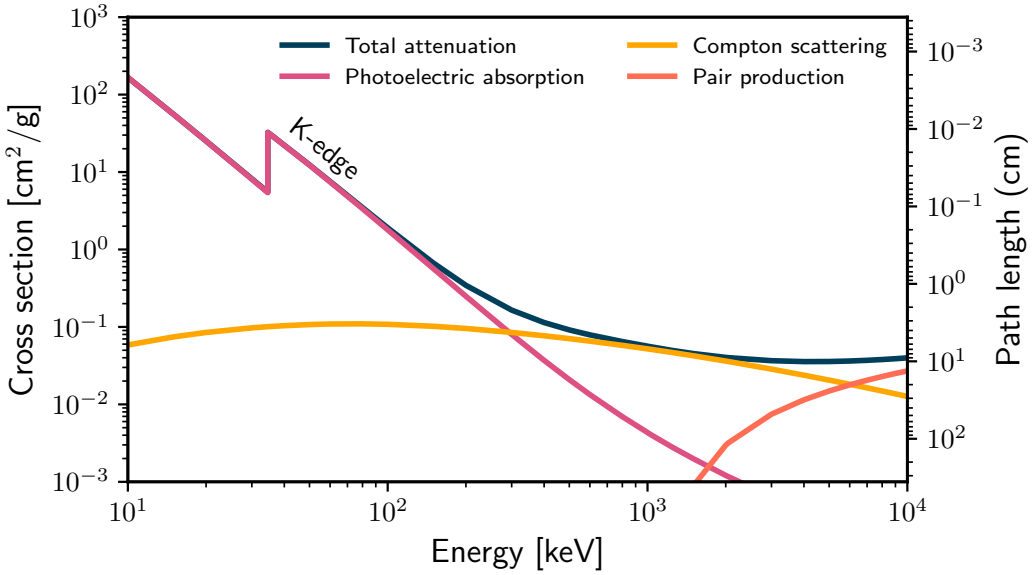

Figure 2.1: Attenuation of LXe to electromagnetic radiation. Below approximately $300\,\mathrm{keV}$, the cross section is dominated by photoelectric absorption, while above that energy, Compton scattering becomes more dominant. Above $1.022\,\mathrm{MeV}$, pair production starts to compete with Compton scattering, becoming dominant for energies around $6\,\mathrm{MeV}$. Data from Ref. [172].

2.1.1 Liquid xenon time projection chambers

The working principle of a LXe dual-phase TPC relies on detecting the recoil induced in LXe by an incident particle. After an interaction, the atom produces scintillation, free electrons, and atomic motion (heat). The heat production is, however, not detected in LXe TPCs. The energy is distributed in the production of scintillation and ionisation in a binomial process [175]. With the use of photosensors placed around the liquid target, the photons can be detected. Dual-phase TPCs provide a clever strategy to detect the freed electrons: the cloud is drifted towards a 'gate' electrode, below the liquid-gas interface, where an additional field extracts them from the interface towards the gas phase. In the gas phase, electrons produce electroluminescence with an amplification factor which

yields several photons per electron. With this technique, both scintillation (photons) and the ionization proportional scintillation (electrons) can be read out, and these signals are often referred to as S1 and S2. The use of the two signals provide an excellent energy resolution [176], since the number of photons and electrons is anti-correlated due to energy conservation. Figure 2.2 shows a schematic of the working principle of a TPC. The hit patterns on the top photosensor array are used to reconstruct the x-y position of the electron cloud. The depth of the deposition in the z-coordinate is reconstructed using the drift time by taking the difference in time from the S1 to the S2 signal, providing a complete 3D spatial reconstruction of the interaction site.

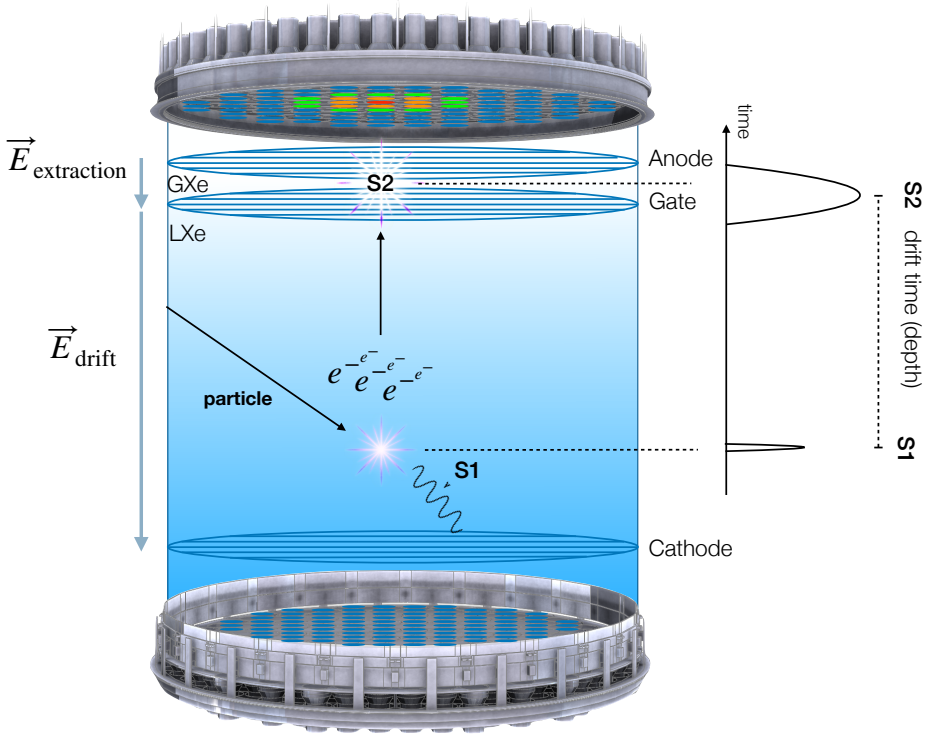

Figure 2.2: Schematic of the working principle of a dual-phase TPC: The incident particle interacts with the xenon atom. The recoil produced due to the interaction produces scintillation and ionisation (free electrons) along the track. The prompt scintillation signal (S1) is recorded by photosensor arrays both at the top and the bottom of the TPC. The drift field ($\vec{E}_{\text{drift}}$) , along the z-direction, transports the electrons towards the gate electrode, below the liquid-gas interface. An additional field ($\vec{E}_{\text{extraction}}$) extracts the electrons towards the gas phase, where they produce the second scintillation signal. The photosensors record this amplified ionisation proportional signal (S2).

The incident particles can produce two types of recoils with the xenon atoms: Nuclear Recoils (NRs) and Electronic Recoils (ERs). In a NR, the incident particle induces the recoil of the xenon nucleus,

and it can be produced either by neutrons or potentially by a WIMP. In an ER, the energy is transferred to an atomic electron, and it is produced by γ-,β-,α-particles, and potentially DM candidates which interact with electrons.

The stopping power of the LXe against different particle species is shown in Figure 2.3. The stopping power depends on the charge density given by a particle in LXe, which changes with the particle species.

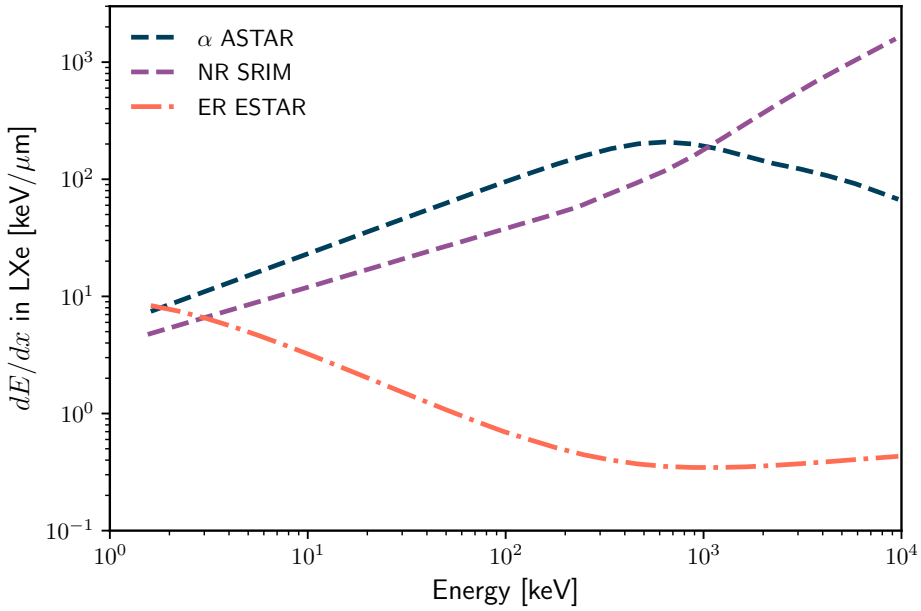

Figure 2.3: Electronic stopping power for alphas, electrons and neutrons, in LXe, as given by ASTAR, ESTAR, and SRIM [177]. The stopping power for alphas and nuclear recoils (labelled as NR) is similar, while the charge density created by electronic recoils (ER) results a lower stopping power. Adapted from Ref. [178].

Using the self-shielding properties of xenon, the sensitive[4] target can be reduced in the analysis of the data acquired by the detector in order to keep only the inner core, with reduced background.

Before continuing with the description of the implementation of the systems in a TPC, we will discuss the microphysics of particle interactions with LXe. Understanding the underlying processes in LXe enables the use of an essential technique in background rejection in LXe dual-phase TPCs, based on the ratio of S2 and S1 signals.

[4]Following existing bibliography (for example Ref. [179]), we refer to sensitive target as the volume where the events are registered by photosensors and the particle interactions with LXe can be reconstructed.

2.1.2 Microphysics of interactions in liquid xenon

The number of free electrons and photons produced when an incident particle deposits its energy in liquid xenon, and their redistribution, can be explained by ion recombination at the event site. The interaction between a particle and xenon will create tracks of excited and ionised xenon atoms. The excitons Xe^* can create excited dimers, Xe_2, which scintillate as they return to the ground state [180]. Electrons can be kicked out of xenon atoms, creating ions Xe^+, which can recombine with electrons in their proximity to create additional dimers, contributing to the scintillation channel. The processes can be described as

$$\begin{aligned} &\mathrm{Xe}^+ + \mathrm{Xe} \rightarrow \mathrm{Xe}_2^+ \\ &\mathrm{Xe}_2^+ + e^- \rightarrow \mathrm{Xe}^{**} + \mathrm{Xe} \\ &\mathrm{Xe}^{**} \rightarrow \mathrm{Xe}^* + \text{ heat} \\ &\mathrm{Xe}^* + \mathrm{Xe} \rightarrow \mathrm{Xe}_2^*, \end{aligned} \tag{2.1}$$

where Xe^{**} is an excited state which loses energy in the form of atomic motion (heat). The later decay to the ground state of Xe_2^* will produce scintillation light

$$\mathrm{Xe}_2^* \rightarrow 2\mathrm{Xe} + h\nu, \tag{2.2}$$

where the scintillation signal depends on the excited atom, which can be in a triplet or singlet state. Figure 2.4 shows a diagram of this process. The energy is distributed between the two processes

$$E_{dep} = fW(N_{ex} + N_i), \tag{2.3}$$

where N_{ex} are the number of excitons produced, N_i number of ions produced, and W average energy required to produce an electron-ion pair. The factor f represents energy losses due to quenching (atomic motion), that for ERs is conventionally taken as 1 (no transfer to atomic motion). In NRs, the quenching factor is called Lindhard factor ($\mathcal{L}$) [181]. Contrary to ERs, there is a higher fraction of the energy which is not converted to observable quantas (0.1 or 0.2, depending on the energy [182]) and represents the partition of energy of the incident ions to nuclear motion and electronic excitation motion [183]. The total number of photons will be related to the recombination probability r,

$$n_\gamma = N_{ex} + rN_i = \frac{E_{dep}}{W}(r + \frac{N_{ex}}{N_i}). \tag{2.4}$$

As a consequence, the effective number of electrons will be less than the initial number of ions

$$n_e = N_i(1-r) = \frac{E_{dep}}{W}(1-r). \tag{2.5}$$

By using the recombination rate r, the yields for charge and light respectively can be calculated

$$Q_y = \frac{n_e}{E_{dep}} \; ; \; L_y = \frac{n_\gamma}{E_{dep}}. \tag{2.6}$$

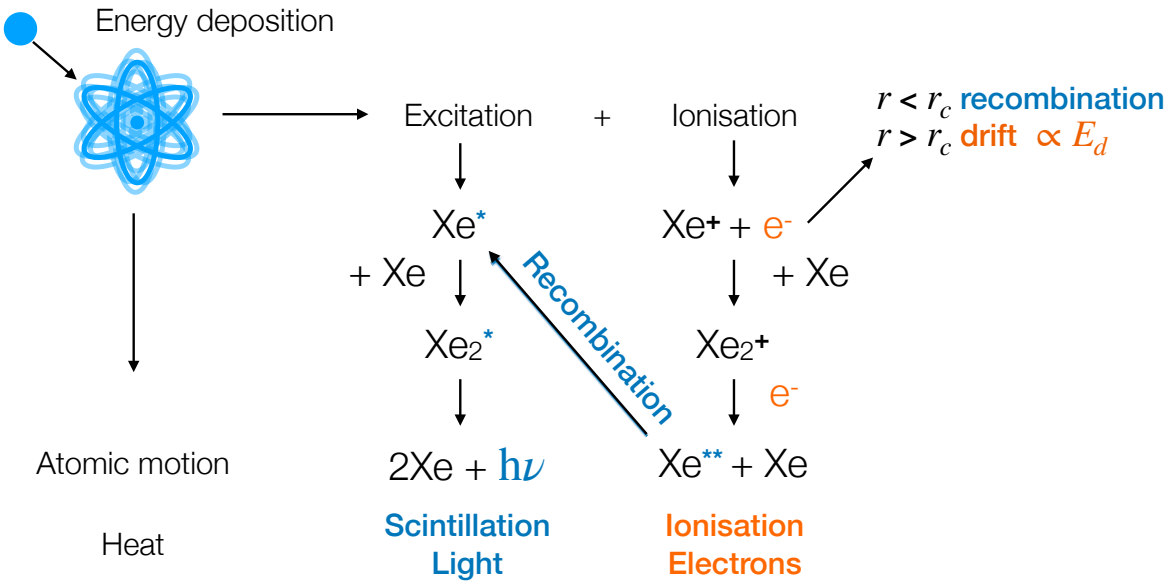

Figure 2.4: Diagram of energy deposition with the following excitation, ionisation and heat channels production: an incident particle will create a track of excited Xe^* and ionised xenon Xe^+. The electrons inside the recombination radius r_c can recombine with the xenon molecules, creating additional scintillation.

Inside the recombination radius, r_c (also called the Onsager radius), electrons can overcome diffusion, and recombination takes place. Outside r_c diffusion is the dominant mode of transport. In the boundary region, the electrons have an equal probability of recombining or escaping. The total recombination rate will be the rate at which electrons and holes move into each others recombination radii and depends on the electric field applied in the volume, the density and the distribution of thermal electrons and ions. A higher electric field will decrease the scintillation signal by removing electrons that could potentially recombine. Therefore, the recombination quantifies the redistribution of the initial binomial process of scintillation and ionisation by the recombination of kicked-out

electrons. The interaction of particles with xenon will leave an ionisation track depending on the properties of the particle. The density of electron-ion pairs produced along the track of a particle [5] affects the recombination probability between electrons and ions, as it increases with the density of electron-ion pairs. For example, alpha particles often have enhanced recombination compared to other particles due to their cylindrical track shape with a very dense core, which results in a bigger recombination radius [178].

On the time scale of the signals, the duration of the S1 pulse is given by three factors: the existence of two exciton states of xenon (singlet and triplet), their lifetime, and the recombination time. The singlet lifetime reaches values up to $22\,\mathrm{ns}$ for low fields, while the triplet lifetime is $4.2\,\mathrm{ns}$ [184]. The distribution between singlet and triplets is different from interactions with γ-, β-, α-particles compared to neutrons, which is modified by the recombination process. Nuclear recoils produce a greater fraction of fast-decaying singlets than electronic recoils [95]. This property translates to a different distribution of S1 and S2 signal for ERs compared to NRs. The S2 time width, which arises from the drift of electrons that escaped recombination, is given by the mean free path of electrons to produce photons in gas xenon, the electron diffusion, and it approaches a Gaussian shape [185].

Background discrimination

The background contributions in the detector can be identified and reduced. The background discrimination technique relies on the difference in the S1 and S2 signals from ERs and NRs. Figure 2.5 shows the yield of the scintillation signal (L_y) and the yield of the ionisation signal (Q_y) for both NRs and γ-rays interacting with LXe taken from the Noble Element Simulation Technique package, NEST [186]. NEST provides parameterised models to perform simulations of particle interactions in LXe, from where the simulated S1 and S2 can be extracted. Due to the Lindhard quenching factor for NRs, the L_y and Q_y are lower than those for ER events.

The ratio between S1/S2 is often taken to highlight the difference in the pulses for ER and NR [170]. The difference in the ratio S1/S2 can be exploited for background discrimination, and most of the ER background can be rejected in the WIMP search region with significant efficiency (around 99% [187] or higher). There are ER events that cannot be rejected due to their proximity to the expected WIMP region at low energies, as illustrated in Figure 2.6. These events are often referred as *leakage events*. Additionally, events coming from neutrons are more likely to deposit their energy in multiple interactions compared to WIMPs signals, which are expected to deposit their energy in a single site. The multiplicity of interactions is a powerful tool to discriminate background NR sources from a WIMP

[5] Also known as Linear Energy Transfer, LET

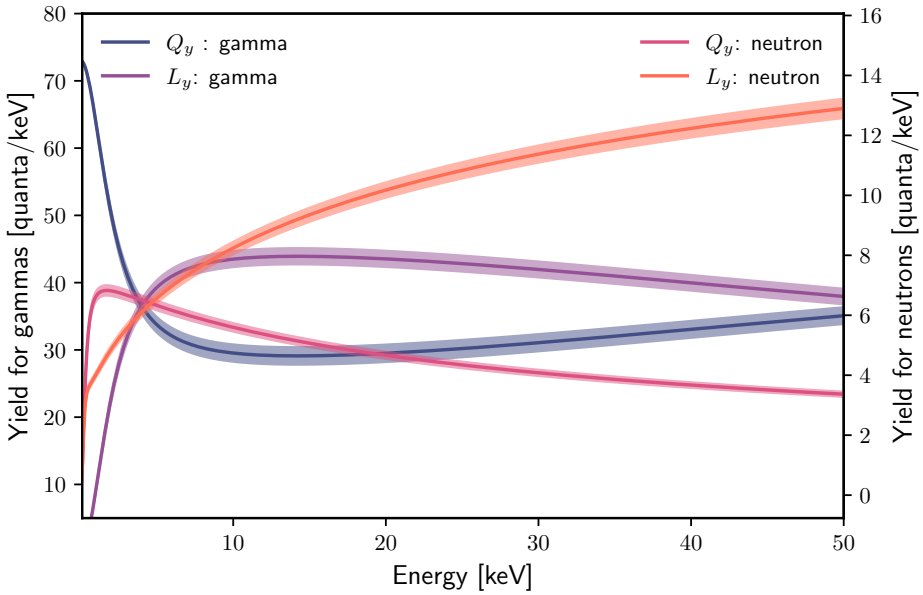

Figure 2.5: Charge Q_y and light L_y yields for γ-rays and neutrons interacting with LXe, according to the simulation package NEST [186]. The quenching factor gives the difference in the magnitude of the yield in nuclear recoils $\mathcal{L}$. The authors provided the error for the γ-ray model, while the error in the yield for neutrons is assumed 5% uniformly in the energy range.

signal.

2.2 Current liquid xenon time projection chambers

As mentioned in the previous chapter, current LXe TPCs include PANDAX-4T [78], LZ [104] and XENONnT [189]. We will focus in this section only on the XENONnT, as an example of the current technologies for LXE TPCs. The XENON project is a direct dark matter detection experiment project using LXe as a detector medium. It is located in an underground facility at the Laboratori Nazionali del Gran Sasso (LNGS), Italy. Three experiments, XENON10, XENON100 and XENON1T, were performed in the past [190]. The XENON1T experiment was commissioned in 2016 and took science data until 2018. The XENON1T experiment has placed the most competitive limits in the WIMP-nucleon spin-independent elastic-scatter cross section for WIMP masses above $6\,\mathrm{GeV/c^2}$, with a minimum of $4.41 \times 10^{-47}\,\mathrm{cm^2}$ at $30\,\mathrm{GeV/c^2}$ at 90% confidence level [191]. Further results include the discovery of the double electron capture process in ^{124}Xe, not observed before but predicted by the SM. The observation of an excess in the low energy region [103] that could be explained by solar axions or neutrino magnetic moment has triggered many papers and motivated a chapter in this

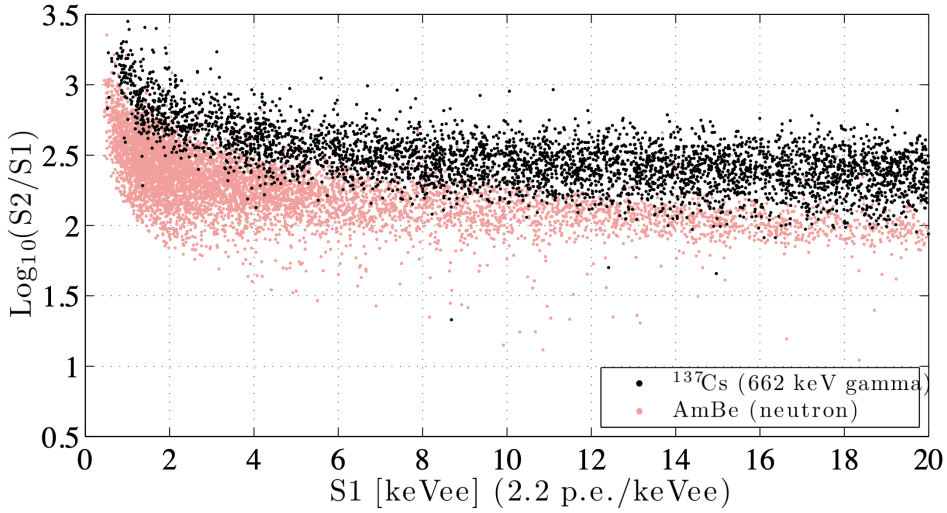

Figure 2.6: Response to low energy electronic recoils from a ^{137}Cs γ-ray source and neutron-induced elastic nuclear recoils from an AmBe source in XENON100 [188]. keV$_{ee}$ stands for electron-equivalent energy, obtained after reconstructing the detected signals in the ER channel. The fraction of ER events that cannot be excluded from the NR region is often referred as *leakage events*. Past experiments have been able to reject ER events in the WIMP search region with a 99% efficiency or higher.

thesis. XENON1T has also placed limits on neutrinoless double beta decay with ^{136}Xe [125], also discussed in this thesis as a potential channel for DARWIN.

The next phase, XENONnT, has been commissioned at LNGS and is taking data, utilizing 5.9 tonnes of instrumented LXe with 4 tonnes fiducial mass. The detector is placed in hall B of the LNGS underground facility, which provides an average depth of 3600 meters water equivalent against cosmic muons. The experiment employs a double wall cryostat made of stainless steel (SS). The external gammas and muon-induced neutrons from the materials and walls of the cavern are reduced by the deep underground facility and the placement of the detectors inside a 10-meter diameter water tank doped with gadolinium. The water tank functions as neutron veto and Cherenkov muon veto, instrumented with light sensors. The gadolinium-loaded water muon veto system, instrumented with PMTs and reflectors, surrounds the cryostat. Figure 2.7 shows the diagram of the XENONnT experiment, showcasing the cryostat, the Gd-loaded water muon veto system and the broader water tank shield.

Field shaping rings (FSRs) keep the electric field homogeneously focused in the vertical drift direction. The homogeneity of the field is of critical importance, as it affects several detector parameters, such as the drift velocity used to estimate the depth of the interaction. The FSRs provide a voltage

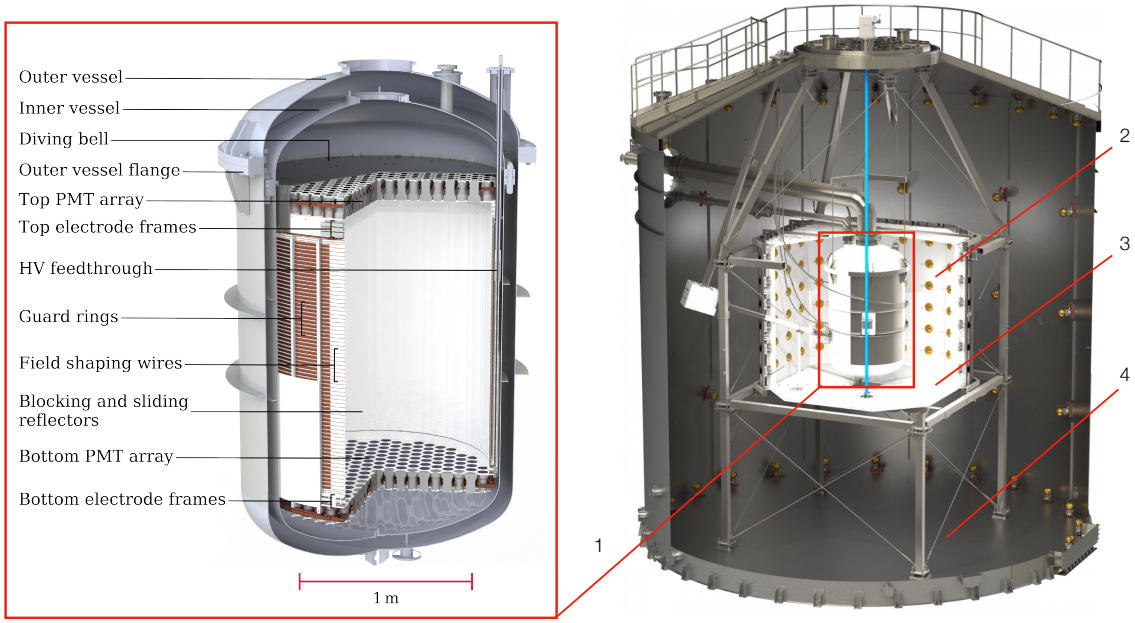

Figure 2.7: CAD rendering of the XENONnT cryostat and TPC (1). The TPC has a diameter of 1.3m and is 1.5 m-tall. (Right) Geant4 rendering of the three nested detectors, including muon and neutron veto (2), with the reflector material (3). The water tank walls (4), which support the muon veto PMTs, the neutron veto support structure, and other components (e.g. calibration systems) are omitted for clarity. The neutron veto PMT windows face the neutron veto region through openings in the panels. Credit: XENON Collaboration.

drop from the cathode to the gate electrode, achieved with high Ohmic resistors with low heat dissipation between the FSRs. The FSRs are made of oxygen-free high conductivity copper (OFHC), which provides high conductivity and little outgassing and oxidation. The cathode, gate, and anode grids are made of SS meshes with parallel wires. SS provides the required tensile strength to prevent the sagging of the wires[6]. The electrodes and rings comprise the $1.3\,\mathrm{m}$ diameter and $1.5\,\mathrm{m}$ long field cage.

For the light detection systems, a high light collection efficiency (LCE) of the scintillation from the S1 pulse is achieved by covering the field cage with panels of Polytetrafluoroethylene (PTFE). The panels provide the needed reflectivity to ensure that reflected photons can be later detected. The top (bottom) photosensor array consists of 253 (241) R11410-21 3" photomultiplier tubes (PMTs). The PMT design was a joint effort between the XENON collaboration and the Hamamatsu company, in order to produce highly radio-pure photosensors [192].

[6]That could be produced not only due to gravitational sag, but also due to the attraction of the wires to conductors at a different potential

The expected background in XENONnT for the ER channel comes from materials, and uniformly diffused ^{85}Kr, ^{222}Rn, ^{220}Rn and the double beta decay of ^{136}Xe, while background events from NRs arise from neutrons emitted by (α, n) reactions from materials due to their traces of ^{238}U and ^{232}Th, and neutrons cosmogenically produced, while neutrons coming from the cavern are shielded by the water tank. We have listed only a selection of the most important backgrounds in each channel, while Section 2.4 will discuss their origins and interactions with LXe more in detail.

For xenon purification, a krypton distillation column has helped to achieve an activity from ^{85}Kr of 0.2 ppt of natural krypton in XENON1T, and the xenon purification line has achieved a ^{222}Rn background of $10\,\mu\mathrm{Bq/kg}$. XENONnT aims to further reduce the ^{222}Rn content to $1\,\mu\mathrm{Bq/kg}$ and $0.1\,\mathrm{ppt}$ (mol/mol) for $^{\mathrm{nat}}$Kr/Xe [193].

All the materials are selected based on their potential contribution to the detector background. Samples from the materials are procured from companies and screened beforehand in low-background germanium counting detectors or other spectrometers. All the materials are cleaned, passivized, and assembled in a clean room [194].

2.3 The DARWIN observatory

The context of this work is the next generation of LXe TPCs, the DARWIN Observatory. DARWIN aims to cover the accessible parameter space for the SI WIMP coupling, to reach the region where the neutrino background will produce discernible signals. The baseline design includes 40 tons of LXe as sensitive target in a cylindrical TPC $2.6\,\mathrm{m}$ wide and $2.6\,\mathrm{m}$ tall, as shown in Figure 2.8. This baseline concept includes two arrays of 950 R11410-21 PMTs, used to detect DM signatures, while other photodetectors are also considered. DARWIN aims to reduce the activity concentration of ^{222}Rn further to the $0.1\,\mu\mathrm{Bq/kg}$, and $2\,\mathrm{ppq}$ (mol/mol) for $^{\mathrm{nat}}$Kr/Xe.

Besides dark matter searches, DARWIN will have a competitive neutrino program. This program includes measuring the low-energy solar neutrino flux with $< 1\%$ precision [126], potential observation of supernova neutrinos [195], coherent neutrino-nucleus interactions, solar axions and the neutrinoless double beta decay of ^{136}Xe [1] (the latest two are part of this work). A white paper has been released by the LXe TPCs communities, which plan to join efforts for the next generation LXe TPC. The XLZD consortium consists of DARWIN, LZ and XENON collaborations. The list of new physics channels that could be probed in this type of detector can be found with more detail in Ref. [196].

The realization of a next generation LXe TPC entails addressing different challenges on the up-scaling

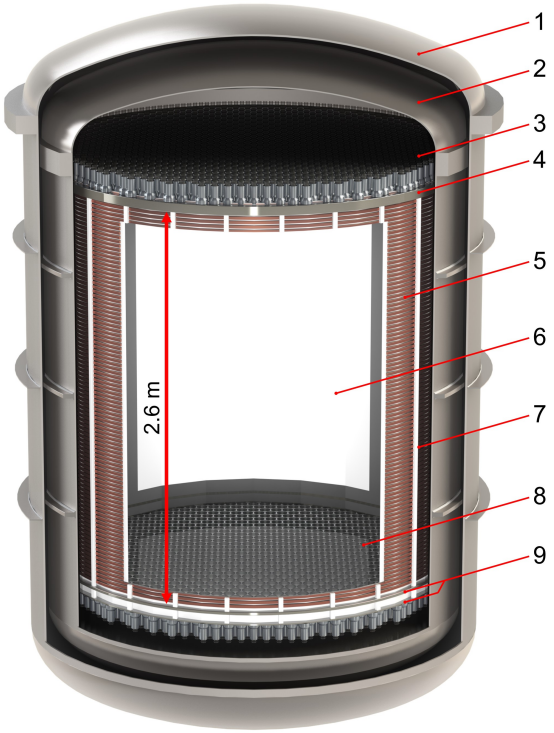

Figure 2.8: Drawing of a possible realisation of DARWIN TPC and the double-walled cryostat. The TPC has a diameter of 2.6 m and is 2.6 m tall. The cryostat (1,2) design was optimised for lightweight and made of titanium with low radioactivity. Approximately 1800 PMTs (3) register the particle interactions inside the LXe target. The 92 FSRs (5), from OFHC copper, define the field cage covered by PTFE reflectors (6). Torlon or PTFE pillars (7) provide structural support to the field cage. The electrodes (4, 8) material is titanium, while a PTFE reflector panel (9) covers the bottom photosensor array. Render from Ref [197].

of different systems, background reduction, and signal quality, among other features. With the up-scaling of the linear dimensions of TPCs, the high voltage to be delivered to the cathode is altogether increased up to 100 kV, which poses a major challenge. A high drift field is needed to acquire quality data, as the particle identification method relies on the difference in the produced scintillation and ionization between particles, which is enhanced at higher electric fields. Besides this, a lower electric field implies a lower drift velocity, which allows more time for the electron cloud to diffuse, and electronegative molecules to capture the electrons in the drifting cloud, reducing the detectable signal size. Furthermore, the low energy thresholds and the energy resolution achieved by noble liquid TPCs, and their S2-only analysis [198] depend on the stability and uniformity of these systems. The increasing diameter for the electrodes provides another set of challenges, as sagging of wires and

light emission, among others, could degrade the signal quality.
A full-scale demonstrator in the vertical dimension, called Xenoscope, was built in the University of Zurich in order to demonstrate electron drift for the first time in a LXe TPC over a $2.6\,\mathrm{m}$ distance [199]. The purity of the LXe and the high voltage (HV) delivery and homogeneity are some of the objectives of this demonstrator for LXe TPCs. In addition to demonstrating electron drift over $2.6\,\mathrm{m}$, the near-future plans with Xenoscope include the measurement of the longitudinal and transverse diffusion of electrons emitted from the photocathode. The longitudinal diffusion affects the width of the signals, with wider signals for larger drift distances. The capability of the TPC to resolve multiple scatters along the z-coordinate would be affected, which is needed in rare-event searches to distinguish background-like events. The transverse diffusion, on the other hand, affects the $x-y$ resolution of the detector. Previous measurements were performed over short drift lengths ($< 20\,\mathrm{cm}$) and feature large systematic errors [200, 201], revealing the need of new measurements for tonne-scale LXe TPCs, where charge diffusion is more relevant given the longer drift lengths. Xenoscope will provide the appropriate conditions to perform diffusion measurements at different drift fields for lengths up to $2.6\,\mathrm{m}$. A section in this thesis is dedicated to such measurements.
Analogously to Xenoscope, the University of Freiburg has been commissioning a $2.6\,\mathrm{m}$ diameter detector, in order to test different electrode materials and geometries.
On the xenon purification and gas system side, different technologies were developed for XENONnT, such as cryogenic distillation for radon removal [202] and a heat exchanger with higher performance than the requirements of XENONnT, that allows in the future up-scaling of liquefaction of xenon and radon distillation [203]. The liquid purification of xenon at higher flows for multi-tonne LXe TPCs was developed in Ref. [204], allowing the XENONnT experiment to achieve electron lifetimes (which is a value related to the mean path of electrons in LXe) greater than 10 ms in an 8.6-tonne total mass.
PMT and other photosensor technologies are being evaluated for DARWIN, such as bubble-assisted liquid-hole multipliers [205], hybrid photosensor solutions such as ABALONE [206], and Vacuum Silicon Photomultiplier Tubes [207]. These photosensors could be tested in conditions similar to those of the DARWIN observatory environment with the use of Xenoscope.

2.4 Expected sources of background in DARWIN

This section enumerates commonly found sources of background in LXe TPCs and the impact that they will have in DARWIN. Understanding the background contribution and its sources is important to develop new analysis techniques, background mitigation when constructing the detector via material selection, location of the detector, and other vital design choices aiming for a successful

operation. Modelling the background is crucial in order to study the sensitivity of DARWIN to different channels, which will be the goal in the following chapters. The backgrounds can be studied given their signature in the detector, and ER and NR backgrounds are often distinguished due to their different S1/S2 ratio, which was described in the previous section. Consequently, the list of ER and NR backgrounds is presented here.

2.4.1 Electronic recoil sources in liquid xenon

The ER channel is of interest for searches such as the $0\nu\beta\beta$ of ^{136}Xe and solar axions, among others, which are two of the main chapters of this work. These two processes, if existent, would leave their signature in the detector in the ER channels due to their interaction with electrons, which will be explained in detail later. These two channels ultimately motivate the lengthy focus on the ER channel backgrounds, which will be brought back often in the following chapters. As supplement, appendix A shows details on the decay schemes of a selection of relevant isotopes.

Radioactivity in the Earth mantle and materials

The terrestrial radioactivity is produced by the natural content of ^{238}U, ^{232}Th, and ^{40}K. The abundance in the crust is around $2.6\,\mathrm{ppm}$, $10\,\mathrm{ppm}$ and 1%, respectively [208]. There is as well a contribution from the ^{235}U chain. Their long half-lives enable them to be present on Earth, producing a constant heat source. Uranium deposits are formed from evolved leucogranites or volcanic rocks, followed by continental collisions (orogenesis) [209], with isotopic abundances of 99.3% for ^{238}U and 0.07% for ^{235}U. Uranium forms complexes that are stable in solutions, and can migrate over long distances. Thorium is more abundant in nature, but its minerals are relatively insoluble. The isotope ^{40}K decays to ^{40}Ar by electron capture (EC) with the emission of a $1505\,\mathrm{keV}$ γ-ray or by β-decay to ^{40}Ca accompanied by the emission of a $1311\,\mathrm{keV}$ γ-ray.
All rocks and soils emit ionizing radiation as a result of these isotopes: α-particles are the least penetrating, followed by β-particles, with γ-rays being the most penetrating. The characterization of the ambient radiation in underground laboratories is important for low background searches. In LNGS, the γ-ray flux, averaged over 8 different positions in different Halls, was measured as $0.25\,\mathrm{cm^{-2}s^{-1}}$ [210] in an energy range of 7–2734 keV, and the sedimentary rocks and concrete surrounding the lab were found to have relatively low concentrations of uranium and thorium ($1.7\,\mathrm{Bq\,kg^{-1}}$ and $1.4\,\mathrm{Bq\,kg^{-1}}$, respectively).

The materials used for the construction of the detector also contain traces of these elements[7], including other isotopes from anthropogenic or cosmogenic activation sources. For example, ^{60}Co is a synthetic isotope that is incorporated into SS by the re-utilization of scrap material exposed to a neutron source [211]. It has a half-life of $5.27\,\text{years}$ [212], and it β-decays to excited levels of ^{60}Ni, that γ-decay with six different channels. The main γ-ray emissions are $1173.2\,\text{keV}$ and $1332.5\,\text{keV}$. Another isotope of interest is ^{137}Cs, a common fission product of ^{235}U, with trace quantities originating from ^{238}U. Its half-life is of $30.05\,\text{years}$ [213], and the most distinctive transition is the β-decay to ^{137m}Ba which later decays to its stable state by a γ-ray emission of $662\,\text{keV}$.

^{222}Rn, ^{220}Rn and ^{85}Kr

Xenon contains the homogeneously diffused ^{222}Rn, ^{220}Rn and ^{85}Kr contaminants. The content of ^{222}Rn in diverse media, including air, comes from its emanation from the soil, rocks and granite through the decay of the naturally abundant ^{226}Ra (with $T_{1/2}$ =1600 years)[8]. Through adsorption, absorption and diffusion processes, materials end up containing this isotope, depending on their permeability and the equilibrium of the diffusion equation [214]. Their ^{222}Rn content is steadily outgassed, and due to its relatively long half-life ($T_{1/2} = 3.82\,\text{d}$), ^{222}Rn diffuses into the target LXe mass. A selection campaign was performed by XENON1T to selectively eliminate problematic materials [215].

The decay of ^{214}Bi to the excited and ground level of ^{214}Po through β-decay can contribute to the background in the low energy-region. However, due to the release and the subsequent α-emission from the decay of ^{214}Po, a technique for its tagging can be derived [216]. The decay from ^{214}Bi and ^{214}Po occur close in time, with a mean lifetime of ^{214}Po of $237\,\mu\text{s}$, and the correlation can be used to exclude these events. When the event occurs in the core of the LXe volume in the detector, the coincidence tagging efficiency is close to 100%. However, it decreases if the ^{214}Po is plated out on detector surfaces, and the α-particle loses energy before entering the sensitive region. It can also decrease if the α event occurs in a region with low light collection [217].

From the thorium decay series, there is also a concentration of ^{220}Rn. Given its short half-life of $55.3\,\text{s}$, the concentration is lower than the one from ^{222}Rn, nonetheless, its daughter ^{210}Pb can β-decay, and the β-decay of either ^{214}Pb (from ^{222}Rn) or ^{212}Pb (from ^{220}Rn) can enter in the low-energy region of the detection range. Moreover, its decay is called a 'naked β' due to the lack of a α- or γ-particles associated with the transition to the ground state in the daughter nucleus. Therefore,

[7] We will discuss in detail the calculation of the background coming from detector materials in Chapter 3, that requires dedicated simulations and it is part of this work.

[8] From the ^{228}U chain

the spectral shape, branching ratio of this process and rate should be carefully characterised. These isotopes decay through first-forbidden non-unique transitions, making their spectral shape depend strongly on the particular nuclear structure. The effects of the nuclear structure were taken into account using large-scale shell-model calculations in Ref. [218]. It is remarked in the study that the first-forbidden non-unique β-decays depends strongly on the value of the effective weak axial-vector coupling g_A, and the study calculates the spectra assuming different values ($g_A = 0.7, 0.85, 1$). The spectrum obtained using $g_A = 0.85$ predicts an event rate 19.0% lower in the region 1–15 keV from ^{214}Pb. The comparison for these assumptions can be seen in Figure 2.9. The estimated rate from ^{214}Pb and ^{212}Pb is calculated assuming the goal activity of $0.1\,\mu$Bq/kg from ^{222}Rn. The branching ratio of the ^{214}Pb decay to the ground state of the daughter nucleus is taken as BR $= 0.109 \pm 0.01$ [172, 219]. For ^{212}Pb, and a relative concentration of ^{220}Rn/^{222}Rn $\sim 0.3\%$ is taken [193].

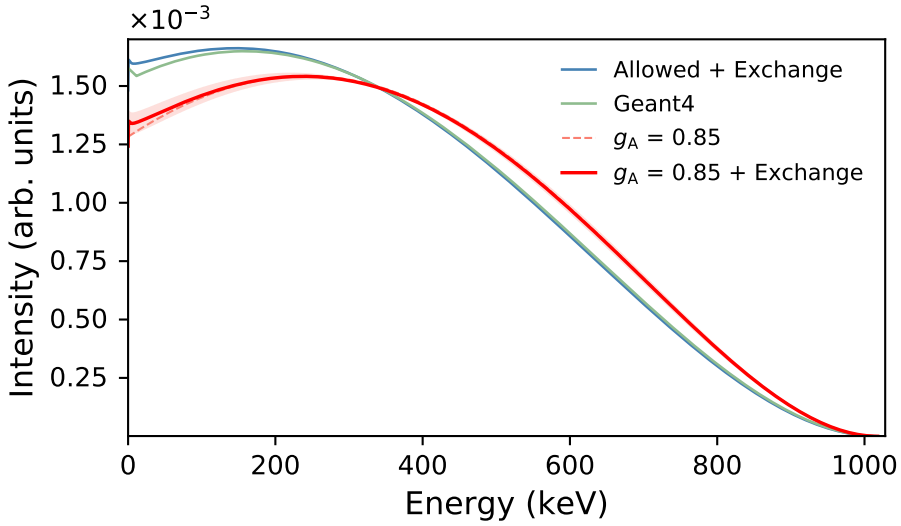

Figure 2.9: Comparison of β^- spectra for the ground-state decay of ^{214}Pb shown over the full energy range. The blue line was used in the XENON low energy region searches result [103], while the red line shows the improved calculations from Ref [218].

The isotope ^{85}Kr is a radioactive noble gas that β decays with a half-life of (10.752 ± 0.023) years and a Q-value of 687 keV [220]. Because of its abundance in the atmosphere [9], commercial xenon contains ^{85}Kr that must be removed with a purification system. The decay of ^{85}Kr is a first-forbidden unique transition, and the corrections to the spectrum due to the nuclear structure are only minor [218]. By combining the spectra given in Ref. [218] for ^{214}Pb, ^{212}Pb and ^{85}Kr, the calculation of

[9] Although it can be produced naturally in the atmosphere by interacting cosmic rays with krypton in the air, most of its production is antropogenic by at least four orders of magnitude [221].

the expected event rate can be made for DARWIN. The estimated rate of ^{85}Kr for DARWIN is calculated assuming a relative abundance of $^{85}\mathrm{Kr}/^{\mathrm{nat}}\mathrm{Kr} = (1.7 \pm 0.3) \times 10^{-11}$mol/mol [222], which was observed in XENON1T. The target concentration for DARWIN is 2 ppq $^{\mathrm{nat}}$Kr/Xe. Figure 2.10 shows the expected event rate from the β^- decay of ^{214}Pb, ^{212}Pb and ^{85}Kr in DARWIN.

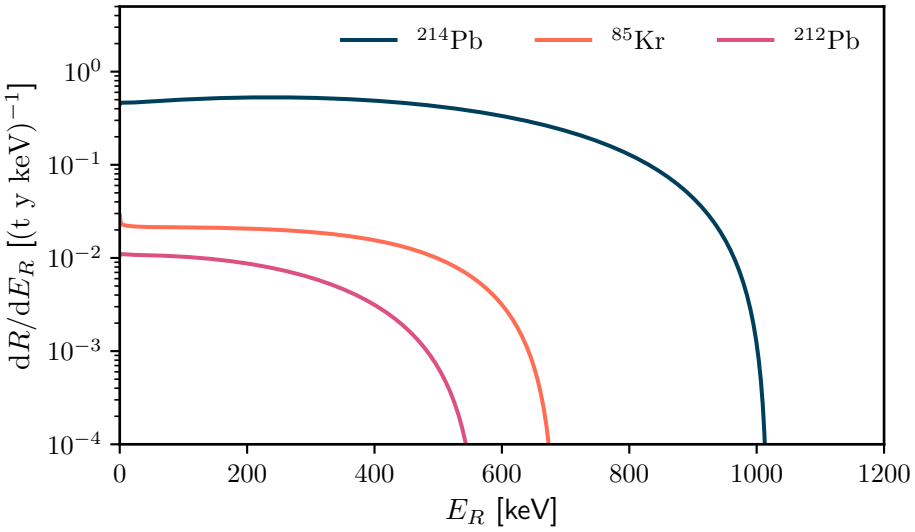

Figure 2.10: Comparison of the event rate in DARWIN for ^{214}Pb, ^{212}Pb and ^{85}Kr, where the spectra are taken from Ref. [218]. The following assumptions were made: 0.1 µBq/kg activity from ^{222}Rn, concentration ratio $^{220}\mathrm{Rn}/^{222}\mathrm{Rn} \sim 0.3\%$, and a concentration of 2 ppq $^{\mathrm{nat}}$Kr/Xe.

Solar neutrinos

Solar neutrinos originate inside the core of the Sun through nuclear fusion processes. The solar luminosity constraints the flux due to energy conservation, assuming most of it comes from nuclear reactions of its lightest elements, according to the Standard Solar Model. Most neutrinos are produced in the proton-proton chain (pp) reaction of the Sun (around 91% of the total flux), in which it converts hydrogen to helium, and ^{7}Be neutrinos are produced further in the pp-chain (7%) [139]. The CNO cycle contributes as well to the neutrino production, representing $\sim 1\%$ of the total solar neutrino flux [223]. More details of the cycles can be found in Appendix B. Table 2.2 shows the different solar neutrino fluxes, taken from Ref. [224], and Figure 2.11 shows the solar neutrino fluxes spectra, together with atmospheric and diffuse supernova neutrino background (DSNB)[10].

[10]Theoretical population of neutrinos and anti-neutrinos originating from supernova events in the Universe

Table 2.2: Neutrino total fluxes for the different solar processes [224].

Family	Q [keV]	Φ_0 [$\mathrm{cm^{-2}\ s^{-1}}$]	Uncertainty (%)
pp	420	5.98×10^{10}	0.1
^{7}Be	862(90%)	4.93×10^{9}	1.2
	364(10%)		
pep	1442	1.44×10^{8}	0.7
^{13}N	1200	2.78×10^{8}	5.4
^{15}O	1732	2.05×10^{8}	8.3
^{17}Fe	1732	5.29×10^{6}	3.8
^{8}B	18773	7.98×10^{6}	1.1

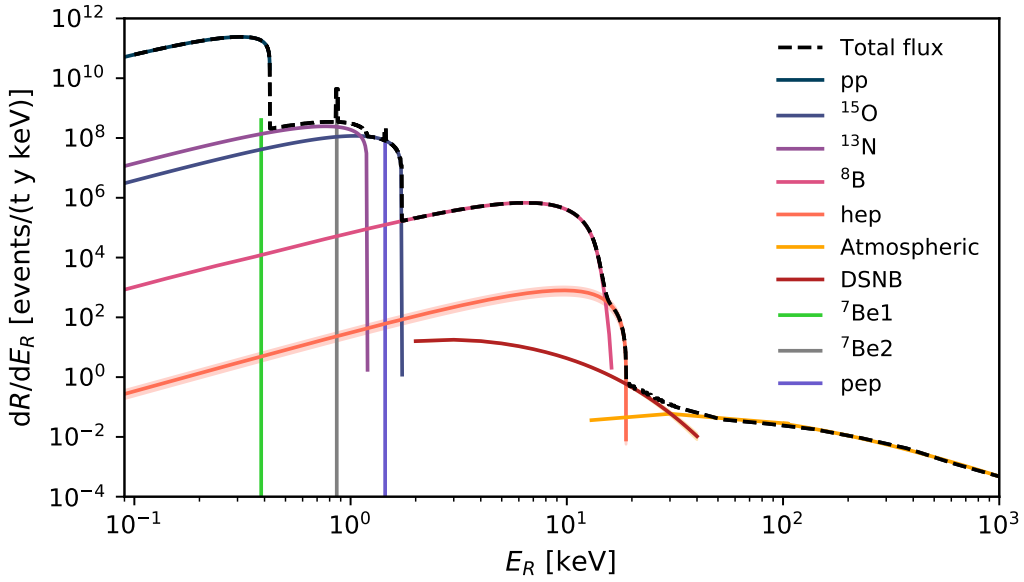

Figure 2.11: Solar neutrino fluxes for the different reactions in the Sun, where the continuous spectra follow a β^- spectrum. The solar fluxes are from Ref. [224]. The DSNB and Atmospheric neutrino fluxes from Refs. [225, 226].

Neutrino interactions with electrons

Neutrinos can interact with atomic electrons in both neutral and charged current reactions. These interactions are within the SM with the exchange of $W^{\pm}$ and Z^0 bosons, as shown in Figure 2.12. Because the electrons in the xenon atom are bound, one needs to consider the atomic form factor in the cross section calculation. The recoil of the atomic nucleus can be neglected due to the difference between the momentum transfer and the ratio of neutrino energy and nuclear mass.

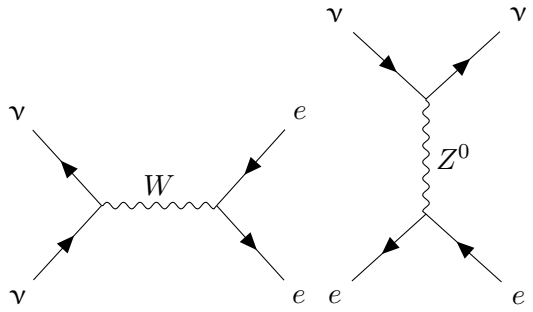

Figure 2.12: Scattering of neutrinos with electrons for charged (W) and neutral (Z^0) currents. The W-boson channel is absent in the cases of the muon and tau neutrinos.

When a neutrino with energy E_ν scatters off a free electron in the process:

$$\nu + e^- \rightarrow \nu + e^-, \tag{2.7}$$

the neutrino transfers the momentum q, assumed initially at rest in the laboratory frame. The kinematic relation in an ultra-relativistic limit where $m_\nu = 0$ is given by [227]

$$\cos\chi = \frac{E_\nu + m_e}{E_\nu}\sqrt{\frac{T}{T+2m_e}}, \tag{2.8}$$

where T is the energy transferred, m_e is the electron mass, and χ is the outgoing angle with respect to the incident neutrino. The maximum energy transfer is then given by

$$T_{\max} = \frac{2E_\nu^2}{2E_\nu + m_e}. \tag{2.9}$$

Using this information, the cross section can be written as [228, 229]

$$\frac{d\sigma_{\nu_e}^{SM}}{dT} = \frac{G_F^2 m_e}{2\pi}\left[(g_V + g_A)^2 + (g_V - g_A)^2\left(1 - \frac{T}{E_\nu}\right)^2 + \left(g_A^2 - g_V^2\right)\frac{m_e T}{E_\nu^2}\right], \tag{2.10}$$

where E_ν is the neutrino energy, G_F is the Fermi constant and g_V and g_A the vector and axial vector coupling constants. In this equation is assumed that $|q^2| \ll m_W^2$. For reactor neutrinos the last term is negligible, as $E \gg m_e$. The free-electron approximation simplifies the cross section for an atomic electron of a nuclear species $N = (A, Z)$ as

$$\frac{d\sigma_{\nu-e}^{(Z,\mathrm{FE})}}{dT} = Z\frac{d\sigma_{\nu-e}}{dT}. \tag{2.11}$$

This approximation holds when the energy transfer T is relatively large compared to the atomic binding energies. For low-energy interactions, a different approach has to be taken. A proposed solution is adding a factor to the free-electron approach by modelling the energy levels as step function. When the moment transfer is equal to the ionisation threshold for the orbital, the electron in the corresponding orbital is not available, producing a sharp step in the dependence of the cross section with the momentum transfer, the effective value Z_{eff} can be written as

$$Z_{eff}(T) = \frac{1}{Z}\sum_{k=1}^{Z} k\Theta(E_R - E_B^k), \tag{2.12}$$

where the sum is over the atomic levels with binding energies E_B^k. This approximation describes the scattering of atomic electrons with a good match for germanium [230]. For xenon, in Ref. [231] it is found that a full RRPA (Relativistic Random Phase Approximation) calculation of the scattering of atomic electrons yields differences of 25% fewer events for $T \sim 10$ keV when considering pp and ^{7}Be solar neutrinos. This suppression is assigned to electron-electron correlation effects. The full spectra also fall off faster at higher energies than the stepping approximation. Taking the previously mentioned points into consideration, the cross section used in this work will be the one calculated in Ref. [231].

Using the expected fluxes and the cross section for a SM interaction, the rate can be calculated as

$$\frac{dR_{\nu_a}}{dT} = \frac{N_a}{A}\int_{E_{\min}} dE_\nu \sum_i \Phi_{i,a}\left(E_\nu\right)\frac{d\sigma_a}{dT} \tag{2.13}$$

where $a = e, \mu, \tau$ is the neutrino species, which have oscillated and changed flavour in their path, $E_{\min}$ is the minimum energy to produce a recoil in LXe, $\Phi_{i,a}$ is the flux from the different solar neutrino families, and $\frac{d\sigma_a}{dT}$ the differential scattering cross section.

Neutrinos from the Sun can modify their flavour content by neutrino oscillation on their path to Earth and their path from the core of the Sun to its surface by the MSW effect. The MSW-large-mixing-angle solution predicts a vacuum-dominated oscillation, approximating the survival probability of electron neutrinos to [232]

$$P_{ee} = \cos^4\theta_{13}\left(1 - \frac{1}{2}\sin^2\left(2\theta_{12}\right)\right) + \sin^4\theta_{13}. \tag{2.14}$$

When assuming $\sin^2(2\theta_{12}) = 0.851 \pm 0.021$, $\sin^2(2\theta_{13}) = 0086 \pm 0.003$, the survival probability is $P_{ee} = 0.55$, with an error of 2% [140]. The remaining part of the pp and ^{7}Be are either ν_μ or ν_τ and will scatter with the same differential cross section. Additionally, this flux will exhibit an

annual modulation due to the changing distance of the Earth to the Sun, which needs to be averaged over a whole year. After applying these corrections, the rate in the LXe target mass was recalculated for this work, using both Equation 2.10 and the RRPA calculation. In Figure 2.13 the effect of the atomic shells is shown for the stepping approximation, alongside the calculation with the stepping approximation compared to the RRPA calculation.

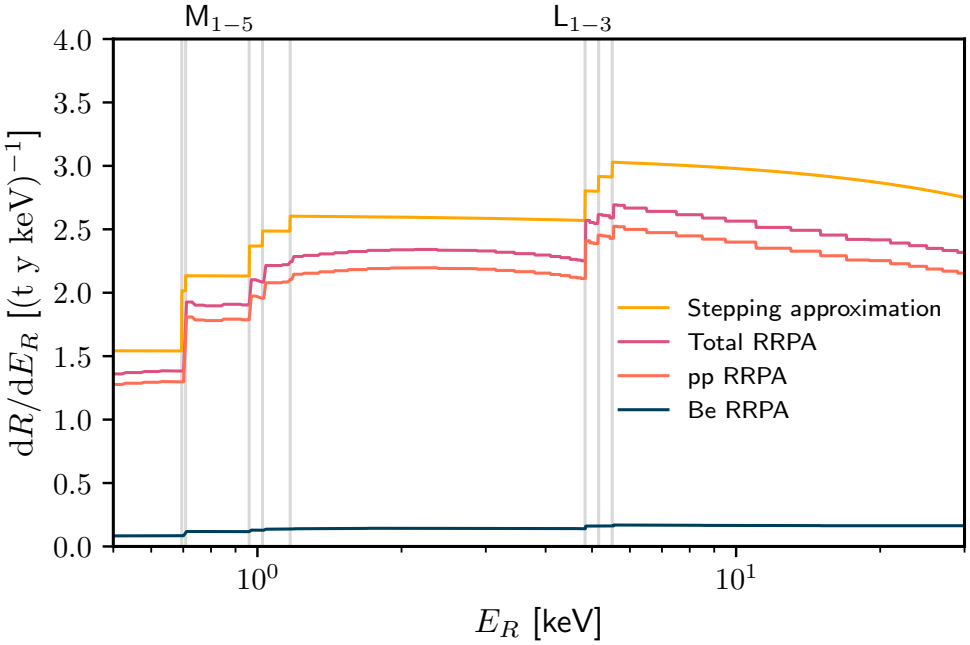

Figure 2.13: Recalculated expected event rate in LXe from neutrino-electron scattering using the stepping approximation compared to the total event rate calculated using RRPA numerical values from Ref. [231]. The rate for the pp and ^{7}Be are shown in order to emphasise the one order of magnitude difference between the two fluxes. The M and L notation on the upper axis represents the xenon atomic shells.

Double beta decay of ^{136}Xe

The double beta decay of ^{136}Xe has a spectrum with a Q-value of $(2457.83 \pm 0.37)\,\mathrm{keV}$, with a half life of $\mathrm{T}^{2\nu\beta\beta}_{1/2} = 2.165 \pm 0.016\ (\mathrm{stat})\ \pm 0.059\ (\mathrm{sys})\ \times 10^{21}$ y , measured in EXO-200 [233]. The $2\nu\beta\beta$-decay of ^{136}Xe introduces a background contribution due to the interaction of the two electrons with LXe. The spectrum depends on the features of the transition. All ground states of even-even nuclei have a spin and parity 0^+; thus, $0^+ \rightarrow 0^+$ transitions are allowed. It is also possible to go to low-lying excited states of the daughter nucleus, giving rise to $0^+ \rightarrow 2^+$ transitions or the excited 0^+

state [143]. Figure 2.14 shows a schematic of the double beta decay in ^{136}Xe.

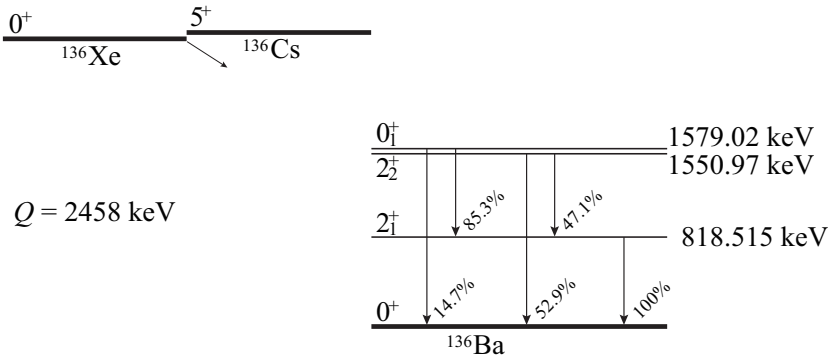

Figure 2.14: Decay scheme of ^{136}Xe to ^{136}Ba. The energy levels and the branching ratios for the de-excitations are taken from Ref. [234]. Only the 0^+ and 2^+ levels are shown. Scheme from Ref. [235].

The precise calculation of this spectrum is important for the background assessment, as the spectrum can change the rate that falls in different energy regions. In Ref. [154], Kotila and Iachello calculated the summed energy spectrum of the two electrons emitted for ^{136}Xe$\rightarrow$ ^{136}Ba, by using the exact Dirac wave function with finite nuclear size and electron screening. The error in the calculations comes from the phase space factors that take for input the Q-value and the nuclear radius. It is also affected by the screening choice (10% uncertainty in the screening assumed when choosing the Thomas-Fermi model in the screening, which often overestimates the electron density at the nucleus) and the excitation energy in the intermediate nucleus. The uncertainty comes mostly from the experimental activity that normalizes the event rate spectra, while the theoretical uncertainty of the spectra is considered negligible [236]. The result from Kotila and Iachello and the decay rate from Ref. [233] are used in this work to calculate the rate of this process, and the expected rate is shown in Figure 2.15.

Cosmogenic activation of xenon

Natural xenon has a composition of isotopes with different abundances, as shown previously in Table 2.1. Interactions with neutrons that were produced either by radioactive processes in materials, cosmic showers, spallation or fission products can activate xenon isotopes and produce unstable nuclei that could decay and potentially introduce background events in the detector [237]. A list of relevant isotopes for this works follows.

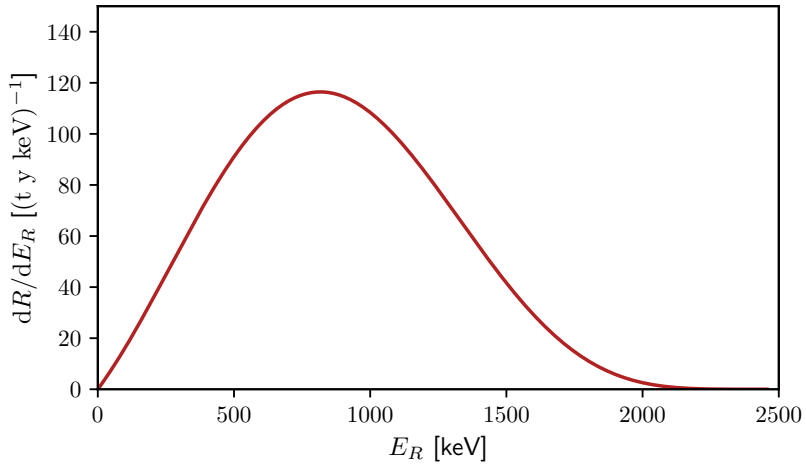

Figure 2.15: Spectra of the sum energy of the electrons released in the double beta decay of ^{136}Xe, taken from the calculation in Ref. [154].

^{137}Xe is not present in natural xenon but can be produced by cosmogenic activation in the detector underground. A fraction of the muon-induced neutrons will thermalise in xenon and they can be captured by a ^{136}Xe nucleus. Since there are no other heavier atoms, ^{137}Xe cannot be produced via spallation. A diagram of the interaction is shown in Figure 2.16. In order to understand this background, the neutron production mechanisms need to be assessed. Neutrons can be produced by the natural activity of the rock and the concrete, the detector materials, muon-induced neutrons from the rock and the concrete and muon-induced neutrons from detector materials. The production of neutrons from (α,n) reactions from the rock is not sufficient to produce a significant amount of neutrons that can activate ^{136}Xe, since neutrons from the rock are stopped by the water tank. This is not the case of the xenon outside the water tank in the purification system, and precise calculations are required in that case in order to estimate its impact. Moreover, muon-induced neutrons in the detector in the xenon are a dangerous activation source since they cannot be easily identified, penetrating directly into the sensitive volume of the detector [1]. These neutrons are produced by the muon interaction with xenon and can thermalise in their path and be captured by ^{136}Xe. The ^{137}Xe isotope proceeds to β^--decay with a Q-value of $4.17\,\mathrm{MeV}$ and a half-life of $3.82\,\mathrm{min}$, covering the whole energy region of the detector. The production rate in DARWIN, assuming the detector is located in LNGS, was calculated to be $(7.85 \pm 0.70) \times 10^{-1}\,\mathrm{isotopes/(t\,y)}$ [238]. The production rate was derived from GEANT4 [239] MC simulations, and the errors represent the difference in the production rate from the chosen models and datasets (SHIELDING, SHIELDINGLEND, BIC) to simulate neutron and gamma interactions.

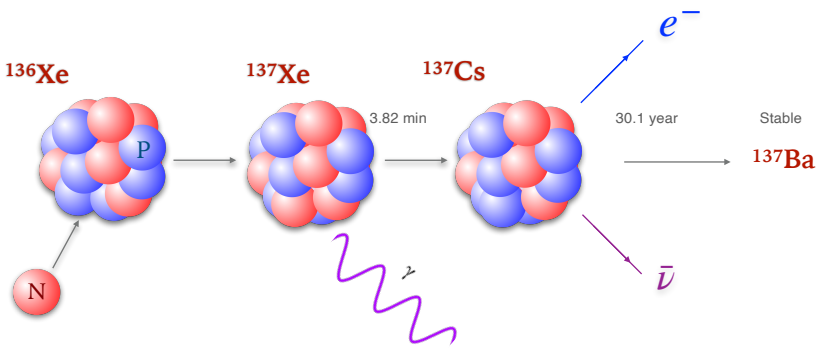

Figure 2.16: Diagram of neutron capture by ^{136}Xe, which produces ^{137}Xe in an excited state, decaying to ^{137}Cs with the emission of a γ-ray, which later β-decays to ^{137}Ba.

^{133}Xe can be as well produced by neutron activation. It is a common background after neutron calibration in TPCs, as observed by XENON1T [192]. In this work we assume negligible contribution to the background from this isotope, as its half-life of $(5.24\,\mathrm{d})$ allows to exclude the data after neutron calibrations.

Double electron capture of ^{124}Xe

The two-neutrino double electron capture (2νECEC) is a second-order weak-interaction process with a recently observed half-life by the XENON1T experiment of $T_{1/2}^{2\nu\mathrm{ECEC}} = \left(1.1 \pm 0.2_{\mathrm{stat}} \pm 0.1_{\mathrm{sys}}\right) \times 10^{22}$y [125]. Analogous to the single-electron capture, double-electron capture rates depend on the overlap between the electron and nuclear wave functions [240]. The electrons in the s-orbitals of the K- and L-shell (L1) have the largest overlap. However, the M-, N- and O-shells with s-, p-, d- and higher orbitals should also contribute to the total double-electron capture decay rate. The values for the squared amplitudes of the radial wave functions up to the N5-shell are tabulated in Ref. [241]. The final values for the relative intensities used in this work are taken from Ref. [125]. The final feature is the superposition of the different peaks from the different shell captures. The values taken are shown in Table 2.3.

2.4.2 Nuclear recoil sources in liquid xenon

Neutrons produce single-site interactions indistinguishable from WIMPs and cannot be discriminated due to their S1/S2 ratio. Fast neutrons penetrate the LXe-sensitive volume and mimic a WIMP signal. The so-called *radiogenic neutrons* are generated by the detector materials themselves, while

Table 2.3: Relative capture fractions and energies of double-electron captures from different shells. The capture fractions considering only the K- and L1-shells were used in [242]. Table from Ref. [125].

Decay	K & L1 [%]	K to N5 [%]	Energy [keV]
KK	76.5	72.4	64.3
$KL_{1,2,3}$	22.0	20.0	$36.7 - 37.3$
$KM_{1,2,3,4,5}$	–	4.3	$32.9 - 33.3$
$KN_{1,2,3,4,5}$	–	1.0	$32.3 - 32.4$
$L_{1,2,3}L_{1,2,3}$	1.6	1.4	$8.8 - 10.0$
Other	–	0.8	< 10

cosmogenic neutrons are produced by cosmic muons traversing the mountain rock and detector materials. Fast neutrons are more likely to produce multi-scatters, and dedicated background suppression techniques exist [182]. Neutrons produced by the cosmic muons interacting with the cavern or the detector materials can penetrate the sensitive detector volume. The expected flux for muon induced neutrons is of energies above $10\,\mathrm{MeV}$ in LNGS is $3.7 \times 10^{10}(\mathrm{cm}^{-2}\mathrm{s}^{-1})$ [238]. The purpose of the external water tank in LXe experiments is to provide an absorption volume and stop such events. The instrumentation of photosensors provide additional vetoing of muon or shower-like events traversing the tank. The isotope that produces most of the neutron yield due to spontaneous fission is ^{238}U. However, in practice, γ-rays and neutrons are produced together in this process and can be tagged [243]. While spontaneous fission is common in high-Z isotopes, (α, n) reactions are important for low and medium-Z nuclei. As shown in Table A.1, uranium and thorium chains produce 6 and 8 α-decays, respectively, and quickly lose their energy while travelling through materials. The energy losses decrease the probability of producing a neutron, which is a process that simulation libraries take into account. There are several libraries for the simulation of the neutron yield in materials, such as EMPIRE [244], TALYs [245] and SαG4N [246].
Finally, the contribution to the background from CEνNS, when a neutrino interacts with a nucleus, can leave an imprint indistinguishable from dark matter, which translates in the neutrino fog discussion in Chapter 1.

2.5 Expected electronic recoil backgrounds in DARWIN and remarks

With the background reduction projected for DARWIN, the detection of solar neutrinos, axions, ALPs, and other searches in the ER channel become promising, as the activity of diverse common contaminants in LXe will be reduced. Table 2.4 shows a list of the assumptions and concentration goals for DARWIN, while Table 2.5 shows the errors from the different models assumed.

Table 2.4: List of backgrounds in the ER channel and the assumptions taken in order to calculate the background in the chapters.

Background Source	Activity/Half-life	References
$2\nu\beta\beta$ of ^{136}Xe	$T_{1/2}^{2\nu\beta} = 2.165\,\mathrm{y}$	Spectra: Ref. [154]
		Cross section: Ref. [233]
β-decay of ^{137}Xe	$7.85 \times 10^{-1}\,\mathrm{isotopes}/(\mathrm{t\,y})$	MC simulations
2νECEC of ^{124}Xe	$T_{1/2}^{2\nu\mathrm{ECEC}} = 1.1 \times 10^{22}\mathrm{y}$	Ref. [125]
Solar neutrinos		Fluxes: Ref. [224]
		Cross sections: Ref. [231]
β-decay of ^{85}Kr	$^{85}\mathrm{Kr}/^{\mathrm{nat}}\mathrm{Kr} = 1.7 \times 10^{-11}\mathrm{mol/mol}$	Relative abundance from Ref. [247]
	2 ppq $^{\mathrm{nat}}$Kr/Xe	Target DARWIN
β-decay of ^{222}Rn	$0.1\,\mu\mathrm{Bq/kg}$	Target DARWIN
	BR $= 0.109 \pm 0.01$[1]	Ref. [172, 219]
β-decay ^{220}Rn	$^{220}\mathrm{Rn}/^{222}\mathrm{Rn} \sim 0.3\%$	Ref. [193]

Table 2.5: List of backgrounds in the ER channel and uncertainties assumed.

Background Source	Uncertainties
^{136}Xe	10% spectra, 28% activity
^{137}Xe	10% in the production from difference between MC libraries
^{124}Xe	27%
Solar neutrinos	3% in the $\nu - e$ cross section
^{85}Kr	18% from relative abundance $^{85}\mathrm{Kr}/^{\mathrm{nat}}\mathrm{Kr}$
^{222}Rn	10% for the branching ratio $^{214}\mathrm{Pb} \rightarrow {}^{214}\mathrm{Bi}$

The next chapter will discuss the production of the background model for DARWIN given the external radiogenic contribution from detector materials in the ER channel. Combining the analytical calculations used in this chapter, a background model will be derived to estimate the sensitivity of DARWIN to the $0\nu\beta\beta$-decay of ^{136}Xe in Chapter 3, and for the sensitivity to solar axions in Chapter 4.

[1] Branching ratio of $^{214}\mathrm{Pb} \rightarrow {}^{214}\mathrm{Bi}$ in the ground state.

Chapter 3

Backgrounds and sensitivity for the neutrinoless double beta decay of ^{136}Xe in the DARWIN observatory

> *After additional checks verified their preliminary results, Wu and her group lifted the veil of secrecy and a shock wave swept through the physics community. (...) I sent a cable to Oppenheimer, who was vacationing in the Virgin Islands: "Wu's experiment yielding large asymmetry showing G equal to G'. Therefore neutrino is a two component wave function." He cabled back "Walked through door" referring to a talk of mine in 1956 in which I had likened the situation in 1956 of the high-energy physicists to that of a man in a dark room. He knows that in some direction there is a door. But in which direction?*
>
> **— C. N. Yang**

As stated in previous chapters, the neutrinoless double beta decay is a forbidden second-order weak nuclear process, yet unseen. This transition would produce two electrons in LXe, with energies distributed by sharing the Q-value of the transition of $(2457.83 \pm 0.37)\,\mathrm{keV}$ for ^{136}Xe [233]. The electrons, emitted with an angular distribution according to the underlying BSM physics, nuclear matrix elements and phase factors, will produce an ER nearby the site where the decay occurred. As a result, the energy depositions of both electrons will produce scintillation and ionisation in LXe,

which can be detected in the TPC. The DARWIN observatory could detect these rare events due to a large amount of ^{136}Xe in the detector ($3.5\,\mathrm{tonnes}$), its excellent energy resolution [248] and its ultra-low background due to the increasing shielding capabilities and a dedicated campaign to screen and select the materials of the detector. To study the sensitivity to this process with DARWIN, the background around the Q-value is carefully examined and modelled in this chapter. Section 3.1 introduces the software used to produce the simulations and the treatment of the radioactive decays. The resulting full background model is discussed in Section 3.2. In Section 3.3, the signal models of the two electrons emitted in the transition in the $0\nu\beta\beta$ process (together with their recoil in LXe), are characterised. Section 3.4 describes the statistical framework used for the inference of the sensitivity and the discovery potential, together with a discussion of the obtained results. To finalise, we discuss the present implications of this study and future perspectives on detecting this physics channel in DARWIN.

3.1 DARWIN Geant4 model

The total ER background consists of the sum of the material contributions and the homogeneously distributed intrinsic contributions in LXe. This section covers how the external radiogenic background is simulated, with details on the software used, while the next section covers which isotopes are simulated and the results of these simulations. The estimation of the expected background was performed using Geant4, a Monte Carlo (MC) simulation toolkit widely used in particle physics. Geant4 simulates the interaction of particles with matter, and it can track its propagation [249]. The package is written in C++, making it fast and robust, and it is continuously maintained by CERN staff and users. The user can model the geometry of a detector and specify its materials, along with their chemical and physical properties. Such properties can be set either from the official Geant4 library or manually added by the user. Once the geometry and the properties are set, the simulation workflow starts by selecting the type of particle/s to be simulated, with its initial momentum and position. A particle is propagated spatially, interacting along its path with the detector materials. In this process, secondary particles can be created. Depending on the type of particle, this can be further propagated, with possible energy loss or decay. This process can be repeated for N simulated particles under the same initial conditions. A complete list of tracking variables can be stored under user demand, for example, variables such as energy deposited, momentum, and type of interaction, among others. In Geant4, an *event* is defined as the information generated by the tracking of an initial particle –known as *primary*– and its *secondaries* as they propagate and interact with matter. An event ends when all the particles are either absorbed or escape the confined volume of the simulation. Geant4 allows

the user to store the relevant tracking information in different formats. The particle tracking and interactions are saved in *ROOT* [250] files. *ROOT* is a software widely used in high-energy physics, and it provides optimised storage of large quantities of data, with a high level of compression and fast query functions. Each file stores the relevant parameters for spectra generation and analysis. The final file will contain information about our simulation that has to be processed to get a realistic event-wise energy deposition.

The geometry modelling is done with objects from Geant4 classes, usually starting from simple forms such as spheres, cubes or cylinders, that the user can combine in Boolean or other types of operations to create more complex shapes. Materials need to be specified through their chemical composition, density, and phase. If optical properties are of interest, the absorption length, reflectance and other parameters can be set. These properties are used for particle tracking and physics processes modelling.

The geometry of the DARWIN detector was implemented following the baseline 3D CAD model. Only the cryostat and the TPC are relevant for the external radiogenic background due to their proximity to the LXe-sensitive volume. Thus, only details on these two components will be shown. Table 3.1 shows the components, the materials used and their masses for the cryostat and TPC elements. The mass is calculated from the volumes and the density, given the specified material.

Table 3.1: List of detector components included in the Geant4 geometry for the cryostat and TPC model of DARWIN, stating their material composition and total mass.

Component	Material	Mass
Outer cryostat	Titanium	3.0 tonne
Inner cryostat	Titanium	2.1 tonne
Bottom pressure vessel	Titanium	0.4 tonne
LXe instrumented target	LXe	39.3 tonne
LXe buffer outside the TPC	LXe	9.0 tonne
LXe around pressure vessel	LXe	270 kg
GXe in top dome + TPC top	GXe	30 kg
TPC reflector (3mm thickness)	PTFE	146 kg
Structural support pillars (24 units)	PTFE	84 kg
Electrode frames	Titanium	120 kg
Field shaping rings (92 units)	Copper	680 kg
Photosensor arrays (2 disks):		
Disk structural support	Copper	520 kg
Reflector + sliding panels	PTFE	70 kg
Photosensors: 3” PMTs (1910 units)	composite	363 kg
Sensor electronics (1910 units)	composite	5.7 kg

One way to visualise the geometry is by simulating virtual particles that are part of the Geant4 software, called 'geantinos'. These particles do not interact with materials and are used for track propagation. As no interaction needs to be calculated, the simulation time is significantly reduced, and millions of events can be simulated at once. Hence, they are helpful for debugging transport processes and for visualising geometries. Figure 3.1 shows, as an example, the bottom PMT array and the outer and inner vessels from the cryostat displayed with *geantinos*, that were sampled randomly in the material volume. A 2D projection of the geometry of the TPC and the cryostat, together with the list of materials used in the detector components, is shown in Figure 3.2.

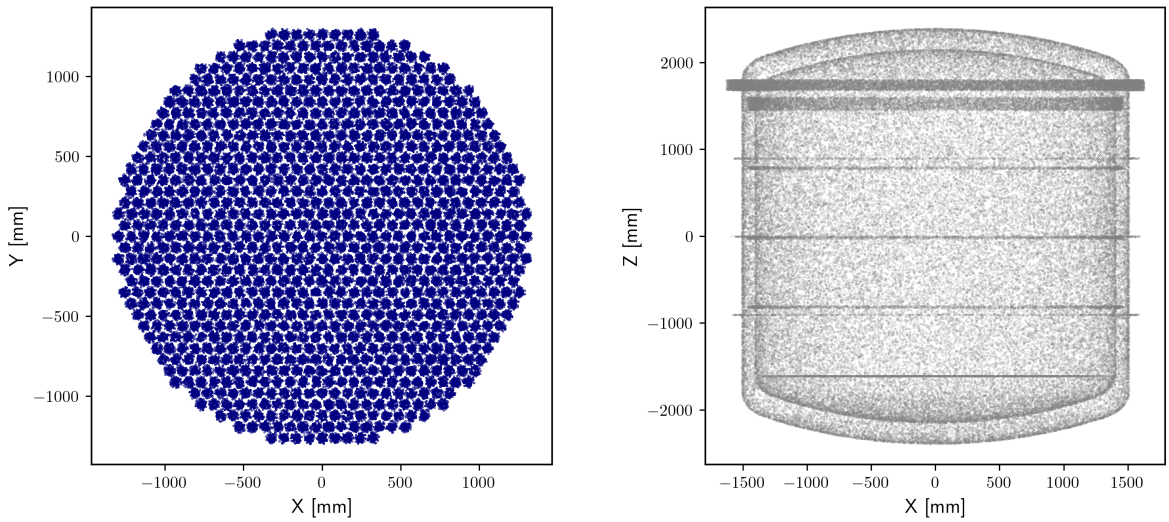

Figure 3.1: Left: Bottom PMT array of the DARWIN TPC in Geant4, where 955 PMTs are placed in a circular distribution to maximise the light coverage; Right: width and height (X-Z, respectively) plane projection of the cryostat implemented in Geant4, where the inner and outer vessels are visible. Stiffener hoops around the cryostat inner and outer vessels, help to reduce the total mass of the cryostat and are incorporated in the Geant4 geometry.

To simulate the radioactive decays from the materials, the corresponding isotopes are placed at rest randomly in the selected material volumes. The number of simulated events depends on the activity of the material and is usually taken to cover at least one year of operation of the detector. In the case of DARWIN, this number varies from 10^6 to 10^7 primary events. Only the energy depositions that take place in the instrumented LXe volume are relevant for the ER background.
After simulating the energy deposited in LXe, the fact that the spatial and temporal resolution of the detector does not have an arbitrary high numerical precision needs to be taken into account. Energy depositions that occur too close spatially will be seen as a single energy deposition in the actual

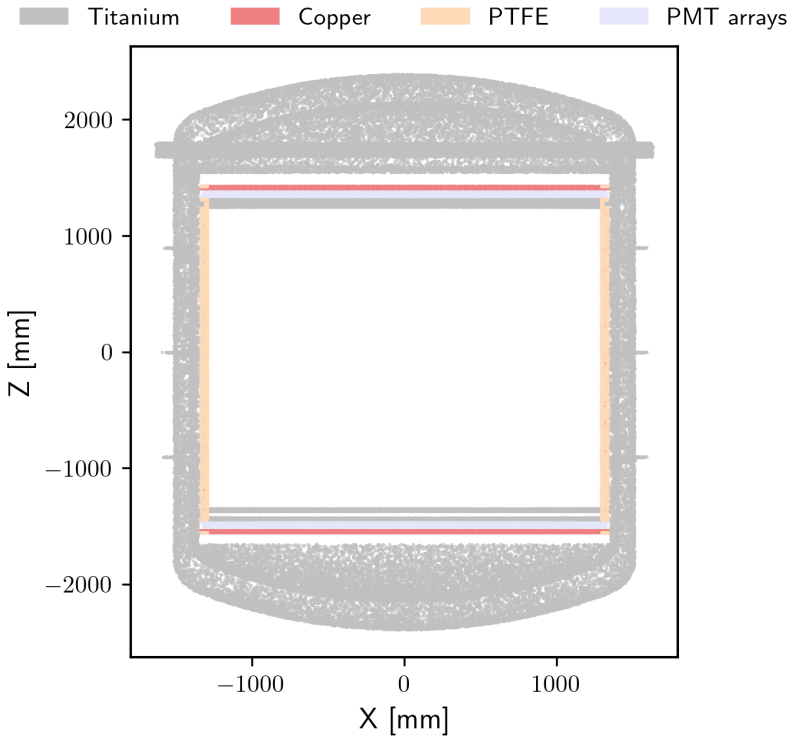

Figure 3.2: X-Z plane cut of the detector geometry inside the double-walled cryostat in Geant4, where the TPC materials are shown. The PTFE reflectors overlap with the field cage made out of copper rings. The electrode grids are implemented using titanium as material.

detector and interactions that occur too close in time. We will define a *cluster* as a region of interactions with distances below the resolution of the detector, inside which multiple interactions with LXe will appear in the detector as a single interaction. Figure 3.3 illustrates how several interactions are seen as a single interaction inside the position resolution of the detector. Clustering algorithms are based on the simulation of S2 waveforms and data matching from previous experiments and takes into account the signal size, the separation and drift effects. These effects are studied in detail in Ref. [251], although with detector-specific properties. In this chapter, we will assume an isometric 3D reconstruction of the depositions. However, the Z-coordinate usually has a greater resolution, being derived from time coincidence measurements. Each cluster event is analysed by the Density-Based Spatial Clustering of Applications with Noise (DBSCAN) algorithm [252], which reconstructs multiple clusters as a single cluster with a scanning parameter chosen to be $\epsilon = 15$ mm. The assumption is based on previous LXe TPCs' resolution and the diffusion of the electron cloud in LXe [253]. The value of $15\,\mathrm{mm}$ is an assumption of what would be feasible in DARWIN given diffusion effects,

based on the clustering distances for XENON1T, which range from $6.5\,\mathrm{mm}$ to $11.5\,\mathrm{mm}$ at the bottom of the TPC [125].

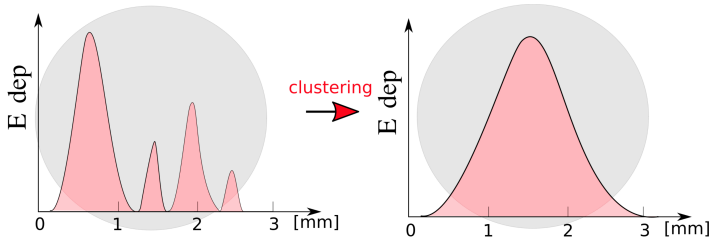

Figure 3.3: Simplified illustration of how multiple interactions are *clustered* as a single interaction due to the position resolution of the detector.

The energy spectrum from the MC simulation has to be smeared with the energy resolution of the detector, as the simulations are produced with a numerical energy resolution higher than the detector itself. The resolution at different energies is usually fit by the function

$$\frac{\sigma}{E} = \frac{a}{\sqrt{E}} + b \tag{3.1}$$

where the assumed values of $a = (0.3171 \pm 0.0065)$ and $b = (0.0015 \pm 0.0002)$ are taken from the high energy region analysis of XENON1T [248]. Geant4 separates the decays of each isotope and daughters into separate events, which overcounts the total number of events produced when a simulation is started from the beginning of a radioactive chain. The events generated in a chain depend on the version of Geant4 and can include excited states of the daughter nuclei or meta-stable states in between decays, with negligible half-lives. Therefore, an average number of states is derived for each decay chain to account for this effect. This number is called the *weight* (W) of the chain. For each material i, N_{ij} primary events are produced per isotope j. Afterwards, the MC simulations are processed with the clustering algorithm, and only events that produced a single energy deposition are saved. The choice of only saving single energy depositions is by the expected signature of the $0\nu\beta\beta$ signal in LXe, as explained in Section 3.3. The final differential rate histogram is generated and normalised with the formula:

$$R_{ij} = \frac{N_{ij}}{(T_{ij} M_{FV} \Delta E)}, \tag{3.2}$$

where M_{FV} is the fiducial mass and ΔE is the bin size of the energy spectrum in keV, and

$$T_{ij} = \frac{N_{ij}^{G}}{W M_i A_{ij}}, \tag{3.3}$$

is related to the lifetime of the primary isotopes in the materials. T_{ij} is the ratio between the generated MC counts (N_{ij}^{G}), normalised by the weight (W) of each chain, the mass of the simulated material in which these events were generated (M_i), and the activity value of that material and isotope (A_{ij}).

3.2 ER background rates and models

This section will describe in detail the isotopes that contribute to external radiogenic and homogeneously distributed background components. These backgrounds are discussed in this section for the energy region 2200–3000 keV.

3.2.1 External radiogenic background simulation results

The decay of long-lived radionuclides present in the detector materials produces daughter particles interacting with LXe. These interactions have a non-isotropic distribution. The most relevant contributions to this analysis are the thorium and uranium chains, as well as ^{60}Co and ^{44}Ti.
The contribution to the background from the uranium and the thorium chains comes from the decay of the isotopes ^{214}Bi and ^{208}Tl, respectively. The decay of ^{214}Bi introduces several peaks that can be found in between 2200–3000 keV, and Table 3.2 shows a list of the most relevant decays. Most of them have a relatively low intensity, and only the peak located at 2447.86 keV contributes significantly around the Q-value of the $0\nu\beta\beta$ of ^{136}Xe [254]. The decay of ^{208}Tl with the emission of a 2614.53 keV γ-ray introduces a continuum spectrum below that energy [254].

Table 3.2: Relative intensities of ^{214}Bi peaks that appear in the region 2200–3000 keV. Data from Ref. [254].

Energy [keV]	Intensity
2204.21 (4)	5.08 (4)
2266.51 (13)	0.018 (1)
2293.40 (12)	0.305 (9)
2331.3 (2)	0.0221 (14)
2447.86 (10)	1.57 (2)
2694.7 (2)	0.031 (2)
2769.9 (2)	0.025 (2)
2921.9 (2)	0.014 (2)
2978.9 (2)	0.0138 (5)

The material contamination is simulated given the radioactivity of the chosen materials. Table 3.3 shows a list of the main contributors to the radioactivity of materials selected for the TPC and cryostat. SS is a common choice for the double-walled cryostat used in current TPCs [255, 256]. However,

Ref. [257] identified titanium samples with low radioactivity, making titanium an attractive candidate. Additionally, titanium has higher stiffness than SS, with a tensile yield strength two times greater than SS [258], requiring less mass to construct the pressure vessel. The cosmogenic activation of materials can take place [259] in the materials used in the detector. Titanium may contain the isotope ^{44}Ti, which is of special interest due to the decay of its daughter nucleus, ^{44}Sc. This isotope has a long half-life of $T_{1/2} = 59.1$ yr, and a γ-emission at 2.66 MeV [254]. The electronics used for the bases of the PMTs are made of polyimide and can generate a potentially dangerous background due to its relatively high radioactivity and proximity to the target volume [257, 260]. For this reason, the electronics are included in the study as a separate element in the simulations.

Table 3.3: Measured activity levels of the materials selected to compose the TPC and cryostat, used in the MC simulation. The titanium radioactivity measurements are from Ref. [257], and the remaining measurements from Ref. [260].

Material	Unit	^{238}U	^{226}Ra	^{232}Th	^{228}Th	^{60}Co	^{44}Ti
Titanium	mBq/kg	<1.6	<0.09	0.28	0.25	<0.02	<1.16
PTFE	mBq/kg	<1.2	0.07	<0.07	0.06	0.027	-
Copper	mBq/kg	<1.0	<0.035	<0.033	<0.026	<0.019	-
PMT	mBq/unit	8.0	0.6	0.7	0.6	0.84	-
Electronics	mBq/unit	1.10	0.34	0.16	0.16	<0.008	-

Once the simulation is performed, the output is analysed, and the contributions to the ER background are calculated. The contribution from the continuum of higher energy peaks of ^{214}Bi decays around $Q_{\beta\beta}$ is negligible compared to the contribution from ^{208}Tl. The decays of ^{60}Co can introduce a deposition at 2505.7 MeV when decays at 1173.2 keV and 1332.5 keV are detected as a single site event [254]. The continuum contribution of this peak accounts for less than 0.01% of the external radiogenic background. Likewise, the continuum contribution from γ-rays emitted in the ^{44}Sc decay, the daughter isotope of ^{44}Ti, accounts for less than 1% of the external background.

Figure 3.4 shows the breakdown of the ER background rate from each detector component for a fiducial mass of 30 tonnes of LXe target. This fiducial mass is shown as an example due to being the target mass for previous analyses [261, 126] and containing the distinctive features from the external radiogenic background with a high number of events. Most of the contribution to the background comes from the PMT arrays and the cryostat. Low energy β,γ and α particles are stopped to a high degree by the LXe itself, and few of them reach the innermost region of the detector. High energy γ and β particles above 2200 keV have a longer penetration path in LXe, of around $\mathcal{O}(10$ cm$)$ for a 2 MeVγ-ray. As a consequence, the fiducialisation of the LXe target volume becomes less effective in removing undesired events.

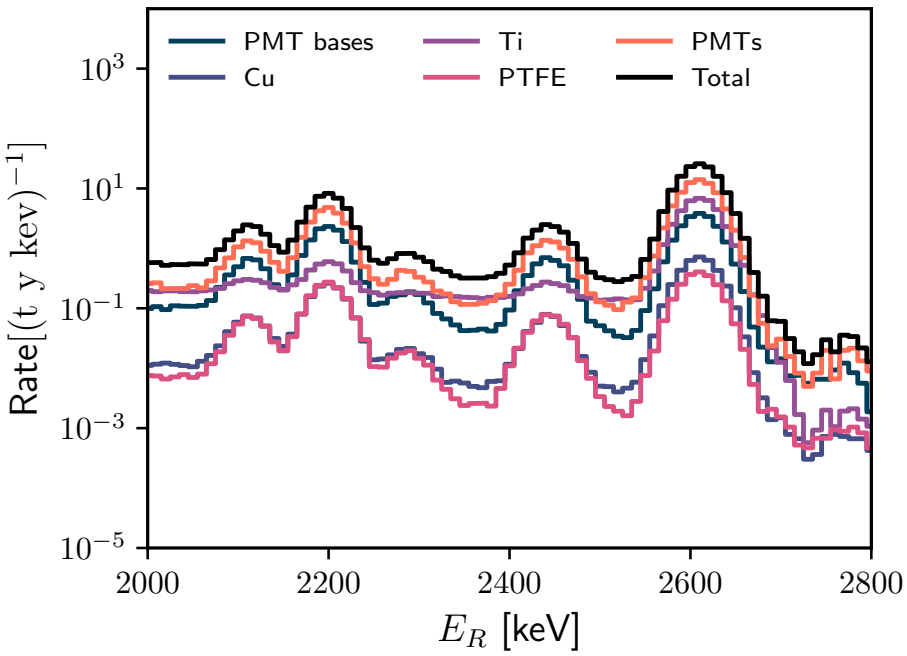

Figure 3.4: ER background rate for a fiducial mass of 30 tonne of LXe target coming from detector materials. The most important backgrounds come from the cryostat (Ti) and the PMTs and their electronics. The electrode frames, included in the Ti spectrum, have a negligible contribution.

For lower fiducial masses, the finite number of simulated events starts to have a higher impact. The unavoidable low statistics in smaller fiducial masses from MC simulations due to the attenuation from LXe motivated the development of an MC-simulated data-driven analytical model.

The first step in deriving an analytical model to reproduce the background is to study the rate of the decay from the isotopes in an energy window of 2200–2800 keV at different fiducial masses. The background for each isotope is described by absorption peaks above a continuum component from Compton scatters. The absorption peaks are modelled as Gaussian functions with a spread that corresponds to the energy resolution of the detector. The peaks taken into account are those at energies 2614.53 MeV 2656.41 MeV and those from Table 3.2, which come from the isotopes ^{208}Tl, ^{44}Sc and ^{214}Bi, accordingly. By these assumptions, the energy spectrum of each isotope is described by

$$\mathcal{B}_{\text{isotope}} = \sum_i \left[a_i \, I_i \, \text{Gauss}(E, E_i^{\text{peak}}) + b_i \text{Continuum}(E, E_i^{\text{peak}}) \right], \tag{3.4}$$

where i stands for the corresponding absorption peak at energy E_i^{peak}, I_i is the relative intensity

between peaks from Table 3.2, and a_i and b_i are the relative intensity scales for peak and continuum contributions. The continuum is described by

$$\text{Continuum}(E, E_i^{\text{peak}}) = \frac{\exp\Big(-m(E - Q_{\beta\beta})/E_i^{\text{peak}}\Big)}{(1 + \exp\Big((E - E_i^{\text{peak}})/5\Big)}, \tag{3.5}$$

where the divisor term ensures a smooth transition to the absorption peak, m is a slope parameter, and the term $E - Q_{\beta\beta}$ ensures the normalisation with the Q-value of the $0\nu\beta\beta$ decay. For ^{214}Bi, the focus is on the 2447.86 keV peak, which falls critically close to $Q_{\beta\beta}$. In the case of isotopes that deposit a single absorption peak (^{208}Tl and ^{44}Sc), the relative intensity between peaks is taken as $I_1 = 1$. The spectrum of each fiducial mass from 4–30 tonnes is fitted with the total background function

$$\mathcal{B}_{\text{total}} = \mathcal{B}_{^{214}\text{Bi}} + \mathcal{B}_{^{44}\text{Sc}} + \mathcal{B}_{^{208}\text{Tl}}, \tag{3.6}$$

obtaining the scaling parameters a_i and b_i for the absorption peaks and the continuum. Figure 3.5 shows the fit of the total background function $\mathcal{B}_{\text{total}}$ to the MC simulated data, for 15 tonnes fiducial mass of LXe.

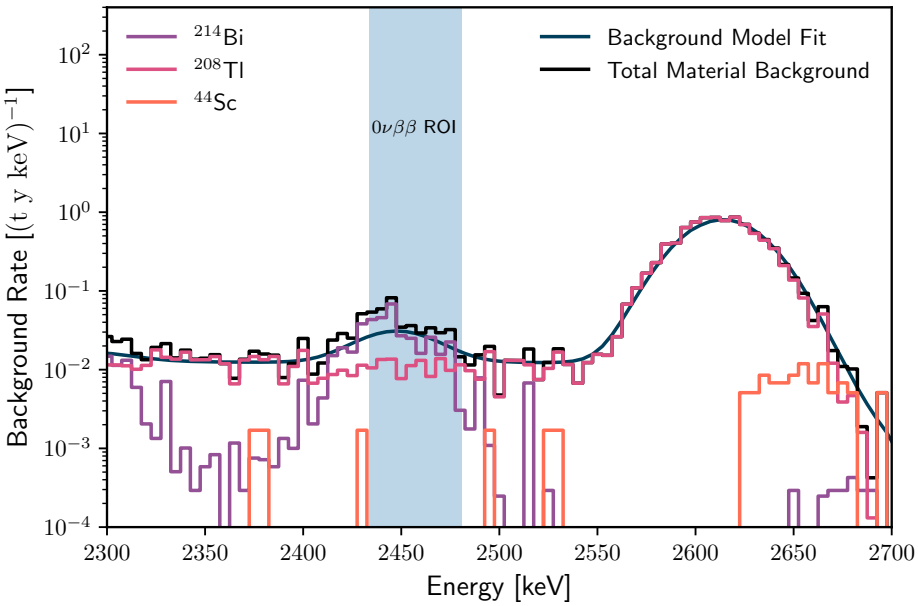

Figure 3.5: ER background rate for a fiducial mass of 15 tonne of LXe target coming from the isotopes ^{44}Sc, ^{214}Bi and 208 Tl present in detector materials from MC simulated data. The black line depicts the total background from MC simulated data, while the blue line shows the best fit to the model from Equation 3.6.

The effect of the electromagnetic attenuation in LXe in the rate $\mathcal{R}$ is expected to follow an exponential reduction given by

$$\mathcal{R}(M_{\mathrm{FV}}) \propto A \cdot \exp\left(-B \cdot M_{\mathrm{FV}}^{C}\right), \tag{3.7}$$

which is used to fit the rate, with A, the amplitude of the rate, B, a parameter similar to an attenuation constant and C, reflecting the exponential drop of the radiation in the fiducial volume, with mass M_{FV}.

Figure 3.6 shows the scale intensity a of the $2447.86\,\mathrm{keV}$ and $2614.53\,\mathrm{MeV}$ absorption peaks from ^{214}Bi and ^{208}Tl isotope decays obtained with the fitting of Equation 3.4, for each fiducial mass. The intensity of the peak and the continuum contribution are fitted using Equation 3.7. The statistical error in the MC simulated data comes from a Poisson error in the energy bin for N counts contained in that bin.

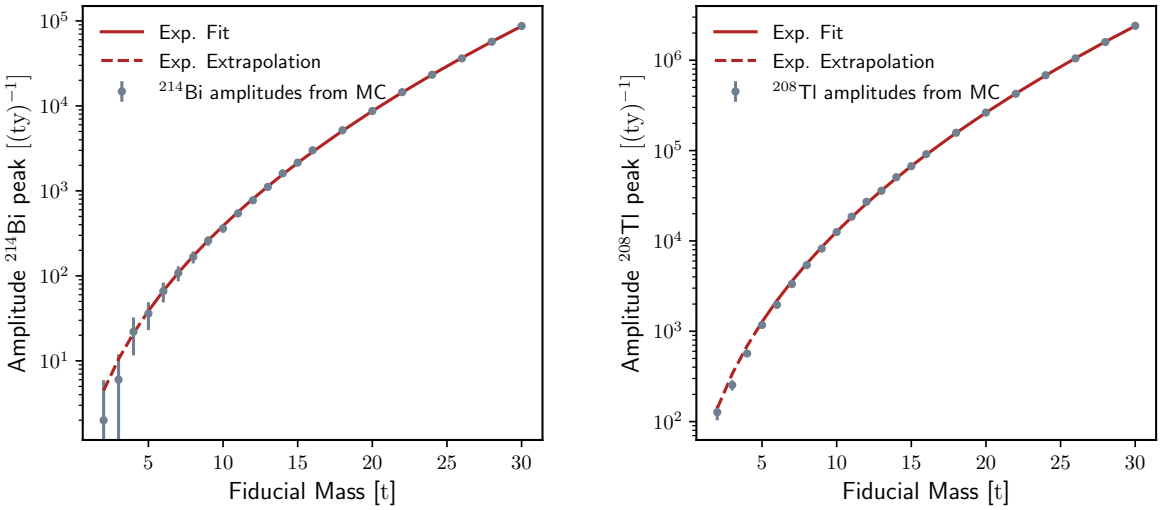

Figure 3.6: Left: Intensity of the ^{214}Bi decay at $2447.86\,\mathrm{keV}$ from the parameter $a_{2.447\mathrm{MeV}}$ obtained by fitting Equation 3.4 to the MC simulated data. The dashed red line corresponds to the fit of Equation 3.7 to this intensity parameter. Right: Intensity of the ^{208}Tl decay at $2614.53\,\mathrm{keV}$ from the parameter $a_{2.614\mathrm{MeV}}$ obtained by fitting Equation 3.4 to the MC simulated data. The dashed red line corresponds to the fit of Equation 3.7 to the intensity parameter.

The parameter minimisation results from fitting Equation 3.7 to the MC simulated data, corresponding to the decays of ^{214}Bi, ^{208}Tl and ^{44}Sc are shown in Table 3.4. While the parameter B shows a high consistency among isotopes, the parameter C varies by $\sim 10\%$ for each isotope. One possible explanation is the different attenuation from material radioactivity, mainly due to two reasons: The

attenuation length changes with energy, which would be reflected in the parameter B, and the radioactivity has a geometrical dependence not reflected in the mass term due to the location of the detector components, affecting mainly on the term C.

Table 3.4: Parameter minimisation results from the fit of MC simulated data with Equation 3.7, reflecting the attenuation in the LXe fiducial mass.

Isotope	A	B	C
^{214}Bi peak	0.052 ± 0.001	3.29 ± 0.18	0.4320 ± 0.0006
^{208}Tl peak	0.098 ± 0.001	3.75 ± 0.008	0.4016 ± 0.0001
^{44}Sc continuum	0.018 ± 0.003	2.12 ± 1.18	0.51 ± 0.02
^{208}Tl continuum	0.22 ± 0.005	3.17 ± 0.04	0.43745 ± 0.00001

The decay from ^{208}Tl produces the highest number of counts in the energy region of 2200–2800 keV and is used to constrain the other parameters. The intensity scale parameters a and b from Equation 3.4 are constrained by the intensity scale of the ^{208}Tl absorption peak, using fiducial masses above 15 tonnes in order to ensure high statistics. Figure 3.7 shows as an example the ratio of the intensity scale for ^{214}Bi and ^{208}Tl absorption peaks, compared to the MC simulated data. A linear fit is performed to extrapolate the intensity scale of ^{214}Bi at lower fiducial masses and constrain its value.

The linear fit constrains the intensity scale value a for ^{214}Bi, while the extrapolation from Equation 3.7 shows a slight increase. This could be due to the different attenuation lengths for a 2447 keV γ-ray compared to 2614.53 keV, which could enhance discrepancies at low fiducial masses. Nonetheless, the estimation of the background will be performed with the linear fit for the ratios due to its simplicity. The slopes from the continuum of ^{214}Bi and ^{44}Sc are constrained similarly to ^{208}Tl.

An example of the external radiogenic background model, using the results of the minimisation and extrapolating at lower masses, is shown in Figure 3.8 for a fiducial mass of 5 tonnes. The motivation for choosing this fiducial mass is explained in the next section. In the future, methods to reduce the error at lower fiducial masses should be developed.

3.2.2 Homogeneously distributed background sources

The fiducialisation technique cannot tackle homogeneously distributed backgrounds. Hence, the proper characterisation of these backgrounds and the possible strategies to reduce them, although challenging, are essential for the study presented in this chapter. This section provides an overview of the distributed contributions around ROI of $0\nu\beta\beta$, taken as 2435–2481 keV, motivated later in this chapter. Most models used are described in Chapter 2, although there are some changes, as

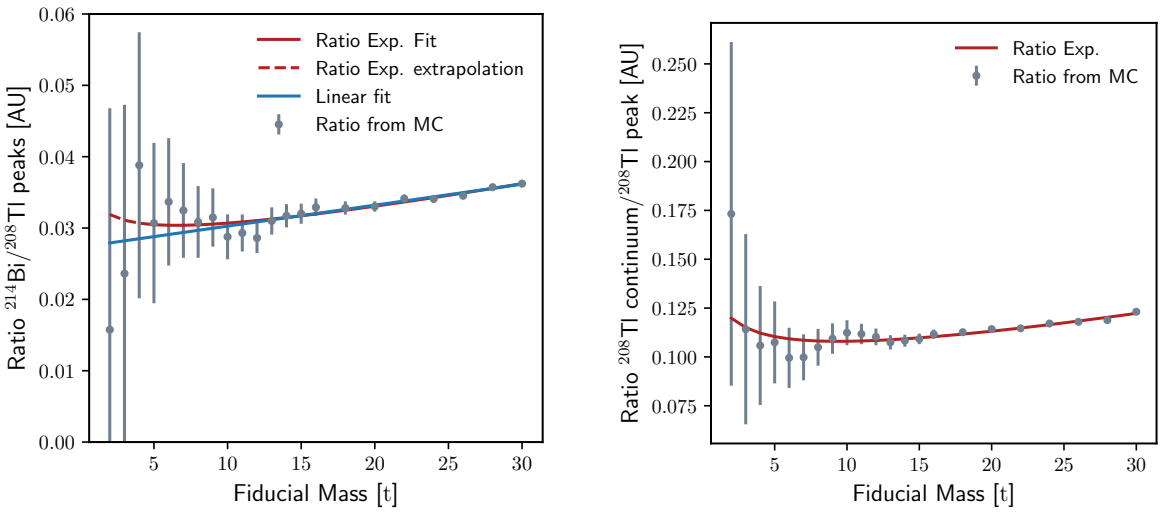

Figure 3.7: Left: Ratio of the intensity parameter scale $a_{2.447\mathrm{MeV}}$ from ^{214}Bi 2447.86 keV absorption peak and the intensity parameter scale from ^{208}Tl 2614.53 keV absorption peak. Right: Ratio of the continuum parameter scale b and the intensity parameter scale $a_{2.613\mathrm{MeV}}$ for ^{208}Tl. The ratio of Equation 3.7 with the scaling factors obtained from the fit is used as well to validate the model, labelled as 'Ratio Exp. Fit'. In the case of the ^{214}Bi peak, at lower fiducial masses an extrapolation is shown, as the values from the MC were not used to fit the model.

explained in this section.

Double beta decay of ^{136}Xe: The two neutrino double beta ($2\nu\beta\beta$) decay of ^{136}Xe was modelled in Ref. [1] using the Primakoff-Rosen approximation. This approximation is a handy model to produce the energy spectra of the two electrons described in more detail in Ref. [262]. Compared to the model proposed by Iachello and Kotila described in the previous chapter, it does not consider the screening nor the intermediate states involved in the decay. Figure 3.9 shows the difference between the Primakoff-Rosen approximation and the calculations from Iachello and Kotila around the Q-value ($Q_{\beta\beta}$), where the activity of the decay is taken as in Section 2.4.

In a region between 2435–2481 keV, the rate taken from Iachello-Kotila calculations is approximately 8.5 times greater than the Primakoff-Rosen approximated rate. This would result in a total of 0.1 events after 50 t · y exposure. Compared to the total background of 9.1 events in the same exposure, the error incurred by choosing the Primakoff-Rosen approximation is negligible for this study.

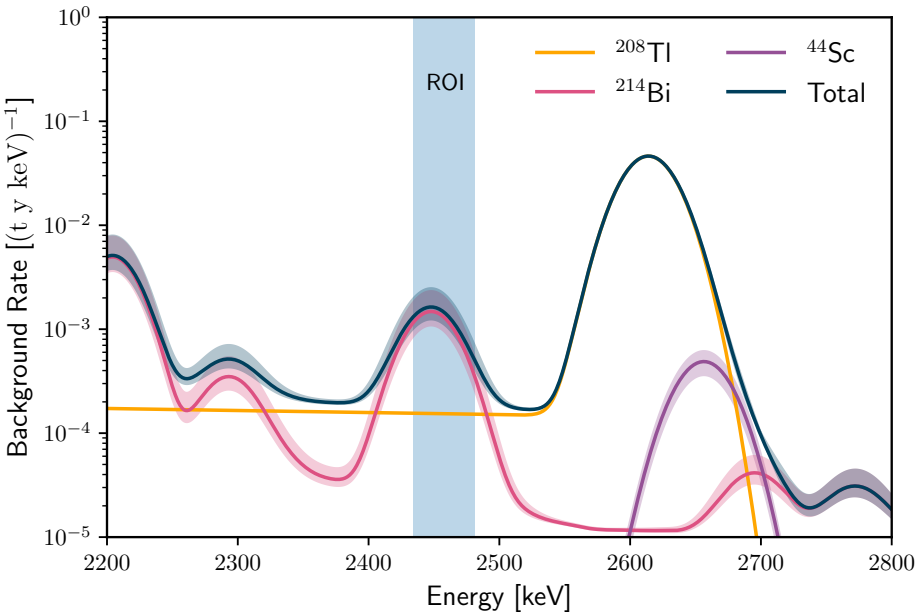

Figure 3.8: External radiogenic background contribution from ^{208}Tl, ^{214}Bi in 5 tonnes fiducial mass derived from the fit of MC simulated data to Equations 3.7 and 3.4.

β-decay of ^{137}Xe: The capture of a cosmogenic neutron by a ^{136}Xe isotope produces ^{137}Xe, as discussed previously. The homogeneously diffused ^{136}Xe can be activated in the purification loop of the experiment and the TPC. The β^--decay, with a Q-value of 4173 keV, can contribute significantly to the background. The production rate is taken as $(7.85 \pm 0.70) \times 10^{-1}$ isotopes/(t y), as given in Section 2.4. The background rate in this region can be modelled as a linear function, and it is one of the most significant backgrounds for this analysis.

Solar neutrinos (^{8}B): The $Q_{\beta\beta}$ energy is above most of the endpoints of the solar neutrinos spectra, except for ^{8}B neutrinos. The contribution in the ROI is $\sim 17\%$).

^{222}Rn: Naked betas[1] from the decay of ^{214}Bi, a daughter product of ^{222}Rn with a Q-value of 3.27 MeV, are a source of background around the $0\nu\beta\beta$ Q-value. The main technique for removing this background is the BiPo tagging, described in Section 2.4, which is taken as 99.8% [263]. Although a tagging efficiency of 99% can be derived with MC simulations, using the Geant4 framework described before, the value of 99.8% was chosen conservatively. The target background rate of ^{222}Rn for DARWIN is 0.1 µBq/kg. Decays can also occur and be stopped outside the sensitive

[1]Beta particles that cannot be tagged with coincidence technique, as described in Chapter 2.

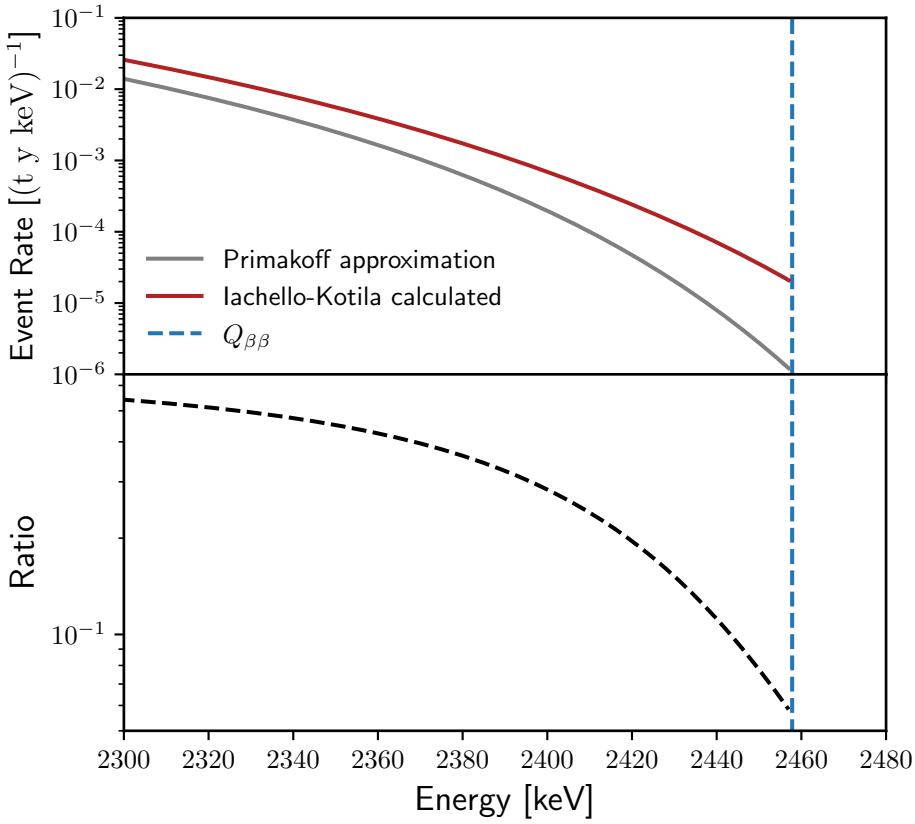

Figure 3.9: Comparison of the expected rate of events as a function of the energy for the deposition of the two electrons emitted by the $2\nu\beta\beta$ decay of ^{136}Xe using the Primakoff-Rosen approximation and the calculation from Kotila and Iachello. The difference around the Q-value (2435–2481 keV) is a factor ~ 8.5, making it negligible in the overall estimation.

volume, in the encapsulating LXe from the region where the detector is not instrumented. In that case, the BiPo tagging becomes inefficient. Nonetheless, it has been calculated for this study that the non-homogeneously distributed contribution is well below the aforementioned backgrounds.

Figure 3.10 shows the total background rate contribution together with a hypothetical signal with $T_{1/2} = 2 \times 10^{27}$y, set for comparison. The rate is calculated for a 5 tonne fiducial mass, which will be later justified in this chapter. The spread in the curves represents the statistical error in calculating these backgrounds. The figure shows that the most important backgrounds are from the decay of ^{137}Xe and the detector materials contribution. From all the external radiogenic backgrounds, 46.8% comes from titanium in the cryostat, followed by PMTs (24.3%), PMT-related electronics (12.7%), copper (9.6%) and PTFE (6.5%).

After having identified all the background contributions, either from intrinsic backgrounds or from

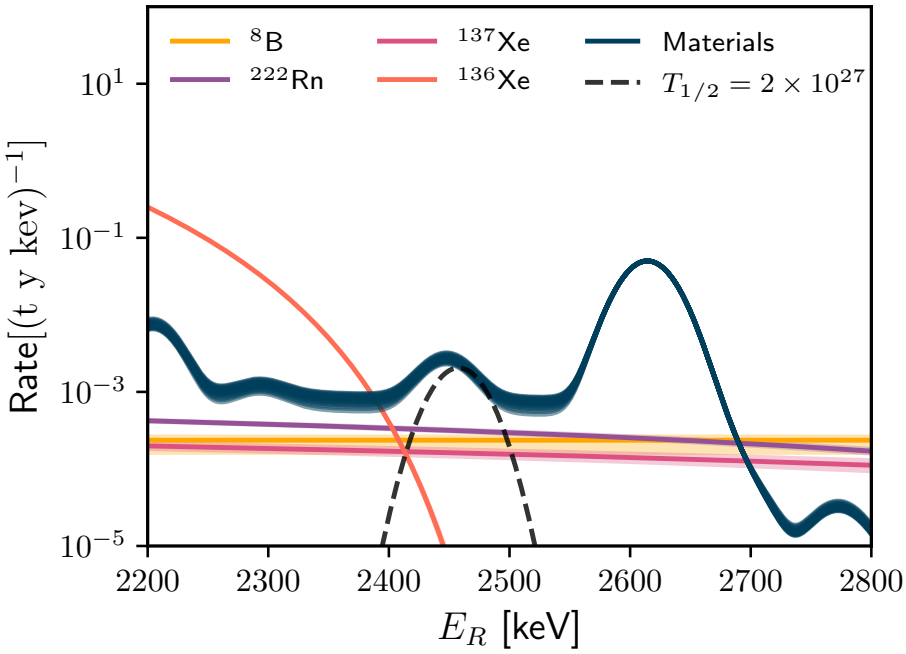

Figure 3.10: ER background model for DARWIN in the region 2200–2800 keV, together with a hypothetical signal of $T_{1/2} = 2 \times 10^{27}$y for comparison purposes. The most dominant backgrounds come from the β^--decay of ^{137}Xe, and the ^{214}Bi peak and continuum of ^{208}Tl from detector materials.

detector materials, an analytic background model is developed. This will be used for the statistical inference of the sensitivity and discovery potential of the $0\nu\beta\beta$ decay of ^{136}Xe in Section 3.4. Only events with energy inside the $0\nu\beta\beta$ region-of-interest (ROI) of 2435–2481 keV, defined by the expected full width at half maximum (FWHM) of the signal given the energy resolution, are considered. Table 3.5 shows the expected contribution to the ROI of the $0\nu\beta\beta$ decay.
Their variances are obtained either by the model fit on the spectrum corresponding to 5 tonne (^{208}Tl peak intensity and slope parameter of the continuum) or by extrapolation of the model parameters from larger fiducial volumes into the low fiducial mass range (^{214}Bi / ^{208}Tl peak ratio, ^{208}Tl continuum / ^{208}Tl peak intensity). For the intrinsic contributions, the variances correspond to the square of the errors listed in Table 3.5.

3.3 $0\nu\beta\beta$ signal in liquid xenon

The detection of the $0\nu\beta\beta$ signal in LXe is based on the two electrons emitted in the decay process. In the standard $2\nu\beta\beta$ decay, the energy is released in the form of the kinetic energy of the two

Table 3.5: Expected total background index averaged in the $0\nu\beta\beta$-ROI of [2435 - 2481] keV, corresponding event rate in the 5 tonne FV and relative uncertainty.

Background source	Background index [events/(t·y·keV)]	Rate [events/y]	Rel. uncertainty
External sources (5 tonnes FV):			
^{214}Bi peaks + continuum	1.36×10^{-3}	0.313	$\pm 3.6\%$
^{208}Tl continuum	6.20×10^{-4}	0.143	$\pm 4.9\%$
^{44}Sc continuum	4.64×10^{-6}	0.001	$\pm 15.8\%$
Intrinsic contributions:			
^{8}B ($\nu - e$ scattering)	2.36×10^{-4}	0.054	$+13.9\%, -32.2\%$
^{137}Xe (μ-induced n-capture)	1.61×10^{-4}	0.037	$\pm 10.0\%$
^{136}Xe $2\nu\beta\beta$	4.91×10^{-5}	0.01	$\pm 10\%$
^{222}Rn in LXe (0.1 μBq/kg)	3.09×10^{-4}	0.071	$\pm 1.6\%$
Total:	$\mathbf{7.10 \times 10^{-4}}$	**0.910**	$+\mathbf{6}\%, -\mathbf{5.0}\%$

electrons and the neutrinos. Hence, the electrons share the available energy of the decay (Q-value) with the neutrinos, and the energy distribution of each electron is extended towards lower energy values. As low energy β particles (<1.5 MeV), their mean free path in LXe is short, and simulations performed in this work using Geant4 place their mean free path below ~ 5 mm.

In the $0\nu\beta\beta$ decay, the energy of the Q-value is distributed as the kinetic energy of the two electrons. As the electrons in LXe thermalise within $\mathcal{O}(\text{mm})$, the interaction would result in single-site events due to the detector not being capable of resolving their absorption in LXe. Bremsstrahlung photons could be emitted in the process of electron thermalisation in LXe, and they could travel longer distances without depositing energy before being scattered and absorbed. Consequently, when the bremsstrahlung photon induces additional interactions within the LXe, the $0\nu\beta\beta$ can be deemed by the single scatter clustering algorithm as a multi-site event and therefore discarded. With the spatial clustering algorithm using $\epsilon = 15$ mm the signal acceptance value is 90.4%.

The $0\nu\beta\beta$ decay mechanism is, until this date, unknown, and the mediator could affect the angular distribution of the electrons emitted. An angular distribution generator is available, taken from Ref. [264]. The models implemented are discussed in Chapter 1. Figure 3.11 shows the frequency of the angular distribution based on the two different models. The generator was used to simulate the $0\nu\beta\beta$ decay under different models. Once the $0\nu\beta\beta$ signal is simulated, the results are then processed using the clustering algorithm described previously, and the difference between models is below the experimental uncertainty ($\sim 5\%$). Therefore, the simulations show that the DARWIN detector cannot discriminate between the subtleties that these models introduce. Thus, the signal

model used for this study is a mono-energetic peak smeared with the detector resolution and with a signal acceptance of 90.4%.

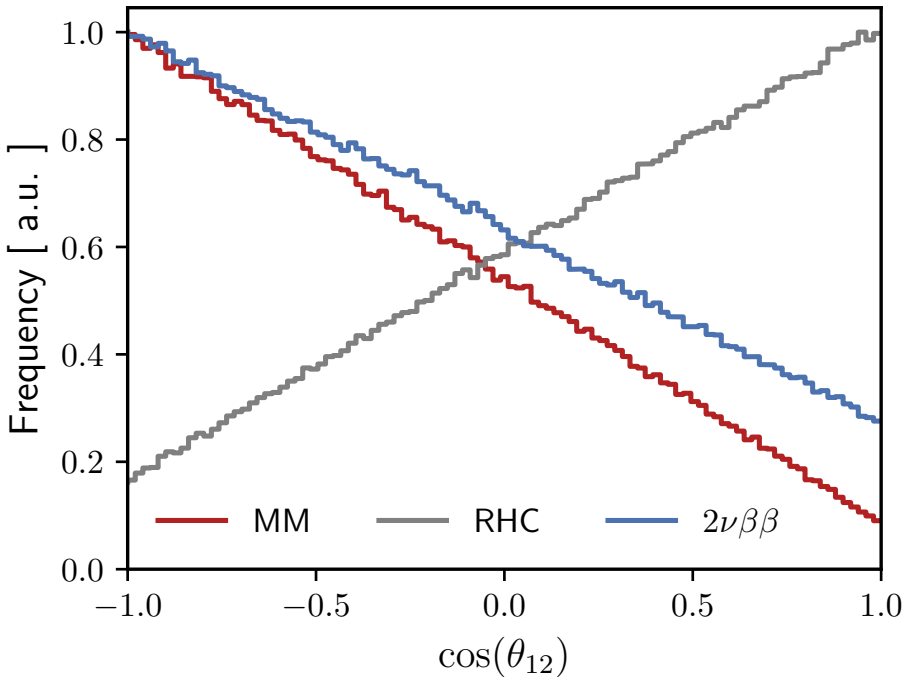

Figure 3.11: Model dependent frequency distribution for $0\nu\beta\beta$ and $2\nu\beta\beta$, for comparison, for the right-handed currents (RHC) and the mass mechanism (MM) models. The parameter θ_{12} stands for the angle between the two electrons emitted. Although the angles between electrons in the RHC and MM models are different, DARWIN would not be able to identify the underlying angular distribution of the electrons.

3.4 Inference of the sensitivity and discovery potential

The primary goal of this analysis is the calculation of the exclusion limit of a signal hypothesis –which is related to the half-life– of the $0\nu\beta\beta$ process, given the expected background. Standard asymptotic methods are not applicable in the low background regime (low number of events per bin of energy). One option is to resort to MC simulations to infer the underlying posterior probability distribution for the likelihood of the null and alternate hypotheses. As the total number of events is low, there is a high dependence on the number of toyMCs performed, which consists of simulated datasets of possible experiment outcomes. These datasets can incorporate constraints and systematic errors for

the expected value of nuisance parameters[2]. Before simulating these datasets, the optimal target mass needs to be identified, as the shielding properties of the LXe volume will help to reduce the non-homogeneously distributed backgrounds.

3.4.1 Target mass selection

The selection of the fiducial mass is based on a trade-off between maximising the mass for the exposure while minimising the impact of the background. Only the external radiogenic background is not homogeneously distributed in the active LXe volume, and the optimal mass depends strongly on this rate. The approach is to optimise the mass in terms of the FoM $\propto \sqrt{(Mt/B)}$ from Equation 1.60, introduced in the first chapter, and find its maximum. To obtain the external radiogenic background rate at different fiducial masses, the fiducial volume at constant mass is optimized. The process of selecting the optimal fiducial volume is performed by scanning values in a super-ellipsoid of the shape:

$$\left(\frac{Z+Z_0}{Z_{max}}\right)^t + \left(\frac{X^2+Y^2}{R_{max}^2}\right)^{\frac{t}{2}} < 1, \tag{3.8}$$

where Z_{max} and R_{max} stands for the maximum value for the dimensions Z (height) and R (radius), Z_0 corresponds to a vertical offset in the TPC, and t gives the shape to the super-ellipsoid, which lower t values makes it more oval-like. The offset reflects the asymmetry of the TPC in the Z-dimension, mainly given by the poorer screening power of GXe to different backgrounds. The background accumulates around the walls of the cryostat and close to the photosensor arrays, as shown in Figure 3.12.

The optimal fiducial volumes are used to calculate the background index from the material contribution at different fiducial masses. Figure 3.13 shows the event rate of all backgrounds at different masses, where the only contribution that increases along with the fiducial mass comes from materials.

Figure 3.14 shows the FoM for different fiducial masses for a livetime of $10\,\mathrm{y}$. The maximum is located at $5\,\mathrm{t}$, and would be the fiducial mass for this analysis.

3.4.2 Statistical inference approach

The upper limit and the discovery potential from $0\nu\beta\beta$ decay is inferred with the use of MC toy experiments (toyMCs). A toyMC data set D_i contains the events from the i-th experiment performed, where the parameter of interest for the sensitivity inference is the strength of a potential $0\nu\beta\beta$ signal,

[2]Parameters that are not of interest but are nonetheless profiled and taken into account in the inference.

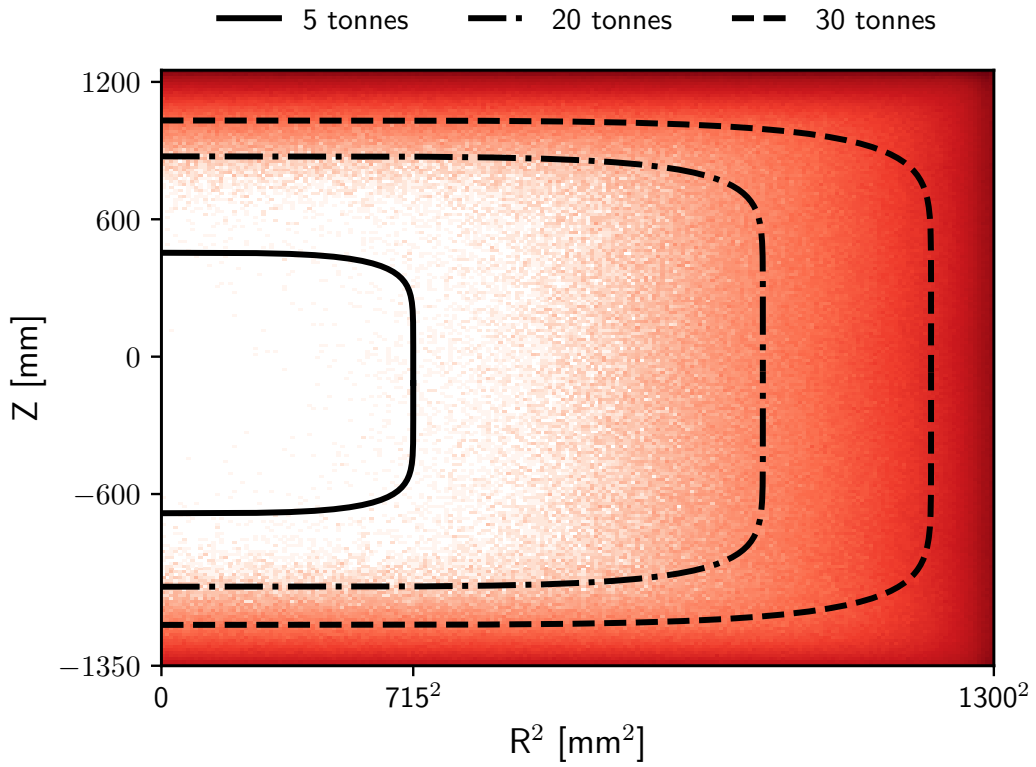

Figure 3.12: Fiducial cuts of the TPC in terms of the height (Z) and width (R^2) with masses 5,20 and 30 tonnes, respectively. Color map: external radiogenic background hits in LXe in the energy region 2200–2700 keV.

$\mathcal{S}$, related to the half-life:

$$\mathcal{S} = \frac{1}{T^{0\nu}_{1/2}}, \tag{3.9}$$

and the number of expected events in the data set D_i is given by:

$$\mu_i^{\mathcal{S}} = \ln 2 (N_A/m_a)\epsilon_i \varepsilon_i \mathbf{S}_i, \tag{3.10}$$

where N_A is Avogadro's number, m_a is the molar mass of xenon and $\epsilon_i, \varepsilon_i$ are the efficiency and the exposure in the i-th data set, respectively. Each of these possible realizations is carried out for a discrete set of signal strength hypotheses $\{\mathcal{S}_i\}$, and a Poissonian fluctuation in the total number of observed events $\mu_{tot} = \mu_i^{\mathcal{S}} + \mu_i^{\mathcal{B}}$ is incorporated. For each of these experiment realisations, the data set of generated events at different energies is fitted with the likelihood function composed by the signal and background models: a Gaussian distribution is assumed for the signal, while the

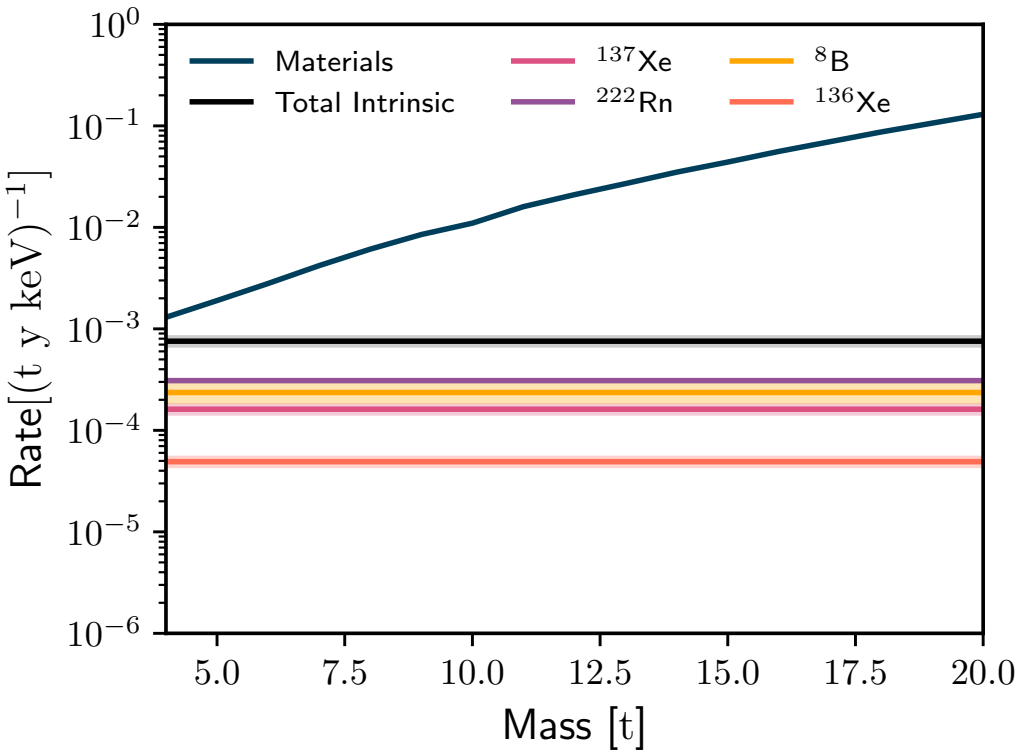

Figure 3.13: ER background rate for different fiducial masses for the intrinsic background (^{137}Xe, ^{222}Rn, solar neutrinos from ^{8}B), distributed homogeneously, and the external radiogenic background, which is affected by the fiducialisation of the target volume.

background is described by a Gaussian distribution mounted on a polynomial of order 1 component:

$$\begin{aligned}\mathcal{L}(\mathcal{D}|\mathcal{S},\mathrm{BI},\theta) &= \mathrm{Poisson}\left(N \mid \mu_{tot}\right) \\ &\times \prod_{n=1}^{N} \frac{1}{\mu^S + \mu^{B1} + \mu^{B2}} \left[\mu^S \frac{1}{\sqrt{2\pi}\sigma} \exp\left(\frac{-\left(E_\mathrm{n} - Q_{\beta\beta} - \delta\right)^2}{2\sigma^2}\right)\right. \\ &\left. + \mu^{B1} \frac{1}{\sqrt{2\pi}\sigma} \exp\left(\frac{-\left(E_\mathrm{n} - Q_{^{214}Bi} - \delta\right)^2}{2\sigma^2}\right) + \mu^{B2}(E_\mathrm{n} + \frac{1}{\Delta E})\right] \times \prod_n C_{\theta_n}\left(\theta_n\right),\end{aligned} \tag{3.11}$$

where $\mu_i^{B_1}$ and $\mu_i^{B_2}$ are the expected background events in the region of interest for the ^{214}Bi peak and flat background components respectively, with $\mu^{B_{ji}} = \mathbf{BI_{ji}} \cdot \epsilon_i$, σ is the energy resolution and δ is a shift between data acquisitions periods, taken as the energy resolution. The entire set of nuisance parameters is defined as $\boldsymbol{\theta} = \{\epsilon, \varepsilon, \delta, \sigma\}$. Background uncertainties from the model are treated as

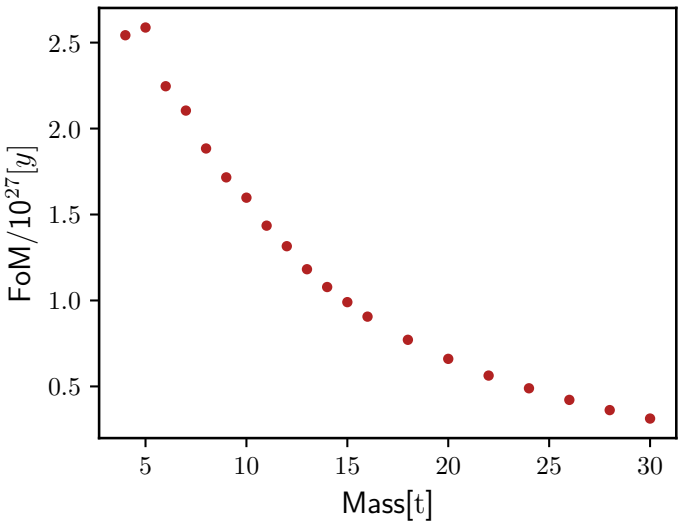

Figure 3.14: FoM calculation for different fiducial masses. The optimal mass is considered as the mass that maximizes this function. Lower masses mean that the detector uses more passive LXe to shield from the external backgrounds.

nuisance parameters, sampled from a Gaussian distribution,

$$C_{\theta_n} = \frac{1}{\sigma_{\theta i}\sqrt{2\pi}} e^{-\frac{1}{2}\left(\frac{E_i-\mu_{\theta i}}{\sigma_{\theta i}}\right)^2}, \tag{3.12}$$

where $\mu_{\theta i}$ is the expected value of the parameter θ_i and $\sigma_{\theta i}$ its deviation.
A profile likelihood ratio is performed as a test of the compatibility of the null hypothesis against the alternate hypothesis, defined as

$$q_0 = \begin{cases} -2\ln\lambda(0) & \hat{\mu} \geq 0 \\ 0 & \hat{\mu} < 0 \end{cases} \tag{3.13}$$

where μ is the signal strength, and λ, the profile likelihood ratio, is defined by

$$\tilde{\lambda}(\mu) = \begin{cases} \frac{\mathcal{L}(\mu,\hat{\hat{\boldsymbol{\theta}}}(\mu))}{\mathcal{L}(\hat{\mu},\hat{\boldsymbol{\theta}})} & \hat{\mu} \geq 0, \\ \frac{\mathcal{L}(\mu,\hat{\hat{\theta}}(\mu))}{\mathcal{L}(0,\hat{\hat{\theta}}(0))} & \hat{\mu} < 0. \end{cases} \tag{3.14}$$

where $\hat{\hat{\theta}}(\mu)$ and $\hat{\hat{\theta}}(0)$ are the maximum likelihood estimators of θ given the assumptions of signal

strength of μ and 0, respectively, and $\hat{\mu}$ and $\hat{\theta}$ are the best fit of the parameters μ and θ, respectively [265].

The chosen power of the test α is defined as the probability of rejecting the null hypothesis when the alternate hypothesis is true. In the case of a discovery, the null hypothesis represents the background-only model, while the alternate includes both the signal model and background. In simpler terms: in case of detection of a *true* signal, it is a requirement for the background only hypothesis to be rejected with a high probability. For every signal model hypothesis, a p-value is calculated as

$$1 - \alpha = p = \int_{q_{0,\,\mathrm{obs}}}^{\infty} f\left(q_0 \mid 0\right) dq_0, \tag{3.15}$$

where $f\left(q_0 \mid 0\right)$ represents the probability distribution of the performed tests.

A discovery of a signal can be claimed when the signal strength provides a p-value corresponding to, for example, 2.9×10^7, corresponding to a 5σ significance level, which is a convention in particle physics [266]. In $0\nu\beta\beta$ experiments is common to take the assumption of $\alpha = 3\sigma$ or 99.87% of rejecting the background only hypothesis, which is interchangeably reported as discovery or *evidence* [267]. In case no discovery can be claimed, a limit of the highest signal strength that would be compatible with the data can be placed, which defines an exclusion plot, as signals higher than the limit would have been detected by the experiment. In this case, the alternate hypothesis to reject is the background-only hypothesis: if the background-only hypothesis is taken as *true*, what is the probability of rejecting the signal hypothesis, for each signal strength? [268]. The power of the test is usually taken as 90% for exclusion plots, although other values are commonly assumed. The upper limit would be the signal strength value that fulfils the required threshold. A frequentist inference of an upper limit is performed using a one-sided test statistic based on the profile likelihood:

$$q_{\mathcal{S}} = -2 \ln \frac{\mathcal{L}(\mathcal{S}, \hat{\hat{\mathbf{BI}}}, \hat{\hat{\theta}})}{\mathcal{L}(\hat{\mathcal{S}}, \hat{\mathbf{BI}}, \hat{\boldsymbol{\theta}})}. \tag{3.16}$$

The procedure to find the distribution of p-values and confidence belts is defined as:

1. Identify a null hypothesis $\mathcal{H}_0$ and its alternative, $\mathcal{H}_1$.
2. Choose a threshold α: the maximal probability of false rejection that one is willing to tolerate.
3. Derive a distribution of the test statistic under the null hypothesis.
4. Compute the p-value by comparing the observed value of the test statistic against its reference distribution.

5. Reject the null hypothesis if the p-value is less than the threshold α.

The probability distribution of the test statistic is found for each signal strength hypothesis, where the used MC data simulation is generated with and without an injected signal, according to the null and alternate hypothesis. The determination of the upper limit for each data set with this construction is then straightforward for the desired confidence level (CL). The value of $\mathcal{S}_i$ is found when the p-value of the observed data for 90% CL satisfies

$$p = \int_{q_{\text{obs}}}^{\infty} f\left(q_{\mathcal{S}} | \mathcal{S}_i\right) \mathrm{d}\left(q_{\mathcal{S}_i}\right) \leq 0.1. \tag{3.17}$$

With 50,000 toyMCs sets for the $\mathbf{S} + \mathbf{B}$ model and 10,000 toyMCs for the only $\mathbf{B}$ model, the exclusion limit at 90% CL of $T^{0\nu}_{1/2}$ is 4×10^{27}y, for a 10 year exposure with a 5 tonne fiducial mass. This result is shown in Figure 3.15.

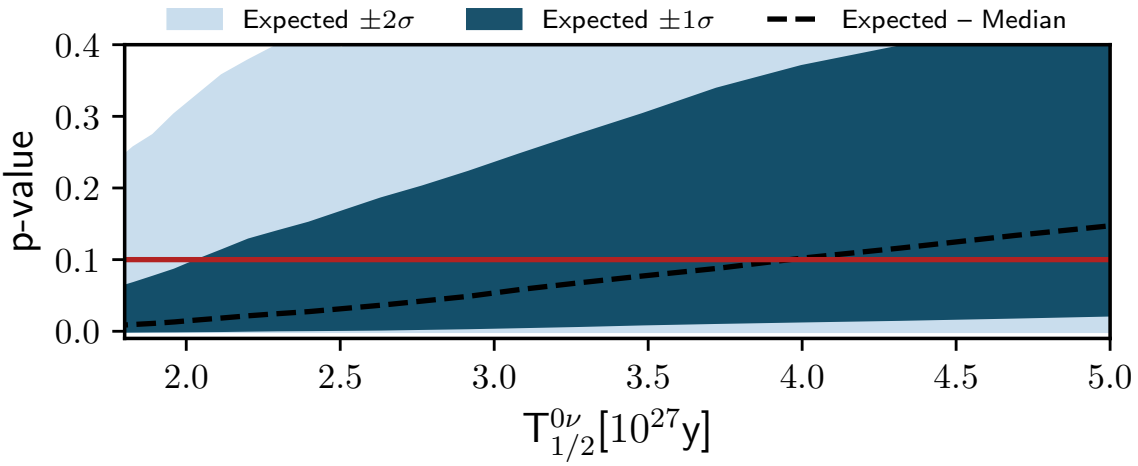

Figure 3.15: Calculation of p-values for different signal strengths assumed in the toyMC analysis, derived from their test distribution. The red line indicates the threshold for 90% C.L., with p-value $= 0.1$.

The corresponding 3σ discovery potential after 10 years exposure, for the same fiducial mass, is 2×10^{27}y.

3.5 Outlook: present and future of this study

This section provides an outlook on the implications of the result given in this study and discusses possible upgrades or improvements that could be made to the design or the analysis to further improve the sensitivity.

3.5.1 Results of this analysis in the neutrino mass landscape

The calculation for the expected effective Majorana neutrino mass is given by Equation 1.54 with the neutrino oscillation data from Ref [269]. For each possible value of the lightest neutrino mass, the range for the effective Majorana neutrino mass is calculated by varying the Majorana phases α_1 and α_2, as explained in Chapter 1, and the phase factor and nuclear matrix elements from Refs. [152, 154, 153]. Figure 3.16 shows the effective Majorana mass term as a function of the lightest neutrino mass. A scenario under the assumption that the background is dominated only by the irreducible solar neutrinos, and all other backgrounds can be mitigated, is used, and a FoM of 7×10^{27} can be achieved. The neutrino-dominated background scenario is also included in Figure 3.16, labelled as *neutrino dominated*. This limit does not necessarily need to be realistic; however, it is a useful tool to estimate the impact of different background suppression techniques.
Future dedicated $0\nu\beta\beta$ decay experiments using xenon, like KamLAND-Zen ($m_{\beta\beta}$: 25–70 meV, after 5 yr), PandaX-III (20–55 meV, 5 yr), NEXT-HD (13–57 meV, 10 yr) [270] and nEXO (8–22 meV, 10 yr), are aiming for a similar $m_{\beta\beta}$ reach as DARWIN. They are complemented by experiments using other isotopes like SNO+-II (^{130}Te, 20–70 meV, 5 yr), CUPID (^{130}Te/^{100}Mo, 6–17 meV, 10 yr) and LEGEND-1000 (^{76}Ge, 11–28 meV, 10 yr). The values are taken from Ref. [271].

3.5.2 Future $0\nu\beta\beta$ detection with DARWIN detectors

There are alternatives in the detector design and techniques to the ones presented in this chapter that can help to improve the results presented above. The most significant backgrounds come from materials and the beta decay of ^{137}Xe, and their reduction is not trivial. However, the radiogenic activities assumed for the materials, as Table 3.3 indicates, contain, in many cases, upper limits of the samples and not measured values. It could be possible that these values are indeed lower than the ones assumed in the simulations. For that reason, detailed and specific screening procedures must be developed in order to reduce the radiogenic contribution to the background of ^{214}Bi and ^{208}Tl from materials.

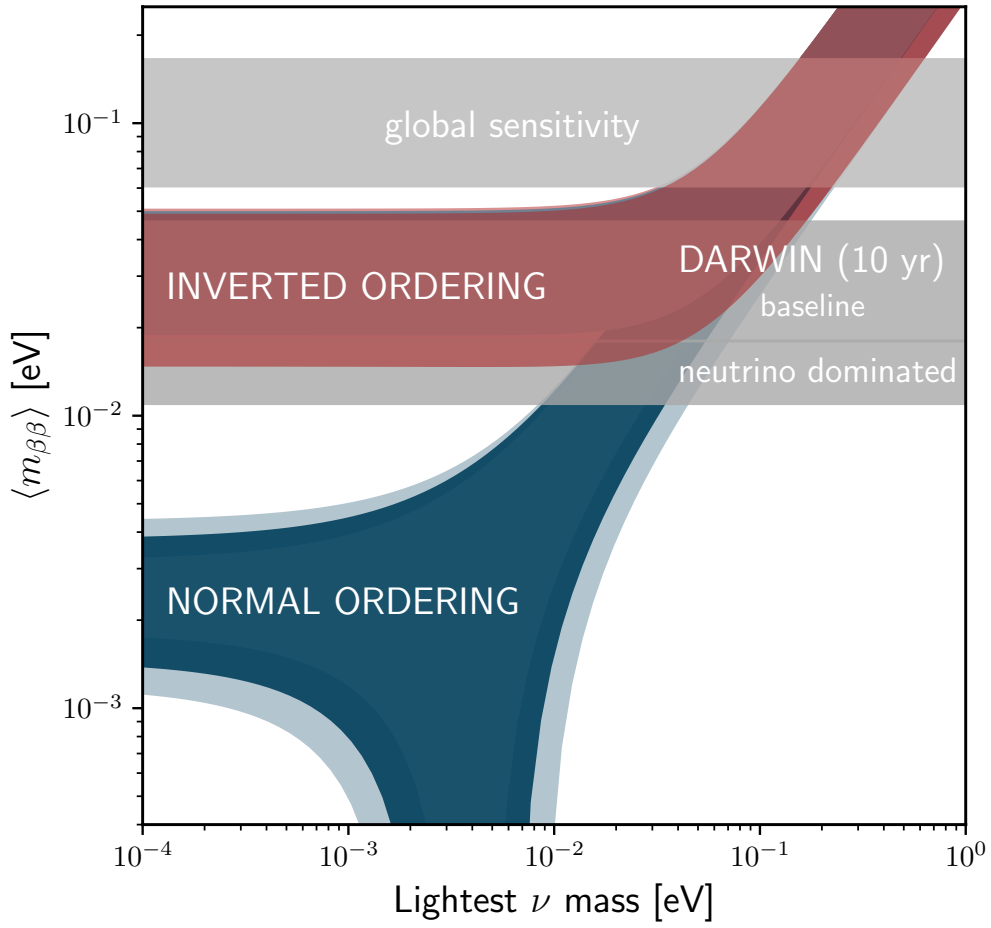

Figure 3.16: Limits from DARWIN experiment translated to the effective Majorana neutrino mass, where the inverted and the normal neutrino ordering regions are shown. The solar neutrino dominated limit represents an irreducible background for all LXe detectors.

The ^{137}Xe background reduction requires dedicated studies. There are some possible techniques for its reduction, such as a coincident muon and gamma emission veto or directional measurements of the muon track with the neutron veto. These two techniques allow the tagging of the potential activation of xenon by cosmogenic neutrons. As an example of veto techniques, the EXO Collaboration uses a coincident veto of μ + γcascade from the neutron capture that produces ^{137}Xe. By detecting the capture of the neutron, a veto of $5t_{1/2}$ ($t_{1/2} \sim 3.82$ m) is used to remove potential ^{137}Xe induced background [272]. Nonetheless, if the approximate flux of muons in LNGS is 2-3 muons

per hour [238], then a veto would imply a $1/3$ of a year of downtime, which is undesirable for any search. The second technique could imply a group of photosensors in a water Cherenkov tank that register and reconstruct the tracks of the muons. The information collected from each event could tell, for example, if the muon entered the TPC, the presence of a gamma cascade, and the disappearance of such muon. Additional algorithms could reconstruct the energy of the muon and the probability that it would be captured by the detector materials. The probability that the muon could induce a neutron, based on the reconstructed path and its distance to the sensitive volume, could also be used to develop a veto. There are multiple properties to be studied, such as the probability of a muon producing a neutron and that neutron being captured by ^{136}Xe, which would later produce a gamma. Another option is to locate the detector in a deeper underground laboratory. More studies will provide the necessary tools to develop these techniques fully.

An alternative to the proposed scenarios would be to enrich the xenon target with ^{136}Xe. The impact of the enrichment of ^{136}Xe in other physics channels has not been studied. However, $2\nu\beta\beta$ decay of ^{136}Xe is one of the highest backgrounds in the low ER region (1–100 keV). The enrichment could be scheduled after the dark matter, and solar neutrino searches end. The enrichment would entail as well the increase of ^{137}Xe beta decay background in the ROI. Nonetheless, if one considers Equation 1.60, assuming a linear increase of the ^{137}Xe decay rate in the background, the increase behaves as a square root function. The enrichment is directly proportional to the signal rate, and there still would be a positive impact on the sensitivity by enriching the target. Figure 3.17 shows the different scenarios with enrichment by using Equation 1.60 rewritten in terms of the ^{137}Xe background rate as

$$B = B_{mat} + B_{\nu} + B_{Rn} + \alpha(B_{2\nu\beta\beta} + B_{^{137}\mathrm{Xe}}), \tag{3.18}$$

where $B_{mat}, B_{\nu}, B_{Rn}, B_{2\nu\beta\beta}$ stand for the material, solar neutrinos, radon and the double beta decay contributions in the ROI, respectively. The factor α stands here as the enrichment of natural xenon with ^{136}Xe, and an exposure of 10 years is assumed. The maximum of the distribution is shifted, on the X-Y plane, towards higher fiducial masses.

On the analysis side, boosted decision trees and other machine learning methods have become a great tool for particle physics and $0\nu\beta\beta$ experiments [273]. Using them would allow exploring the likelihood of a waveform to be a significant event based not only on its energy but also on the distance to the closest surface and different single-site/multi-site scores based on its hit pattern [274, 275]. It might be critical, in order to feed signals to these algorithms, to design a clever system to calibrate the detector around the ROI of the $0\nu\beta\beta$ decay of ^{136}Xe, which can help to shed light on the differences in the charge distribution between γ and β particles around that energies.

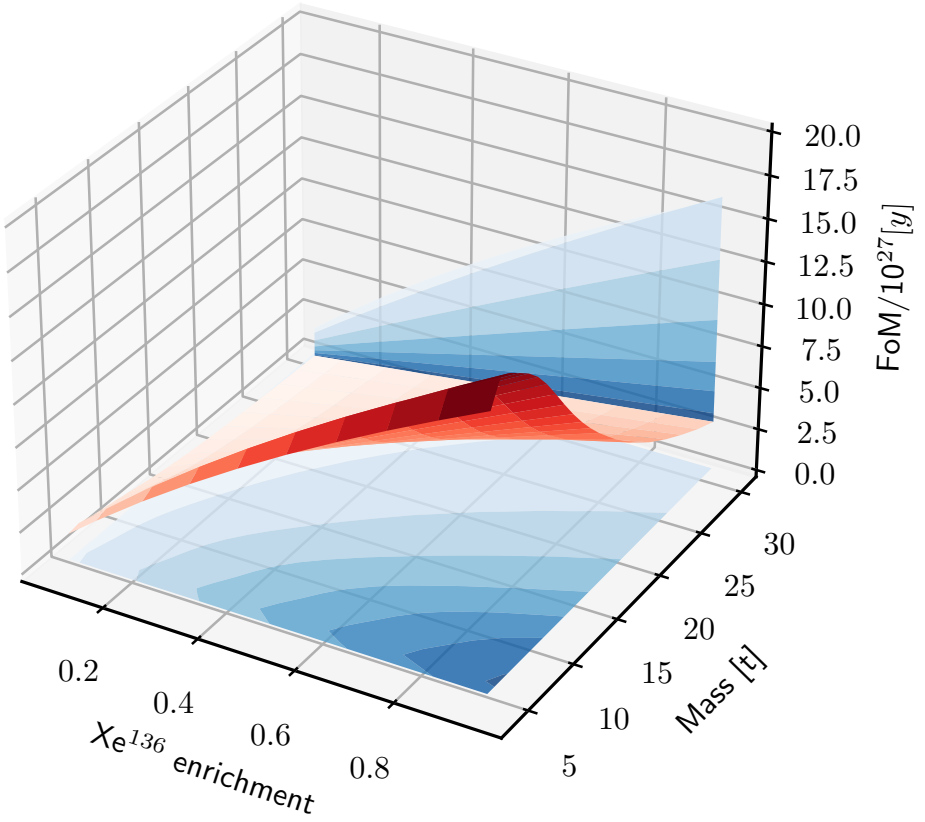

Figure 3.17: Surface plot of how the level of enrichment in ^{136}Xe will affect the sensitivity $0\nu\beta\beta$ decay of ^{136}Xe. The red 3D-surface shows the sensitivity that could be achieved by the combination of enrichment and increasing fiducial mass. The blue shadow on the Mass-^{136}Xe plane indicates region of higher sensitivity with darker shades of blue. The maximum sensitivity for almost 100% enrichment can be achieved with a fiducial mass around 10 tonnes.

In conclusion, an observation of the $0\nu\beta\beta$ decay process will prove that neutrinos are Majorana particles, a discovery that will shed more light on BSM physics. DARWIN could be competitive with other dedicated $0\nu\beta\beta$ decay experiments, with an aimed limit sensitivity of 4×10^{27}y at 90% CL. The background is dominated by the beta decay of ^{137}Xe and the external radiogenic background. As a consequence, improvements for these two backgrounds have been discussed, and special techniques could be developed in the future for background suppression. Further enrichment above the natural abundance of ^{136}Xe can help to improve the sensitivity in this channel, and it should be considered after carefully assessing its impact on other physics channels.

Chapter 4

Solar axion detection in DARWIN

> *I do not believe that the Lord is a weak left-hander, and I am ready to bet a very high sum that the experiment will give symmetric angular distribution of the electrons. I do not see any logical connection between the strength of an interaction and its mirror invariance.*
>
> **— W. Pauli**

> *Now, where shall I start? It is good that I did not make a bet. It would have resulted in a heavy loss of money (which I cannot afford); What shocks me is not the fact that "God is left-handed" but the fact that in spite of this He exhibits Himself as left/right symmetric when He expresses Himself strongly.*
>
> **— W. Pauli, on the discovery of CP violation by C. Wu**

In the previous chapters, we discussed the different backgrounds that contribute to the high-energy region of the DARWIN detector. We used the background contribution model to estimate its reach to the search for the monoenergetic peak of the potential $0\nu\beta\beta$ decay of ^{136}Xe. In this chapter, we will focus on modelling backgrounds in the low end of the ER spectra. This region is of particular interest for complementary searches besides the standard WIMP search, such as hidden photons [276], mirror dark matter [277], leptophilic dark matter [278], and neutrino properties [279]. Additionally, axions and ALPs could leave their imprint in the low-energy region of a LXe detector. Axions might be produced in the Sun, and the recoil energies induced in the xenon target would fall in the region

below 20 keV. DARWIN will have an unprecedented low background in the ROI of solar axions, due to the reduction of ^{222}Rn and ^{85}Kr below the pp-neutrinos rate, which offers an opportunity to explore the parameter space for the axion couplings. The chapter will be organised as follows: In Section 4.1, we discuss the production mechanisms and the expected fluxes from axions produced in the Sun. Section 4.2 presents a discussion on how axions could interact with xenon atoms. Thereafter, the expected fluxes and the potential interactions are combined in Section 4.3 to calculate the expected interaction rate of solar axions in the DARWIN detector, together with the background model at low energies. Section 4.4 describes the statistical framework for the inference of the sensitivity and discovery potential and the results obtained. Finally, Section 4.5 presents a discussion on the implications of these results, together with possible future improvements towards detection in this channel.

4.1 Solar axions: production and expected fluxes

Our closest star is responsible for producing multiple particles that reach the Earth due to different stellar and nuclear processes in its core. This section will discuss the potential production mechanism of axions: hypothetical particles that would provide the missing piece in the strong CP puzzle discussed in Chapter 1.

Primakoff flux

Stars could produce axions from thermal photons in electromagnetic fields of the stellar plasma when a photon converts into an axion in the field of a charged particle [280]. The Primakoff process in the Sun was the first to be studied for axion production. It is dominant in hadronic models such as KSVZ [281], where the axion-electron coupling is absent at the tree level. By using the transition rate of a photon to an axion of the same energy, and taking into account the screening scale in the plasma with a Debye-Huckel approximation at a temperature T, an approximation to this flux can be found as [280]

$$\frac{\mathrm{d}\Phi_a}{\mathrm{d}E} = g_{10}^2 6.0 \times 10^{10} E^{2.481} \mathrm{e}^{-E/1.205} \ \mathrm{cm}^{-2}\,\mathrm{s}^{-1}\mathrm{keV}^{-1}, \tag{4.1}$$

where $g_{10} = g_{a\gamma\gamma}/(10^{-10}\mathrm{GeV}^{-1})$ and $g_{a\gamma\gamma}$ is the coupling parameter of axions to photons in a two-photon vertex interaction for an axion of energy E. This flux has an average energy of 4.2 keV and a maximum around 3.0 keV.

Flux from ABC reactions

The axion-electron coupling is responsible for the flux that comes from the ABC reactions (**A**tomic axio-recombination and axio-deexcitation, axio-**B**remsstrahlung in electron-Ion or electron collisions, **C**ompton scattering). Figure 4.1 shows the Feynman diagrams for all the previously mentioned axion-photon and axioelectric-interactions. Due to the atomic composition of the Sun, electron-ion and electron-electron axio-bremsstrahlung dominate the solar flux. While the ionic metal content in the Sun is low (see Table 4.1 with the photospheric[1] composition of the Sun), axio-recombination has a contribution due to its larger cross section compared with those of bremsstrahlung and Compton [282]. The ABC flux is dominant in non-hadronic axion models where the axion-electron coupling can appear at the tree level.

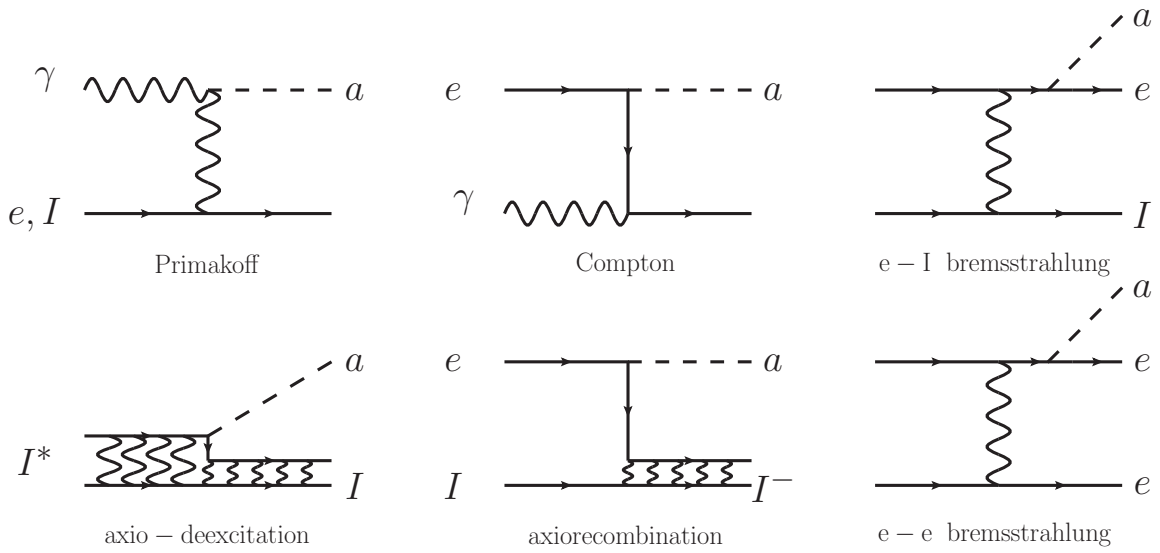

Figure 4.1: Primakoff and ABC postulated interactions of axions with electrons and atoms. Feynman diagrams from Ref. [283].

The ABC flux was calculated by J. Redondo in Ref. [283] by considering the Sun as a plasma in thermal equilibrium. In this scenario, the photon absorption and production rates are related and can be calculated using available monochromatic photon radiative opacities libraries. The results in relative fluxes and luminosities are:

$$\Phi_B : \Phi_C : \Phi_A = 64.9 : 7.6 : 27.6 \tag{4.2}$$

[1]Photosphere is the deepest region of a luminous object that is transparent to photons of certain wavelengths.

Table 4.1: Solar photospheric abundances given as $\log \epsilon_i \equiv \log N_i/N_H + 12$, where N_H is the number density of the element, and N_H is the number density of hydrogen in the Sun [284].

Element	Abundance [$\log \epsilon$]	Element	Abundance [$\log \epsilon$]
C	8.43	Si	7.51
N	7.83	S	7.12
O	8.69	Ar	6.40
Ne	7.93	Ca	6.34
Na	6.24	Cr	5.64
Mg	7.60	Mn	5.43
Al	6.45	Ni	6.22
Fe	7.50		

$$L_B : L_C : L_A = 51.4 : 15.6 : 33. \tag{4.3}$$

Nuclear transition fluxes

Additional to the coupling of the axions to electrons or photons, a coupling to nucleons is considered. An M1 nuclear transition from thermal excitation of ^{57}Fe could produce an axion. The first excited state is at 14.4 keV. The solar core contains a natural abundance of ^{57}Fe of 2.12%, translated to an average number density of $(9.0 \pm 1.2) \times 10^{19}\mathrm{cm}^{-3}$. This value is obtained by assuming that the isotopic abundance of ^{57}Fe in the Sun is homogeneous and identical to the one found on Earth. The number density is found by multiplying the photospheric abundance with the isotope abundance on Earth, from Refs. [284, 285]. Table 4.1 shows the photospheric composition of the Sun. The uncertainty comes from the different metal diffusion models in the core, computed in Ref. [286]. The expected flux is given by the axion-to-photon branching ratio for the decay of the first state of ^{57}Fe[287, 288]:

$$\Phi_a = \left(\frac{k_a}{k_\gamma}\right)^3 \times 4.56 \times 10^{23} \left(g_{AN}^{\mathrm{eff}}\right)^2 \ \mathrm{cm}^{-2}\,\mathrm{s}^{-1}, \tag{4.4}$$

where k_a is the momentum of the outgoing axion, k_γ represents the photon momentum, and $g_{AN}^{\mathrm{eff}} \equiv \left(-1.19 g_{AN}^0 + g_{AN}^3\right)$ stands for an effective coupling that combines the iso-scalar and iso-vector coupling constants, g_{AN}^0 and g_{AN}^3. The new parameter g_{AN}^{eff} is model-independent and relates not only to the axion-nucleon coupling, but it can be interpreted as nucleon coupling to any axion-like particles emitted in the M1 nuclear transition.

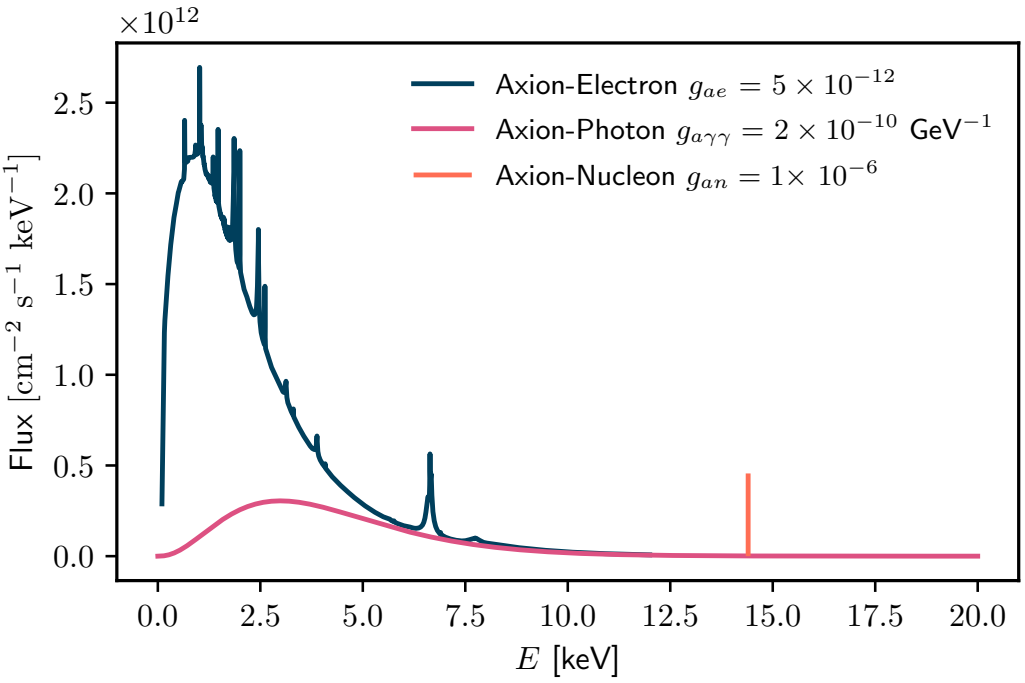

Figure 4.2: Solar axion flux from the Primakoff, ABC interactions and nuclear transitions. The coupling parameters $g_{ae} = 5 \times 10^{-12}$, $g_{a\gamma\gamma} = 2 \times 10^{-10}$ and $g_{an} = 1 \times 10^{-6}$, are assumed.

4.2 Solar axion interactions with liquid xenon

Axioelectric effect: The axioelectric effect is a process equivalent to the photoelectric process, in which an axion is absorbed:

$$a + e + Z \rightarrow e + Z.$$

The relation between the cross sections for the axion absorption and the photoelectric effect can be approximated as [289, 290, 282]

$$\sigma_{Ae}(E) = \sigma_{\text{abs}}(E)\frac{g_{Ae}^2}{\beta}\frac{3E^2}{16\pi\alpha m_e^2}\left(1 - \frac{\beta^{\frac{2}{3}}}{3}\right), \tag{4.5}$$

where β and E are the relativistic velocity and the energy of the axion, respectively, m_e is the electron mass, α is the fine structure constant, and σ_{abs} is the cross section for photoabsorption in LXe. The photoabsorption curve in xenon, provided in Ref [291], is approximated by log-log cubic-spline fits as a function for energies above the K-shell absorption edge. Below that shell, a linear interpolation is used to fit each separate shell to avoid the error by interpolating across absorption edges. The

linear fit in the log-log scale is equivalent to assuming that the photoabsorption cross section is proportional to the power of the photon energy, giving better results than the log-log cubic-spline fit. The photoabsorption in xenon is shown in Figure 4.3.

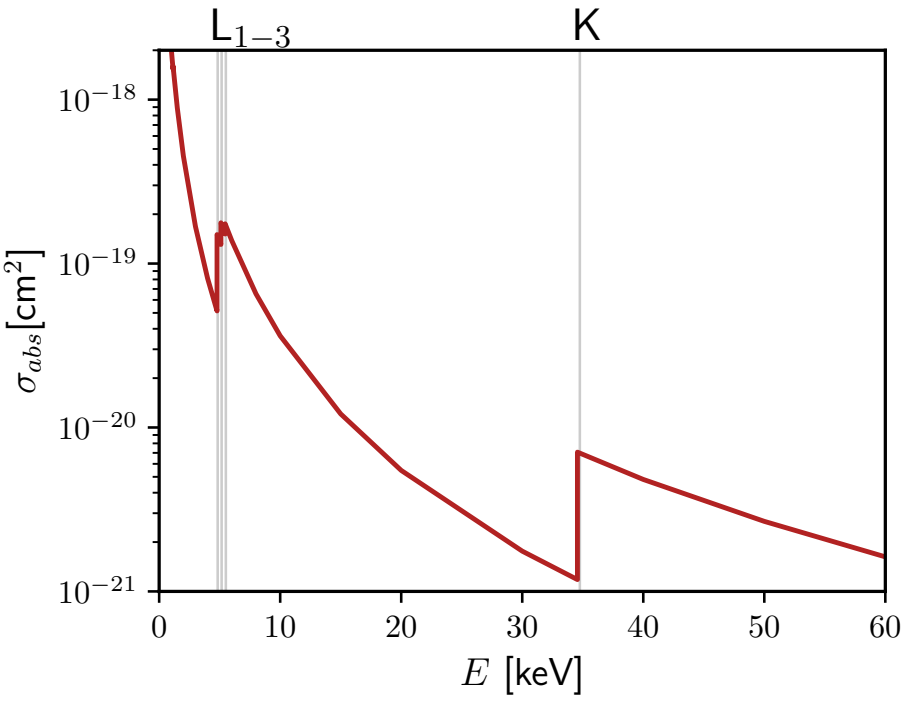

Figure 4.3: Cross section of the photoabsorption process in xenon. The process is analogous to the one of an axion being absorbed in the atom, and it is used to calculate this cross section. Data from Ref [291].

Inverse Primakoff effect: The incoming axion can be converted into a photon through the electromagnetic field generated by the atom. Previous studies have mentioned the potential contribution of the inverse Primakoff process in LXe [292, 293]. For solar axions, whose wavelength is similar to or higher than the atomic size[2], the effects of the atomic form factors are significant. The atomic form factors represent how the charge distribution screens the internal electric field, and it is defined as the Fourier transform of the charge distribution of the electrons in the atom. In other words, it provides the amplitude of the scattering of a single waveform with the atomic electrons [294]. The cross sections for the coherent and incoherent interactions depend on the distribution of the electrons in

[2]The de Broglie length of the solar axion ($E \sim 2$ keV), with the relativistic approximation, would be $\lambda = \frac{h}{p} = \frac{2\pi\hbar c}{pc}$ where $\hbar c = 1973\,\text{eV Å}$, and $\lambda \sim \mathcal{O}(4\,\text{Å})$

the target. For a coherent interaction, it can be written as [295]

$$\frac{d\sigma_{\rm el}}{d\Omega} = \frac{g_{a\gamma\gamma}^2 E^3 p_a \sin^2\theta}{16\pi^2 \left(E^2 + p_a^2 - 2Ep_a\cos\theta\right)^2} \left| \int d^3\boldsymbol{x} e^{-i\boldsymbol{q}\cdot\boldsymbol{x}} \langle A_0|\rho(\boldsymbol{x})|A_0\rangle \right|^2, \tag{4.6}$$

where E is the energy of the axion, $\boldsymbol{q} = \boldsymbol{p}_\gamma - \boldsymbol{p_a}$ with $\boldsymbol{p}$ the momentum of the outgoing photon and axion, respectively, θ is the scattering angle, $\rho(x)$ is the charge density operator, and $|A_0\rangle$ the ground state of the atom A. By replacing the charge density operator with the charge of all electrons, minus the correction for the correlation of electron interactions, the cross section can be written as:

$$\frac{d\sigma}{d\Omega} = \frac{\alpha g_{a\gamma\gamma}^2 E^3 p_a \sin^2\theta}{4\pi \left(E^2 + p_a^2 - 2Ep_a\cos\theta\right)^2} |Z - F(\boldsymbol{q})|^2, \tag{4.7}$$

where $F(\boldsymbol{q}) = \sum_i \left\langle A_0|e^{-i\boldsymbol{q}\cdot\boldsymbol{x}_i}\middle|A_0|e^{-i\boldsymbol{q}\cdot\boldsymbol{x}_i}\right\rangle$ is the atomic form factor, and Z the atomic number. The total cross section can be obtained by integrating over the solid angle and the allowed energies of the axions

$$\sigma = \frac{\alpha g_{a\gamma\gamma}^2}{8} \int_{E-p_a}^{E+p_a} dq \frac{\left[q^2 - (E-p_a)^2\right]\left[(E+p_a)^2 - q^2\right]}{p_a^2 q^3} |Z - F(q)|^2 \tag{4.8}$$

Some experiments rely on the enhancement by Bragg scattering in crystals to detect the inverse Primakoff process, where the photon-axion transition probability is determined by the field seen by the axion and the penetration depth in the lattice [296, 297]. In Ref. [295], Nagata et al. implement the atomic form factors obtained in Ref [298] by using Relativistic Hartree-Fock (RHF) methods, which are well approximated by the empirical formula:

$$F(q) \simeq \sum_{i=1}^{4} a_i \exp\left[-b_i \left(\frac{|\boldsymbol{q}|}{4\pi}\right)^2\right] + c, \tag{4.9}$$

with a, b and c empirical parameters. The total cross section is obtained by integrating Eq. 4.8. Alternatively, Gao et al. [292] and Dent et al. [293] assumed initially that the atomic form factors follow a spherically symmetric Coulomb potential with a screening radius r_0. Compared with Nagata et al., their results show more than an order of magnitude difference in cross sections, more pronounced at low energies. Figure 4.4 compares the two models for the atomic factors used.

Both papers from Gao et al. and Dent et al. have updated their results following the results from Nagata et al. In addition to the coherent scattering, the cross section for inelastic processes can also be calculated in a similar manner as

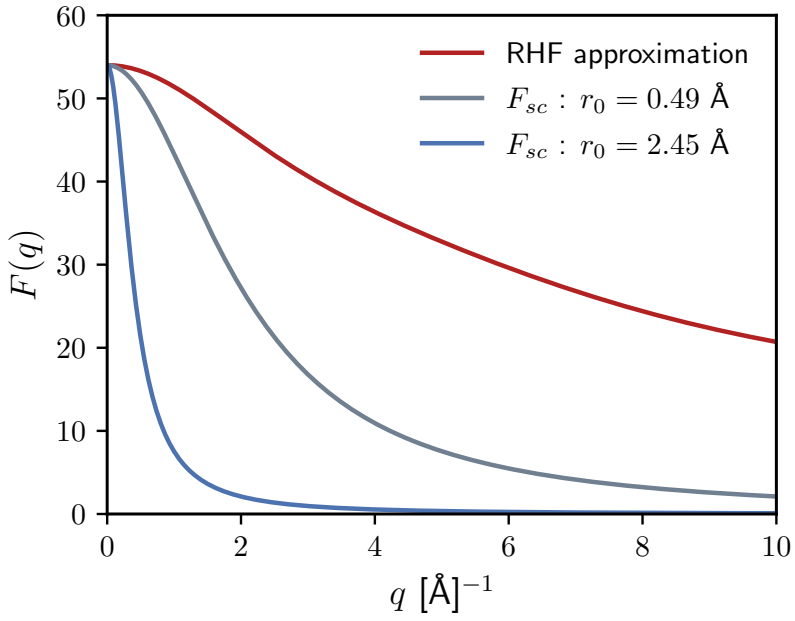

Figure 4.4: Atomic form factor comparison between the RHF values from Ref. [298] and the screened Coulomb potential, used initially in Refs. [292, 293]. Nagata et al. were the first to show the relative high discrepancy between both assumptions.

$$\sigma_{\text{inel}}^{\text{invPrim}} = \frac{\alpha g_{a\gamma\gamma}^2 E^3 p_a \sin^2\theta}{4\pi \left(E^2 + p_a^2 - 2Ep_a\cos\theta\right)^2} S(\boldsymbol{q}, Z). \tag{4.10}$$

Compared to elastic scattering, inelastic scattering becomes more important at low energies (around 2 keV), as the wavelength of the incoming particle is not sufficiently large to scatter the whole atomic nuclear radius coherently. The comparison of both cross sections is shown in Figure 4.5. It can be noted from Eqs. 4.10 and 4.8 that the only difference with the coherent cross section is the factor $S(\boldsymbol{q}, Z)$. Independently of the coupling parameter, the incoherent cross section will be larger than the coherent interaction at lower energies.

The inverse Primakoff contribution in LXe does not have the enhancement of the coherent interaction with a crystal, a property exploited in other experiment searches [299, 300, 301, 302, 303]. Figure 4.6 shows the cross section for the axioelectric effect compared with the sum of the coherent and incoherent inverse Primakoff processes in LXe.

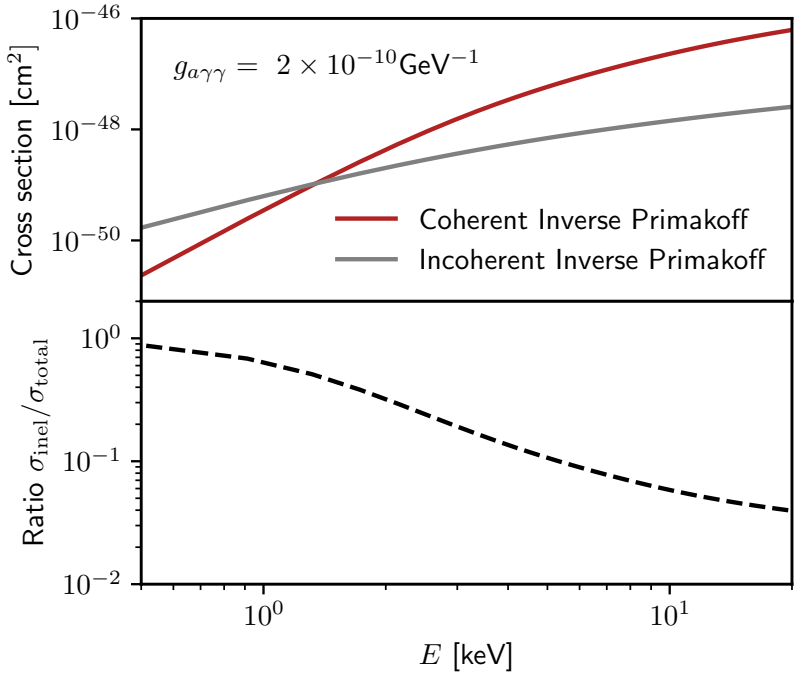

Figure 4.5: Atomic form factors of the coherent and incoherent inverse Primakoff effect compared. At low energies, the axion cannot scatter the whole nucleus coherently, and the incoherent scattering becomes more dominant.

4.3 Solar axion rate in liquid xenon

The estimation of the total rate in LXe of solar axions from the three different fluxes includes both the possibility of axioelectric and inverse Primakoff interactions. The inclusion of the inverse Primakoff process results in three additional terms to the signal model, compared with Ref. [248]:

$$\frac{dR}{dE_R} = \eta(E_R)\frac{N_A}{A}\left(\frac{d\Phi_a^{\text{ABC}}}{dE}(E_R) + \frac{d\Phi_a^{\text{Prim}}}{dE}(E_R) + \frac{d\Phi_a^{^{57}\text{Fe}}}{dE}(E_R)\right) \times \left(\sigma_{a\to\gamma}^{\text{invPrim}}(E_R) + \sigma_{ae}(E_R)\right), \tag{4.11}$$

where $\sigma_{a\to\gamma}^{\text{invPrim}} = \sigma_{inel}^{\text{invPrim}} + \sigma_{el}^{\text{invPrim}}$. The rate is affected by the detection efficiency $\eta(E_R)$ of the signal reconstruction, which is energy-dependent and reduces the sensitivity at low energies. The detection efficiency is taken from the XENON1T ER search [248], derived from different signal quality cuts, single-site reconstruction cuts and threefold coincidence in PMTs from the combined energy scale from S1 and S2 signals. Additionally, the energy threshold, assumed to be at 1 keV, is artificially added to this efficiency, as shown in Figure 4.7.

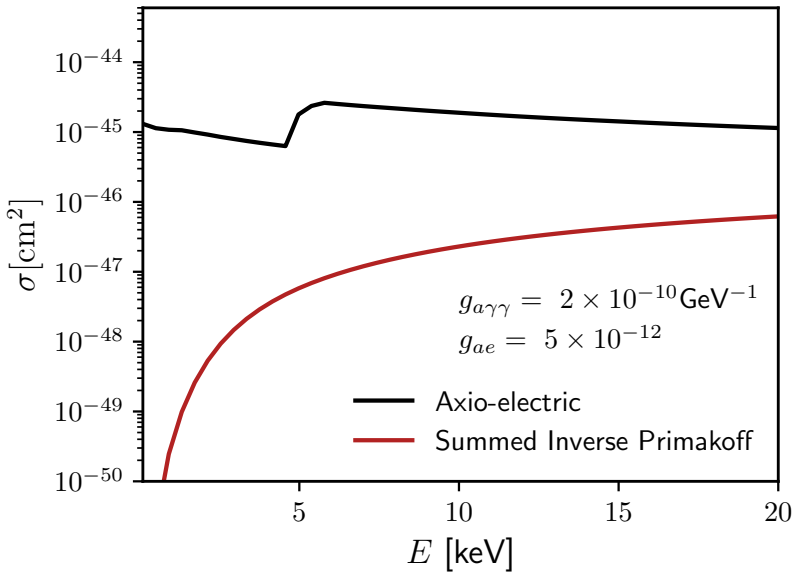

Figure 4.6: Comparison of the cross section of axioelectric effect with the sum of the coherent and incoherent inverse Primakoff effect, assuming $g_{ae} = 5 \times 10^{-12}$ and $g_{a\gamma\gamma} = 2 \times 10^{-10}$ GeV^{-1}.

The reconstructed signals are smeared by the energy resolution of the detector at low energies (obtained from the fit of the Equation 3.1 to data) from XENON1T [125]. The values assumed for the energy smearing are $a = 0.339$ and $b = 2.3\ 10^{-3}$. Figure 4.8 shows the expected rate in DARWIN in a tonne-year exposure for each flux, where both detection channels are summed in the same curve. Noticeably, the ABC and the Primakoff flux share the same energy region. In contrast, the nuclear flux, which is affected by the coupling to axions and photons, is recognisable further away in the energy space.

The coupling parameters appear combined in most of these terms. Since all these interactions produce photons or electrons at low energy, they are treated as single-site interactions due to the short mean path. In this analysis, we consider a model-independent approach, where the coupling constants are unconstrained free parameters.

4.3.1 Expected background rate around the region of interest

The background around the energy of the discussed solar axion fluxes limits the discovery potential of an experiment. The extent of these background sources has been thoroughly discussed in Chapters 2 and 3. Consequently, in this section, we will only focus on those that appear in the low energy region (i.e. 0–20 keV) around the signal model of solar axions. In this region, we have as background

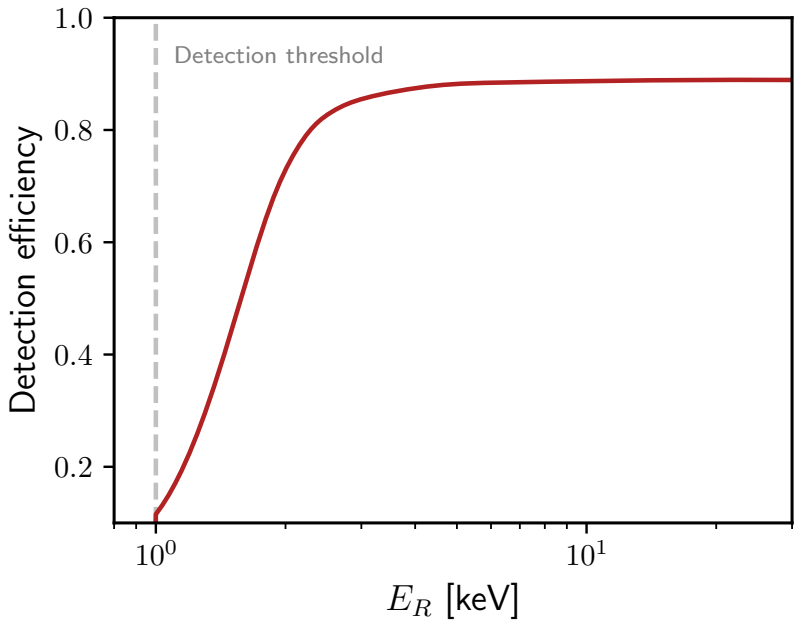

Figure 4.7: Signal reconstruction efficiency in the low energy region, with an artificial threshold assumed to be 1 keV. The detection efficiency curve is taken from Ref. [248].

components the solar neutrinos (mostly from pp-neutrinos, with a smaller component from ^{7}Be), β-decays of ^{222}Rn, ^{85}Kr, the $2\nu\beta\beta$ contribution from ^{136}Xe and the beta decay of its activated nucleus from neutron capture, ^{137}Xe. The background model also includes multiple lines from the double electron capture of ^{124}Xe. The isotopes ^{214}Pb, ^{212}Pb and ^{85}Kr contribute to the low energy region due to their low energy beta emission. As discussed in Chapter 2, their decays to the ground state of the daughter nuclei produce no γ-rays or conversion electrons and their removal through multi-site or coincidence cuts is thus not possible. In DARWIN, the low-energy gammas from detector materials are strongly screened by the target LXe, and at lower fiducial masses, they will contribute negligibly to the background rate. However, they are still accounted for in the background model. Figure 4.9 shows the expected background counts in the region 1–20 keV for different fiducial masses.
The chosen fiducial target to extract the material background is 33 t, which will be justified later in this chapter. Figure 4.10 shows the expected background around the ROI for solar axion detection (1–20 keV) after the detection efficiency curve and the smearing by the energy resolution is applied. The most dominant backgrounds around these energies are the $2\nu\beta\beta$ decay of ^{136}Xe and solar pp-neutrinos. Table 4.2 summarises the contribution of the different backgrounds with their activity uncertainty.

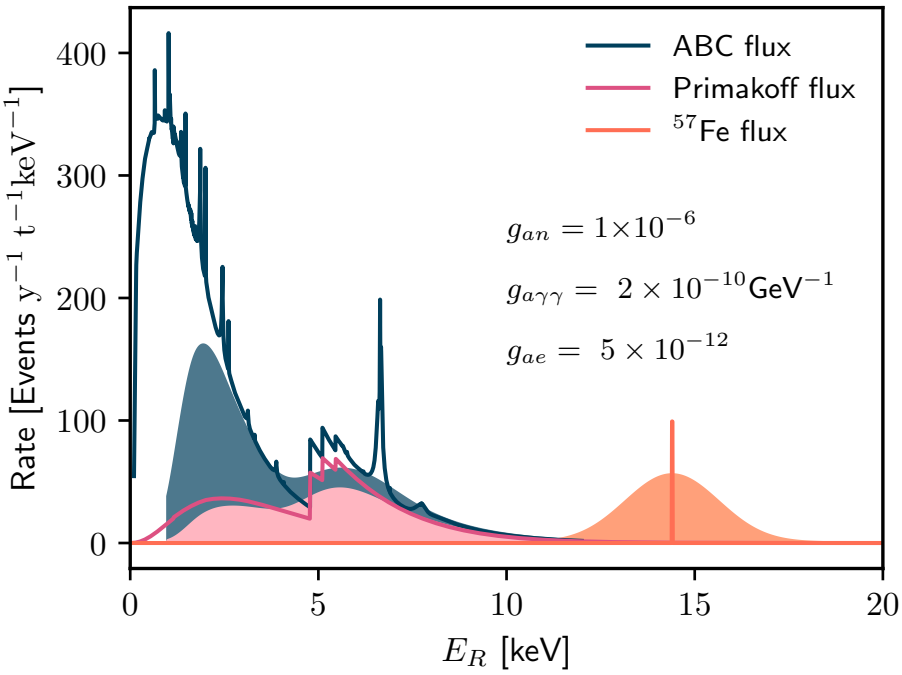

Figure 4.8: Expected rate of events from ABC, Primakoff and ^{57}Fe fluxes via axioelectric and inverse Primakoff effects in LXe, assuming values for the coupling constants of: $g_{ae} = 5 \times 10^{-12}$, $g_{a\gamma\gamma} = 2 \times 10^{-10}\text{GeV}^{-1}$ and $g_{an} = 1 \times 10^{-6}$. The energy smearing, threshold and detection efficiency of the detector is applied.

4.4 Procedure of the statistical inference of upper limits and discovery potential

The statistical inference procedure is performed similarly to the one described in Chapter 3. However, there is a difference compared to the $0\nu\beta\beta$ search, where the signal model is a monoenergetic peak at a known energy, and only one parameter of interest is involved in the inference. The search for solar axion implicates three fluxes that can be detected in two different channels. Consequently, the three coupling parameters of interest are mixed for the rate of each signal model. Since three parameters are entangled, asymptotic methods are highly non-trivial in this case. Given Equation 4.11, it can be shown that the coupling parameters are mixed in the event rate for each signal channel coming

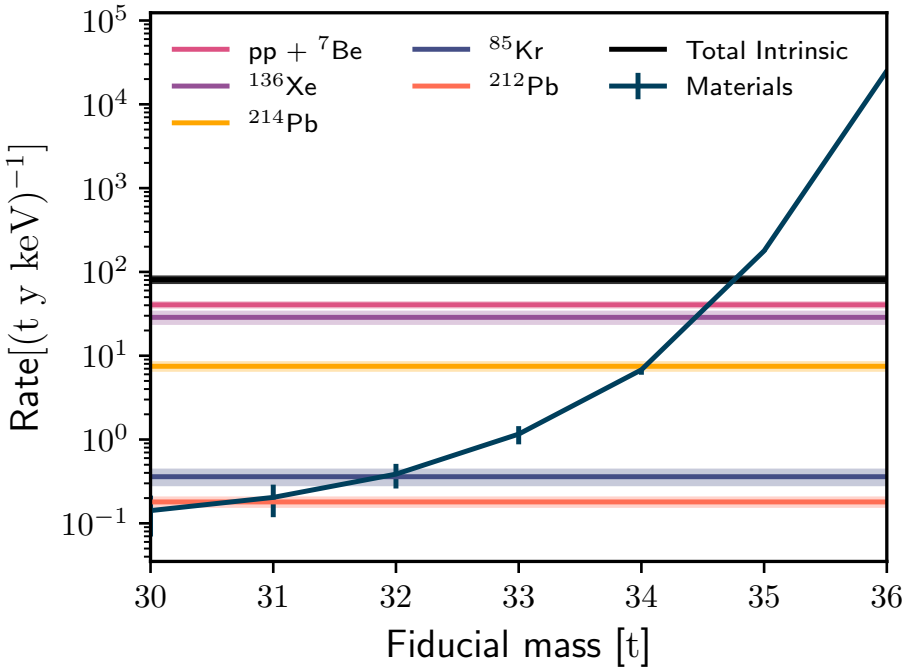

Figure 4.9: Background contributions in the region 1–20 keV for different choices of fiducial mass. The surrounding LXe strongly screens the detector materials background at lower fiducial masses. The biggest contributions, when the material background is negligible, arise from solar neutrinos (pp neutrinos, with a smaller component of ^{7}Be neutrinos) and the $2\nu\beta\beta$ of ^{136}Xe.

from the flux of solar axions,

$$N_{ABC} = \frac{N_A}{A}\left(g_{ae}^2 g_{a\gamma\gamma}^2 \varsigma_{a\to\gamma}^{\text{invPrim}}\left(E_R\right) + g_{ae}^4 \varsigma_{ae}\left(E_R\right)\right)\frac{d\phi_a^{\text{ABC}}}{dE}\left(E_R\right), \tag{4.12}$$

$$N_P = \frac{N_A}{A}\left(g_{a\gamma\gamma}^4 \varsigma_{a\to\gamma}^{\text{invPrim}}\left(E_R\right) + g_{a\gamma\gamma}^2 g_{ae}^2 \varsigma_{ae}\left(E_R\right)\right)\frac{d\phi_a^{\text{Prim}}}{dE}\left(E_R\right), \tag{4.13}$$

$$N_{Fe} = \frac{N_A}{A}\left(g_{an}^2 g_{a\gamma\gamma}^2 \varsigma_{a\to\gamma}^{\text{invPrim}}\left(E_R\right) + g_{an}^2 g_{ae}^2 \varsigma_{ae}(E_R)\right)\frac{d\phi_a^{\text{Fe}}}{dE}\left(E_R\right), \tag{4.14}$$

where $\frac{d\varsigma_x}{dE} = \frac{d\sigma_x}{dE}/g_x^2$, and $\frac{d\phi_x}{dE} = \frac{d\Phi_x}{dE}/g_x^2$ are reduced versions of the cross sections. Given this notation, the rate of ABC axions, for example, detected via the axioelectric effect would be proportional to $N_{ABC_{ae}} \propto g_{ae}^4 \varsigma_{ae}(E_R)\frac{d\phi_a^{\text{ABC}}}{dE}(E_R)$.

Before continuing with the description of the inference procedure given the signal and background model, a Poisson counting approach to select an optimal exposure and parameter space to scan over will be discussed.

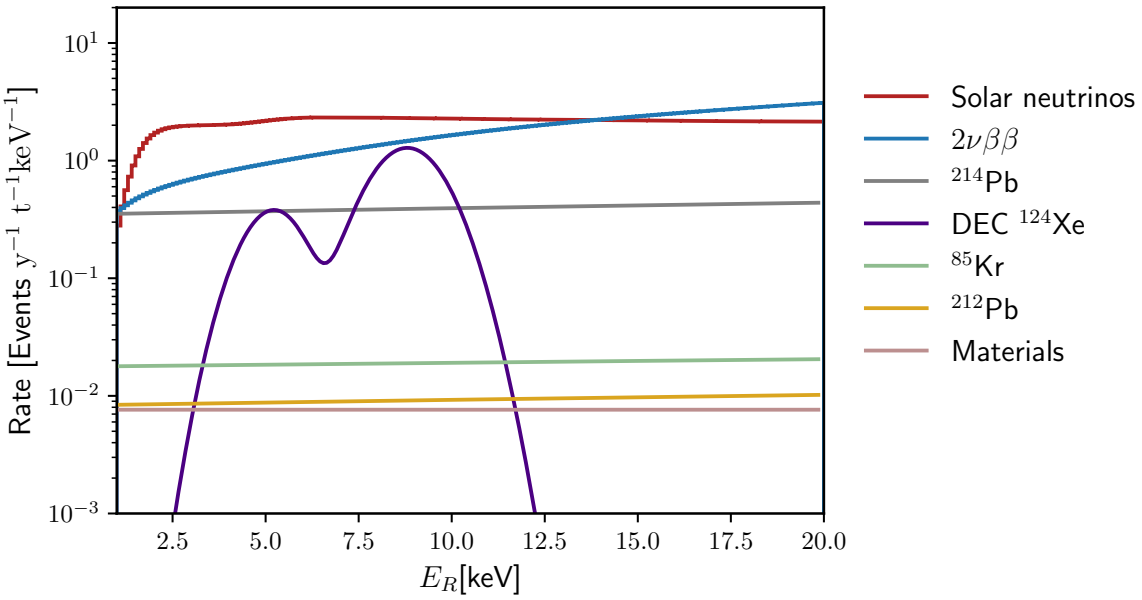

Figure 4.10: Background contributions in the region 1–20 keV. The most relevant for this analysis are the double beta decay of ^{136}Xe and the solar neutrino from the pp chain and ^{7}Be electron capture.

Table 4.2: Background rate in the region $[1, 20]$ keV in the ER channel. Solar neutrinos interacting with the detector (mainly pp-neutrinos) and the double beta decay of ^{136}Xe account for more than 85% of the total background.

Source	Assumptions	Rate [(t y)$^{-1}$]	Uncertainty [(t y)$^{-1}$]
Solar neutrinos	pp and ^{7}Be	40.5	2.4
^{136}Xe	$T_{1/2}^{2\nu\beta} = 2.165$ y	28.7	4.3
^{214}Pb	0.1 µBq/kg	7.48	0.75
	BR $= 0.109 \pm 0.01$		
^{124}Xe	$T_{1/2}^{2\upsilon\mathrm{ECEC}} = 1.1 \times 10^{22}$y	3.63	0.73
	LM, LN, LL from EC peaks		
Materials	MC simulations (GEANT4)	1.13	0.28
^{85}Kr	^{85}Kr/$^{\mathrm{nat}}$Kr $= 1.7 \times 10^{-11}$mol/mol	0.36	0.07
	2 ppq $^{\mathrm{nat}}$Kr/Xe		
^{212}Pb	^{220}Rn/^{222}Rn $\sim 0.3\%$	0.18	0.02
	Total background rate	(81.95 $\pm$6.15) (t y)$^{-1}$	

4.4.1 Selection of the exposure and parameter space to scan

A simplified counting analysis was used for the exposure optimisation, following the procedure indicated in Ref. [267]. The method relies on simplifying the problem by counting expected signal and background events as if they were in the same *bin* and treated with Poissonian statistics. It does not consider the signal shape and background energy spectra. This method allows for avoiding computationally expensive toy Monte Carlo (toyMC) to select the optimal exposure range at the cost of losing the precision that the shape parameters in the likelihood offer. As a simplified method, it does not consider that the signals could lie in the same energy region nor the correlation between signal rate and coupling parameters; thus, the signal models are treated independently.
Given an expectation of background counts in the ROI, $B = \mathrm{B}\,\epsilon$, where ϵ stands for the exposure in $[t \cdot y]$ and B is the background index in units of $(\mathrm{t\,y})^{-1}$, we aim to find the signal expectation at which 50% of the experiments would report a 90% fluctuation above B. First, the $C_{90\%}$ total counts are found by requiring the Cumulative Density Function $\mathrm{CDF}(C_{90\%}, B) = 90\%$, defined as

$$\mathrm{CDF}_{\mathrm{Poisson}}\left(C \mid B\right) = \frac{\Gamma(C+1, B)}{\Gamma(C+1)} \tag{4.15}$$

where its definition is via the normalised upper incomplete gamma function Γ. Consequently, $S_{90\%}$, the signal counts at 90% CL, is found by requiring the survival function $\mathrm{SF}(C_{90\%}, S_{90\%} + B)$ to be 50%, obtaining a median sensitivity in the case of an excess. The survival function SF is defined as the complementary CDF, i.e. $\mathrm{SF} = 1 - \mathrm{CDF}$.

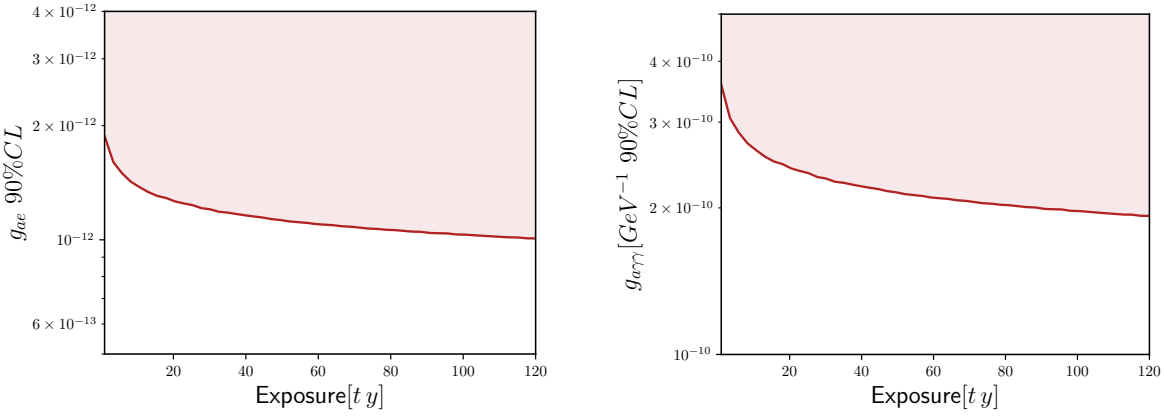

Figure 4.11: Median sensitivity in case of a 90% significance for the axioelectric (right) and Primakoff (left) couplings, using a counting approach as described in Ref. [267] and this section.

Using this approach, the optimal fiducial mass is found by calculating $S_{90\%}$ from scanning background indices for each fiducial mass. The background index for each mass due to the contributions

of materials is shown in Figure 4.9, where at lower fiducial mass (i.e. longer attenuation paths) the background coming from materials is strongly suppressed. This is performed for a signal arising from the ABC flux in the axioelectric channel, where the rate is $\propto g_{ae}^4$ (see Equation 4.12). Figure 4.12 shows the result of this scan, where the optimal fiducial mass results in 33 t. The same procedure is performed to find an optimal range for the coupling to nucleons, g_{an}.

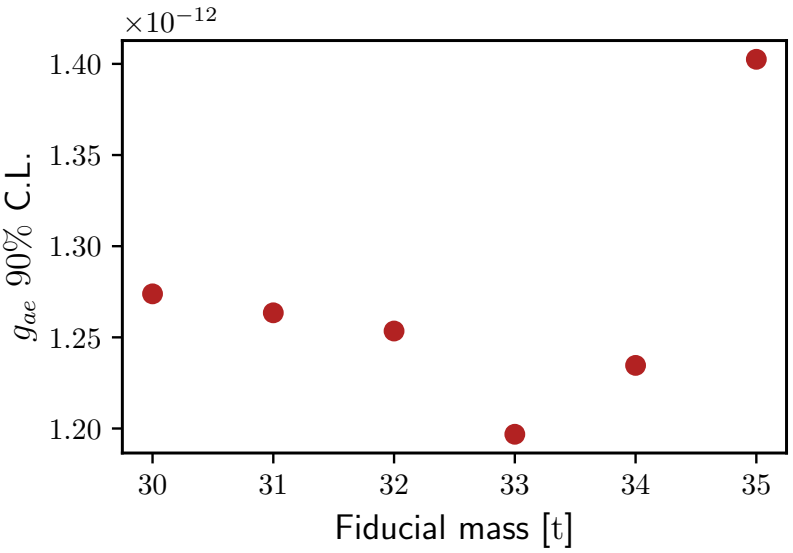

Figure 4.12: Calculated g_{ae} values at 90% C.L. by varying the fiducial mass, and thus, the expected background rate due to the decreased attenuation of the material background at higher fiducial masses. The minimum is around 33 t, which is taken later for the sensitivity analysis.

This approach can also be used to find the optimal exposure that will be taken to calculate the sensitivity. Figure 4.11 shows the result of applying this approach to the couplings g_{ae} and $g_{a\gamma\gamma}$ and varying the exposure, using the background index that corresponds to 33 t. The rate terms that mix the couplings are neglected. After one year of exposure, the coupling reach improves slowly. Longer exposure will place stricter limits, with the caveat of longer simulation times for the toyMC-generated data. Thus, an exposure of 33 t y is assumed here to optimise computation time.
A scan in the parameter space of the axioelectric and the Primakoff coupling is performed to obtain an estimated map of the significance of a signal $\mathcal{S}$ based on the expected number of signal events given the background $\mathcal{B}$. The exposure is taken as 33 t y. This scan takes into account the event rates from Equations 4.12, 4.13 and 4.14. Figure 4.13 shows the significance scan for the couplings g_{ae} and $g_{a\gamma\gamma}$, assuming $g_{an}^{\text{eff}} = 0$, where the significance is taken as the usual chi-square[3] limit of

[3] Assuming the validity of Wilk's theorem

$\mathcal{S}/\sqrt{(\mathcal{B})}$. The scan provides an estimation of the region in the parameter space where the signal is well below a detection or constraint limit. The same procedure is repeated for the third coupling parameter not shown in the figure, g_{an}^{eff}. This first analysis motivates the region to scan without the need for more complex methods. Observing a signal below $1 \times 10^{-10}\,\text{GeV}^{-1}$ and 1×10^{-12} for the axion photon and axion electron couplings, respectively, is likely out of reach for the experiment given the background level.

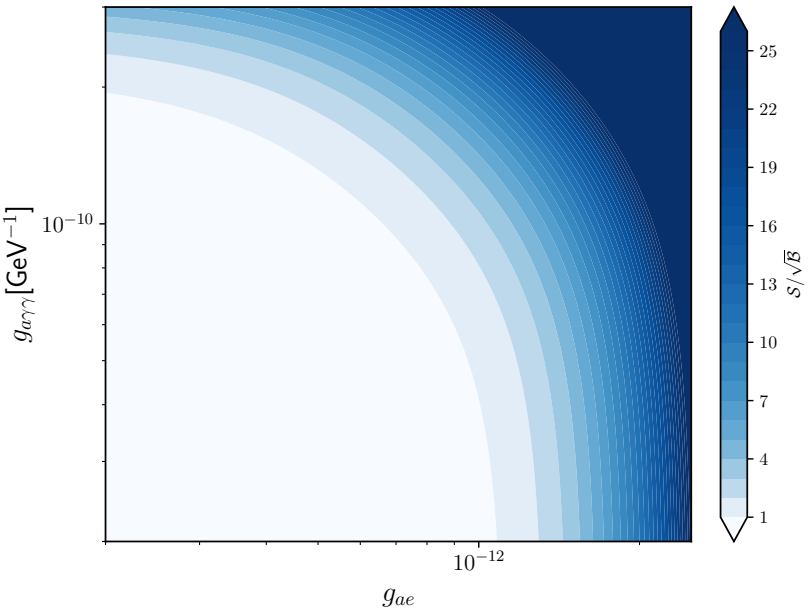

Figure 4.13: Scan in the $g_{ae} - g_{a\gamma\gamma}$ of the signal significance, calculated with a chi-squared limit. The scan only serves as an estimation of which regions are out of reach for the detector, given its background and exposure.

It can also be useful to calculate the rate of events from the ABC flux detected via the axioelectric effect compared to the background rate. Due to the allowed region for g_{ae} and $g_{a\gamma\gamma}$ and the cross sections for axioelectric and inverse Primakoff effect, LXe TPCs are more sensitive to the ABC channel detected via the axioelectric effect. Following this observation, the expected background rate and the expected signal rate from the ABC flux detected via axioelectric effect for $33\,\text{t}$ is shown in Figure 4.14, for different values for the axioelectric coupling parameter g_{ae}. With this simple comparison, it can be inferred that reaching values below 1×10^{-12} represents a challenge. It should also be noted that the previous estimations do not take into account the shape of the *pdf* from the background or signal hypothesis, which will be used in the next section for the toyMC production and fitting.

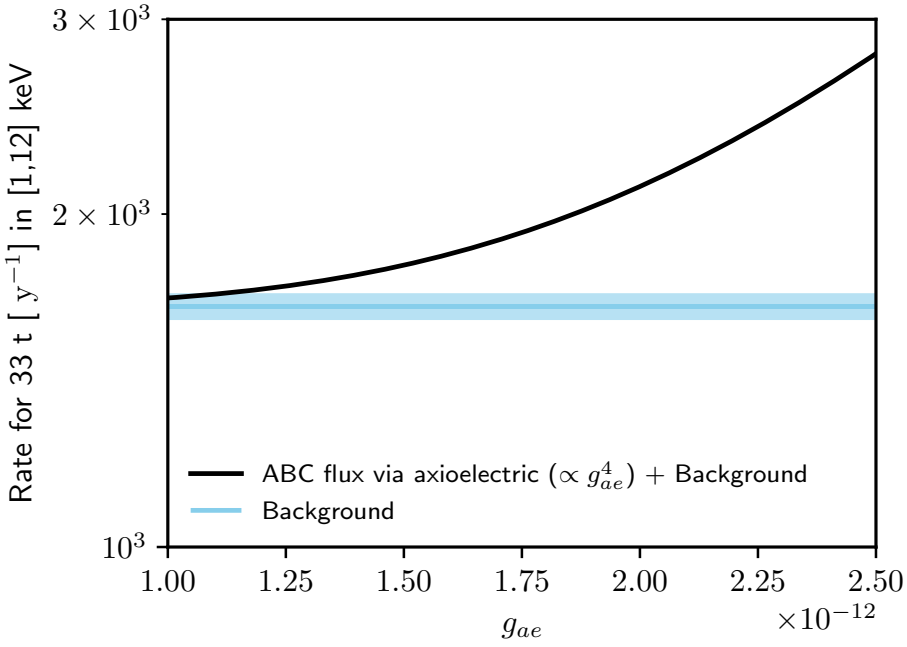

Figure 4.14: Expected background rate and expected signal rate from the ABC flux detected via the axioelectric effect for 33 t in the energy region 1–12 keV. The blue band represents a Poissonian uncertainty in the background calculation.

4.4.2 Upper limit inference

The inference procedure is performed by profiling the log-likelihood ratio, where the unbinned extended likelihood is given by

$$\begin{aligned} \mathcal{L}\left(\mu_s, \boldsymbol{\mu}_b, \boldsymbol{\theta}\right) &= \text{Poisson}\left(N \mid \mu_{tot}\right) \\ \times \prod_i^N \varepsilon \left(\sum_j \mu_{b_j} f_{b_j}\left(E_i, \boldsymbol{\theta}\right) + \sum_k \mu_{s_k} f_{s_k}\left(E_i, \boldsymbol{\theta}\right) \right) \\ \times \prod_m C_{\mu_m}\left(\mu_{b_m}\right) \times \prod_n C_{\theta_n}\left(\theta_n\right), \end{aligned} \tag{4.16}$$

where μ_{s_k} is the expected number of signal events in the channel k, μ_{b_j} the expected number of background events in the component j, f_{bj} is the *pdf* of the background j, f_{sk} is the *pdf* of the signal in the channel k. The error in the efficiency curve given by η, taken from the data provided by the ER analysis in XENON1T from Ref. [248], is approximated to 10% over the extent of the ROI. The terms C_{θ_n} and C_{μ_m} are soft constraints on the nuisance parameters given by shape or expectation signal uncertainties. The expectation values for each background components μ_{b_j} are

the ones listed in Table 4.2. Table 4.3 shows a summary of the model assumptions of the *pdf* (f_{bj}) for each background component.

Table 4.3: Description of the models for the different sources incorporated, where the *pdf* from each source, f_{bj} and the expected background strength μ_{b_j} for the component j is shown.

Source	f_{sk} or f_{bj}
ABC flux detected via axioelectric/inverse Primakoff	Template *pdf*
Primakoff flux via axioelectric/inverse Primakoff	Template *pdf*
^{57}Fe via axioelectric/inverse Primakoff	Gaussian
Solar neutrinos	Template *pdf*
^{136}Xe	Template *pdf*
^{214}Pb	Chebychev $\mathcal{O}(1)$
^{124}Xe	Sum of Gaussian peaks
^{85}Kr	Chebyshev $\mathcal{O}(1)$
^{212}Pb	Chebychev $\mathcal{O}(1)$
Materials	Chebychev $\mathcal{O}(1)$

The sum of the six signal *pdf*s and the seven background *pdf*s listed in Table 4.3 comprise the total model. Each signal *pdf* has a corresponding factor related to the coupling parameters, as shown in Equations 4.12, 4.13 and 4.14. The parameter $\mu_{s_{tot}} = \sum_k \mu_{s_k}$ is the sum of all rates in Equations 4.12, 4.13 and 4.14 given the coupling parameters, and it is allowed to change given a Poissonian expectation. The square of the coupling parameters

$$\begin{aligned} ga &= \left(\frac{g_{ae}}{10^{-12}}\right)^2 \\ gb &= \left(\frac{g_{a\gamma\gamma}}{10^{-10}}\right)^2 \\ gc &= \left(\frac{g_{an}}{10^{-6}}\right)^2, \end{aligned} \tag{4.17}$$

appear combined in the six expected signal channels as

$$\begin{aligned} N_{ABC_{ae}} &\propto ga^2, & N_{ABC_{iP}} &\propto ga \cdot gb \\ N_{P_{ae}} &\propto ga \cdot gb, & N_{P_{iP}} &\propto gb^2 \\ N_{Fe_{ae}} &\propto ga \cdot gc, & N_{Fe_{iP}} &\propto gb \cdot gb \ , \end{aligned} \tag{4.18}$$

where the labels iP and ae stand for detection in the inverse Primakoff and axioelectric channel, respectively.

Each toyMC dataset is sampled given the values to scan of g_{ae}, $g_{a\gamma\gamma}$ and g_{an}. The parameters ga, gb and gc are fitted in each toyMC experiment realisation, and the total expected number of signal

events given the sum of each channel k is allowed to float but fixed in a limited range of its Poissonian uncertainty. In this way, the coupling parameters appear in the likelihood as 'shape' parameters of the signal *pdf*. The soft constraints are implemented as Gaussian functions, centered around the expected value of the background components–which are left floating– with the uncertainties coming from either different experiments, simulations, or theory, explained in Chapter 2 and shown in Table 4.2 for this specific ROI. The nuisance parameters are resampled in each toyMC event. The confidence volume is defined as the volume boundary where $\alpha = 0.1$ for the case of a limit.
Using a two-sided or one-sided test statistic depends on the assumption that the experiment will exclude a parameter or make a discovery. The coverage of both statistical tests is correct by construction, but deciding which one to use when one observes real data results in the so-called flip-flop issue, discussed in Ref. [304]. Feldman and Cousins proposed a method using Neyman construction of intervals. A discovery can be claimed if there is a convergence in the lower limit to a value different from zero. If this value does not converge to a value different from zero, then one has the usual one-sided test for an upper-limit calculation.
The test followed to determine the limits is the Feldman-Cousins likelihood ratio, where the ordering principle for the confidence belt construction is the decreasing likelihood ratio:

$$\mathrm{R}(\mu_s, \theta) = \frac{\mathcal{L}\left(\mu_s, \mu_b, \theta\right)}{\mathcal{L}\left(\hat{\mu}_s, \hat{\mu}_b, \hat{\theta}\right)}. \tag{4.19}$$

The computation of the confidence volume for the three coupling parameters is performed by generating toyMCs, where the following algorithm is applied:

1. At the considered value of g_{ae_0}, $g_{a\gamma\gamma_0}$, g_{an_0}, generate a toyMC experiment by sampling the *pdf*, where the number of events μ_0 is calculated with the background and signal expected events with a Poissonian fluctuation.

2. Compute Equation 4.19 for the toyMC experiment.

3. Compute Equation 4.19 for the observed dataset.

4. The $1 - \mathrm{CL} = 1 - \alpha\left(\mu_0\right)$ is given by the fraction of toyMC experiments that have higher $\mathrm{R}(\mu_s, \theta)$.

The confidence volume of coverage α_0 for the true parameters g_{ae_0}, $g_{a\gamma\gamma_0}$, g_{an_0} by the $1 - CL$ algorithm is given by:

$$I_\mu = \left\{\mu \mid 1 - \alpha\left(\mu_0\right) > 1 - \alpha_0\right\}, \tag{4.20}$$

where $1 - \alpha(\mu_0)$ is the value obtained in the fourth step of the algorithm mentioned before. The library used for the statistical inference was *zfit* [305], a Python-based framework for model building and fitting. The model was first validated by injecting a signal given by the Equation 4.17 parameters taken as

$$\begin{aligned} ga &= 4 \\ gb &= 4 \\ gc &= 0.001, \end{aligned} \tag{4.21}$$

which imply $g_{ae} = 2 \times 10^{-12}$, $g_{a\gamma\gamma} = 2 \times 10^{-10}$ and $g_{an} = 1 \times 10^{-8}$, in order to study only the correlation between the ABC and Primakoff flux components. The total number of events for an exposure of $33\,\mathrm{t\,y}$ is allowed to float with a Poissonian fluctuation. Figure 4.15 shows a corner plot of all the nuisance and signal parameters, with median and one standard deviation quantiles marked in grey for 10,000 toyMCs. The distribution of the best values for each μ_{bj} follows a Gaussian shape, as expected when there are no unstable minima for the likelihood function. The contour plots outside the diagonal provide information about the correlation between the parameters. As expected, backgrounds with linear *pdf*s show a slight correlation but have no substantial impact on the minimisation due to the combined number of expected events. The values for the $\mu_{\text{solar-}\nu}$ and $\mu_{2\nu\beta\beta}$ hypotheses show at first glance a correlation, but the origin can be explained due to the relatively high uncertainty in the $\mu_{2\nu\beta\beta}$ background, as shown in Table 4.2, and it does not originate from minimisation or model instabilities. The parameters ga, gb and gc are recovered in the minimisation of each toyMC. The ABC and Primakoff fluxes overlap in the same energy region and have no distinctive features. Therefore, a correlation between the two parameters is expected. The minimisation of the likelihood is performed successfully for a signal hypothesis containing three parameters proportional to the signal rate. The minimisation of each toyMC is successful in reproducing the initial parameters without a rigid constraint (i.e. setting narrow limits on the parameters) or strongly biasing their terms, as nuisance parameters are allowed to float. Only soft penalty terms in the likelihood function, $C_{\mu_m}(\mu_{b_m})$ and $C_{\theta_n}(\theta_n)$, prevent the nuisance parameter estimator from falling in a non-physical region.

After the inference approach was validated by examining the distribution and correlation of the parameters at different signal hypotheses, a sweep in the parameter space of the couplings g_{ae}, $g_{a\gamma\gamma}$ and g_{an} was performed. The coupling parameters were sampled focusing mainly in the volume defined by $\{g_{ae} = [0.1 - 3] \times 10^{-12}, g_{a\gamma\gamma} = [0.5 - 3] \times 10^{-10}, g_{an} = [0.01 - 1] \times 10^{-5}\}$.

For each combination found in the volume, 10,000 toyMCs are performed, and the likelihood from

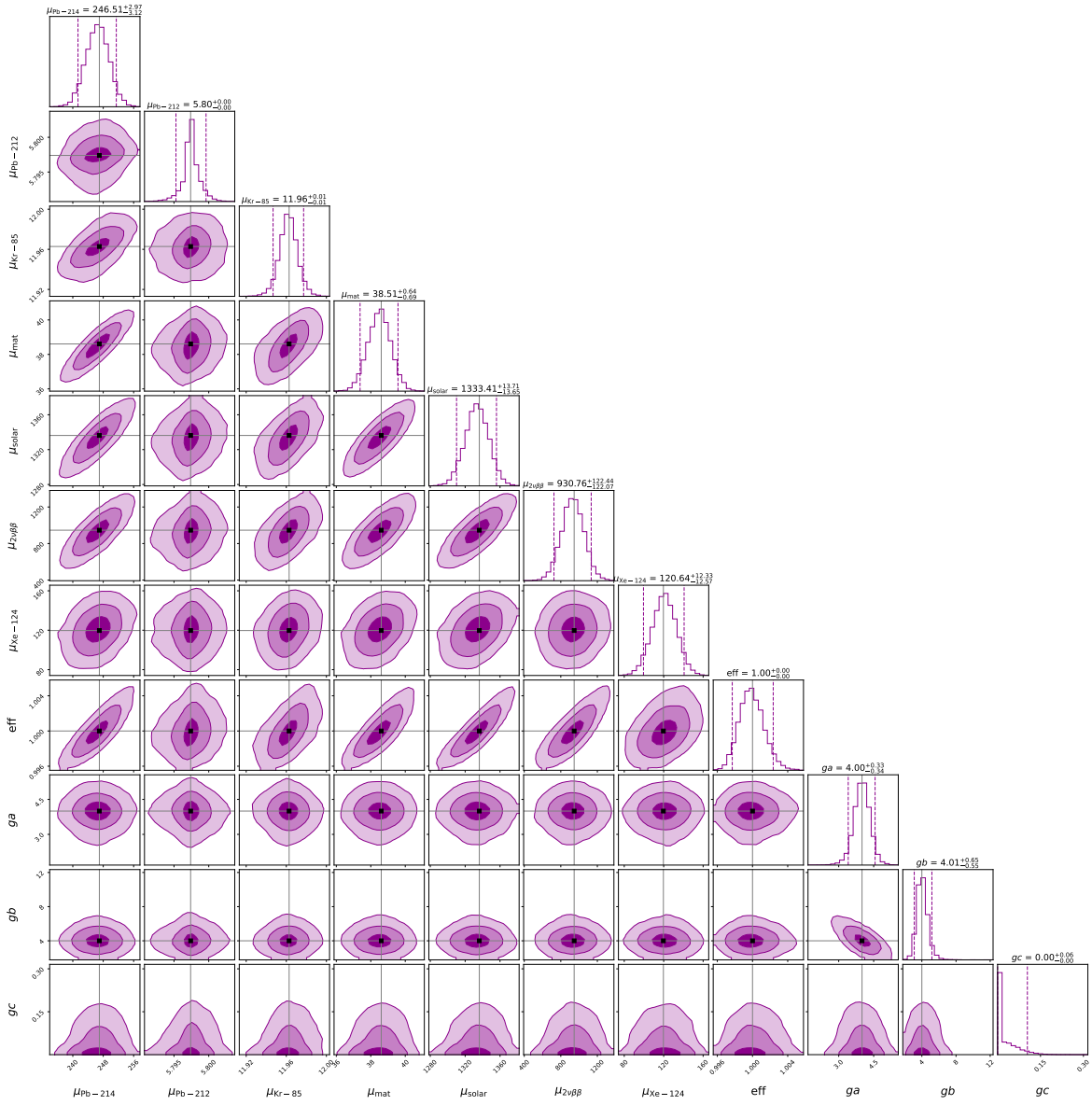

Figure 4.15: Corner plot of the result of the likelihood minimisation for 10,000 toyMCs with values $g_{ae} = 2 \times 10^{-12}$,$g_{a\gamma\gamma} = 2 \times 10^{-10}$ and $g_{an} = 1 \times 10^{-8}$. The plots in the diagonal show the variance of the parameters found to minimise the likelihood function, while the plots outside the diagonal contain information about the correlation between parameters.

Equation 4.16 is minimised. Once the likelihood is minimised, another fit procedure is performed by fixing μ_s, g_{ae}, $g_{a\gamma\gamma}$ and g_{an} on the sampled values in the toyMC. The test given in Equation 4.19 can be calculated from the ratio of the values found in the floating and fixed minimisation procedures. The values found in each minimisation for the thirteen parameters and the test value are saved in

a database. Around 1000 values were scanned, and a computer cluster is needed to perform these calculations. Therefore, the script to perform the minimisation is highly paralleled to occupy all the computation threads allowed in the ScienceCloud cluster, a multi-purpose computing and storage infrastructure of the University of Zurich.
A background-only hypothesis is assumed for the 'observed' dataset, as it represents an experiment without reaching the signal as an upper limit. Two approaches are possible to obtain the median value of the distribution of tests in the case of 'observed' data without signal injected. The first approach relies on performing toyMC as described before and doubling the number of computations required and thus the time. Another possible approach is to use the expected background as an Asimov dataset, i.e. the one dataset in which all observed quantities are set equal to their expected values. This assumption holds in the asymptotic limit, given the Wald theorem [306]. A comparison between the median test from the Asimov dataset and derived from toyMCs were performed for certain choices of signal strength, with a matching outcome. Thus, the Asimov dataset is used to derive the median value of the 'observed' distribution.

4.4.3 Inference results

The results of the inference procedure described previously are presented. For each coupling combination, the values of $g_{ae}, g_{a\gamma\gamma}, g_{an}$ and the test result from Equation 4.19 are retrieved from the database. The test result is compared to the one derived from the Asimov dataset to create an ordering principle based on Equation 4.19. This procedure is performed for each scanned value in the couplings parameter space. The result from the toyMCs for the confidence volume are shown in Figure 4.16 as a 2D projection of the 3D confidence volume in $g_{ae} - g_{a\gamma\gamma}$ with surface levels of g_{an}, since displaying a 3D volume is often unclear. The surface levels show the different values for the third coupling parameter found in the label. The choice of showing a shaded area that represents the projection of the confidence volume on the 2D planes is used in other works. However, it can often hide the values of the third coupling parameter that would allow that limit, which is also valuable information for the interpretation of the plot.
The results show an improvement of approximate factor 4 from the LUX/XENON1T upper limits on the axio-electron coupling g_{ae} [103, 309]. The inclusion of the inverse Primakoff channel in this work allows for setting a limit on $g_{a\gamma\gamma}$ independent from g_{ae} at low g_{ae} values. These limits are, however, far from those from experiments such as CAST at lower axion masses ($m_a < 10$ meV), with a limit of 6.66×10^{-11} at 95% CL [115]. Moreover, the R-parameter, which defines a favoured region from stellar cooling processes, discussed in Chapter 1, is a factor 2 smaller even in the less

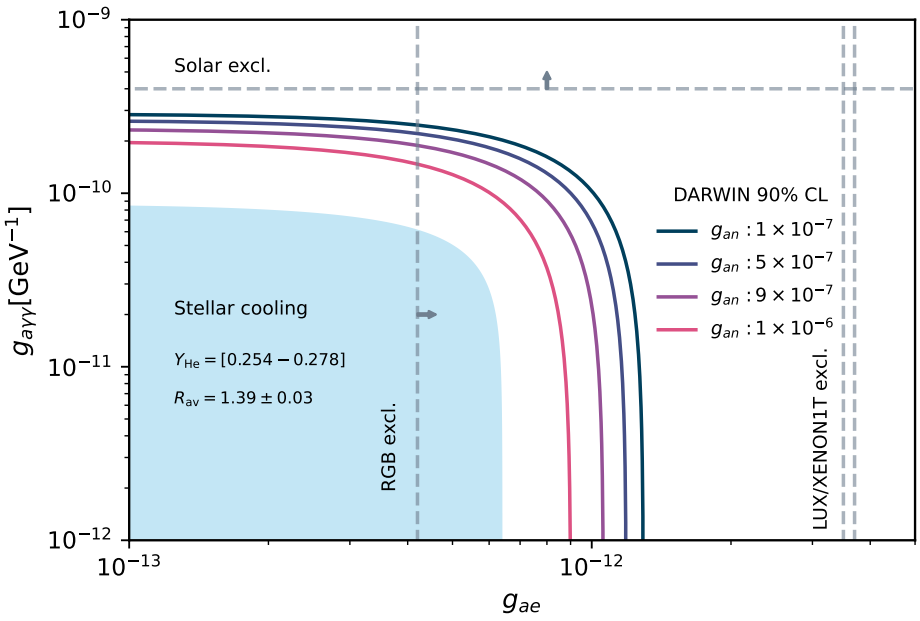

Figure 4.16: Constraints on the coupling parameters g_{ae} and $g_{a\gamma\gamma}$. The solid colour lines indicate surface levels of the confidence volume for the g_{an} coupling parameter. Shown as well are the RGB limit [307], Solar limit [308], XENON1T [103], LUX [309] and stellar cooling limits calculated from Refs. [310, 311, 312, 313].

stringent models for both coupling parameters. Nonetheless, direct detection experiments that can test astrophysical bounds are of great importance, and DARWIN will be able to improve the limits from direct detectors to the axioelectric coupling g_{ae}.

The results at 90% C.L for the coupling of axions to nucleons, g_{an}^{eff}, are shown in Figure 4.17. The limits shown are less constraining than astrophysical bounds in the axion-nucleon coupling by neutron stars and supernova observations, which place the limit to g_{an}^{eff} around 1.1×10^{-9} [314, 315]. The limit placed by CAST at (95% CL) in the search for the axion-nucleon related flux is shown as *CAST-Fe [287]*, where the vertical line at $3.5 \times 10^{-10}\,\mathrm{GeV}^{-1}$ is the limitation due to the detector resolution. The limit was calculated assuming an axion mass of $0.03\,\mathrm{eV}$, where the axion-photon conversion process is coherent and has maximum probability. For higher masses, the loss of coherence provokes a loss in sensitivity for the experiment, and the limit becomes weaker. The limit from the solar luminosity on the axion-nucleon coupling of 3.6×10^{-6} is additionally shown [308]. DARWIN could probe the parameter space beyond the limit placed by CAST, as the nucleon coupling can be investigated simultaneously in the axioelectric and inverse Primakoff production channels and provide a direct measurement which is complementary to the astrophysical bounds without

assuming the underlying model or axion mass.

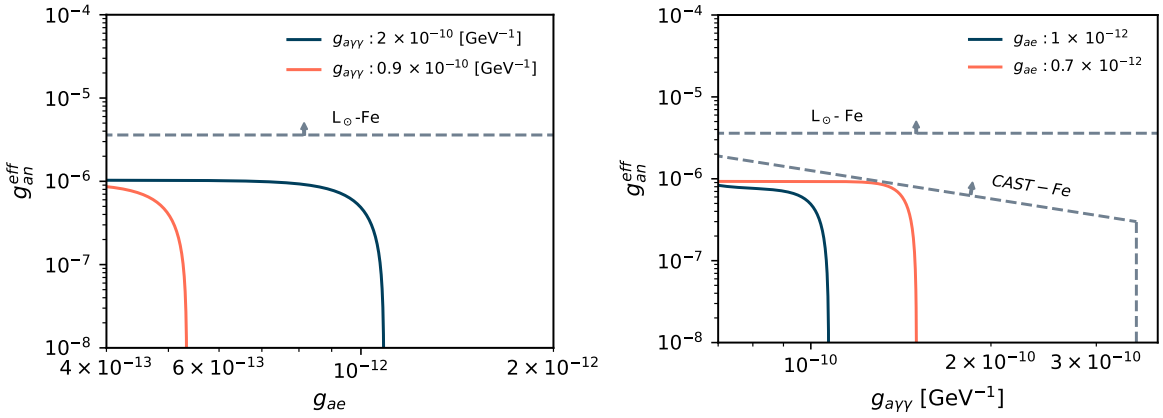

Figure 4.17: Results are marking a 90% C.L. on the coupling of axions to nucleons, g_{an}. Left: Constraints on the axion-nucleon coupling g_{an}^{eff} and the axion-electron coupling, g_{ae}. Right: Constraints on the axion-nucleon coupling g_{an}^{eff} and the axion-photon coupling, $g_{a\gamma\gamma}$. The limits from CAST [287] and from the solar luminosity [308] are shown for comparison.

4.5 Conclusions and remarks

We have found that DARWIN can be sensitive to solar axions, which can be detected via the axioeletric or inverse Primakoff effects in the energy region of 1–20 keV. The largest background in this range is the irreducible solar neutrino background (mainly from the pp-chain) and the $2\nu\beta\beta$ decay of the naturally abundant ^{136}Xe isotope. Given the expected reduction on the ^{222}Rn background, the contribution from ^{214}Pb is approximately only $\sim 14\%$ of the total expected background. Given the scale of DARWIN, the material background contributes negligibly to the ROI of this search for 33 t. We have performed the first study of this kind to set limits simultaneously in the three coupling parameters g_{ae}, $g_{a\gamma\gamma}$ and g_{an}^{eff}, taking into account the correlation between the parameters and implementing the detection channel model for the inverse Primakoff effect in LXe. Other studies have only focused on the first two couplings [292, 293], or have not implemented the correlation between the parameters or the inverse Primakoff effect [103]. This study shows that a 4-fold improvement in the limit placed by previous LXe TPCs can be achieved and provides an independent measurement from the astrophysical bounds placed by RGB energy conservation constraints, which covers a region where no other direct detection experiment reached to date.

The detection efficiency curve $\eta(E_R)$ used in this analysis from Ref. [103] was improved later by the XENON collaboration and used in Ref. [125]. An improvement of this analysis in the future consists

of replacing the efficiency assumption, which will lead to greater detection efficiency in the low keV range, where the axions coming from ABC and Primakoff fluxes could be found in LXe.
As the strongest signals are expected from the signal models proportional to coupling parameters to the power fourth (such as the ABC flux detected via axioelectric effect), improving the limit becomes more challenging. The irreducible neutrino background restricts the achievable sensitivity for LXe TPCs, as most of the expected signal is in the region where pp-neutrinos are expected to become a dominant signal. This is, however, a good sign for neutrino detection and the Sun metallicity open question, as investigated in Ref. [126].

Chapter 5

Design and operation of a liquid xenon purity monitor for Xenoscope

> *Beyond Ghor, there was a city. All its inhabitants were blind. A king with his entourage arrived nearby; he brought his army and camped in the desert. He had a mighty elephant, which he used to increase the people's awe. The populace became anxious to see the elephant, and some sightless from among this blind community ran like fools to find it. As they did not even know the form or shape of the elephant, they groped sightlessly, gathering information by touching some part of it. Each thought that he knew something, because he could feel a part. The man whose hand had reached an ear said: "It is a large, rough thing, wide and broad, like a rug." And the one who had felt the trunk said: "I have the real facts about it. It is like a straight and hollow pipe, awful and destructive." The one who had felt its feet and legs said: "It is mighty and firm, like a pillar."*
>
> **— Ancient Sufi story**

> *This ancient Sufi story was told to teach a simple lesson but one that we often ignore: The behavior of a system cannot be known just by knowing the elements of which the system is made.*
>
> **— Donella H. Meadows**
> (Thinking in Systems, 2008)

We have discussed in the Chapters 3 and 4 some examples of the science reach of DARWIN for low and high ER energies, respectively. DARWIN will comprise a large and complex system, and its realisation will require the demonstration of different technologies. For this purpose, a full-scale demonstrator in the vertical dimension, called Xenoscope, was built at the University of Zurich [316], introduced in Chapter 2. The Xenoscope program consists of designing, commissioning and operating a $2.6\,\mathrm{m}$ TPC that will serve as a demonstrator, in the vertical dimension, for DARWIN. The facility goals are the study of the drift of electrons over this length and the test of new technologies for DARWIN. In addition to demonstrating electron drift over $2.6\,\mathrm{m}$, Xenoscope will provide information about TPC properties that are needed in order to build a larger detector. For example, the longitudinal and transverse diffusion (parallel and perpendicular to the drift, respectively) of electrons can be studied by measuring the spread of the signal after drifting electrons. Diffusion studies are important, since a higher spread of the signal can affect, for example, the efficiency of the detector to resolve multiple scatters. In addition, the Rayleigh scattering length in LXe given different detector conditions (such as xenon purity) will be studied as well.

In this chapter, we will focus on the modular design of a $2.6\,\mathrm{m}$ long field cage of the TPC for Xenoscope. This design was used to produce the components of the field cage and to build, commission, and operate a Purity Monitor (PM) of $53\,\mathrm{cm}$. The PM provides a measurement of the achievable electron lifetime τ_e, which is the mean time for the charge to drop by a factor of e [317]. The electron lifetime is related to the charge signal degradation in LXe TPCs, as the electrons can be trapped by impurities. The chapter is divided as follows: Section 5.1 provides an overview of the Xenoscope facility and the xenon purification system. Section 5.2 describes the electrical and mechanical design of the field cage for the $2.6\,\mathrm{m}$ long TPC. Section 5.3 describes the working principle of liquid xenon PMs and the design, characterisation, and assembly of a $53\,\mathrm{cm}$ PM for Xenoscope. Section 5.4 describes the electron lifetime measurements in Xenoscope by operating the PM, and shows further studies of transport of electrons in LXe. Finally, Section 5.5 summarises the work and its implications and gives an outlook on the upgrade to a TPC for Xenoscope and future studies.

5.1 The Xenoscope facility overview

The facility infrastructure was designed, constructed and assembled in the assembly hall of the Department of Physics at the University of Zurich. The facility is composed of a structural support, a xenon cooling system, a purification line, a storage system with bottles, two recovery systems, and a detector housed in a double-walled cryostat. Figure 5.1 provides an overview of the facility and the different systems that compose it. These systems are described in great detail in Ref. [316], whereas this work focuses on the detector side for Xenoscope. The design, commissioning and operation of it was the work of three different PhD thesis [197, 318], including this work.

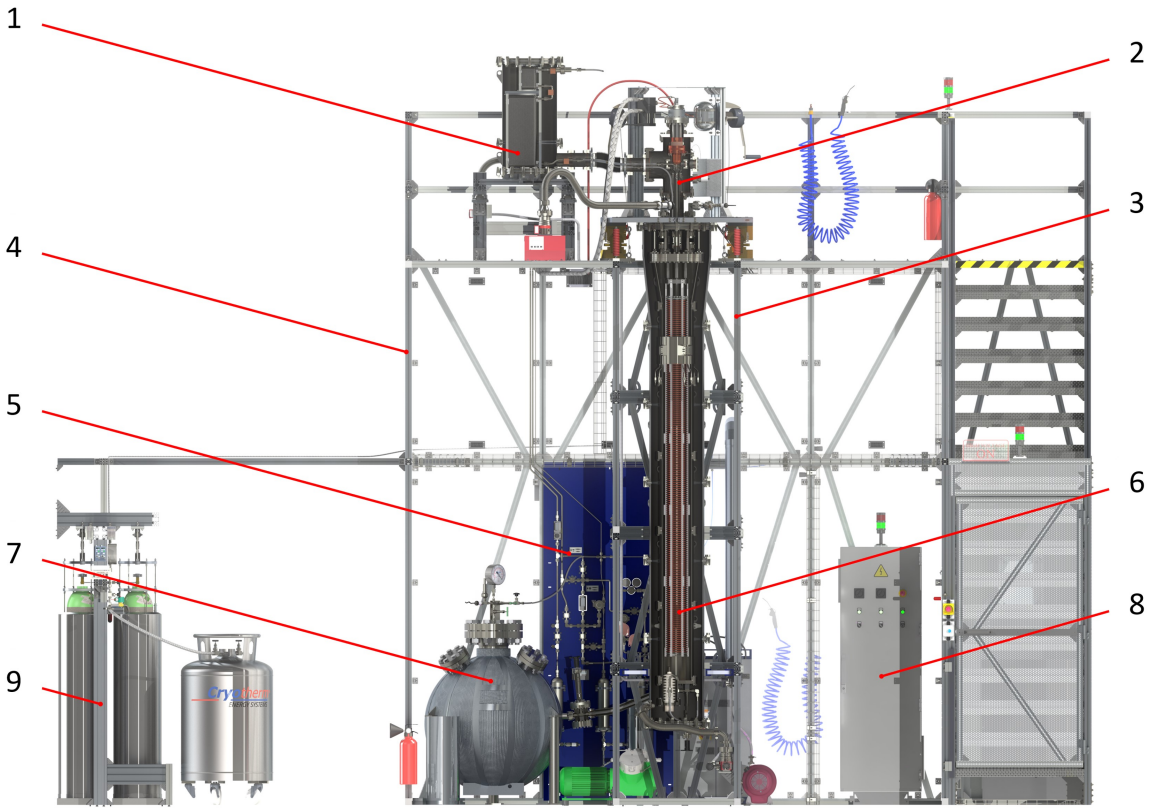

Figure 5.1: Schematic view of the Xenoscope facility with the 2.6 m TPC installed in the cryostat. Legend: (1) Heat exchanger, (2) Cooling tower, (3) Inner frame, (4) Outer frame, (5) Purification gas panel, (6) TPC in the 24.8 cm diameter and 312 cm height cryostat, (7) High-pressure storage vessel of liquid recovery system, (8) Power distribution cabinet, (9) Gas recovery and storage system. Figure from Ref. [316].

The structural support consists of 50 mm × 50 mm extruded aluminium profiles, assembled to provide an enclosed room to minimise dust exposure and an additional floor at the height of the top of the

cryostat for assembly and operation purposes. The upper level can be accessed by a staircase, which during operation with high voltages is secured to prevent access to it and the space dedicated to the HV power supply. The assembly hall is served by a crane that can withstand up to 4-tonne weight, a water cooling system and a ventilated storage closet for gas bottles. The structure supports the top flange assembly of the cryostat. An engineering study was carried out to foresee issues with the thermal and mechanical conditions of the top flange and the cryostat, as the bottom half of the flange can cool down to temperatures around those of LXe. The top flange contains six feedthroughs that host the cooling tower, cabling and instrumentation, joined by six axial displacement bellows. Figure 5.2 shows a render of the top flange in Xenoscope.

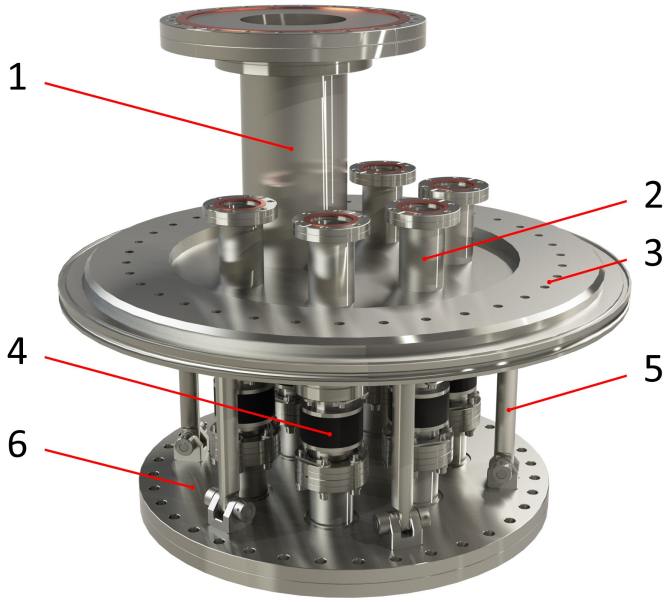

Figure 5.2: Top flange assembly of the cryostat. Legend: (1) Cooling tower feedthrough, (2) Instrumentation feedthroughs, (3) ISO-K500 flange, (4) Axial displacement bellows, (5) Swivel rods, (6) DN350CF flange. Figure from Ref. [316].

The inner vessel is composed of six DN250CF[1][2] sections, with a total usable height of 312 mm and a usable diameter of 248 mm each, and the system can withstand together up to 400 kg of xenon. A conical section that acts as an expander for the inner vessel is placed from the top flange to the next section in the gas phase. It provides enough space for assembly and connections. The outer

[1]ConFlat flanges, that use a oxygen-free high thermal conductivity copper gasket and knife-edge flange to achieve an ultrahigh vacuum seal

[2]DN: ISO 6708 norm for nominal pipe diameters

vessel is composed of six K-400[3] sections. The cooling tower and heat exchanger is responsible for the xenon liquefaction and thermal stability. The cooling tower consists of a cold head connected to an Iwatani PC-150 Pulse Tube Refrigerator (PTR), rated 200 W cooling power at 165 K, that liquifies the gas xenon and controls the temperature of the system [319]. The heater is controlled with a proportional–integral–derivative (PID) controller connected to four PT100 Resistance Temperature Detectors (RTDs) screwed on the side of the cold head. Two heat exchangers were designed and assembled to provide additional cooling power while minimising the heat leak from cold outgoing and warm incoming GXe [320]. Heat exchangers allow for the transfer of heat between the two (in/out) xenon streams: the outgoing xenon stream, that needs to evaporate to enter the purification system, absorbs the heat from the incoming gas, which is at warmer temperature. Thus, the incoming stream gets cooler and the outgoing stream gets warmer. This provides additional cooling power to the system, as PTRs cooling power is limited. Additionally to the heat exchanger and cooling tower, a pre-cooler system is placed around a section of the inner vessel, where liquid nitrogen (LN) can be circulated through a system of pipes. This additional cooling provides a method to bring the detector from closer to LXe temperatures and reduces the time needed to fill the detector by a factor ~ 3. Inside the detector, a funnel siphons the xenon out to be carried through the purification system. The gas is then recirculated through the purification system using a double diaphragm compressor. The xenon purifier is a hot metal getter[4] [321]. A flow controller is placed before the compressor, and a flow meter is further downstream in the system. The xenon extraction line is protected by a $40\,\mu\mathrm{m}$ metal strainer element, while on the supply line, a $3\,\mathrm{nm}$ ceramic filter is placed.

The storage system consists of an array of aluminium bottles suspended from the top, with a mass sensor incorporated. A slow control monitors the subsystems. The slow control consists of readouts connected to the sensors, which can be displayed in a Grafana dashboard. A check valve is placed for cases of emergency, in which case it will allow for the gas in the system to be transferred to a gas bottle. This gas bottle is always maintained empty and cryopumped in case of emergencies. The recuperation of the xenon from the detector is performed partially with a spherical pressure vessel called BoX (Ball of Xenon), connected to the bottom flange of the cryostat. The concept behind this element is that the liquid will flow automatically from the cryostat given gravity, once the valve is opened, to BoX. Liquid recuperation is more effective the higher the liquid column is in the cryostat. Hence, it is used to partially transfer the total mass in the detector. The last kilograms are removed by evaporating the LXe and transferring it to a cryopumped bottle, where the mass sensors provide information about the mass transferred to the system. Nonetheless, liquid recuperation allows for

[3] ISO-K or K flanges are joined with double-claw clamps, and clamp to a circular groove on the flange.
[4] In a getter, gaseous impurities irreversibly bind and diffuse into the purification cartridges.

the recovery of tens of kilograms per hour, while the gas recuperation time is more prolonged ($\sim 40\,\mathrm{kg/d}$).

A power distribution cabinet connects all the electrical components. In case of an electric grid delivery failure, an Uninterruptible Power Supply (UPS) of $20\,\mathrm{kW}$ can provide the necessary power to operate necessary detectors until the emergency system of the institute turns on. A Heinzinger PNC 100000-1 [322] power supply allows for voltages up to $100\,\mathrm{kV}$, with a maximum current of $1\,\mathrm{mA}$. This power supply is connected to the cathode at the bottom of the TPC, to provide the design electric field up to $200\,\mathrm{V/cm}$.

Due to the aimed drift length, the design of the detector was conceived in an modular approach: the field cage consists of five modules, that together compose the total drift length of $2.6\,\mathrm{m}$. Three different lengths for the field cage will be operated, to troubleshoot different aspects of the system such as xenon purification and field homogeneity. In the first phase, electrons were drifted in a $53\,\mathrm{cm}$ long Purity Monitor (PM) fully immersed in LXe, with the use of only one module of the total field cage. In the second stage, the PM will be upgraded to a dual-phase $1\,\mathrm{m}$ tall TPC with liquid level control. The gas region with a high electric field will allow for the extraction of electrons from the liquid into the gaseous phase, thus generating electroluminescence and providing amplification. An array of photosensors will be placed at the top to detect the resulting charge proportional light signal. Finally, the field cage will be extended to its final length to host a dual-phase TPC. The three detector phases are shown together with the cryostat in Figure 5.3.

As the cathode is fully immersed in LXe (as seen in Chapter 1), there are some challenges in creating a cryogenic liquid feedthrough that delivers the HV from the power supply to the cathode. The feedthrough should not leak or deform the electric field in the drifting region. An option is to introduce it from the top flange, going from the gas phase to the liquid phase [323], placing it in the outer non-instrumented region of the TPC. Since the FSRs at the top section drop their potential until they reach 0 V in the gate electrode and the cryostat walls are at ground potential, the conductor needs a strong insulator covering and a conductor shielding (at ground) to prevent discharges. The initial design of the feedthrough for the Xenoscope TPC consisted of a SS rod cryofitted[5] with an insulator made of Ultra High Molecular Density Polyethylene (UHMDPE). This design coming from the top flange was used in XENON1T/nT [324], and in LAr in ICARUS [323] and ProtoDUNE [325], while the LZ experiment utilizes a feedthrough connecting through the side of the cryostat [326]. A 3D

[5] Cryofitting is the process in which the inner conductor rod (HV) is placed inside an insulator, and both placed inside an outer conductor (ground), and cooled down to LN temperatures. The different thermal expansion coefficients of the materials ensure the vacuum tightness between inner conductor, insulator, and outer ground.

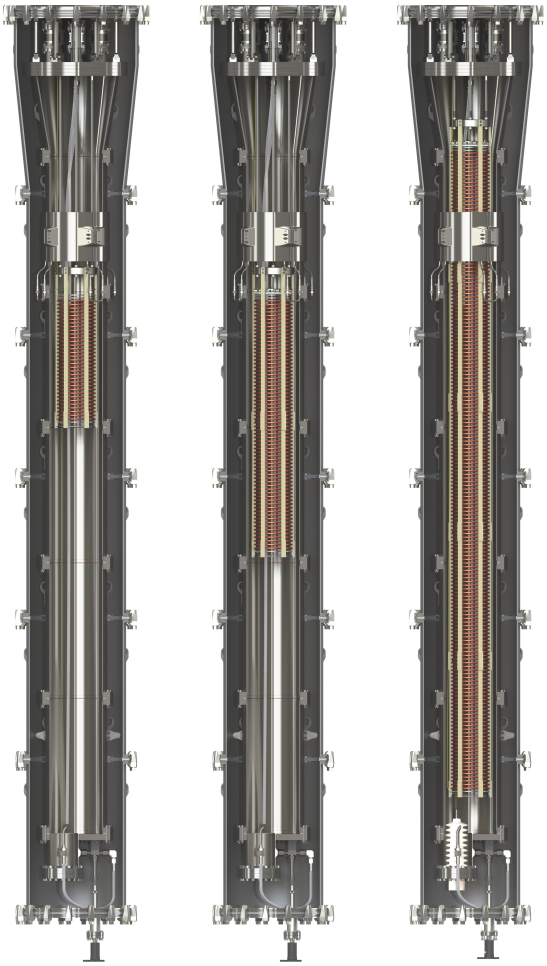

Figure 5.3: The three phases of Xenoscope. From left to right: purity monitor, $1.0\,\mathrm{m}$ tall TPC, $2.6\,\mathrm{m}$ tall TPC. All three phases are built by assembling a number of the field cage modules. The goal of the three phases is to measure the purity of xenon and the homogeneity of the drift field gradually, upgrading the detector with photosensors and a gas-liquid interface. The purity monitor uses two charge readouts, while a photosensor array replaces the top charge readout in the $1.0\,\mathrm{m}$ and $2.6\,\mathrm{m}$ TPCs. Figure from Ref. [316].

drawing of the termination of the design feedthroughs and their components are shown in Figure 5.4. The implementation of this type of feedthrough is considered in the next section, where electric field simulations for the design of the field cage will be described.

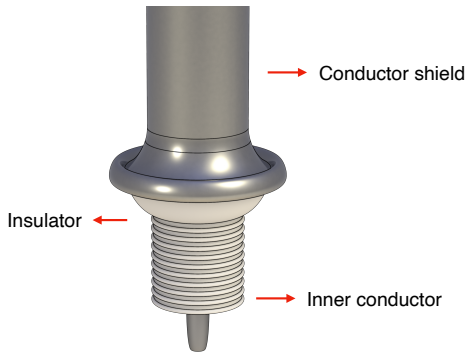

Figure 5.4: HV feedthrough termination for the standard design coming from the top flange of the cryostat to the cathode. This type of feedthroughs consists on an inner conductor at HV, an insulating material with corrugated surface to prevent surface charges, and a conductor shield at ground potential surrounding both to prevent deformation of the electric field in the drift region.

5.2 Design of the field cage for a 2.6-m time projection chamber

A field cage is essential in order to drift electrons over distances without charge loss due to diverging electric field lines. The field cage followed the modular cryostat design, allowing for the operation of the facility in smaller drift regions by assembling a reduced number of its modules. Figure 5.5 shows the design for the first section of the field cage of $53\,\mathrm{cm}$, which can be extended with four additional modules to complete the $2.6\,\mathrm{m}$ field cage.

The design consists of four modules of $525\,\mathrm{mm}$ height, and one top module of $530\,\mathrm{mm}$, that define an inner diameter of $15\,\mathrm{cm}$. The field cage consists of a cathode, 173 field shaping rings that confine the electric field in the drift direction (FSRs, see Chapter 2), a gate electrode, and an anode that extracts the ionisation proportional signal from the GXe phase. The design of the field cage includes Oxygen-Free High Conductivity Copper (OFHC) for the FSRs, selected due to its low oxygen content and good conductivity. Six support pillars, made of PAI (polyamide-imide), are selected instead of the usual choice of PTFE due to its tensile strength, chemical stability, low outgassing and a higher dielectric constant [327]. Interlocking PTFE blocks hold the copper FSRs in place against the PAI pillars. A SS ring, connected with SS rods to the top flange, holds the six support pillars. Resistors in between the FSRs provide the potential drop to confine the electric field in the drift direction.

The diameter of the field cage is limited by the previously discussed concept design of the HV feedthrough that would traverse the drift region from the top flange to deliver the HV to the cathode. Additionally, the TPC is off-center by $20\,\mathrm{mm}$ with respect to the cryostat, to provide enough space for the HV feedthrough and maximize the sensitive LXe volume. Since the LCE[6] is expected to be low

[6]Defined previously as the mean light collection efficiency of the photosensors for photons emitted in the sensitive

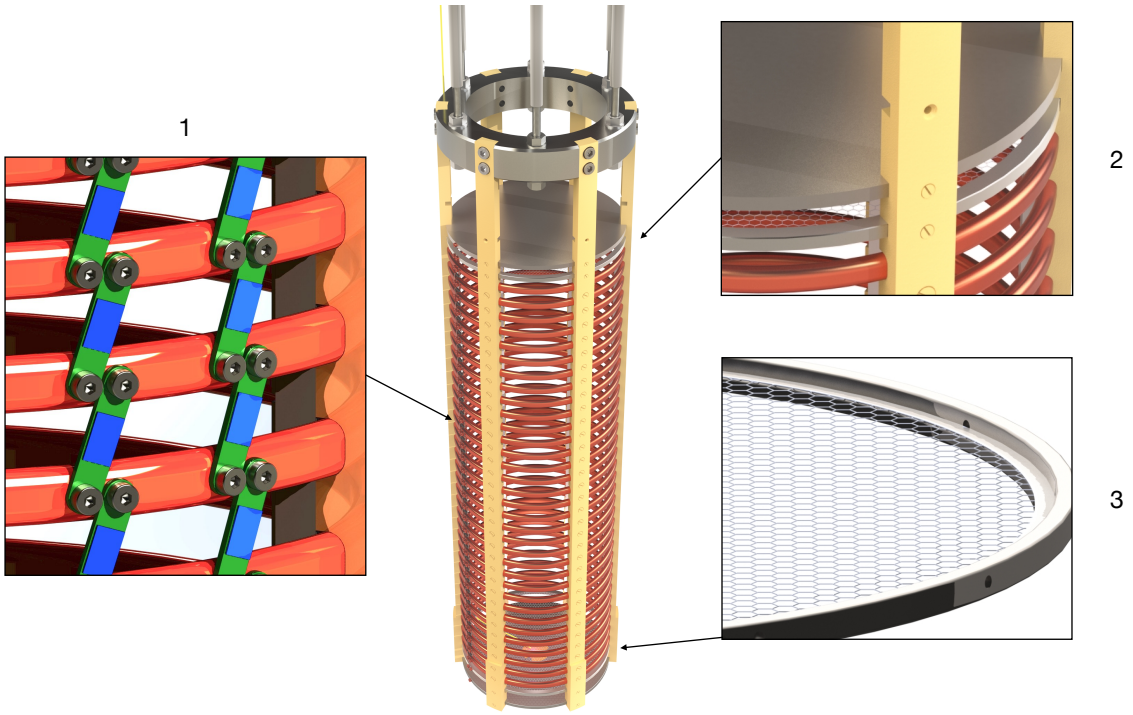

Figure 5.5: First section of the 260 cm field cage. The 53 cm module consists of a SS ring, supported by six SS rods connected to the top flange, and hold in place the six PAI pillars. The PAI pillars constrain the electrodes, made of SS, and the FSRs, made of OFHC, in place. Interlocking PTFE blocks prevent further motion of the components, which results in a mechanically robust module. Zoom 1: FSRs and the resistor chain. Zoom 2: Electrode grid and anode, where the pillars contain additional slots to place a photosensor array in the upgrade to a TPC, above the anode. Zoom 3: Electrode holder and hexagonal patterned mesh.

due to the aspect ratio of the TPC[7], the initial design does not include PTFE reflectors. Nonetheless, it was a requirement in the design to include the possibility of an upgrade to include reflector panels on the sides. After accounting for these constraints, a preliminary mechanical design was defined. In the design of the TPC, the electric and the mechanical designs are not independent of each other, and the materials and geometries are selected taking into account this feedback.

5.2.1 Electric field simulations for the field cage

The field cage was modelled and developed using COMSOL Multiphysics [328], a simulation software that for allows static and dynamic simulations of electromagnetic interactions between materials.

volume.

[7]LCE depends on the coverage of the solid angle of the photons emitted in a interaction, and hence, in the aspect ratio: Height/Width $\sim$ 16.

The double-wall cryostat, HV feedthrough, the FSRs and the support pillars were modelled in a simplified 2D geometry with a cut plane on the centre of the cryostat. The materials used can be specified in COMSOL by giving their electrical properties and densities. Table 5.1 shows the relative permittivity values assumed for the dielectric materials.

Table 5.1: Relative permittivity (ϵ) values of the dielectric materials assumed for the electric field simulations in COMSOL.

Material	ϵ	Reference
LXe	1.84 (1.93 at the triple point)	[329]
GXe	~ 1	[329]
UHMDPE	2.3	[323]
PTFE	2.1	[330]

The space and shape of the FSRs are optimised by means of electric field simulations. As seen in other works [331], the optimal configuration for the drift field consists of a ring with a flat side facing the drift volume, while softening the borders to avoid charge accumulation. The design of the FSRs consists of 7.5 mm high and 5 mm wide rectangular section with 2.5 mm chamfers to smooth the corners. Each ring is separated by 15 mm in the vertical direction from centre to centre, ensuring a homogeneous drift field across the full drift length. Figure 5.6 shows a plane cut of one FSR, exhibiting an elliptical shape.

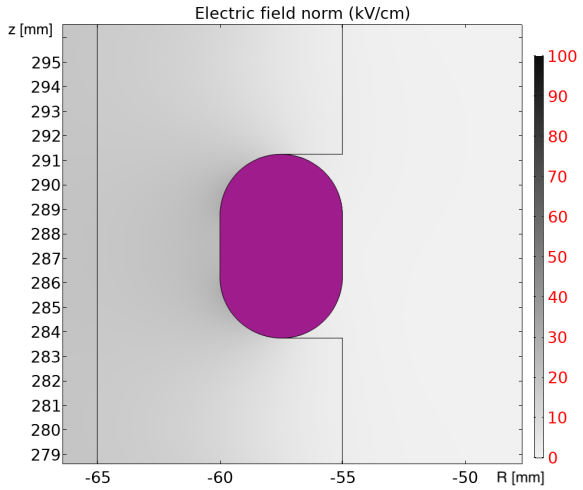

Figure 5.6: Planar cut of the field shaping ring implemented in COMSOL, the flat side facing the inner volume confines the electric field in the drift direction, while the rounded parts prevent electric field lines accumulation. Left Axis: Electric field norm [kV/cm].

The complete geometry implemented in COMSOL is shown in Figure 5.7, where the colour gradient in the surfaces indicates the electric field norm, and the magenta lines represent the electron drift path or field lines from cathode to anode. Overall, the electric field norm stays below the $50\,\mathrm{kV/cm}$ threshold estimated in the LXe, above which sparks could occur [332].

The simulations also show that a HV feedthrough design from the top flange deform the electric field lines in its vicinity. One solution to avoid deformation of the electric field lines consists of extending the conductor shield to cover more of the inner conductor. The ground, terminated in a lower position where the FSRs have a higher surrounding electric field, entails challenges in its fabrication and assembly. The ground termination shape introduces a challenge by itself, as it can produce a high electric field, influencing the drift field inside the field cage. In the work performed for the ICARUS experiment in Ref. [333], a solution in LAr consists of incorporating a gradual departure from the insulator, by defining an ellipsoidal shape in the termination that avoids sharp corners (See Figure 5.4). A similar design was implemented in COMSOL simulations for Xenoscope, as shown in Figure 5.8.

However, the constrained space inside the cryostat and detector limits the design of the ground termination, and the ground termination introduces a deformation of the drift field, as shown in Figure 5.9. This effect and the increasing complexity when the ground termination needs to be extended, motivated the purchase of a commercial HV feedthrough rated for $-100\,\mathrm{kV}$ from Ceramtec [334], which will be placed on the bottom of the cryostat. Such an HV feedthrough can sustain the pressure column from LXe and has proved in other LXe setups not to leak [335]. The insulation consists of alumina ceramic, a well-known insulator for HV. Unfortunately, this material cannot be used in the current LXe TPCs due to its radiopurity levels. The geometry of the Ceramtec HV feedthrough was implemented in COMSOL, as shown in Figure 5.10, where its overall good electrical properties are visible.

Although simplified in the COMSOL simulation as wires, the electrode mesh design was chosen as a hexagonal mesh. The mesh is mounted on a SS ring supported by the IPA pillars. This type of mesh provides a better solution against the sagging of electrode wires, and the focusing of electrons towards the hexagon centres provides additional information for position reconstruction algorithms, as seen in Ref. [336]. Other experiments have used as well hexagonal meshes for electrodes [191, 337, 336]. The design of the mesh can be seen in Figure 5.11, together with a simulation of the focusing effect of the hexagonal meshes on the electron population.

The simulations performed provided information for the design of FSRs and their spacing, in order to produce an homogeneous drift field in the volume. The simulations have also shown that due to the restrictions in space inside the cryostat, a HV feedthrough coming from the top represents a greater

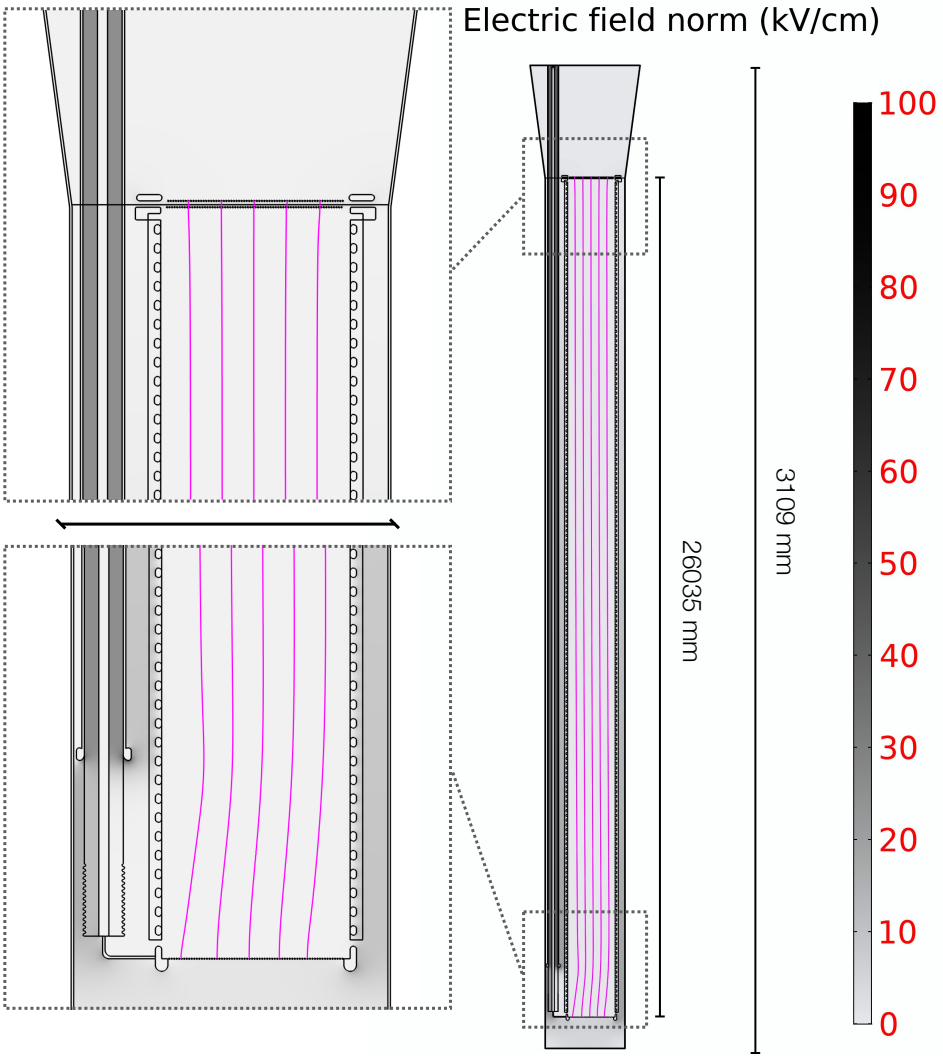

Figure 5.7: Implementation of the TPC design inside the cryostat in COMSOL. The colour gradient indicates the norm of the electric field inside the TPC. The electric field inside the drift region is optimised to be homogeneous along the z-coordinate inside the TPC. All regions are below the chosen $50\,\mathrm{kV/cm}$ limit for the electric field norm [332]. Right: Overview of the full $2.6\,\mathrm{m}$ TPC. Left Top: Zoom into the top section of the TPC, where the extraction field, GXe/LXe, electrodes (gate and anode), FSRs and top conical section of the cryostat were modelled. Left Bottom: Zoom into the bottom region, where the termination of the HV and the shape of electrodes carrying HV are optimised to reduce the magnitude of the electric field, avoiding sharp edges.

challenge due to its influence on the homogeneity of the drift field. The design of this type of HV was postponed to a later stage.

After the electrostatic requirements for the field cage were obtained, the mechanical design was

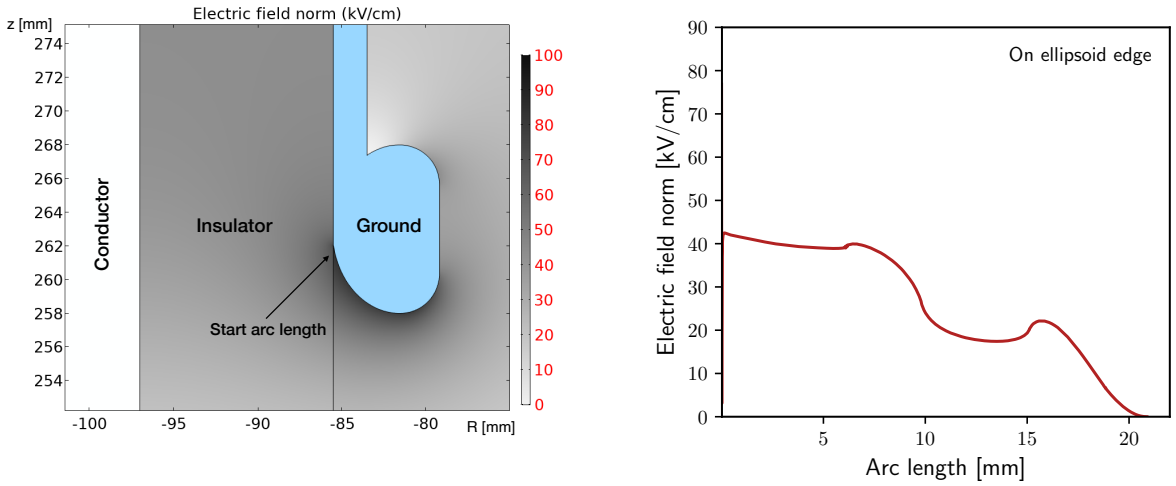

Figure 5.8: Left: Ground termination of the HV feedthrough coming from the top flange. To prevent the formation of a high electric field in the LXe around, the ground termination shape was softened to recreate a gradual departure curve from the insulator with a rounded shape for the borders. Right: Electric field norm on the arc length of the ground termination of the HV feedthrough.

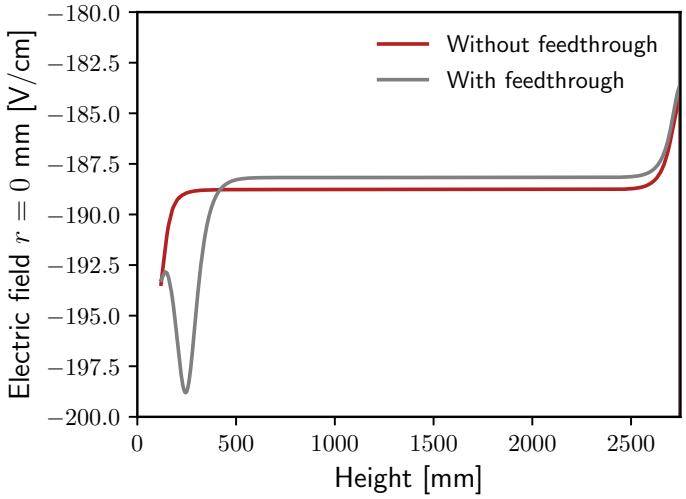

Figure 5.9: Comparison of the electric field in the z-direction for a model with a HV feedthrough coming from the top flange and a model without HV feedthrough, for the center of the TPC. The position where the HV ground termination is shows a deformation in the electric field.

implemented as a CAD[8] drawing in SolidWorks [339]. This software allows for the production of 2D technical drawings from 3D modelled objects, that mechanical workshops and companies require to produce components. Additionally, the software allows to perform mechanical simulations, which is

[8]Computer-aided design

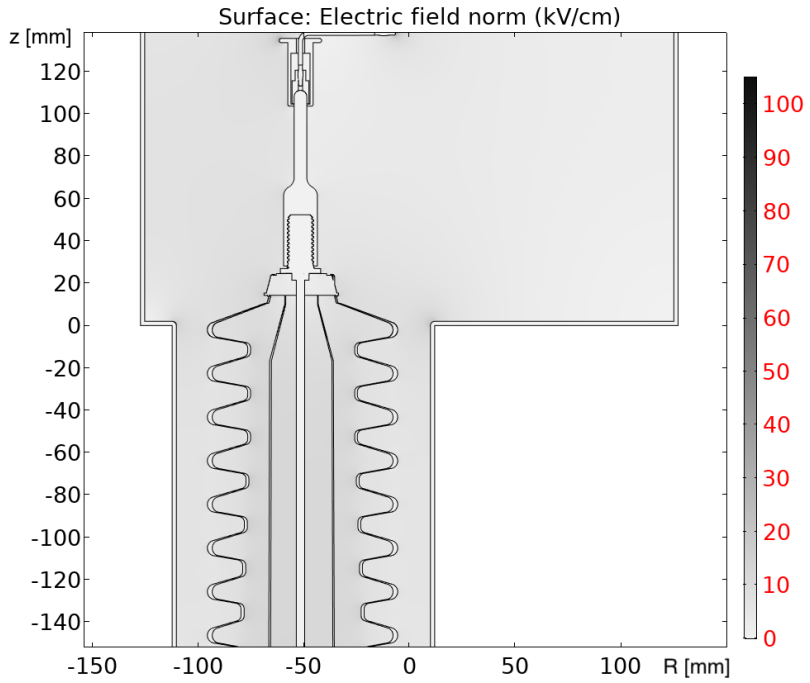

Figure 5.10: Implementation and simulation results of the commercial HV feedthrough from Ceramtec in COMSOL. The electric field is substantially lower compared to the standard HV feedthrough design.

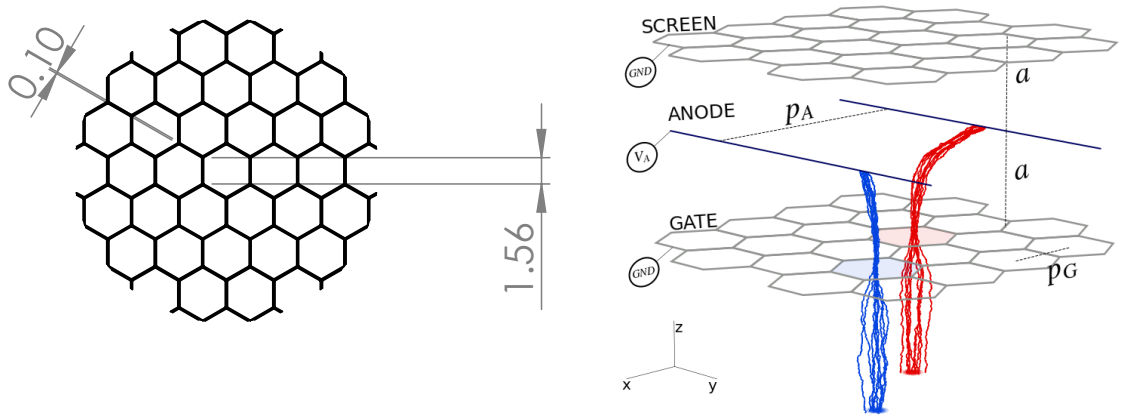

Figure 5.11: Left: Mesh design for the electrodes as an hexagonal grid, which has an effect of focusing the electrons in the center point of the hexagons. Right: Simulations of the focusing effect of the electron cloud due to the distribution of the electrodes. Drift lines correspond to two electron clouds being funnelled by two different mesh hexagon. The screen electrode refers to a grid placed to shield electrically the photosensor array. Figure from [338].

advantageous as the field cage needs to sustain the weight of the FSRs, pillars, and electrodes. Static simulations confirmed the robustness of the design from the strength of the support components when connected to the top flange.

5.3 Liquid purity monitor design

The detector was operated as a first phase with only one module of the total field cage as a PM, to measure the concentration of impurities diffused in LXe. This first stage allows to benchmark and troubleshoot different characteristics of the system, such as the purification in the recirculation of the gas and the electric field stability in the field cage. The working principle of PMs is by charge production followed by a measurement of charge deficit after a known exposure to the LXe. The charge deficit is the result of electrons being captured by electronegative impurities in the LXe. Typical impurities in commercially available xenon consist of ppm[9] levels of O_2, N_2, H_2O, as well as other organic molecules. Table 5.2 shows the concentration of various impurities in xenon in one of the acquired bottles, provided by Carbagas [340].

Table 5.2: Concentrations of impurities in the xenon purchased. Information from Carbagas [340].

Gas	Required Concentration	Measured concentration Vol-ppm
Krypton	<5	<5
Argon	<1	<1
Nitrogen	<1	<1
Water	<1	<1
Hydrocarbons	<0.1	<0.1
Oxygen	<0.5	<0.5
Tetrafluormethane	<0.5	<0.5

An important aspect for the purity of LXe is the outgassing of the detector materials. As observed in Chapter 2, materials are continuously outgassing ^{222}Rn, introducing impurities to LXe that need to be removed with an online purification system (see Ref. [189]). As discussed in Chapters 3 and 4, ^{222}Rn represents a background in LXe TPCs. Water and organic molecules are often found as well in the surface of materials. Thus, detector materials are often placed in vacuum and warmed up, in a process known as *baking*, to evaporate the dissolved impurities in their surface at a faster rate [341]. Moreover, the outgassing rate depends on the medium where the materials are exposed and temperature, with different values for GXe, LXe, and vacuum. The outgassing of electronegative impurities

[9] Part-per-million, 10^6 in scientific notation

contributes to the degradation of the ionisation-proportional signal. The electron cloud population is decreased by the electron capture from electronegative impurities, and the charge signal reaching the gate electrode of the detector is reduced. The complexity of the subsystems in a LXe detector and the interaction between them deem the design of these systems as non-trivial.

The concentration of impurities diffused in the xenon target can be measured either in gas or in liquid. A past measurement in gas consisted of a tungsten filament heated up to produce thermionic emission (i.e. electrons), which are drifted towards an anode where the current can be measured [342]. However, GXe can contain a different impurity concentration than its liquid phase due to the different outgassing rate of materials. This section will refer to an implementation in LXe, and it will refer to the system simply as PM, without mentioning the material phase. The design of the PM explained in this chapter has been implemented similarly in experiments such as ICARUS [343], ProtoDUNE [344] and XENONnT [345]. Figure 5.12 shows the conceptual design of the PM and signal acquisition. Free electrons are produced by incident photons on the cathode material due to photoelectric effect, where the photons are generated in a xenon gas-discharge lamp. An optical fibre transmits the light from the xenon flash lamp, which is triggered by a pulse generator. Due to its double-function as signal source and electrode, the cathode is often referred in a PM as photocathode. The four electrodes define three drift regions: cathode (or photocathode), cathode grid, anode grid, and anode. The population of photoelectrons induces a current signal in the photocathode as they drift towards the first screening mesh (cathode grid), producing a maximum once it enters the second drift region. These electrons are drifted towards the anode at the top by the applied drift field. When the electron cloud reaches the third drift region, a second signal is acquired at the anode as the electrons move away from the second screening grid (anode grid), until they are fully collected. The cathode and anode grids are meshes with high transparency to electrons ($\sim 93\%$), while the photocathode and anode are solid disks. The solid anode and cathode disks allow the electrons to be 'collected', and prevents further induced current detected in the electrodes. The cathode and anode grids screen the photocathode and anode electrodes from observing the charges in other drift regions. Without the screening, the linearity between drifting charges and current induced would be affected, and the pulse duration would be extended in time. Two pre-amplifiers read out the currents induced in the photocathode and anode, and an oscilloscope acquires these signals. The flash of the lamp provides a clear trigger for data acquisition.

The charge deficit depends on the exposure to the LXe and can be modelled as a decaying exponential

$$N(t_{\text{drift}}) = N_0 \, \mathrm{e}^{-t_{\text{drift}}/\tau} \, , \tag{5.1}$$

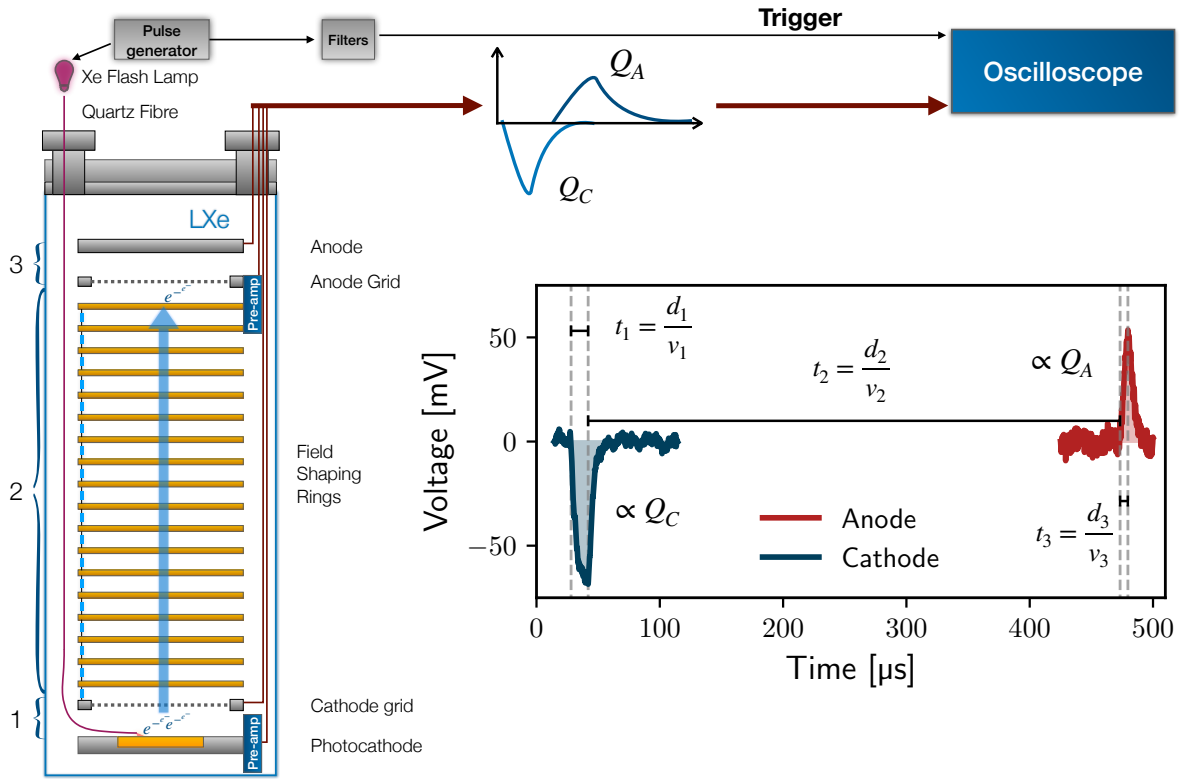

Figure 5.12: Working principle of a purity monitor (PM) and concept design of the signal acquisition: a pulse generator triggers the flash from the xenon lamp, where the light is transmitted, through an optical fibre, inside the cryostat. The fibre points to the photocathode, and the light produces photoelectrons, which are drifted through three different regions. In region 1, a current is induced in the photocathode by the drifting charges. The signal in the photocathode ends when the last electron enters region 2. The electrons continue drifting towards region 3, and they induce a current on the anode. The currents induced in the photocathode and anode are readout. The signal sent to the xenon lamp is used as a trigger for the data acquisition (oscilloscope).

where t_{drift} is the drift time, N_0 is the initial number of charges, and the lifetime τ is related to the electronegative impurities by

$$\tau = \frac{1}{\sum_i k_i n_i} , \tag{5.2}$$

where k_i is the attachment rate specific to the impurity type in units of volume per time (usually given in L/(mol s)), n_i the impurity concentration in units of inverse volume (mol/L) and the sum extends over the different electronegative species. The attachment rate coefficient depends on the electric field strength and the impurity species. Figure 5.13 shows the electron attachment rate in LXe for O_2 and N_2O. An O_2 concentration of less than $0.2\,\text{ppb}$[10] is necessary to successfully drift

[10]By assuming the value for the attachment rate (averaged to all electronegative species) of $K = 2 \times 10^{11}\text{M}^{-1}\text{s}^{-1}$,

electrons across the full length of the TPC [346].

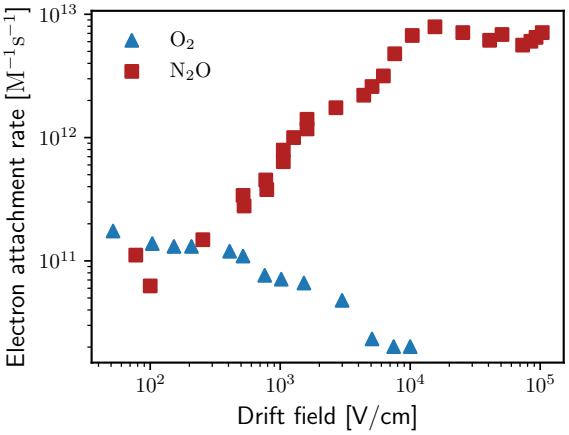

Figure 5.13: Attachment rate of electrons in LXe to electronegative impurities at 165 K for O_2 and N_2O per molar concentration (M) per second. Data from Ref. [346].

Both charges are readout by the pre-amplifiers and the time between the two signals, which corresponds to the drift time accordingly to the electric field applied, can be used to estimate the electron lifetime as

$$\tau \approx \frac{1}{\ln Q_{\mathrm{A}}/Q_{\mathrm{C}}} \left(t_2 + \frac{t_1 + t_3}{2} \right), . \tag{5.3}$$

The parameters Q_A and Q_C are the charges measured in the anode and photocathode, respectively, t_1 is the rise time of the first signal, t_2 is the time between the maximum of the signal in the cathode and the start of the rise of the signal in the anode, and t_3 is the rise time of the signal in the anode, as shown in the schematic from Figure 5.12. The second factor corresponds to the drift time

$$t_{\mathrm{drift}} = \left(t_2 + \frac{t_1 + t_3}{2} \right), \tag{5.4}$$

and the drift velocity can be calculated as

$$v_{\mathrm{drift}} = \left(d_2 + \frac{d_1 + d_3}{2} \right) \left(t_2 + \frac{t_1 + t_3}{2} \right)^{-1}, \tag{5.5}$$

The design of the PM for Xenoscope is shown in Figure 5.14, consisting of four parallel electrodes. The cathode and anode grids are SS rings with hexagonal meshes mounted on them, as described previously. The first section of 53 cm was implemented in COMSOL, following the CAD design,

where M is the molar concentration

with the targeted voltages for the first run of $-2710\,\mathrm{V}$, $-2560\,\mathrm{V}$, $0\,\mathrm{V}$, $500\,\mathrm{V}$ for the cathode, cathode grid, anode grid and anode electrodes, respectively. This choice of voltages provides a uniform $52\,\mathrm{V/cm}$ drift field in the first two regions, while $500\,\mathrm{V/cm}$ in third region ensures the full collection of the drifted electrons. The first screening mesh (cathode grid) is positioned $18\,\mathrm{mm}$ above the photocathode, the second screening grid (anode grid) is $503\,\mathrm{mm}$ further above, and the anode is placed $10\,\mathrm{mm}$ above the anode grid. The implementation in COMSOL is shown in Figure 5.15, where the converging electric field lines in the anode represent the charge collection efficiency of nearly 100%.

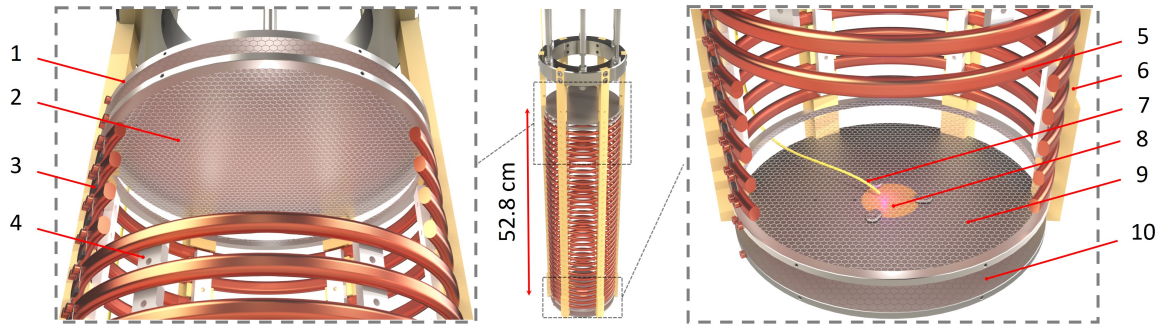

Figure 5.14: CAD design of the PM, consisting of four parallel electrodes (1, 2, 9, 10). The photocathode (10) is flashed by a xenon lamp via an optical fibre (7) pointing to centre of the photocathode (8) which is coated with a thin metal film. The copper field shaping rings (FSRs) (5) are held by polyamide-imide pillars (6) and PTFE interlocking blocks (4). The resistor chain (3) provides the potential drop between the FSRs. Figure from Ref. [316].

5.3.1 Charge generation components

We summarise here the components that contribute to the generation of photoelectrons in the cathode.

Xenon lamp The xenon lamp is a 60 W flash lamp with a built-in reflective mirror (model number L7685) from Hamamatsu [347]. The glass is a single crystal made out of sapphire that allows for short wavelengths ($\sim 190\,\mathrm{nm}$) to reach the output of the lamp. The spectral region is from $190\,\mathrm{nm}$ to $2000\,\mathrm{nm}$, providing photon energies of 0.6–$6.5\,\mathrm{eV}$. The lamp generates a gas-discharge, and reflective mirrors direct photons from all directions towards the output of the lamp. A UV sapphire lens with an SMA[11] connector from Hamamatsu is placed at the lamp output to collimate the light signal into the input of the optical fibre. The xenon lamp can be triggered internally or externally with a waveform generator. The voltage for the gas-discharge can be set from $600\,\mathrm{V}$ to $1\,\mathrm{kV}$, with

[11] SubMiniature version A, a standard connector used for optical fibres.

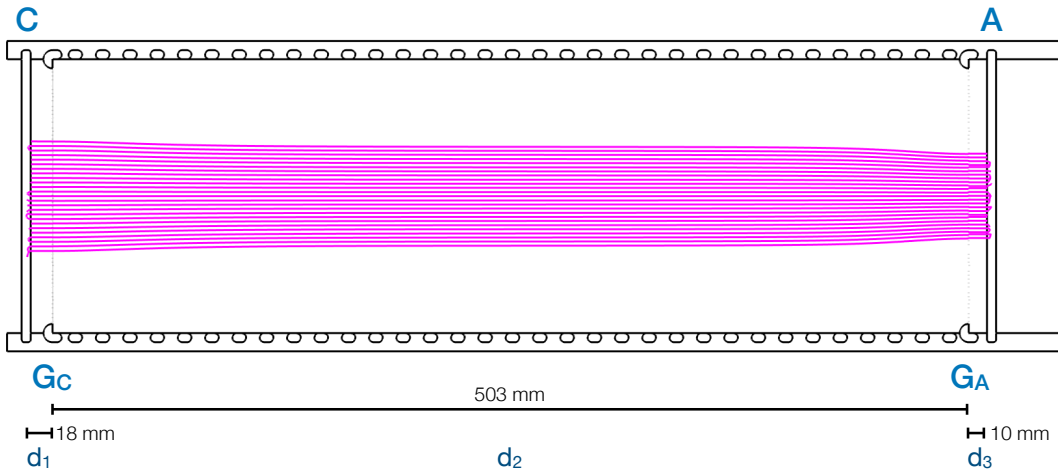

Figure 5.15: Electric field simulations for the 53 cm PM, where the voltage values for the electrodes are −2710 V, −2560 V, 0 V, 500 V for the photocathode (C), cathode grid (G_C), anode grid (G_A) and anode (A) electrodes, respectively. The magenta lines show the trajectory (or the electric field lines) of the drifting electrons, with a collection efficiency of nearly 100%. In the pillars are visible the FSRs and the holders of the electrodes, which were implemented as well in COMSOL.

increasing light emitted. The pulse from the lamp is reported to have an FWHM of 2.90 µs when operated at its maximum voltage of 1 kV. Figure 5.16 shows the reported time duration of the pulse and the spectral distribution provided by Hamamatsu.

The xenon flash lamp had to be rehoused in a stray electromagnetic interference box due to the noise produced by the discharge in other electric components. The box includes a potentiometer, allowing to manually change the gas-discharge size, a trigger system connected to a waveform generator, and an additional ventilation cooling system.

Optical fibre and optical fibre feedthrough As the xenon lamp is placed outside the cryostat, an optical fibre is needed in order to transfer the light from the output of the lamp to the photocathode surface. The selected fibre has to be resistant to solarization, i.e., the degradation in the fibre material, and therefore, transmission due to the impact of high energy photons in the inner walls of the fibre. This effect is more likely to occur when the fibre is exposed to light below 300 nm. Figure 5.17 shows the transmission of a solarization resistant fibre[12], compared to standard silica fibres. The loss is estimated to be 10% per metre of fibre. A fibre that accepts wavelengths with spectral distribution such as the light from the xenon lamp (i.e. a continuum instead of a single wavelength emitted) is called *multimode* fibre, opposite to *singlemode*, where the transmission is optimised for a single

[12]The resistance in the fibre is achieved by using polyimide or aluminium buffers that mitigate the effects of UV exposure.

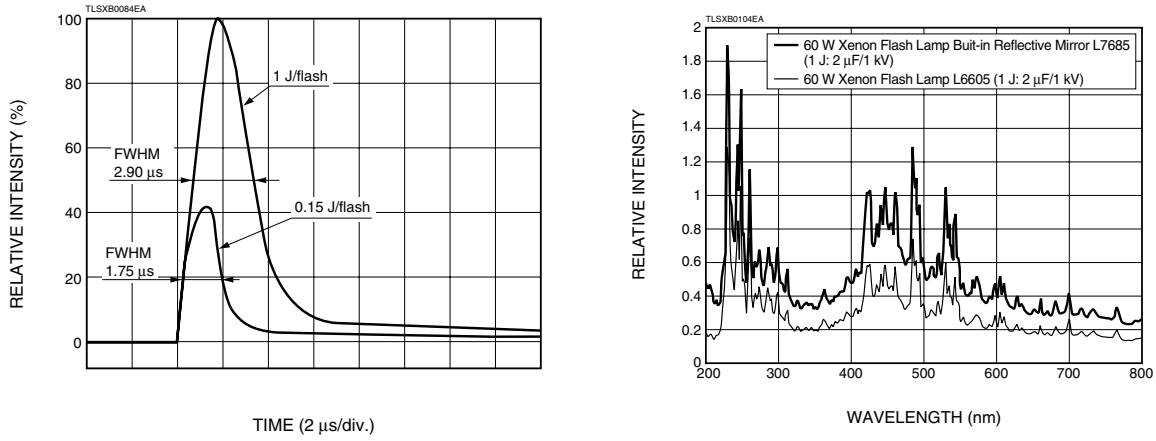

Figure 5.16: Left: Reported time duration of the xenon lamp pulse reported by Hamamatsu; Right: Reported spectrum of the lamp from Hamamatsu [347].

wavelength. The fibre selected for the PM is a UHV (Ultra High Vacuum) $600\,\mu\mathrm{m}$ polyimide buffer from LewVac [348], with a numerical aperture NA$= 0.22$, where $\mathrm{NA} = n \sin\theta$ defines the maximum angle that the fibre accepts or emits light, with n the refraction index of the medium.

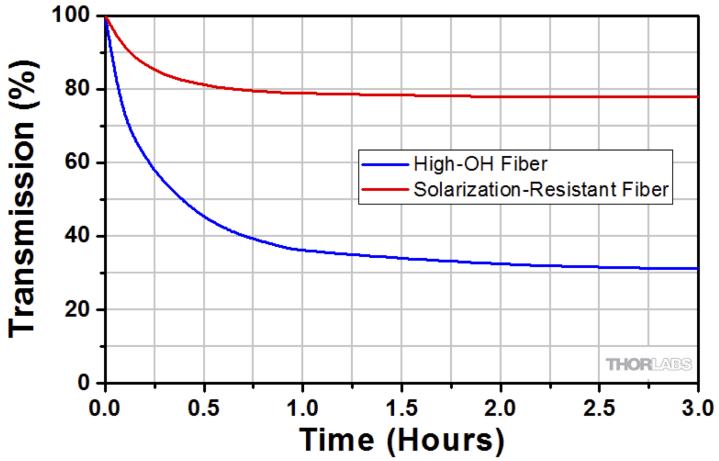

Figure 5.17: Attenuation of solarisation resistant fibres at $215\,\mathrm{nm}$ over exposure in hours. Source: Thorlabs [349].

The fibre is fed into the cryostat with the use of an optical fibre feedthrough. optical fibre feedthroughs for vacuum and over-pressure vessels are available in two types. In one type, the fibre is fitted on a flange without any discontinuation of the fibre. This requires the shipping of the total length of the fibre to the provider to fit the fibre in a tube that is later sealed and welded on a flange.
In the other approach, the fibre is terminated with a connector (often SMA, which is suitable for

multimode fibres) that is plugged into a flange in the air-side and continued with an additional fibre in the vacuum/pressure-side, with a SMA connector. The approach introduces two connectors that have to be aligned, with potential losses. Moreover, the fibre surface on the termination fed into the connector has to be sufficiently polished. Figure 5.18 shows an example of both optical feedthrough designs.

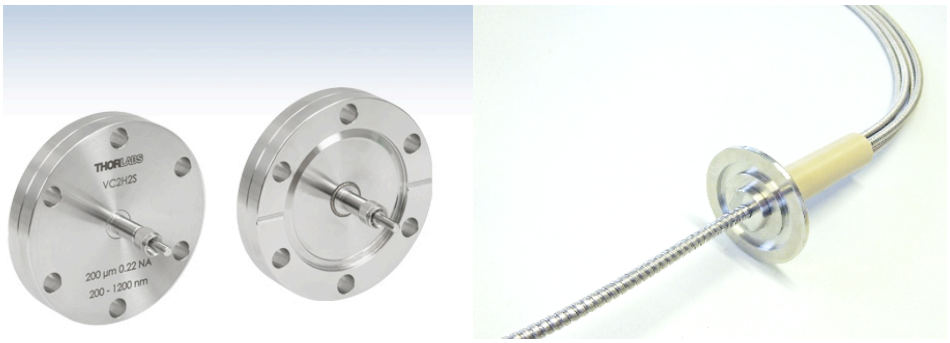

Figure 5.18: Optical feedthrough designs a fibre (left) that can be fitted in a flange without discontinuation or the fibre (right) can terminated with a SMA connector, connected to the feedthrough, and continued with an additional fibre connected inside the cryostat. Source: Thorlabs [349], Art Photonics [350]

The feedthrough selected for the PM is the latter, due to its availability, and it was purchased from Thorlabs [351]. The feedthrough has a $600\,\mu m$ multimode SMA connector, in match with the fibre, which is welded on a CF40 flange. As it is rated for UHV, it was tested locally up to $4\,bar$, without any leakage. The leak test was performed with a helium leak tester, by connecting the flange in a small setup and using the helium leak tester in its *sniffer* mode. As the feedthrough requires the fibres to be terminated, the optical fibres were prepared and polished in-house. The smooth polished surface is achieved with a set of 8 different sizes of polishing sheets made of aluminium oxide, silicon carbide, and calcined alumina, starting from grits of $30\,\mu m$ grit and finishing with a $0.02\,\mu m$.

Photocathode selection and production One of the most critical parts of a PM setup is the photocathode. The photocathode will produce the photoelectrons when the fibre projects the photons, from the xenon lamp, on its surface. A photocathode consists of a thin layer of metal with a low work function on top of a substrate material. The substrate consists of a material that provides good adherability to the metal layer and does not absorb UV photons. Its reflectivity enhances the production of more electrons as they interact again with the thin film[13]. Some choices for substrate materials in

[13]There is no rigorous definition in terms of thickness for *thin film*, it is used for layers that span from nanometers to several micrometers.

photocathodes are polished aluminium, quartz or SS. The quartz substrate has low absorption of UV photons and is chosen for the PM photocathode [352]. The thin-film material is chosen by its work function, thickness, production, and stability. The reported work function of a selection of metals is shown in Table 5.3.

Table 5.3: Work function of metals, from Ref. [353]

Material	Work function [eV]
Al	4.06 - 4.26
Ag	4.26 - 4.74
Au	5.10 - 5.47
Cr	4.5
Ti	4.33

The thickness of the film affects the electron escape probability. Due to the absorption length, the probability of an electron being emitted at higher depth decreases. Once generated, the photoelectrons need to travel to the surface of the material in a process characterised by the inelastic scattering mean free path. If the thin film thickness is relatively large, the electron emitted will not reach the surface of the material, as the electrons that were raised above the Fermi level are attenuated by inelastic scattering. If the thin film thickness is too small, the number of electrons absorbed decreases. These two effects counteract each other in defining the Quantum Efficiency (QE) of the photocathode, i.e., the percentage of photons above the work function of the thin film yield a photoelectron escaping the surface. Table. 5.4 provides some quantities for these effects in gold, where p_{eff} is an 'Effective' probing depth, as defined in Ref. [354], related to the photon escape probability in the surface and the thickness of the layer, given by $p_{\text{esc}} = \lambda_s/(\lambda_s + p\cos\alpha)$, where α is the angle of the incident light, and the subscript s stands for scattering. By optimising the thickness of the layer, the photons that are not absorbed in the thin film can be reflected by the substrate and produce photoelectrons again with a higher escape probability.

Table 5.4: Gold properties for UV light 200–250 nm, taken from Ref. [354]

Property	Value [nm]
Penetration depth, p	12–13
Inelastic mean free path α_s	5–8
Effective depth $p_{\text{eff}=\alpha_s p/(\alpha_s+p)}$	3.5–4.9

The photocathodes are produced in-house using a turbomolecular pumped coater Q150T Plus from

Quorum [355]. It provides a vacuum chamber where argon gas can be bled, ionized, and the ions accelerated towards the desired target. The ions impacting the target will vaporize it, and the evaporated material is deposited on the substrate, placed inside the coater chamber. The coater provides control on the desired thickness deposited on the substrate with the use of a quartz crystal microbalance, which measures the mass variation per unit area by from the change in frequency of a quartz crystal resonator. The coater is rated for materials that do not oxidise, as the argon gas used, depending on its purity, will introduce oxygen that interacts with the coating material. The coater was used to produce photocathodes of $50\,\mathrm{nm}$ thickness made of gold[14], silver, aluminium, and chromium on a quartz substrate of $(30.00 \pm 0.05)\,\mathrm{mm}$ diameter and $2\,\mathrm{mm}$ thick. The thickness of the layer for gold was based on the effective probe depth and previous works [356]. The thin-film thickness of the other materials was not optimised. The substrate has to be flat in order to provide homogeneous response in the photocathode. The substrate selected has a flatness parameter of $\lambda/4$, where λ is a commonly used unit. The flatness λ is measured in fractions of a reference wavelength, $632.8\,\mathrm{nm}$. A $\lambda/20$ value will have a maximum peak to valley deviation of $632.8/20$ or $31.64\,\mathrm{nm}$ [357]. The cleaning procedure for the substrates, before the coating, is very important for a homogeneous material deposition, and it includes three steps: cleaning with acetone, isopropyl alcohol in an ultrasonic bath, and blow-drying with gaseous nitrogen.

The produced photocathodes were tested in a vacuum setup with a screening grid $18\,\mathrm{mm}$ away from the photocathode and the anode $10\,\mathrm{mm}$ away from the screening grid. The xenon lamp flashed over the photocathode material with a frequency of $1\,\mathrm{Hz}$. Figure 5.19 shows the performance of gold and silver photocathodes in terms of the charge measured in the photocathode, which feature low reactivity and high lifetime. Due to different signal-to-noise ratios, the drift field selected for the gold photocathode was of $70\,\mathrm{V/cm}$, whereas the silver photocathode was tested under a drift field of $200\,\mathrm{V/cm}$. Both materials showed an increasing signal after several hours of being exposed to the lamp, and the signal size did not decrease after the lamp was stopped and resumed. This effect was also observed in Ref. [356], which is explained as a process of photo-outgassing, where energetic UV photons remove the first layers of materials, where oxides are present. When comparing the performance, both materials showed potential for signal generation, although the gold photocathode reached a stable state with fewer hours of exposure to the UV signal. A Residual Gas Analyser (RGA) model Prisma Pro from Pfeiffer [358], was used to test the photo-outgassing hypothesis, but no detection of additional molecular content above the base level was found. The gold photocathode was selected due to its stability over time and higher signal production than the silver photocathode, requiring smaller electric fields to produce a higher charge. In the case of photocathodes prepared

[14] Which requires $5\,\mathrm{nm}$ thick layer of Ti for adherence.

with chromium and aluminium, the two have a higher reactivity and oxidise quickly, with low signal production, and therefore, were discarded.

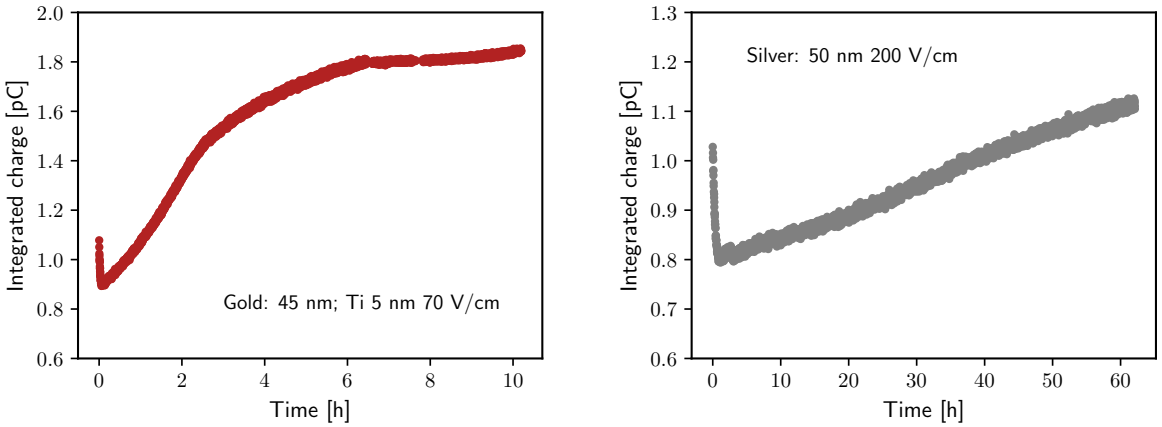

Figure 5.19: Left: Signal strength over time of a gold photocathode, where the photoelectrons are extracted with 70 $\mathrm{V/cm}$ drift field; Right: Signal strength over time of a silver photocathode using a 200 $\mathrm{V/cm}$ drift field.

The silver photocathode can be optimised in the future in terms of the thickness of the thin film, and a different coating process with lower levels of oxygen. The same applies to the other materials.

Charge produced in the photocathode

The number of electrons produced in the photocathode, by the photons from the light pulse, can be estimated as

$$N_{e^-} \propto \mathrm{Ps} \times \frac{\Omega}{4\pi} \times \mathrm{QE} \times \sigma_{\mathrm{losses}}, \tag{5.6}$$

where Ps is the power of the lamp, Ω the solid angle coverage of the fibre into the cathode, the QE of the photocathode, and σ_{losses} is the transmission loss from the lamp to the endpoint of the fibre due to attenuation in the fibre and connectors coupling losses. The solid angle Ω is related to the NA and the core diameter of the fibre. The energy of one photon is

$$E = \frac{hc}{\lambda} \tag{5.7}$$

where h is Planck's constant, c the speed of light and λ is their wavelength (assumed 200 nm). Inverting Equation 5.7 we get the number of photons per Joule, E_{ph}. The photons produced, N_{ph}, are

collimated and fed to the optical fibre, where they suffer an attenuation,

$$N_{\text{ph}} = \frac{1}{E_{\text{ph}}} \times \text{Ps} \times \frac{\Omega}{4\pi} \times \sigma_{\text{losses}} \tag{5.8}$$

The photons are converted to electrons via photoelectric effect with efficiency QE

$$N_{e-} = N_{\text{ph}} QE \tag{5.9}$$

The total charge Q will be the number of electrons times the charge of one electron, Q_{e^-}:

$$Q = N_{e-} Q_{e^-} \tag{5.10}$$

Assuming values of 0.22 and $600\,\mu\text{m}$ for NA and core diameter of the fibre, $100\,\text{mJ}$ energy above the work function of the photocathode per pulse[15], an attenuation of $\frac{3\%}{\text{m}}$ over $3\,\text{m}$, and a QE of 1×10^{-7} (for gold from Refs. [359, 360]), we obtain a value of the photoelectrons generated of

$$N_{e^-} \sim 10^6, \tag{5.11}$$

where N_{e^-} is proportional to the charge, $Q = q\ N_{e^-}$, and q is the charge of one electron. The estimated charge is then $Q \sim \mathcal{O}(100\ \text{fC})$.

5.3.2 Current induced in electrodes

As described before, the photoelectric effect generates electrons in the photocathode after a source of photons that have energy higher than the work function of the surface material illuminates it. The current induced on the electrodes depends on the number of electrons generated and the electric field between the electrode grids. The current can be modelled by applying the Shockley-Ramo theorem [361], which states that the current induced i in a conductor A due to the motion of charges is

$$i = q\mathbf{v} \cdot \mathbf{E}_{\text{A}}, \tag{5.12}$$

where v is the velocity of the charge carrier, and $\mathbf{E}_{\text{A}}$ is the electric field that would exist under the following conditions:

- the charge carrier is removed,
- the conductor A is set on a unit potential,
- all the other conductors are grounded.

[15] Given the spectrum from the xenon lamp and the percentage of photons below the WF of gold.

The potential of the conductor φ_A is called the weighting potential, which is found by solving the Laplace equation

$$\nabla^2 \varphi_A = 0 \tag{5.13}$$

The weighting potential is not affected by the applied voltages and only depends on the geometry. The integration of the current gives the charge of the carriers,

$$\Delta Q = -\int i dt = q\left[\varphi_A(\mathbf{r}) - \varphi_A\left(\mathbf{r}_0\right)\right]. \tag{5.14}$$

As an example, Figure 5.20 shows two electrodes, A and C, separated by $p + d$ distance, where at a distance d, a screening grid is placed. The screening grid is simplified as parallel wires of radius r and pitch between the wires a. In this scenario, the solution for the weighting potential of the conductor A is [362, 363, 364]

$$\varphi_A(y) = \begin{cases} 0 & \text{if } d < y < p, \\ \frac{y}{d} & \text{if } 0 < y < d, \end{cases} \tag{5.15}$$

from where it can be observed that one effect of the screening grid, besides screening the charge placed on the other side of the grid, is to shorten in time the induced current pulse in the conductor C. The longer the distance between the electrodes, the longer the pulse of induced charge, which provides another reason to place screening grids in a PM.

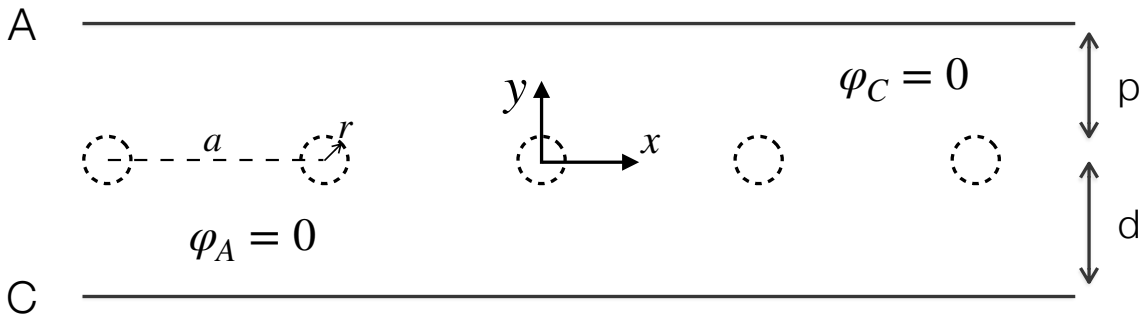

Figure 5.20: Diagram of the derivation of the weighting potential: two electrodes (A and C), separated by a screening grid consisting of wires of radius r and separation pitch a. The screening grid is at distance d from the electrode C, and distance p from the electrode A.

In a realistic case, the screening grid has an efficiency given by its geometry, materials and overall

transparency to the charges. The Equation 5.15 is modified as

$$\varphi_A(y) = \begin{cases} \sigma\left(1+\frac{y}{d}\right), & \text{if } -d < y < 0, \\ \sigma + (1-\sigma)\frac{y}{p}, & \text{if } 0 < y < p, \end{cases} \tag{5.16}$$

where σ quantifies the inefficiency of the grid to screen the charges from other drift regions. Ref. [365] quantifies the screening inefficiency in the electrode A for plane-parallel wire electrodes, as

$$\sigma \sim \frac{a}{2\pi p}\log\left(\frac{a}{2\pi r}\right), \tag{5.17}$$

where p is the distance between the screening grid and the anode A. Equation 5.17 is used to observe qualitatively that increasing the relative distance between wires decreases the screening of charges. There is a trade off between the screening efficiency and the transparency of the grid, necessary to allow for all the electrons to drift through the grids.

5.3.3 Readout electronics

The readout circuit for the Xenoscope PM was conceived to be placed inside the cryostat to avoid having signal losses over the $9\,\mathrm{m}$ long signal cables. The circuit was designed together with the Electronics Workshop at the University of Zurich. The readout electronics must be tested at LXe temperatures, and demonstrate overall stability in signal reconstruction. The readout circuit, shown in Figure 5.21 features a noise filter, an AC-coupling component, a transimpedance amplifier, AC-coupling to remove noise offset, and a final voltage amplifier, with a $50\,\Omega$ impedance termination to match the one from the data acquisition. The transimpedance and voltage amplifiers are implemented with two operational amplifiers (op-amps) model AD806, with a FET[16] input amplifier [366][17].
The filter removes high-frequency noise, which enhances the signal quality. The AC-coupling removes the DC component along the HV applied in the electrode. The capacitor in series at the input of the first amplification stage increase the dielectric strength of the circuit. Each capacitor is rated for voltages of $3.3\,\mathrm{kV}$, giving a total voltage rating of approximate $10\,\mathrm{kV}$. Both pre-amplifier circuits for the cathode and anode were tested before installation and show equal gain and frequency

[16] Field-effect transistor

[17] The applied voltage across the two terminals of the op-amp controls the current flowing in the third terminal, i.e., the carriers (electrons in n-type material and holes in p-type). The output voltage V_{OUT} due to the amplification in the transimpedance amplifier is given by

$$V_{\mathrm{OUT}} = \frac{-R_F}{1 + C_F R_F} \times I_{\mathrm{IN}},$$

where I_{IN} is the input current, and R_F, C_F the resistor and the capacitance in the feedback loop of the amplifier, respectively.

response.

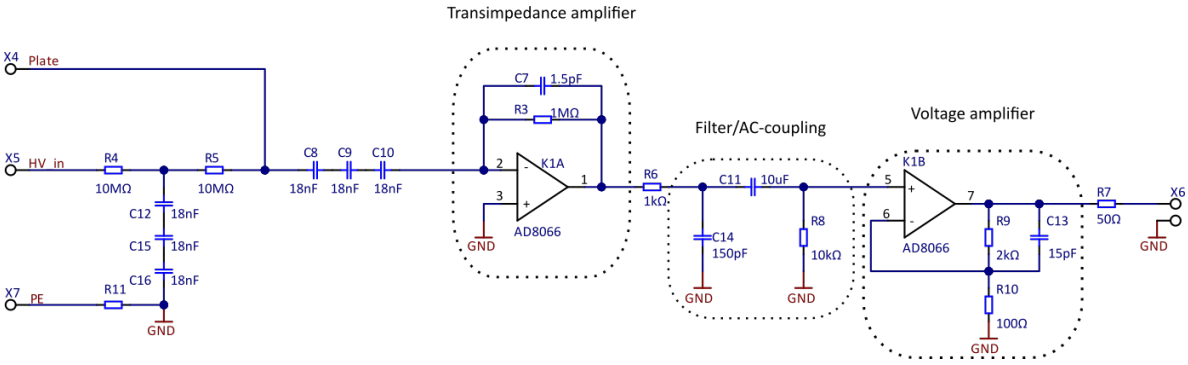

Figure 5.21: Circuit design for the cathode signal readout in the PM, with a HV stabilising filter and a two-stage signal amplification. The labels X4, X5 and X7 stand for the connection to the electrode plate/disk, a direct connection to the HV supply, and protection Earth (PE) for grounding, respectively. The initial filter removes AC components in the HV supply before it feeds the electrode. The elements C and R stand for the capacitors and resistors in the circuit, given in units of Ohm (Ω) and farad (F). The capacitors C8, C9 and C10 decouple the AC component of the voltage from the cathode/anode. The signal is then pre-amplified in the transimpedance amplifier, filtered and amplified again in the voltage amplifier. Figure credit: David Wolf.

The stability of the circuit was tested in a climate chamber in steps of 10 K from room temperature down to 190 K. A test charge was connected into the input side of the circuit (X4 in the Figure 5.21), and a calibration curve was acquired at 190 K, as shown in Figure 5.22. The calibration shows a charge amplification of $0.18\,\frac{\mathrm{fC}}{\mathrm{mV\,\mu s}}$ and overall good thermal stability. Additionally, the RC decay constant of the circuit, which could be a source of systematic error, was estimated as $\sim 200\,\mathrm{ns}$, and thus negligible for most calculations compared to the $\sim 7\,\mu\mathrm{s}$ spread of the pulse from the flash lamp. The charges seen in the cathode Q_C and anode Q_A will be the integration of the current pulse in the first and third drift regions

$$Q_{\mathrm{C}} = \int_0^{t_1} I_{\mathrm{C}}(t)\mathrm{d}t = \frac{Q_0\tau}{t_1}\left(1 - \mathrm{e}^{-\frac{t_1}{\tau}}\right), \tag{5.18}$$

$$Q_{\mathrm{A}} = \int_{t_1+t_2}^{t_1+t_2+t_3} I_{\mathrm{A}}(t)\mathrm{d}t = \frac{Q_0\tau}{t_3}\mathrm{e}^{-\left(\frac{t_1+t_2+t_3}{\tau}\right)}\mathrm{e}^{\frac{t_3}{\tau}} - 1, \tag{5.19}$$

where Q_0 is the initial charge generated, τ is the electron lifetime, t_1 is the time at the minimum of the current pulse in the cathode, t_2 is the drift time from the cathode to the anode, and t_3 is the time at the maximum of the current pulse in the anode. The previous equation is a simplification, where the width of the pulse from the lamp, that creates the initial signal, is neglected. By including this

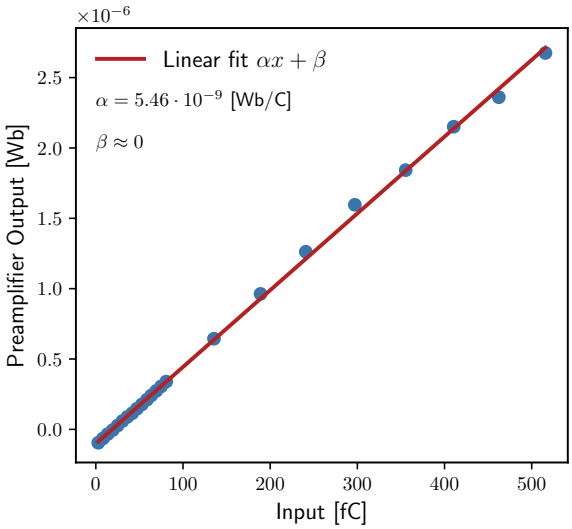

Figure 5.22: Calibration curve obtained by applying a test charge in the circuit and observing the integral of the current at 190 K.

effect, the initial charge population will be a function of time depending of the lamp pulse

$$I_i = Q_0(t)\frac{d_i}{v_i}e^{t_i/\tau}. \tag{5.20}$$

where I_i is the induced charge in the electrodes, d_i, v_i, and t_i are distance, electron velocity and time in the drift region i, v_i, and $Q_0(t)$ is the time-dependent charge given by the duration of the light pulse from the lamp.

5.4 Purity monitor assembly and measurements inside the Xenoscope cryostat

The PM mechanical and electrical components were fabricated following the design in Section 5.2. The hexagonal meshes were fabricated by CMT Rickenbach [367], where the selected material was SS (AISI 304) with a mesh thickness of 0.1 mm. The FSRs were milled from solid blocks of OFHC copper, to reproduce the soft borders shown before. The FSRs were electropolished to remove scratches on the surface. To produce the desired drop in the voltage in each ring, HV and moisture resistant resistors rated for cryogenic temperatures of (5 ± 1) GΩ and 1 W from Ohmite [368] were installed. The resistors were soldered on PCBs[18] and the contact is given by a vacuum compatible screws

[18]Printed circuit boards

attaching the board to the FSR.

After testing the components, the assembly of the 53 cm PM followed. The full inventory of the components in the assembly is shown in Table 5.5. Before assembling, a cleaning protocol was followed for each component to prevent additional contamination from entering the cryostat. All components were cleaned with Elma®soap 1%[369], with a final cleaning of alcohol and gaseous nitrogen dry blowing. Some components had an additional treatment of passivisation to remove and chemically neutralize the first surface layers of material, where impurities can concentrate. The PM was assembled in Xenoscope in June 2021. The mechanical stability of the components proved to be sufficient to sustain the weight of the field cage. Additionally, twelve PT100s were distributed over the whole length of the inner vessel to provide a readout of the liquid level. Figure 5.6 shows the first phase of the detector assembled. As mentioned before, the field cage for the PM consists of the first module of the full field cage of the TPC. The funnel that transports the liquefied xenon in the cryostat is placed around the expected liquid level. In contrast, a longer funnel that recirculates the LXe is extended up to the bottom of the inner vessel.

Component	Quantity
Copper FSRs	35
PAI pillars	6
PTFE connectors	12
PTFE locking blocks	210
PAI screws	210
Electrode mesh	2
SS disks (anode and cathode)	2
Copper nails	3
M2 vented screws	70
Resistors on PCB	70
Nuts support	12
Screws support	12
Fibre holder PTFE	1

Table 5.5: Inventory of components for the first phase of the Xenoscope PM.

Table 5.6: First section of the PM assembled, where the PAI pillars, held by a SS ring on the top, holds the copper FSRs, and electrodes. The pre-amplifier PCB can be seen around the top electrode of the PM.

5.4.1 Calibrations in vacuum

Once installed in the Xenoscope cryostat, the PM was operated in vacuum. The acquisition of signals in vacuum was performed to investigate the signal shape in a configuration with negligible charge losses due to impurities. This measurement provides as well the delay time of the electronics in the setup, from the pulse generator for the xenon lamp to the signal amplification. Figure 5.23 shows the response of the cathode and anode circuits when the photocathode is flashed at a level of vacuum 5×10^{-5} mbar in the inner cryostat vessel. Low voltage was chosen to not saturate the photocathode and anode readout, namely 80 V, 78 V, 0 V and 10 V for the cathode, cathode grid, anode grid and anode, respectively. When corrected with the velocity of electrons in vacuum $v = \sqrt{\frac{2\Delta V}{mc^2}}$, the gain of the amplifier circuits for the photocathode and anode signals exhibit equal response. A time delay of 19 µs due to electronics is observed and the width of the signals were compatible with those of the lamp. If a screening inefficiency is present, long tails would appear in the pulses, incompatible with the decay of the RC circuit convoluted with the weighting potential in the drift region described before. No signs of the grid screening inefficiency are seen, which is likely due to the distance between the cathode and anode grids (see Equation 5.17).

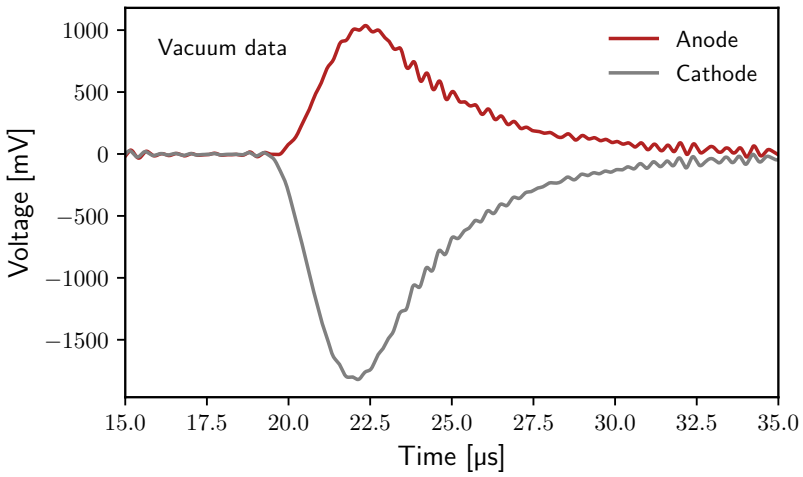

Figure 5.23: Signals acquired in vacuum for both photocathode and anode. Low voltage was chosen to not saturate the photocathode and anode readout, namely 80 V, 78 V, 0 V and 10 V for the cathode, cathode grid, anode grid and anode, respectively. The delay from the electronics can be seen in the delay time from the trigger of the pulse generator. The width of the pulse corresponds to the reported width from the xenon lamp provider.

After the calibration of the PM in vacuum, gas xenon was flushed and purified inside the detector through its recirculation in the gas system. An attempt to observe signals in gas xenon was made,

but the measurement proved difficult due to the reduction in the QE from back-scattering of the photoelectrons in gas xenon [370]. Moreover, the boards had a short circuit around 5 kV. While the capacitor was undamaged, the op-amps needed to be replaced. This issue motivated the decision to coat the PBC with Parylene to increase the dielectric strength of the electronics. Parylene is a chemically resistant dielectric with low outgassing that can be evaporated to deposit a layer of $\mathcal{O}(\mu m)$ on the boards, which has been studied in other works [371]. The coating was performed by *Specialty Coating Systems* [372].

5.4.2 Liquid xenon study

The LXe run started 28/02/2022 with the detector filling, and finished 01/06/2022 with the recuperation of 348 kg of xenon. An additional goal of this study, besides the operation of the PM, was to benchmark the purification of LXe at different recirculation speeds. With the recirculation of xenon through the getter and filters, the purity of xenon increases, along with the electron lifetime measured by the PM. The evolution of the electron lifetime is divided by an initial behaviour where it increases rapidly, and a latter part where the change is slow, although continuously increasing, referred as *plateau*. Therefore, at different recirculation speeds, the electron lifetime reaches different plateau levels.

The LXe was recirculated through the gas system with flows of 30 slpm[19], 35 slpm and later 40 slpm, with the xenon lamp illuminating the photocathode with a frequency of 1 Hz. Although the purity increases with the xenon recirculation flow, the purification speed is limited by the pressure rating of the inlet and outlet of the compressor, and thus it could not be increased beyond 40 slpm. Due to the unknown initial impurity level in the xenon from the purchased bottles, 26 days with no data above noise level due to electronegative impurities, recirculating the xenon gas continuously at 30 slpm , were observed. Datasets were taken with applied voltages to the electrodes of 2710 V, 2650 V and 500 V for the cathode, cathode grid, and anode, respectively. Figure 5.24 shows an example of the signals acquired in LXe from the cathode and anode at 40 slpm, as well as the times between the different drift regions, acquired with an oscilloscope model Waverunner Teledyne from LeCroy [373]. Each waveform is obtained by averaging 1000 signals to reduce the noise. The data is analysed by integrating the signal peak to obtain the charge-proportional readout. To decrease electronic noise, a low pass filter is applied in some cases, allowing only frequencies below 10 kHZ.

[19] Standard liter per minute (SLM or SLPM) given by

$$1\ \text{lpm} = 1\ \text{slpm} \cdot \frac{T_{\text{gas}}}{273.15\ \text{K}} \cdot \frac{14.504\ \text{psi}}{P_{\text{gas}}}$$

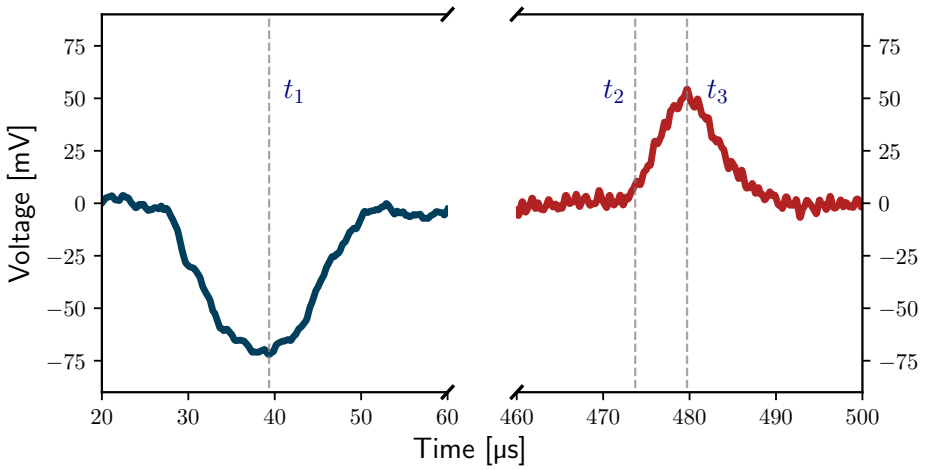

Figure 5.24: Signals acquired in the PM at $40\,\mathrm{slpm}$ xenon recirculation speed, where blue (cathode) has its minimum at t_1, and red (anode) starts to increase at time at t_2 and a maximum at t_3. These values are later used to calculate the electron lifetime due to charge deficit in the anode signal.

The measured current was used to calculate the charge and the drift times for a given drift field. Figure 5.25 shows the anode and cathode signals with their integral, where the integrated signals shows a 'step', after the charges moves entirely to the next drift region, or are collected in the anode. The charge seen in the cathode would correspond to approximately $N_{e^-} \cong 10^6$ electrons being produced (by recalling the calibration factor derived of $0.18\,\frac{\mathrm{fC}}{\mathrm{mV\,\mu s}}$), matching the estimate given before in Section 5.3.1. Figure 5.26 shows the electron lifetime from signals acquired from the cathode and anode, for $30\,\mathrm{slpm}$, $35\,\mathrm{slpm}$ and $40\,\mathrm{slpm}$ xenon recirculation speeds. The electron lifetime is obtained by applying Equation 5.3. The signal size increases with increasing purification speed. Periods with no data are marked and reflect the system being offline due to noise hunting or improvements in other subsystems. When the recirculation speed is changed, and therefore, the flow of the incoming and outcoming xenon in the system, the LXe level has a sudden change, which releases impurities trapped at the interface of GXe and LXe. The same effect was observed at the time of the label 'pump stopped', with the same explanation. The last value achieved for the electron lifetime was of $(660 \pm 60)\,\mu\mathrm{s}$, using Equation 5.3 and the values from Table 5.7, which shows the summary of the drift times using all datasets from the LXe run. The drift time showed overall robust stability, indicating that the electric field must be mostly homogeneous in the drift regions of the PM. The main source of errors in the calculated values for electron lifetime and time is statistical. The errors are calculated by Gaussian propagation of uncertainties in the charges and times.

An upgrade of the compressor is current being carried out, where its two diaphragms will be adjusted

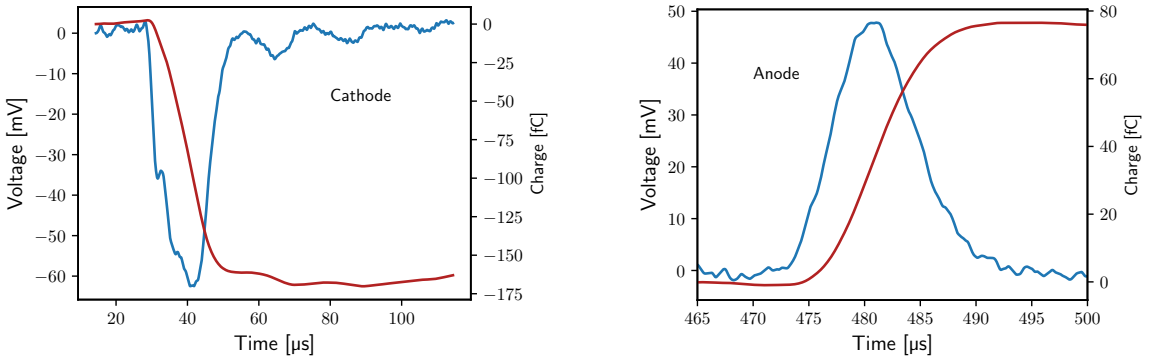

Figure 5.25: Left: Current readout in the cathode (blue) with the integrated charge signal (red). Right: Current readout in the anode (blue) with the integrated charge signal (red).

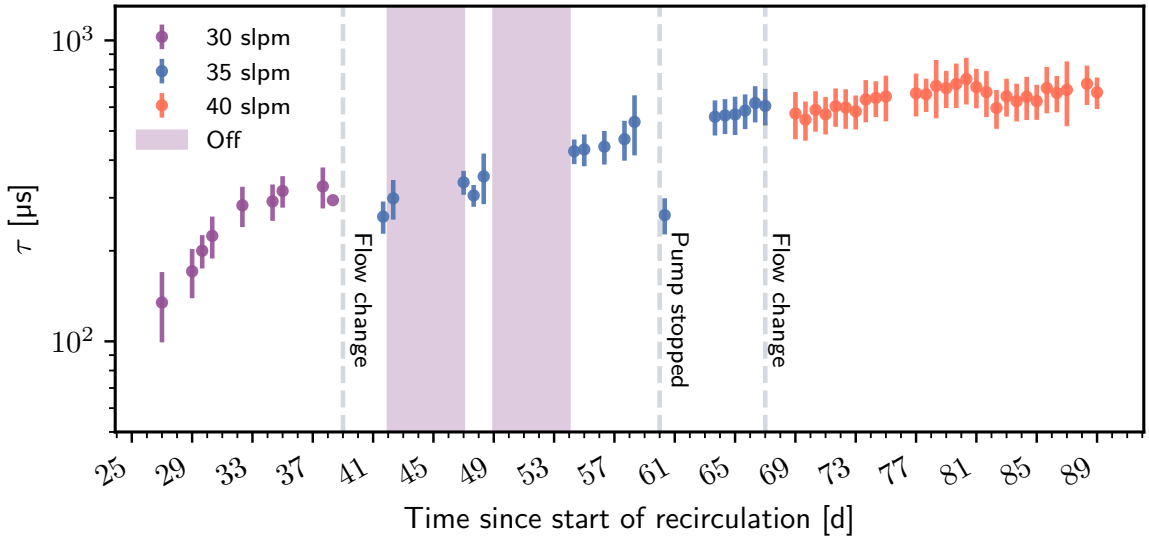

Figure 5.26: Electron lifetime measured in the Xenoscope demonstrator operating the PM at xenon recirculation speeds of 30, 35 and 40 slpm. In this plot, the datapoints are averaged every 12 hours. The behaviour explained in the text is observed: for each recirculation speed, a plateau value is reached. When the recirculation speed is changed, and therefore, the flow of the incoming and outcoming xenon in the system, the LXe level has a sudden change, which releases impurities trapped in the interface of GXe and LXe. The same effect was observed at the time of the label 'pump stopped', with the same explanation. The errors are obtained by propagation of Equation 5.3 and the statistical error from the acquisition.

to allow for higher recirculation flows, up to 100 slpm. This will allow for higher electron lifetimes in the system.

Table 5.7: Distance, electric field and drift time calculated from the cathode and anode signal for the three different regions in the PM, with voltages 2710, 2650, and 500 V for the cathode, cathode grid, anode grid and anode, respectively.

Region	Distance [mm]	Drift field [V/cm]	Drift time [µs]
1	18 ± 1	33 ± 3	13 ± 3
2	503 ± 1	52 ± 5	440 ± 4
3	10 ± 1	500 ± 5	9 ± 2

5.4.3 Measurements of electron transport in liquid xenon at different drift fields

After the electron lifetime measurement in LXe, data at the different electric fields was taken. This provides information on drift time, from where the drift velocity can be calculated. It is important for this measurements that the electron lifetime value stays constant to avoid systematic uncertainties, and thus they were performed at the end of the LXe run, when the electron lifetime entered the plateu region. Drift fields from $25\,\mathrm{V/cm}$ to $75\,\mathrm{V/cm}$ in steps of $5\,\mathrm{V/cm}$ were scanned, where the former represents the threshold for signal detection in the photocathode. The maximum voltage was decided based on the limitation of the HV connection to the cathode grid. Figure 5.27 shows the measured drift velocity at different electric fields, with a good match between the acquired data and previously measurements acquired in Refs. [374, 201, 375].

The same data can be used to study the spread in the anode signal after a drift time with different applied drift fields, as shown in Figure 5.28 for $75\,\mathrm{V/cm}$ and $35\,\mathrm{V/cm}$. The spread of the pulse can be used to derive the longitudinal diffusion of the electron cloud in LXe. The FWHM of the signal spread in each drift field extracted from the anode signal is shown in Figure 5.29. A wider spread is observed at lower fields, which indicates a change in the diffusion regime seen as the change in the slope in the FWHM.

The simulation package NEST [186], introduced before in Chapter 2, utilizes an empirical model based on previous measurements to model the diffusion effects. Currently, it lacks data at low drift fields (below $\sim 100\,\mathrm{V/cm}$), and the model used in the package predicts lower diffusion (smaller signal spread) with lower drift fields, contrary to the measured increasing spread in this work.

This work provides strong evidence that the longitudinal diffusion increases at lower drift fields, and the coefficient for the longitudinal diffusion will be derived from the signal spread data. With a PM, only the longitudinal diffusion can be observed, as there is no time information of the charges arriving to the anode in the x-y plane (transverse diffusion). Electron diffusion effects in LXe become more significant for meter-long TPCs, and its study is of importance for next generation experiments.

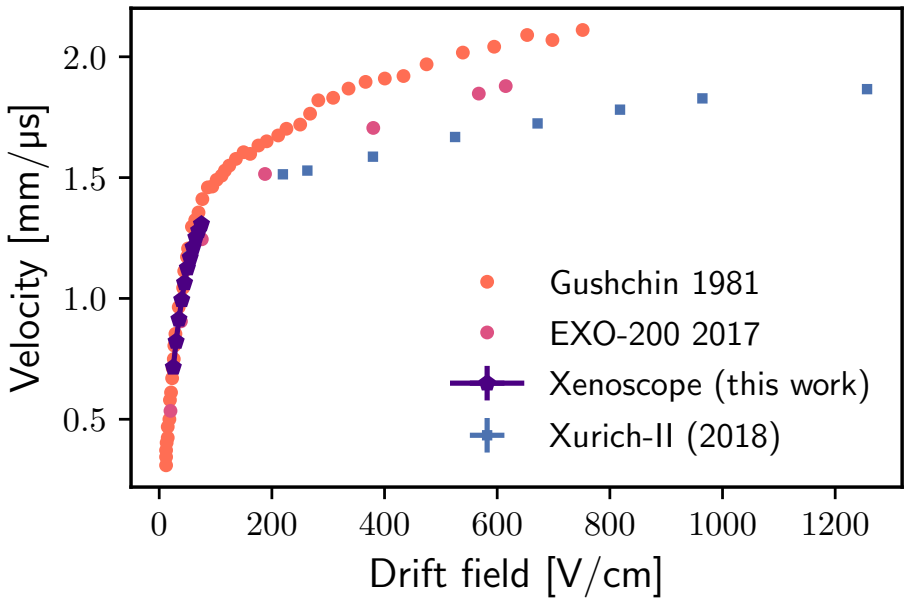

Figure 5.27: Drift velocity acquired in the Xenoscope PM with electric field values from 25 V/cm to 75 V/cm, compared to literature values from Refs. [374, 201, 375]. Values from Xurich-II appear at lower velocities due to the temperature in LXe of 184 K.

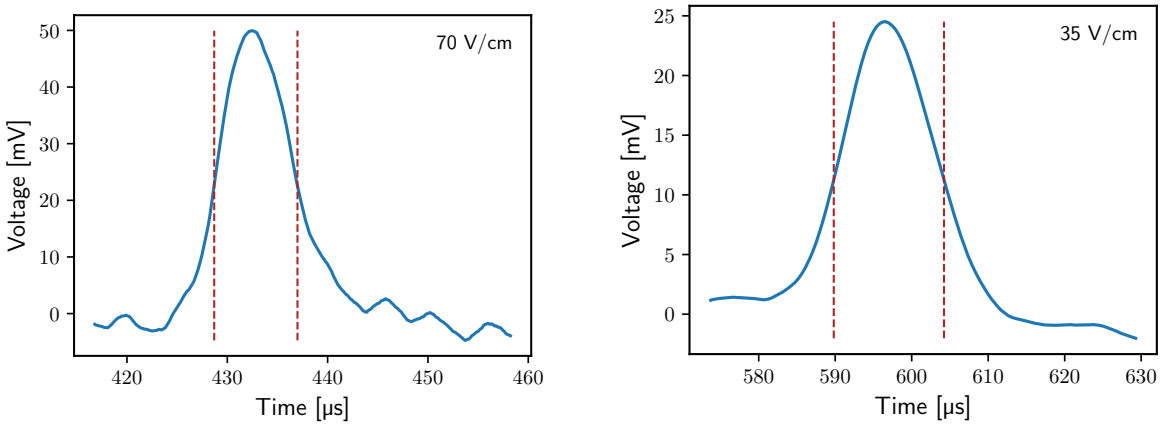

Figure 5.28: Anode signals for the PM at 75 V/cm (left) and 35 V/cm (right), showcasing the different signal widths and arrival times to the anode. The dashed red lines indicate the FWHM of the signals.

From the original number of photoelectrons in the cloud up to the measured signal width in the anode, the following effects play a role:

- Time dependence of the pulse from the lamp, which introduces the original spread in the signal

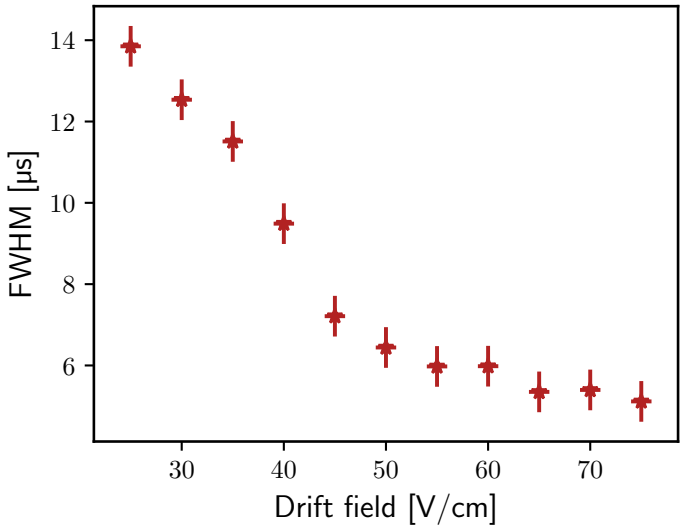

Figure 5.29: FWHM of the anode signal at different electric fields will be used later to calculate the diffusion of electrons in LXe. The width of the signal increases at lower electric fields, which indicates a change in the diffusion regime (change in the slope), likely from thermal to electric field dominated electron energies.

- Weighting potential of the screening region, where the time is re-scaled according to the velocity and distance of the drift region, as shown by Equation 5.15.
- Coulomb repulsion between electrons, where each electron is affected by the electric field induced by other electrons.
- Diffusion of the electron population, given by the diffusion coefficient D_L in the longitudinal component (parallel to drift field).
- Electron capture by electronegative impurities, which can potentially change the distribution of the electron cloud and therefore, the Coulomb repulsion. This is one of the reasons to always report the electron lifetime in diffusion measurements.
- Circuit response, namely the rise and decay times of the pre-amplifiers.

Assuming an initial δ-like deposition in the LXe in the origin of coordinates at time $t = 0$, the position can be found at time t by resolving a 3-dimensional equation that describes a Gaussian charge distribution that diffuses while being drifted in the +z direction with velocity v_d [363],

$$n(\vec{x},t) = \frac{N}{4\pi D_T t\sqrt{4\pi D_L t}} \exp\left[\frac{-\left(x^2+y^2\right)}{4D_T t}\right] \times \exp\left[\frac{-\left(z-v_d t\right)^2}{4D_L t}\right], \tag{5.21}$$

where D_T and D_L stand for transverse and longitudinal diffusion, respectively. The transverse diffusion can be modelled as independent degrees of freedom; thus, it can be treated as a random walk for the X and Y-axis where the time step dt is sampled from a Gaussian distribution with variance $\sigma^2 = 2D_T dt$. An initial point-like distribution will have a radial variance $R(t)$ of

$$\left\langle R(t)^2 \right\rangle = \left\langle x(t)^2 \right\rangle + \left\langle y(t)^2 \right\rangle = 4D_T t. \tag{5.22}$$

The longitudinal diffusion will be related to the pulse from the lamp, and can be defined as

$$D_L = \frac{d^2\sigma_L^2}{2t^3}, \tag{5.23}$$

with

$$\sigma_L^2 = \sigma^2 - \sigma_0^2, \tag{5.24}$$

where σ_L is the width related only to diffusion effects, σ_0 is the width of the light signal from the lamp, and σ is the measured width of the charge signal in the anode, and d is the distance travelled at time t. By rewriting Equation 5.24, we obtain

$$\sigma^2 = \sqrt{\frac{D_L 2t^3}{d^2}} + \sigma_0^2 \tag{5.25}$$

The signal in the anode is convoluted with the response function of the signal going through two grids, which is modelled with Equation 5.15, and the rise and decay constants of the RC circuits. The circuit response was estimated when bench-marking the electronics as described in Section 5.3, and has negligible effect in the signal shape. The light pulse duration is 2.9 µs and was crosscheck with the data in vacuum, matching the value reported by the manufacturer. The electron capture could influence the width of the signal if electrons outside the bulk of the charge distribution are more susceptible to be captured. The capture of electrons could change the Coulomb forces between electrons and change the charge distribution. This effect and the Coulomb repulsion will be neglected but discussed later. Combining all these elements, a response function can be obtained to deconvolute the observed signal.

Following the formalism described above, the detector response function is deconvoluted from the measured signal, to yield the original electron cloud spread in the z-direction. The measured signal, detector response function, and deconvoluted signal are shown in Figure 5.30. The results of this deconvolution, for each measurement at different drift fields, are shown in Figure 5.31. There is a strong evidence of increasing diffusion at lower fields, and the values match those of previous

measurements that covered low drift fields. In contrast, the model by NEST [186] predicts decreasing longitudinal diffusion for smaller drift fields. The errors are due to statistics, and they are calculated by Gaussian propagation of uncertainties from Equation 5.25.

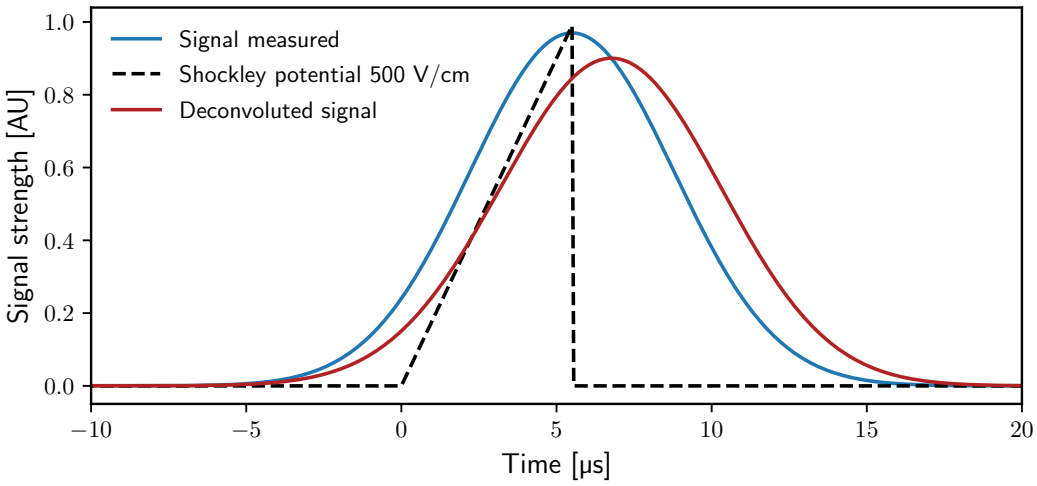

Figure 5.30: Signal measured in the anode for 25 V/cm (blue), together with the modelled detector response function of the two grids and the electronics (dashed black), and the deconvoluted anode signal (red). The spread in the red curve corresponds with the charge distribution of the electrons after drift.

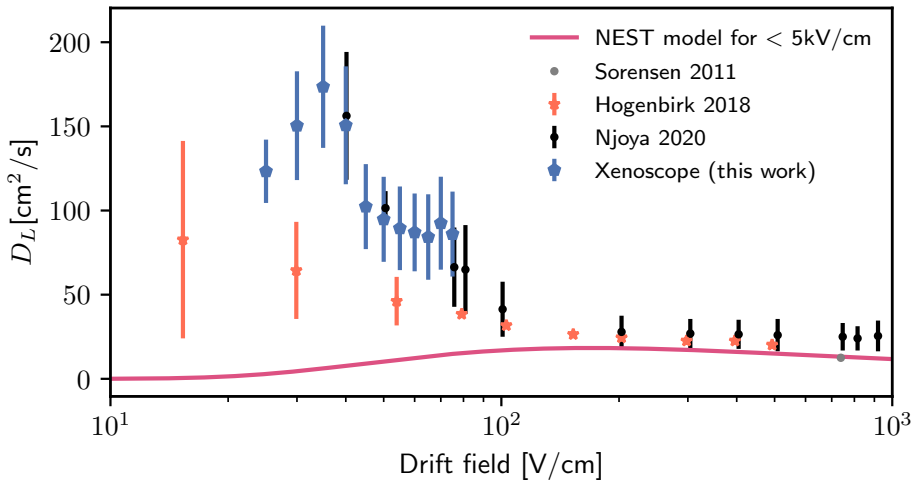

Figure 5.31: Longitudinal diffusion calculated in this work, compared to the results from Njoya et. al. [359]($\tau \sim 1$–$35\,\mu s$), Hogenbirk [251] ($\tau \sim 430\,\mu s$), Sorensen [180] and NEST [186]. The model by NEST predicts diffusion values approaching zero for lower drift fields.

5.4.4 Further discussion on diffusion effects

The increase in the longitudinal diffusion at lower electric fields is currently under investigation. It can be seen as well in Figure 5.29 in the change of slope in the curve, before the deconvolution is applied. In order to understand the diffusion, the spread of the pulse can be expressed in terms of the electron mobility μ as [363]

$$\sigma_0^2 = 2D_L t = \frac{2D_L L}{\mu E} = \frac{4\varepsilon L}{3eE}, \tag{5.26}$$

where t is the time of arrival, L the distance travelled, E the electric field, ε the energy of the electrons, and e the electron charge. The ratio between diffusion D_L and electron mobility μ, when they exhibit a thermal behaviour, follows the Nernst–Townsend formula

$$\frac{D_L}{\mu} = \frac{kT}{e} \sim 0.015\,\mathrm{V}, \text{ at T=178 K.} \tag{5.27}$$

In the PM data presented, this value is around $(0.04 - 0.06)[\mathrm{V}]$. In the presence of an electric field, an electron can acquire energies distinctly larger than thermal, and the diffusion is decreased. One explanation for the change of diffusion is that the energy of the electrons goes through a change-over from thermal behaviour to field-dominated behaviour. Moreover, the presence of impurities in LXe can change the momentum transfer cross section of electrons due to the Ramsauer effect [376, 377, 378]. Moreover, it was observed that impurity molecules can increase the drift velocity of electrons [73, 379]. The mobility of electrons is related to the electron lifetime through the average time between collisions of an electron in LXe [379, 377],

$$\mu_e = \frac{e\tau_c}{m_e^*} \tag{5.28}$$

As the diffusion is related to the mobility of electrons in the medium (see Equation 5.26), it is important for diffusion studies to always report the electron lifetime, to account properly for systematic effects.

Coulomb repulsion between electrons

The calculated results for the longitudinal diffusion omitted the effect of Coulomb repulsion between electrons, which can increase the final width observed. Depending on the charge distribution, Coulomb repulsion can be a non-negligible source in diffusion constants, when the derived constant is aimed to be related to any charge distribution from electrons. The electrons in the cloud will have a repulsive moment relative to the centre of the cloud. The effect is expected to be more dominant

when the photoelectrons are generated, and the charge density is the highest, with lesser impact as the electron cloud diffuses through the drift path. The repulsive velocity can be written as

$$v_r = E_r \mu, \tag{5.29}$$

where E_r is the repulsive field generated by the other electrons in the cloud and μ the electron mobility assumed to be constant ($E_r << E_d$, with E_d the drift field in the z-direction). The random walk of the electrons can be modified to include the repulsive force as:

$$\Delta r = \Delta t v_r + \Delta r_d, \tag{5.30}$$

where Δr_d is the position step in the random walk. The previous formulas requires a correct modelling of the involved electric fields. The Coulomb force by the remaining electrons in the cloud is (following Ref. [380])

$$E_r = \frac{-(r_i P i N_{e^-})}{4\pi\epsilon_{\text{LXe}}|r_i|^3}, \tag{5.31}$$

where $P_i = 1/10i$ with $i = \{1, ..., .10\}$ for a cloud of mean-square radius of R_0 of N_{e^-} electrons divided in 10 clouds, a spherical distribution of charge, and ϵ_{LXe} is the dielectric constant in LXe. The value r_i of each sphere is obtained by integrating the differential volume element times the density distribution in a way that the sphere enclosures 1/10 of the N_{e^-} electrons. This approach was used in Ref. [381]. However, in Ref. [359], the approach used was from Ref. [382], where they find that for $N_{e^-} \sim 2 \times 10^5$ electrons, the broadening due to Coulomb repulsion is small but becomes more significant when $N_{e^-} \sim 8 \times 10^5$. The correction due to Coulomb repulsion ranges from 6.1% to 17.4% for LXe. However, it should be remarked that in Ref. [359], a laser of 71 ns FWHM pulse was used, which generates electrons in a shorter time, thus creating a localized charge distribution. The concentrated charge density likely impacts their estimation of the Coulomb repulsion, as the electrons are generated closely in time. It is unknown if the Refs. [251, 180] have taken into account the Coulomb repulsion in their calculations.
The work presented here will be improved by adding the effect of Coulomb repulsion from electric field simulations.

5.5 Concluding remarks and future plans

We have described in this chapter the electrical and mechanical design of the field cage for a 2.6 m tall TPC, and the design, commissioning and operation of a PM of 53 cm inside the double-walled

cryostat in Xenoscope. The PM has successfully measured the electron lifetime of the system, allowing troubleshooting of possible issues in the purification system and the drift path of electrons. We have achieved an electron lifetime of $(660 \pm 50)\,\mu s$, close to the values achieved in larger setups by XENON1T and LUX, of $660\,\mu s$ and $750\,\mu s$, respectively [383, 384]. We have shown how these measurements can be used to calculate the drift velocity of electrons in LXe, with a good match with previous measurements. Apart from providing the most recent measurements of the drift velocity at different electric fields where the electron lifetime is monitored, the data was used to calculate the longitudinal diffusion of electrons in LXe at relatively low electric fields. These measurements are important as well for packages like NEST, which lacks input at low drift fields. We have shown how these measurements match the values from two previous works, validating the hypothesis of a regime change in the diffusion of electrons under low drift fields, from a regime where their spread is thermally dominated to a field dominated regime. Further measurements in Xenoscope will advance these studies and provide more information about xenon properties needed for the next generation of LXe TPCs, especially DARWIN.

The PM will be upgraded to a dual-phase TPC in fall 2022, and will include a photosensor array on top of the field cage. The upgrade will be divided into two phases: a first phase with a $1\,m$ field cage, and a second phase extending the field cage to a total length of $2.6\,m$. Extending the field cage will probe longer drift regions, where not only the longitudinal diffusion can be measured, but with the use of a photosensor array, transversal diffusion can be studied as well. Measurements in transversal diffusion are scarce [201], and Xenoscope can provide valuable information for the community. The photosensor array consists of VUV $12\,mm \times 12\,mm$ Multi-Pixel Photon Counter (MPPC), also known as silicon photomultiplier (SiPM) from Hamamatsu, following the successful implementation of these in Ref [336]. The array will hold 192 $6 \times 6\ mm^2$ single detectors, distributed in 12 tiles of four 2×2 detectors ($12 \times 12\ mm^2$) modules, and 16 SiPM tiles will be read out. These will be the only light sensors in the array since the bottom of the TPC will host the electron-emitting photocathode, coupled to the xenon lamp via an optical fibre, as in the PM configuration.

The setup will also allow studies on the attenuation of VUV light in LXe, where current values contain large uncertainties. [190]. Figure 5.32 shows the current design of the $1\,m$ TPC and the top photosensor array with 12 tiles, together with gas–liquid interface level sensors (labelled as *short levelmeters*, which were designed as part of this work but are not covered in this dissertation). An in-depth characterisation of the array is currently ongoing to assess the single photoelectron (SPE) resolution and their behaviour at cryogenic temperatures, investigated as well previously in Refs. [385, 386]. The Xenoscope facility will also serve as the infrastructure needed to test new HV delivery technologies and operating different photosensor technologies in the bottom array that will sustain the same

hydrostatic pressure as in DARWIN.

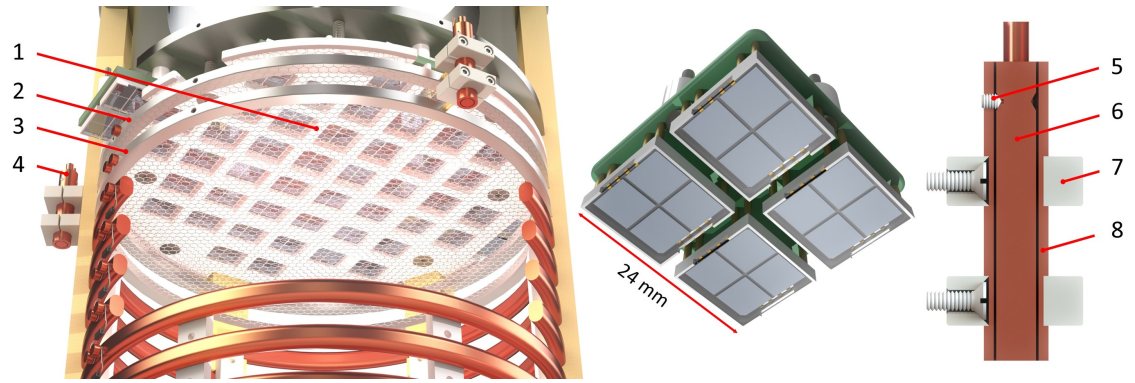

Figure 5.32: Left: Upper section of the TPC, showing the SiPM array. Legend: (1) SiPM array; (2) Anode mesh; (3) Gate mesh; (4) Short level meter. (Middle): SiPM tile containing four quad modules of SiPMs. Right: Short level meter. Legend: (5) Positioning screws; (6) Inner cylinder; (7) Mounting holders, (8) Outer cylinder.

Chapter 6

Summary and conclusions

There is extensive evidence of a DM component in the Universe that has been not yet detected. In addition, the SM does not provide a definite answer for some problems, such as CP-violation and the mechanism by which neutrinos acquire mass. These missing pieces in our current understanding of the elementary particles in the SM have motivated the existence of numerous astroparticle detectors that could potentially observe DM candidates, among others. One of these detectors is the LXe TPC direct DM XENONnT experiment at LNGS, which is currently acquiring science data.

With the continuous sensitivity improvement of LXe TPCs, the detectors will eventually observe the signature of solar neutrinos interacting with the xenon target, with similar imprints to those of WIMP DM particles. At this point, the neutrino flux will need to be constrained in order to observe the excess due to the interaction of WIMP particles with the detectors.

The DARWIN observatory will be a next-generation dual-phase LXe TPC of $50\,\mathrm{t}$, ($40\,\mathrm{t}$ active target), which aims to cover the parameter space of SI WIMP interactions up to the region in which solar neutrinos will be observed. Due to its high sensitivity, the DARWIN observatory will have as well a competitive program for detecting other rare interactions. This program includes measuring the low-energy solar neutrino flux with $< 1\%$ precision, potential observation of supernova neutrinos, galactic axion-like particles and the neutrinoless double beta decay of ^{136}Xe.

One of the goals of this thesis was to estimate the sensitivity of DARWIN to rare interactions, such as the $0\nu\beta\beta$-decay of the naturally abundant ^{136}Xe (Chapter 3) and solar axions (Chapter 4). For the $0\nu\beta\beta$-decay of ^{136}Xe, the backgrounds in the ROI (2434–$2481\,\mathrm{keV}$) of this process were dominated by the β-decay of ^{137}Xe and radiogenic background from materials. The backgrounds were estimated via analytical calculations and the development of a Geant4 geometry followed by MC simulations for the radiogenic background contribution. The modelling of the background spectra

and rates, together with the signal model, was used to build a profile likelihood in order to estimate the sensitivity. By minimising the profile likelihood based on the null and the alternate hypothesis by performing toyMCs, the sensitivity at 90% C.L and the discovery potential of DARWIN for the $0\nu\beta\beta$ process were estimated. The sensitivity after ten years exposure of 5 tonnes fiducial mass of LXe was calculated as 2×10^{27}y, with a discovery potential of 2×10^{27}y.

A hypothetical flux of solar axions could interact with DARWIN, and the sensitivity of DARWIN to such particles was estimated in order to constrain the couplings of axions to electrons, photons and nucleons (g_{ae}, $g_{a\gamma\gamma}$ and g_{an}, respectively) was estimated. We have performed one of the first studies, which includes the inverse Primakoff process from solar axions interacting with the xenon atoms, together with the axioelectric effect, for the ABC, Primakoff and ^{57}Fe hypothetical solar fluxes. The cross section of the inverse Primakoff process was implemented by utilising tabulated values from relativistic Hartree Fock methods for the atomic form factor of xenon. We have used the analytical estimations of the backgrounds in the ROI of this search (1 20keV), together with the estimation of the radiogenic contribution, to find an optimal mass to perform the study to increase the sensitivity to the axion coupling parameters, obtaining a fiducial mass of 33 tonnes. In this choice, the main background contributions are from solar neutrinos (mostly pp-neutrinos) and the $2\nu\beta\beta$-decay of ^{136}Xe, together with the β-decays of ^{214}Pb, ^{212}Pn and ^{85}Kr. An statistical framework was built in order to sample the coupling parameters in a 3D volume, constraining in the toyMCs simultaneously the coupling values for the null and alternate hypotheses. Finally, we presented the limits for the couplings g_{ae} $g_{a\gamma\gamma}$ and g_{an} by projecting the boundary region of the sampled volume from which a 90% C.L can be obtained.

Besides performing sensitivity studies, we have worked in the R&D for LXe TPC in the local Xenoscope facility at the University of Zurich. We have designed by performing electric field and mechanical simulations a $2.6\,\mathrm{m}$ field cage of $15\,\mathrm{cm}$ diameter of modular construction, which will serve as a demonstrator for necessary technologies in order to build DARWIN. We have also worked on the design of a PM for Xenoscope. We have selected the optical system, developed cold electronics amplifiers and produced in-house photocathodes to develop the charge source. We have produced, alongside the Mechanical Workshop at the Institute, the first module of the field cage of $53\,\mathrm{cm}$ for the PM. With the operation of the PM, we observed the evolution of the electron lifetime, which is related to the concentration of electronegative impurities in the system. A value of $(660 \pm 50)\,\mu\mathrm{s}$ was achieved, which is comparable to those achieved by the XENON1T and LUX experiments. Studies of the electron transport in LXe at drift fields, where previous data is scarce, were performed. In particular, regime change in the diffusion of electrons was observed, and an explanation was provided based on energy acquired by the electrons from thermal to electric dominated.

Bibliography

[1] DARWIN collaboration, *Sensitivity of the DARWIN observatory to the neutrinoless double beta decay of ^{136}Xe*, *Eur. Phys. J. C* **80** (2020) 808 [2003.13407].

[2] ATLAS collaboration, *Discovery of a new boson - the ATLAS perspective*, *CERN Cour.* **52N7** (2012) 43.

[3] P. Langacker, *Introduction to the Standard Model and Electroweak Physics*, in *Theoretical Advanced Study Institute in Elementary Particle Physics: The Dawn of the LHC Era*, pp. 3–48, 2010, DOI [0901.0241].

[4] S. Troitsky, *Unsolved problems in particle physics*, *Phys. Usp.* **55** (2012) 72 [1112.4515].

[5] P. Draper, G. Lee and C.E.M. Wagner, *Precise estimates of the Higgs mass in heavy supersymmetry*, *Phys. Rev. D* **89** (2014) 055023 [1312.5743].

[6] Muon g-2 collaboration, *Measurement of the Positive Muon Anomalous Magnetic Moment to 0.46 ppm*, *Phys. Rev. Lett.* **126** (2021) 141801 [2104.03281].

[7] T. Aoyama et al., *The anomalous magnetic moment of the muon in the Standard Model*, *Phys. Rept.* **887** (2020) 1 [2006.04822].

[8] J. Christenson, J. Cronin, V. Fitch and R. Turlay, *Evidence for the 2π Decay of the K_2^0 Meson*, *Phys.Rev.Lett.* **13** (1964) 138.

[9] T. Lee and C.-N. Yang, *Question of Parity Conservation in Weak Interactions*, *Phys.Rev.* **104** (1956) 254.

[10] C.-S. Wu, *The discovery of the parity violation in weak interactions and its recent developments*, *Lect. Notes Phys.* **746** (2008) 43.

[11] J. Hisano, J.Y. Lee, N. Nagata and Y. Shimizu, *Reevaluation of Neutron Electric Dipole Moment with QCD Sum Rules*, *Phys. Rev. D* **85** (2012) 114044 [1204.2653].

[12] C. Abel et al., *Measurement of the permanent electric dipole moment of the neutron*, *Phys. Rev. Lett.* **124** (2020) 081803.

[13] R.D. Peccei and H.R. Quinn, *CP Conservation in the Presence of Instantons*, *Phys.Rev.Lett.* **38** (1977) 1440.

[14] H. Quinn, *B physics and CP violation*, *ICTP Lect. Notes Ser.* **10** (2002) 1 [hep-ph/0111177].

[15] S. Weinberg, *Gravitation and Cosmology: Principles and Applications of the General Theory of Relativity*, John Wiley and Sons, New York (1972).

[16] F. Wilczek, *Problem of strong P and T invariance in the presence of instantons*, *Phys. Rev. Lett.* **40** (1978) 279.

[17] L. Di Luzio, M. Giannotti, E. Nardi and L. Visinelli, *The landscape of QCD axion models*, *Phys. Rept.* **870** (2020) 1 [2003.01100].

[18] L.F. Abbott and P. Sikivie, *A Cosmological Bound on the Invisible Axion*, *Phys. Lett. B* **120** (1983) 133.

[19] M. Dine, W. Fischler and M. Srednicki, *A Simple Solution to the Strong CP Problem with a Harmless Axion*, *Phys. Lett. B* **104** (1981) 199.

[20] M.A. Shifman, A.I. Vainshtein and V.I. Zakharov, *Can Confinement Ensure Natural CP Invariance of Strong Interactions?*, *Nucl. Phys. B* **166** (1980) 493.

[21] A.R. Zhitnitsky, *On Possible Suppression of the Axion Hadron Interactions. (In Russian)*, *Sov. J. Nucl. Phys.* **31** (1980) 260.

[22] J.E. Kim, *Weak Interaction Singlet and Strong CP Invariance*, *Phys. Rev. Lett.* **43** (1979) 103.

[23] G.G. Raffelt, *Axions: Motivation, limits and searches*, *J. Phys. A* **40** (2007) 6607 [hep-ph/0611118].

[24] G. Bertone, D. Hooper and J. Silk, *Particle dark matter: Evidence, candidates and constraints*, *Phys. Rept.* **405** (2005) 279 [hep-ph/0404175].

[25] L. Bergström and A. Goobar, *Cosmology and particle astrophysics*, Springer Science & Business Media (2006).

[26] S. Dodelson, *Modern Cosmology*, Academic Press, Amsterdam (2003).

[27] H. Stephani, *Relativity: An introduction to special and general relativity*, Cambridge university press (2004).

[28] Planck collaboration, *Planck 2018 results. VI. Cosmological parameters*, *Astron. Astrophys.* **641** (2020) A6 [1807.06209].

[29] A.A. Penzias and R.W. Wilson, *A Measurement of excess antenna temperature at 4080-Mc/s*, *Astrophys. J.* **142** (1965) 419.

[30] WMAP collaboration, *Nine-Year Wilkinson Microwave Anisotropy Probe (WMAP) Observations: Final Maps and Results*, *Astrophys. J. Suppl.* **208** (2013) 20 [1212.5225].

[31] A. Challinor, *Cmb anisotropy science: a review*, *Proceedings of the International Astronomical Union* **8** (2012) 42.

[32] Planck collaboration, *Planck 2015 results. XI. CMB power spectra, likelihoods, and robustness of parameters*, *Astron. Astrophys.* **594** (2016) A11 [1507.02704].

[33] G.A. Campbell and R.A. Matzner, *A model for peaking of galactic gravitational radiation*, *J. Math. Phys.* **14** (1973) 1.

[34] DES collaboration, *Wide-Field Lensing Mass Maps from Dark Energy Survey Science Verification Data*, *Phys. Rev. Lett.* **115** (2015) 051301 [1505.01871].

[35] Y. Sofue, *Rotation Curve of the Milky Way and the Dark Matter Density*, *Galaxies* **8** (2020) 37 [2004.11688].

[36] V.C. Rubin, W.K. Ford, Jr. and N. Thonnard, *Extended rotation curves of high-luminosity spiral galaxies. IV. Systematic dynamical properties, Sa through Sc*, *Astrophys. J. Lett.* **225** (1978) L107.

[37] M. Lisanti, *Lectures on Dark Matter Physics*, in *Theoretical Advanced Study Institute in Elementary Particle Physics: New Frontiers in Fields and Strings*, pp. 399–446, 2017, DOI [1603.03797].

[38] L. Roszkowski, E.M. Sessolo and S. Trojanowski, *WIMP dark matter candidates and searches—current status and future prospects*, *Rept. Prog. Phys.* **81** (2018) 066201 [1707.06277].

[39] J.-W. Lee, *Brief History of Ultra-light Scalar Dark Matter Models*, *EPJ Web Conf.* **168** (2018) 06005 [1704.05057].

[40] G. Arcadi, M. Dutra, P. Ghosh, M. Lindner, Y. Mambrini, M. Pierre et al., *The waning of the WIMP? A review of models, searches, and constraints*, *Eur. Phys. J. C* **78** (2018) 203 [1703.07364].

[41] J.L. Feng, *Dark Matter Candidates from Particle Physics and Methods of Detection*, *Ann. Rev. Astron. Astrophys.* **48** (2010) 495 [1003.0904].

[42] J.F. Navarro, C.S. Frenk and S.D.M. White, *The Structure of cold dark matter halos*, *Astrophys. J.* **462** (1996) 563 [astro-ph/9508025].

[43] G. Jungman, M. Kamionkowski and K. Griest, *Supersymmetric dark matter*, *Phys. Rept.* **267** (1996) 195 [hep-ph/9506380].

[44] M. Battaglieri et al., *US Cosmic Visions: New Ideas in Dark Matter 2017: Community Report*, in *U.S. Cosmic Visions: New Ideas in Dark Matter*, 7, 2017 [1707.04591].

[45] T. Alanne, N. Benincasa, M. Heikinheimo, K. Kannike, V. Keus, N. Koivunen et al., *Pseudo-Goldstone dark matter: gravitational waves and direct-detection blind spots*, *JHEP* **10** (2020) 080 [2008.09605].

[46] M. Farina, M. Kadastik, D. Pappadopulo, J. Pata, M. Raidal and A. Strumia, *Implications of XENON100 and LHC results for Dark Matter models*, *Nucl. Phys. B* **853** (2011) 607 [1104.3572].

[47] S. Bottaro, D. Buttazzo, M. Costa, R. Franceschini, P. Panci, D. Redigolo et al., *The last Complex WIMPs standing*, 2205.04486.

[48] G. Ballesteros, J. Redondo, A. Ringwald and C. Tamarit, *Standard Model—axion—seesaw—Higgs portal inflation. Five problems of particle physics and cosmology solved in one stroke*, *JCAP* **08** (2017) 001 [1610.01639].

[49] D. Abercrombie et al., *Dark Matter benchmark models for early LHC Run-2 Searches: Report of the ATLAS/CMS Dark Matter Forum*, *Phys. Dark Univ.* **27** (2020) 100371 [1507.00966].

[50] P.J. Fox, R. Harnik, J. Kopp and Y. Tsai, *Missing Energy Signatures of Dark Matter at the LHC*, *Phys. Rev. D* **85** (2012) 056011 [1109.4398].

[51] CMS collaboration, *Search for dark matter, extra dimensions, and unparticles in monojet events in proton–proton collisions at* $\sqrt{s} = 8$ *TeV*, *Eur. Phys. J. C* **75** (2015) 235 [1408.3583].

[52] F. Kahlhoefer, *Review of LHC Dark Matter Searches*, *Int. J. Mod. Phys. A* **32** (2017) 1730006 [1702.02430].

[53] J. Conrad, J. Cohen-Tanugi and L.E. Strigari, *WIMP searches with gamma rays in the Fermi era: challenges, methods and results*, *J. Exp. Theor. Phys.* **121** (2015) 1104 [1503.06348].

[54] T. Daylan, D.P. Finkbeiner, D. Hooper, T. Linden, S.K.N. Portillo, N.L. Rodd et al., *The characterization of the gamma-ray signal from the central Milky Way: A case for annihilating dark matter*, *Phys. Dark Univ.* **12** (2016) 1 [1402.6703].

[55] T. Tanimori, H. Kubo, K. Miuchi, T. Nagayoshi, R. Orito, A. Takada et al., *Detecting the wimp-wind via spin-dependent interactions*, *Phys. Lett. B* **578** (2004) 241 [astro-ph/0310638].

[56] R. Catena and P. Ullio, *A novel determination of the local dark matter density*, *JCAP* **08** (2010) 004 [0907.0018].

[57] M. Weber and W. de Boer, *Determination of the Local Dark Matter Density in our Galaxy*, *Astron. Astrophys.* **509** (2010) A25 [0910.4272].

[58] M.C. Smith et al., *The RAVE Survey: Constraining the Local Galactic Escape Speed*, *Mon. Not. Roy. Astron. Soc.* **379** (2007) 755 [astro-ph/0611671].

[59] A.K. Drukier, K. Freese and D.N. Spergel, *Detecting Cold Dark Matter Candidates*, *Phys. Rev. D* **33** (1986) 3495.

[60] XENON collaboration, *Constraining the spin-dependent WIMP-nucleon cross sections with XENON1T*, *Phys. Rev. Lett.* **122** (2019) 141301 [1902.03234].

[61] DAMA collaboration, *First results from DAMA/LIBRA and the combined results with DAMA/NaI*, *Eur. Phys. J. C* **56** (2008) 333 [0804.2741].

[62] DEAP-3600 collaboration, *First results from the DEAP-3600 dark matter search with argon at SNOLAB*, *Phys. Rev. Lett.* **121** (2018) 071801 [1707.08042].

[63] K. Abe et al., *XMASS detector*, *Nucl. Instrum. Meth. A* **716** (2013) 78 [1301.2815].

[64] COSINE-100 collaboration, *Three-year annual modulation search with COSINE-100*, 2111.08863.

[65] J. Amaré et al., *Dark Matter Searches Using NaI(Tl) at the Canfranc Underground Laboratory: Past, Present and Future*, *Universe* **8** (2022) 75.

[66] DAMIC collaboration, *Search for low-mass WIMPs in a 0.6 kg day exposure of the DAMIC experiment at SNOLAB*, *Phys. Rev. D* **94** (2016) 082006 [1607.07410].

[67] SENSEI collaboration, *SENSEI: Direct-Detection Constraints on Sub-GeV Dark Matter from a Shallow Underground Run Using a Prototype Skipper-CCD*, *Phys. Rev. Lett.* **122** (2019) 161801 [1901.10478].

[68] PICO collaboration, *Dark Matter Search Results from the PICO-60 C_3F_8 Bubble Chamber*, *Phys. Rev. Lett.* **118** (2017) 251301 [1702.07666].

[69] SuperCDMS collaboration, *Search for Low-Mass Weakly Interacting Massive Particles with SuperCDMS*, *Phys. Rev. Lett.* **112** (2014) 241302 [1402.7137].

[70] CRESST collaboration, *Results on light dark matter particles with a low-threshold CRESST-II detector*, *Eur. Phys. J. C* **76** (2016) 25 [1509.01515].

[71] P. Cushman et al., *Working Group Report: WIMP Dark Matter Direct Detection*, in *Community Summer Study 2013: Snowmass on the Mississippi*, 10, 2013 [1310.8327].

[72] J.B. Birks, *The Theory and Practice of Scintillation Counting: International Series of Monographs on Electronics and Instrumentation*, *Pergamon Press* **27** (2013) 663.

[73] E. Shibamura, A. Hitachi, T. Doke, T. Takahashi, S. Kubota and M. Miyajima, *Drift velocities of electrons, saturation characteristics of ionization and W-values for conversion electrons in liquid argon, liquid argon-gas mixtures and liquid xenon*, *Nucl. Instrum. Meth.* **131** (1975) 249.

[74] E. Segreto, *Properties of Liquid Argon Scintillation Light Emission*, *Phys. Rev. D* **103** (2021) 043001 [2012.06527].

[75] DARWIN collaboration, *DARWIN: dark matter WIMP search with noble liquids*, *J. Phys. Conf. Ser.* **375** (2012) 012028 [1201.2402].

[76] XENON collaboration, *Dark Matter Search Results from a One Ton-Year Exposure of XENON1T*, *Phys. Rev. Lett.* **121** (2018) 111302 [1805.12562].

[77] LUX collaboration, *First results from the LUX dark matter experiment at the Sanford Underground Research Facility*, *Phys. Rev. Lett.* **112** (2014) 091303 [1310.8214].

[78] PandaX-4T collaboration, *Dark Matter Search Results from the PandaX-4T Commissioning Run*, *Phys. Rev. Lett.* **127** (2021) 261802 [2107.13438].

[79] DarkSide Collaboration, P. Agnes, I.F.M. Albuquerque, T. Alexander, A.K. Alton, G.R. Araujo et al., *Low-Mass Dark Matter Search with the DarkSide-50 Experiment*, *Physical Review Letters* **121** (2018) 081307.

[80] E. Aprile et al., *Measurement of the Scintillation Yield of Low-Energy Electrons in Liquid Xenon*, *Phys. Rev.* **D86** (2012) 112004 [1209.3658].

[81] LZ collaboration, *Direct search for WIMP dark matter particles with the LUX-ZEPLIN (LZ) detector*, *Nucl. Instrum. Meth. A* **936** (2019) 162.

[82] J. Billard, L. Strigari and E. Figueroa-Feliciano, *Implication of neutrino backgrounds on the reach of next generation dark matter direct detection experiments*, *Phys. Rev.* **D89** (2014) 023524 [1307.5458].

[83] COHERENT collaboration, *Observation of Coherent Elastic Neutrino-Nucleus Scattering*, *Science* **357** (2017) 1123 [1708.01294].

[84] D. Aristizabal Sierra, B. Dutta, S. Liao and L.E. Strigari, *Coherent elastic neutrino-nucleus scattering in multi-ton scale dark matter experiments: Classification of vector and scalar interactions new physics signals*, *JHEP* **12** (2019) 124 [1910.12437].

[85] A. Anderson et al., *Coherent Neutrino Scattering in Dark Matter Detectors*, *Phys. Rev.* **D84** (2011) 013008 [1103.4894].

[86] L.E. Strigari, *Neutrino coherent scattering rates at direct dark matter detectors*, *New Journal of Physics* **11** (2009) 105011.

[87] K. Scholberg, *Coherent Elastic Neutrino-Nucleus Scattering*, *J. Phys. Conf. Ser.* **1468** (2020) 012126.

[88] G.B. Gelmini, V. Takhistov and S.J. Witte, *Casting a Wide Signal Net with Future Direct Dark Matter Detection Experiments*, *JCAP* **07** (2018) 009 [1804.01638].

[89] C.A.J. O'Hare, *Can we overcome the neutrino floor at high masses?*, *Phys. Rev. D* **102** (2020) 063024 [2002.07499].

[90] C.A.J. O'Hare, *New Definition of the Neutrino Floor for Direct Dark Matter Searches*, *Phys. Rev. Lett.* **127** (2021) 251802 [2109.03116].

[91] DARWIN collaboration, *DARWIN: towards the ultimate dark matter detector*, *JCAP* **11** (2016) 017 [1606.07001].

[92] CRESST Collaboration, A.H. Abdelhameed, G. Angloher, P. Bauer, A. Bento, E. Bertoldo et al., *First results from the CRESST-III low-mass dark matter program*, *Physical Review D* **100** (2019) 102002.

[93] NEWS collaboration, *NEWS: Nuclear Emulsions for WIMP Search*, 1604.04199.

[94] SuperCDMS collaboration, *Low-mass dark matter search with CDMSlite*, *Phys. Rev. D* **97** (2018) 022002 [1707.01632].

[95] LUX collaboration, *Liquid xenon scintillation measurements and pulse shape discrimination in the LUX dark matter detector*, *Phys. Rev. D* **97** (2018) 112002 [1802.06162].

[96] J. Billard et al., *Direct Detection of Dark Matter – APPEC Committee Report*, 2104.07634.

[97] P.D. Group, P.A. Zyla, R.M. Barnett, J. Beringer, O. Dahl, D.A. Dwyer et al., *Review of Particle Physics*, *Progress of Theoretical and Experimental Physics* **2020** (2020) [https://academic.oup.com/ptep/article-pdf/2020/8/083C01/34673722/ptaa104.pdf].

[98] G. Carosi, A. Friedland, M. Giannotti, M.J. Pivovaroff, J. Ruz and J.K. Vogel, *Probing the axion-photon coupling: phenomenological and experimental perspectives. A snowmass white paper*, in *Community Summer Study 2013: Snowmass on the Mississippi*, 9, 2013 [1309.7035].

[99] G.G. Raffelt, *Astrophysical axion bounds*, *Lect.Notes Phys.* **741** (2008) 51 [0611350].

[100] N. Viaux, M. Catelan, P.B. Stetson, G. Raffelt, J. Redondo, A.A.R. Valcarce et al., *Particle-physics constraints from the globular cluster M5: Neutrino Dipole Moments*, *Astron. Astrophys.* **558** (2013) A12 [1308.4627].

[101] N. Viaux, M. Catelan, P.B. Stetson, G. Raffelt, J. Redondo, A.A.R. Valcarce et al., *Neutrino and axion bounds from the globular cluster M5 (NGC 5904)*, *Phys. Rev. Lett.* **111** (2013) 231301 [1311.1669].

[102] D. Cadamuro, S. Hannestad, G. Raffelt and J. Redondo, *Cosmological bounds on sub-MeV mass axions*, *JCAP* **02** (2011) 003 [1011.3694].

[103] XENON collaboration, *Excess electronic recoil events in XENON1T*, *Phys. Rev. D* **102** (2020) 072004 [2006.09721].

[104] LZ collaboration, *Projected sensitivities of the LUX-ZEPLIN experiment to new physics via low-energy electron recoils*, *Phys. Rev. D* **104** (2021) 092009 [2102.11740].

[105] XENON100 collaboration, *First Axion Results from the XENON100 Experiment*, *Phys. Rev. D* **90** (2014) 062009 [1404.1455].

[106] EDELWEISS collaboration, *Searches for electron interactions induced by new physics in the EDELWEISS-III Germanium bolometers*, *Phys. Rev. D* **98** (2018) 082004 [1808.02340].

[107] LUX collaboration, *First Searches for Axions and Axionlike Particles with the LUX Experiment*, *Phys. Rev. Lett.* **118** (2017) 261301 [1704.02297].

[108] XMASS collaboration, *Search for solar Kaluza–Klein axions by annual modulation with the XMASS-I detector*, *PTEP* **2017** (2017) 103C01 [1707.08995].

[109] P. Gondolo and G.G. Raffelt, *Solar neutrino limit on axions and keV-mass bosons*, *Phys. Rev. D* **79** (2009) 107301 [0807.2926].

[110] A.V. Derbin, I.S. Drachnev, A.S. Kayunov and V.N. Muratova, *Constraints on the axion-electron coupling constant for solar axions appearing owing to bremsstrahlung and the Compton process*, *JETP Lett.* **95** (2012) 339 [1206.4142].

[111] KIMS collaboration, *Search for solar axions with CsI(Tl) crystal detectors*, *JHEP* **06** (2016) 011 [1604.01825].

[112] CDEX collaboration, *Improved limits on solar axions and bosonic dark matter from the CDEX-1B experiment using the profile likelihood ratio method*, *Phys. Rev. D* **101** (2020) 052003 [1911.03085].

[113] K. Van Tilburg, *Stellar basins of gravitationally bound particles*, *Phys. Rev. D* **104** (2021) 023019 [2006.12431].

[114] P. Sikivie, *Experimental Tests of the Invisible Axion*, *Phys. Rev. Lett.* **51** (1983) 1415.

[115] CAST collaboration, *New CAST Limit on the Axion-Photon Interaction*, *Nat. Phys.* **13** (2017) 584 [1705.02290v2].

[116] I. Shilon, A. Dudarev, H. Silva, U. Wagner and H.H.J. ten Kate, *The Superconducting Toroid for the New International AXion Observatory (IAXO)*, *IEEE Trans. Appl. Supercond.* **24** (2014) 4500104 [1309.2117].

[117] ADMX collaboration, *A SQUID-based microwave cavity search for dark-matter axions*, *Phys. Rev. Lett.* **104** (2010) 041301 [0910.5914].

[118] C.P. Salemi et al., *Search for Low-Mass Axion Dark Matter with ABRACADABRA-10 cm*, *Phys. Rev. Lett.* **127** (2021) 081801 [2102.06722].

[119] A.V. Gramolin, D. Aybas, D. Johnson, J. Adam and A.O. Sushkov, *Search for axion-like dark matter with ferromagnets*, *Nature Phys.* **17** (2021) 79 [2003.03348].

[120] M. Regis, M. Taoso, D. Vaz, J. Brinchmann, S.L. Zoutendijk, N.F. Bouché et al., *Searching for light in the darkness: Bounds on ALP dark matter with the optical MUSE-faint survey*, *Phys. Lett. B* **814** (2021) 136075 [2009.01310].

[121] F. Della Valle, A. Ejlli, U. Gastaldi, G. Messineo, E. Milotti, R. Pengo et al., *The PVLAS experiment: measuring vacuum magnetic birefringence and dichroism with a birefringent Fabry–Perot cavity*, *Eur. Phys. J. C* **76** (2016) 24 [1510.08052].

[122] OSQAR collaboration, *New exclusion limits on scalar and pseudoscalar axionlike particles from light shining through a wall*, *Phys. Rev. D* **92** (2015) 092002 [1506.08082].

[123] SAPPHIRES collaboration, *Search for sub-eV axion-like resonance states via stimulated quasi-parallel laser collisions with the parameterization including fully asymmetric collisional geometry*, *JHEP* **12** (2021) 108 [2105.01224].

[124] C. O'Hare, "Axion limits." Link to repository, July, 2020. 10.5281/zenodo.3932430.

[125] XENON collaboration, *Double-Weak Decays of ^{124}Xe and ^{136}Xe in the XENON1T and XENONnT Experiments*, 2205.04158.

[126] DARWIN collaboration, *Solar neutrino detection sensitivity in DARWIN via electron scattering*, *Eur. Phys. J. C* **80** (2020) 1133 [2006.03114].

[127] M. Goldhaber, L. Grodzins and A.W. Sunyar, *Helicity of Neutrinos*, *Phys. Rev.* **109** (1958) 1015.

[128] B. Pontecorvo, *Neutrino Experiments and the Problem of Conservation of Leptonic Charge*, *Zh. Eksp. Teor. Fiz.* **53** (1967) 1717.

[129] Z. Maki, M. Nakagawa and S. Sakata, *Remarks on the unified model of elementary particles*, *Prog. Theor. Phys.* **28** (1962) 870.

[130] R. Davis, Jr., D.S. Harmer and K.C. Hoffman, *Search for neutrinos from the sun*, *Phys. Rev. Lett.* **20** (1968) 1205.

[131] Kamiokande-II collaboration, *Search for day / night and semiannual variations in the solar neutrino flux observed in the Kamiokande-II detector*, *Phys. Rev. Lett.* **66** (1991) 9.

[132] SAGE collaboration, *Results from SAGE*, *Phys. Lett. B* **328** (1994) 234.

[133] GALLEX collaboration, *Solar neutrinos observed by GALLEX at Gran Sasso.*, *Phys. Lett. B* **285** (1992) 376.

[134] Super-Kamiokande collaboration, *Evidence for oscillation of atmospheric neutrinos*, *Phys. Rev. Lett.* **81** (1998) 1562 [hep-ex/9807003].

[135] SNO collaboration, *Direct evidence for neutrino flavor transformation from neutral current interactions in the Sudbury Neutrino Observatory*, *Phys. Rev. Lett.* **89** (2002) 011301 [nucl-ex/0204008].

[136] Particle Data Group collaboration, *Review of Particle Physics*, *Phys. Rev. D* **98** (2018) 030001.

[137] E.K. Akhmedov, *Neutrino physics*, in *ICTP Summer School in Particle Physics*, pp. 103–164, 6, 1999 [hep-ph/0001264].

[138] S.M. Bilenky, *Neutrinos: Majorana or Dirac?*, *Universe* **6** (2020) 134.

[139] BOREXINO collaboration, *Comprehensive measurement of pp-chain solar neutrinos with Borexino*, *PoS* **EPS-HEP2019** (2020) 400.

[140] P. Zyla et al., *Particle data group*, *Prog. Theor. Exp. Phys. 083C01* (2020) .

[141] S.M. Bilenky, *The History of neutrino oscillations*, *Phys. Scripta T* **121** (2005) 17 [hep-ph/0410090].

[142] S. Bilenky, *Neutrinos: Majorana or Dirac?*, 2008.02110.

[143] B. Kayser, F. Gibrat-Debu and F. Perrier, *The Physics of massive neutrinos*, *World Sci.Lect.Notes Phys.* **25** (1989) 1.

[144] M. Goeppert-Mayer, *Double beta-disintegration*, *Phys. Rev.* **48** (1935) 512.

[145] NEMO-3 collaboration, *Measurement of double beta decay of ^{150}Nd to the 0_1^+ excited state of ^{150}Sm in NEMO-3*, 2203.03356.

[146] GERDA collaboration, *Probing Majorana neutrinos with double-β decay*, *Science* **365** (2019) 1445 [1909.02726].

[147] CUORE collaboration, *Measurement of the two-neutrino double-beta decay half-life of ^{130} Te with the CUORE-0 experiment*, *Eur. Phys. J. C* **77** (2017) 13 [1609.01666].

[148] EXO-200 collaboration, *Search for $2\nu\beta\beta$ decay of ^{136}Xe to the 0_1^+ excited state of ^{136}Ba with EXO-200*, *Phys. Rev. C* **93** (2016) 035501 [1511.04770].

[149] M.J. Dolinski, A.W.P. Poon and W. Rodejohann, *Neutrinoless Double-Beta Decay: Status and Prospects*, *Ann. Rev. Nucl. Part. Sci.* **69** (2019) 219 [1902.04097].

[150] M. Doi, T. Kotani, H. Nishiura and E. Takasugi, *DOUBLE BETA DECAY*, *Prog. Theor. Phys.* **69** (1983) 602.

[151] SuperNEMO collaboration, *Probing New Physics Models of Neutrinoless Double Beta Decay with SuperNEMO*, *Eur. Phys. J. C* **70** (2010) 927 [1005.1241].

[152] M.T. Mustonen and J. Engel, *Large-scale calculations of the double-β decay of 76Ge,130Te,136Xe, and 150Nd in the deformed self-consistent Skyrme quasiparticle random-phase approximation*, *Phys. Rev. C - Nucl. Phys.* **87** (2013) 064302.

[153] J. Engel and J. Menéndez, *Status and future of nuclear matrix elements for neutrinoless double-beta decay: A review*, mar, 2017. 10.1088/1361-6633/aa5bc5.

[154] J. Kotila and F. Iachello, *Phase-space factors for double-β decay*, *Physical Review C - Nuclear Physics* **85** (2012) [1209.5722].

[155] J. Albert, *Neutrinoless double beta decay*, *PoS* **FPCP2016** (2017) 033.

[156] F.T. Avignone, G.S. King and Y.G. Zdesenko, *Next generation double-beta decay experiments: Metrics for their evaluation*, *New J. Phys.* **7** (2005) 6.

[157] CUORE collaboration, *CUORE: A Cryogenic underground observatory for rare events*, *Nucl. Instrum. Meth. A* **518** (2004) 775 [hep-ex/0212053].

[158] GERDA collaboration, *Improved Limit on Neutrinoless Double-β Decay of ^{76}Ge from GERDA Phase II*, *Phys. Rev. Lett.* **120** (2018) 132503 [1803.11100].

[159] MAJORANA collaboration, *Search for Neutrinoless Double-β Decay in ^{76}Ge with the Majorana Demonstrator*, *Phys. Rev. Lett.* **120** (2018) 132502 [1710.11608].

[160] LEGEND collaboration, *The Large Enriched Germanium Experiment for Neutrinoless Double Beta Decay (LEGEND)*, *AIP Conf. Proc.* **1894** (2017) 020027 [1709.01980].

[161] EXO-200 collaboration, *Search for Neutrinoless Double-Beta Decay in ^{136}Xe with EXO-200*, *Phys. Rev. Lett.* **109** (2012) 032505 [1205.5608].

[162] NEXO collaboration, *Sensitivity and Discovery Potential of nEXO to Neutrinoless Double Beta Decay*, *Phys. Rev. C* **97** (2018) 065503 [1710.05075].

[163] KAMLAND-ZEN collaboration, *Search for Majorana Neutrinos near the Inverted Mass Hierarchy Region with KamLAND-Zen*, *Phys. Rev. Lett.* **117** (2016) 082503 [1605.02889].

[164] KAMLAND-ZEN collaboration, *The nylon balloon for xenon loaded liquid scintillator in KamLAND-Zen 800 neutrinoless double-beta decay search experiment*, *JINST* **16** (2021) P08023 [2104.10452].

[165] KAMLAND-ZEN collaboration, *First Search for the Majorana Nature of Neutrinos in the Inverted Mass Ordering Region with KamLAND-Zen*, 2203.02139.

[166] LNE-LNHB/CEA. ^{39}Ar from Table de Radionucléides, 2011.

[167] C. Galbiati, D. Acosta-Kane, R. Acciarri, O. Amaize, M. Antonello, B. Baibussinov et al., *Discovery of underground argon with a low level of radioactive 39Ar and possible applications to WIMP dark matter detectors*, in *J. Phys. Conf. Ser.*, vol. 120, p. 042015, Institute of Physics Publishing, jan, 2008, DOI [0712.0381].

[168] L. Baudis, G. Kessler, P. Klos, R.F. Lang, J. Menendez, S. Reichard et al., *Signatures of Dark Matter Scattering Inelastically Off Nuclei*, *Phys. Rev.* **D88** (2013) 115014 [1309.0825].

[169] O. Sifner and J. Klomfar, *Thermodynamic properties of xenon from the triple point to 800 k with pressures up to 350 mpa*, *J. physical and chemical reference data* **23** (1994) 63.

[170] C.E. Dahl, *The physics of background discrimination in liquid xenon, and first results from Xenon10 in the hunt for WIMP dark matter*, Ph.D. thesis, Princeton U., 2009.

[171] M.J. Berger and J. Hubbell, *Xcom: Photon cross sections on a personal computer*, Tech. Rep. National Bureau of Standards, Washington, DC (USA). Center for Radiation. (1987).

[172] *From ENSDF database as of July 21, 2022. Available at link.*

[173] P. Belli, R. Bernabei, S. D'Angelo, A. Incicchitti and D. Prosperi, *Liquid xenon scintillators*, *Nucl. Instruments Methods Phys. Res. Sect. A Accel. Spectrometers, Detect. Assoc. Equip.* **310** (1991) 150.

[174] NIST. Table of xenon properties, 2011.

[175] M. Schumann, *Dual-Phase Liquid Xenon Detectors for Dark Matter Searches*, *JINST* **9** (2014) C08004 [1405.7600].

[176] D. Akerib, S. Alsum, H. Araújo, X. Bai, A. Bailey, J. Balajthy et al., *Signal yields, energy resolution, and recombination fluctuations in liquid xenon*, *Physical Review D* **95** (2017) 012008.

[177] R. Walters, *Stopping-power & range tables for electrons, protons, and helium ions*, *NIST Standard Reference Database 124, NIST* (2017) .

[178] E. Aprile, C.E. Dahl, L. DeViveiros, R. Gaitskell, K.L. Giboni, J. Kwong et al., *Simultaneous Measurement of Ionization and Scintillation from Nuclear Recoils in Liquid Xenon as Target for a Dark Matter Experiment*, *Phys. Rev. Lett.* **97** (2006) [0601552v1].

[179] XENON collaboration, *The XENON dark matter search*, *J. Phys. Conf. Ser.* **308** (2011) 012010.

[180] P. Sorensen and C.E. Dahl, *Nuclear recoil energy scale in liquid xenon with application to the direct detection of dark matter*, *Phys. Rev. D - Part. Fields, Gravit. Cosmol.* **83** (2011) [1101.6080v1].

[181] J. Lindhard, V. Nielsen, M. Scharff and P. Thomsen, *Integral equations governing radiation effects*, *Mat. Fys. Medd. Dan. Vid. Selsk* **33** (1963) 1.

[182] E. Aprile, M. Anthony, Q. Lin, Z. Greene, P. de Perio, F. Gao et al., *Simultaneous measurement of the light and charge response of liquid xenon to low-energy nuclear recoils at multiple electric fields*, *Phys. Rev. D* **98** (2018) [1809.02072v2].

[183] A. Hitachi, *Properties of liquid xenon scintillation for dark matter searches*, *Astropart. Phys.* **24** (2005) 247.

[184] A. Baldini, C. Bemporad, F. Cei, T. Doke, M. Grassi, T. Haruyama et al., *Liquid Xe scintillation calorimetry and Xe optical properties*, Tech. Rep.

[185] J. Mock, N. Barry, K. Kazkaz, D. Stolp, M. Szydagis, M. Tripathi et al., *Modeling pulse characteristics in Xenon with NEST*, *J. Instrum.* **9** (2014) .

[186] M. Szydagis, J. Balajthy, J. Brodsky, J. Cutter, J. Huang, E. Kozlova et al., *Noble element simulation technique v2.0*, July, 2018. 10.5281/zenodo.1314669.

[187] E. Aprile, J. Aalbers, F. Agostini, M. Alfonsi, F.D. Amaro, M. Anthony et al., *Signal Yields of keV Electronic Recoils and Their Discrimination from Nuclear Recoils in Liquid Xenon*, *Phys. Rev. D* **97** (2017) 14 [1709.10149v2].

[188] E. Aprile, K. Arisaka, F. Arneodo, A. Askin, L. Baudis, A. Behrens et al., *Dark Matter Results from 100 Live Days of XENON100 Data*, *Phys.Rev.Lett.* **107** (2011) [1104.2549].

[189] XENON collaboration, *Application and modeling of an online distillation method to reduce krypton and argon in XENON1T*, *PTEP* **2022** (2022) 053H01 [2112.12231].

[190] XENON collaboration, *Physics reach of the XENON1T dark matter experiment*, *JCAP* **1604** (2016) 027 [1512.07501].

[191] XENON collaboration, *Dark Matter Search Results from a One Ton-Year Exposure of XENON1T*, *Phys. Rev. Lett.* **121** (2018) 111302 [1805.12562].

[192] XENON Collaboration, E. Aprile, F. Agostini, M. Alfonsi, L. Arazi, K. Arisaka et al., *Lowering the radioactivity of the photomultiplier tubes for the XENON1T dark matter experiment*, *Eur. Phys. J. C 2015 7511* **75** (2015) 1 [1503.07698].

[193] E. Aprile, J. Aalbers, F. Agostini, M. Alfonsi, L. Althueser, F.D. Amaro et al., *Projected WIMP sensitivity of the XENONnT dark matter experiment*, *JCAP* **11** (2020) 031 [2007.08796].

[194] E. Aprile, K. Arisaka, F. Arneodo, A. Askin, L. Baudis, A. Behrens et al., *Material screening and selection for xenon100*, *Astroparticle Physics* **35** (2011) 43 .

[195] R.F. Lang et al., *A ^{220}Rn source for the calibration of low-background experiments*, *JINST* **11** (2016) P04004 [1602.01138].

[196] J. Aalbers, K. Abe, V. Aerne, F. Agostini, S.A. Maouloud, D.S. Akerib et al., *A Next-Generation Liquid Xenon Observatory for Dark Matter and Neutrino Physics*, 2203.02309.

[197] K. Thieme, *The Low-Energy and Large-Scale Frontier of Dual-Phase Xenon Time Projection Chambers for Dark Matter Search*, Ph.D. thesis, Zurich U., 2022.

[198] XENON collaboration, *Light Dark Matter Search with Ionization Signals in XENON1T*, *Phys. Rev. Lett.* **123** (2019) 251801 [1907.11485].

[199] L. Baudis, Y. Biondi, M. Galloway, F. Girard, A. Manfredini, N. McFadden et al., *Design and construction of Xenoscope — a full-scale vertical demonstrator for the DARWIN observatory*, *JINST* **16** (2021) P08052 [2105.13829].

[200] E. Hogenbirk et al., *Field dependence of electronic recoil signals in a dual-phase liquid xenon time projection chamber*, *JINST* **13** (2018) P10031 [1807.07121].

[201] EXO-200 collaboration, *Measurement of the Drift Velocity and Transverse Diffusion of Electrons in Liquid Xenon with the EXO-200 Detector*, *Phys. Rev. C* **95** (2017) 025502 [1609.04467].

[202] M. Murra, D. Schulte, C. Huhmann and C. Weinheimer, *Design, construction and commissioning of a high-flow radon removal system for XENONnT*, 2205.11492.

[203] M. Murra, D. Schulte, I. Cristescu, J.M. Disdier, C. Huhmann, D. Tatananni et al., *Cryogenic bath-type heat exchangers for ultra-pure noble gas applications*, *JINST* **17** (2022) P05037 [2203.01026].

[204] G. Plante, E. Aprile, J. Howlett and Y. Zhang, *Liquid-phase purification for multi-tonne xenon detectors*, 2205.07336.

[205] E. Erdal et al., *Bubble-assisted Liquid Hole Multipliers in LXe and LAr: towards "local dual-phase TPCs"*, *JINST* **15** (2020) C04002 [1912.10698].

[206] D. Ferenc et al., *The Novel ABALONE Photosensor Technology: 4-Year Long Tests of Vacuum Integrity, Internal Pumping and Afterpulsing*, 2017 [1703.04546].

[207] G. Barbarino et al., *A new generation photodetector for astroparticle physics: the VSiPMT*, *Astropart. Phys.* **67** (2015) 18 [1407.2805].

[208] S.R. Taylor, *Abundance of chemical elements in the continental crust: a new table*, *Geochim. Cosmochim. Acta* **28** (1964) 1273.

[209] J.A. Plant and A.D. Saunders, *The Radioactive Earth*, *Radiat. Prot. Dosimetry* **68** (1996) 25.

[210] D. Malczewski, J. Kisiel and J. Dorda, *Gamma background measurements in the gran sasso national laboratory*, *Journal of radioanalytical and nuclear chemistry* **295** (2013) 749.

[211] Consejo de Seguridad Nuclear (Spain) and International Atomic Energy Agency, *Control and management of radioactive material inadvertently incorporated into scrap metal*, International Atomic Energy Agency (2011).

[212] LNE-LNHB/CEA. ^{60}Co from Table de Radionucléides, 2011.

[213] LNE-LNHB/CEA. ^{137}Cs from Table de Radionucléides, 2011.

[214] D. Pressyanov, S. Georgiev, I. Dimitrova, K. Mitev and T. Boshkova, *Determination of the diffusion coefficient and solubility of radon in plastics*, *Radiation Protection Dosimetry* **145** (2011) 123.

[215] XENON collaboration, *^{222}Rn emanation measurements for the XENON1T experiment*, *Eur. Phys. J. C* **81** (2021) 337 [2009.13981].

[216] LNE-LNHB/CEA. ^{214}Bi from Table de Radionucléides, 2011.

[217] P.A. Amaudruz, M. Batygov, B. Beltran, K. Boudjemline, M.G. Boulay, B. Cai et al., *Radon backgrounds in the DEAP-1 liquid argon based Dark Matter detector*, *Astropart.Phys.* **62** (2015) 178 [1211.0909].

[218] S.J. Haselschwardt, J. Kostensalo, X. Mougeot and J. Suhonen, *Improved calculations of β decay backgrounds to new physics in liquid xenon detectors*, *Physical Review C* **102** (2020) 065501 [2007.13686].

[219] S.C. Wu, *Nuclear Data Sheets for A = 214*, *Nucl. Data Sheets* **110** (2009) 681.

[220] LNE-LNHB/CEA. ^{85}Kr from Table de Radionucléides, 2011.

[221] K. Winger, J. Feichter, M.B. Kalinowski, H. Sartorius and C. Schlosser, *A new compilation of the atmospheric 85krypton inventories from 1945 to 2000 and its evaluation in a global transport model*, *J. Env. Rad.* **80** (2005) 183.

[222] XENON collaboration, *XENON1T dark matter data analysis: Signal and background models and statistical inference*, *Phys. Rev. D* **99** (2019) 112009 [1902.11297].

[223] BOREXINO collaboration, *Data analysis strategy used for the detection of CNO solar neutrinos with Borexino*, *J. Phys. Conf. Ser.* **2156** (2021) 012200.

[224] N. Vinyoles, A.M. Serenelli, F.L. Villante, S. Basu, J. Bergström, M.C. Gonzalez-Garcia et al., *A new Generation of Standard Solar Models*, *Astrophys.J.* **835** (2017) 202.

[225] J.F. Beacom, *The Diffuse Supernova Neutrino Background*, *Ann. Rev. Nucl. Part. Sci.* **60** (2010) 439 [1004.3311].

[226] G. Battistoni, A. Ferrari, T. Montaruli and P.R. Sala, *The atmospheric neutrino flux below 100-MeV: The FLUKA results*, *Astropart. Phys.* **23** (2005) 526.

[227] K.A. Kouzakov and A.I. Studenikin, *Theory of neutrino-atom collisions: The history, present status, and BSM physics*, *Advances in High Energy Physics* **2014** (2014) [1406.4999].

[228] S.L. Glashow, J. Iliopoulos and L. Maiani, *Weak Interactions with Lepton-Hadron Symmetry*, *Phys. Rev. D* **2** (1970) 1285.

[229] G. Radel and R. Beyer, *Neutrino electron scattering*, *Mod. Phys. Lett. A* **8** (1993) 1067.

[230] *Atomic ionization of germanium by neutrinos from an ab initio approach*, *Physics Letters B* **731** (2014) 159.

[231] J.-W. Chen, H.-C. Chi, C.P. Liu and C.-P. Wu, *Low-energy electronic recoil in xenon detectors by solar neutrinos*, *Phys. Lett. B* **774** (2017) 656 [1610.04177].

[232] J.N. Bahcall and C. Peña-Garay, *Solar models and solar neutrino oscillations*, *New J.Phys.* **6** (2004) 63.

[233] J.B. Albert, G. Anton, I. Badhrees, P.S. Barbeau, R. Bayerlein, D. Beck et al., *Search for Neutrinoless Double-Beta Decay with the Upgraded EXO-200 Detector*, *Phys. Rev. Lett.* **120** (2018) 72701 [1707.08707].

[234] R.B. Firestone, V.S. Shirley, C.M. Baglin, S.F. Chu and J. Zipkin, *The 8th edition of the table of isotopes*, in *Proceedings of the 9th International Symposium on Capture gamma-ray spectroscopy and related topics. V. 2*, 1997.

[235] KamLAND-Zen collaboration, *Search for double-beta decay of ^{136}Xe to excited states of ^{136}Ba with the KamLAND-Zen experiment*, *Nucl. Phys. A* **946** (2016) 171 [1509.03724].

[236] *Private communication with Prof. Dr. Jenni Kotila* .

[237] L. Baudis, A. Kish, F. Piastra and M. Schumann, *Cosmogenic activation of xenon and copper*, *Eur. Phys. J.* **C75** (2015) 485 [1507.03792].

[238] *Private communication with Dr. Cuenca Garcia* .

[239] Geant4 collaboration, *An overview of the GEANT4 toolkit*, *AIP Conf. Proc.* **896** (2007) 1.

[240] W. Bambynek, H. Behrens, M.H. Chen, B. Crasemann, M.L. Fitzpatrick, K.W. Ledingham et al., *Orbital electron capture by the nucleus*, *Rev. Mod. Phys.* **49** (1977) 77.

[241] K.H. Lieser, *V. S. Shirley (Ed.): Table of radioactive isotopes , Authors: E. Browne, R. B. Firestone, John Wiley + Sons, New York, Chichester, Brisbane, Toronto, Singapore 1986. Preis: £ 57.45*, *Berichte der Bunsengesellschaft für Phys. Chemie* **91** (1987) 500.

[242] XENON collaboration, *Observation of two-neutrino double electron capture in ^{124}Xe with XENON1T*, *Nature* **568** (2019) 532 [1904.11002].

[243] E. Mendoza, D. Cano-Ott, P. Romojaro, V. Alcayne, P.G. Abia, V. Pesudo et al., *Neutron production induced by α-decay with Geant4*, *Nucl.Instrum.Meth.A* **960** (2019) [1906.03903].

[244] M. Herman, R. Capote, B.V. Carlson, P. Obložinský, M. Sin, A. Trkov et al., *EMPIRE: Nuclear Reaction Model Code System for Data Evaluation*, *Nucl.Data Sheets* **108** (2007) 2655.

[245] A.J. Koning and D. Rochman, *Modern Nuclear Data Evaluation with the TALYS Code System*, *Nucl.Data Sheets* **113** (2012) 2841.

[246] E. Mendoza, D. Cano-Ott, P. Romojaro, V. Alcayne, P. García Abia, V. Pesudo et al., *Neutron production induced by α-decay with Geant4*, *Nucl. Instrum. Meth. A* **960** (2020) 163659 [1906.03903].

[247] XENON collaboration, *Light Dark Matter Search with Ionization Signals in XENON1T*, 1907.11485.

[248] E. Aprile, J. Aalbers, F. Agostini, M. Alfonsi, L. Althueser, F.D. Amaro et al., *Energy resolution and linearity of XENON1T in the MeV energy range*, *Eur. Phys. J. C* **80** (2020) [2003.03825].

[249] S. Agostinelli, J. Allison, K. Amako, J. Apostolakis, H. Araujo, P. Arce et al., *Geant4—a simulation toolkit*, *Nucl. Instruments Methods Phys. Res. Sect. A Accel. Spectrometers, Detect. Assoc. Equip.* **506** (2003) 250.

[250] I. Antcheva, M. Ballintijn, B. Bellenot, M. Biskup, R. Brun, N. Buncic et al., *ROOT — A C++ framework for petabyte data storage, statistical analysis and visualization*, *Comput. Phys. Commun.* **182** (2011) 1384.

[251] E. Hogenbirk, M.P. Decowski, K. McEwan and A.P. Colijn, *Field dependence of electronic recoil signals in a dual-phase liquid xenon time projection chamber*, *J. Instrum.* **13** (2018) [1807.07121v2].

[252] M. Ester, H.-P. Kriegel, J. Sander and X. Xu, *A density-based algorithm for discovering clusters in large spatial databases with noise*, pp. 226–231, AAAI Press, 1996.

[253] J.B. Kaminsky, *Optimizing liquid Xenon TPCs*, Ph.D. thesis, Universität Bern, 2017.

[254] S. Chu, "The Lund/LBNL nuclear data search." (accessed March 25, 2022).

[255] XENON collaboration, *Energy resolution and linearity in the keV to MeV range measured in XENON1T*, 2003.03825.

[256] D.S. Akerib et al., *The LUX-ZEPLIN (LZ) Experiment*, *Nucl. Instrum. Meth. A* **953** (2020) [1910.09124].

[257] LZ collaboration, *Identification of Radiopure Titanium for the LZ Dark Matter Experiment and Future Rare Event Searches*, *Astropart. Phys.* **96** (2017) 1 [1702.02646].

[258] C. Leyens and M. Peters, *Titanium and titanium alloys: fundamentals and applications*, John Wiley & Sons (2003).

[259] S. Cebrian, *Cosmogenic activation in double beta decay experiments*, *Universe* **6** (2020) [2010.02381v2].

[260] XENON collaboration, *Material radioassay and selection for the XENON1T dark matter experiment*, *Eur. Phys. J.* **C77** (2017) 890 [1705.01828].

[261] DARWIN collaboration, *DARWIN: towards the ultimate dark matter detector*, *JCAP* **1611** (2016) 017 [1606.07001].

[262] F. Boehm and P. Vogel, *Physics of Massive Neutrinos*, Cambridge University Press (jun, 1992), 10.1017/cbo9780511622571.

[263] L. Baudis, A. Ferella, A. Kish, A. Manalaysay, T.M. Undagoitia and M. Schumann, *Neutrino physics with multi-ton scale liquid xenon detectors*, *J. Cosmol. Astropart. Phys.* **2014** (2014) 044 [1309.7024].

[264] A. Terliuk. Link to Repository (accessed March 3, 2022).

[265] K. Cranmer, *Practical Statistics for the LHC*, 1503.07622.

[266] S. Algeri, J. Aalbers, K.D. Morå and J. Conrad, *Searching for new phenomena with profile likelihood ratio tests*, *Nat. Rev. Phys.* (2020) .

[267] M. Agostini, G. Benato and J.A. Detwiler, *Discovery probability of next-generation neutrinoless double-β decay experiments*, *Phys. Rev. D* **96** (2017) [1705.02996].

[268] L. Lista, *Statistical Methods for Data Analysis in Particle Physics*, vol. 909, Springer (2016), 10.1007/978-3-319-20176-4.

[269] I. Esteban, M.C. Gonzalez-Garcia, M. Maltoni, T. Schwetz and A. Zhou, *The fate of hints: updated global analysis of three-flavor neutrino oscillations*, *J. High Energy Phys. 2020 20209* **2020** (2020) 1 [2007.14792].

[270] A.S. Barabash, *Possibilities of future double beta decay experiments to investigate inverted and normal ordering region of neutrino mass*, *Front. Phys.* **6** (2019) 160.

[271] A. Giuliani, J.J. Gomez Cadenas, S. Pascoli, E. Previtali, R. Saakyan, K. Schäffner et al., *Double Beta Decay APPEC Committee Report*, 1910.04688.

[272] M. Bhike and W. Tornow, *Neutron-capture cross-section measurements of Xe 136 between 0.4 and 14.8 MeV*, *Phys. Rev. C - Nucl. Phys.* **89** (2014) 031602.

[273] S. Delaquis, M.J. Jewell and O. et al, *Deep neural networks for energy and position reconstruction in EXO-200*, *JINST* **13** (2018) [1804.09641].

[274] J.B. Albert, G. Anton, I.J. Arnquist, I. Badhrees, P. Barbeau, D. Beck et al., *Sensitivity and discovery potential of the proposed nEXO experiment to neutrinoless double- β decay*, *Phys. Rev. C* (2018) .

[275] EXO collaboration, *Measurement of the scintillation and ionization response of liquid xenon at MeV energies in the EXO-200 experiment*, 1908.04128.

[276] N.F. Bell, V. Cirigliano, M.J. Ramsey-Musolf, P. Vogel and M.B. Wise, *How magnetic is the dirac neutrino?*, *Phys. Rev. Lett.* **95** (2005) 151802 [0504134].

[277] R. Foot, *Mirror dark matter: Cosmology, galaxy structure and direct detection*, *https://doi.org/10.1142/S0217751X14300130* **29** (2014) .

[278] J. Kopp, V. Niro, T. Schwetz and J. Zupan, *DAMA/LIBRA data and leptonically interacting dark matter*, *Phys. Rev. D - Part. Fields, Gravit. Cosmol.* **80** (2009) 083502 [0907.3159].

[279] C. Giunti and A. Studenikin, *Neutrino electromagnetic interactions: A window to new physics*, *Rev. Mod. Phys.* **87** (2015) 531 [1403.6344].

[280] G.G. Raffelt, *Axions - Motivation, limits and searches*, *J. Phys. A Math. Theor.* **40** (2006) 6607 [0611118v1].

[281] J.E. Kim, *Weak Interaction Singlet and Strong CP Invariance*, *Phys.Rev.Lett.* **43** (1979) 103.

[282] S. Dimopoulos, J.A. Frieman, B.W. Lynn and G.D. Starkman, *Axiorecombination: A New Mechanism for Stellar Axion Production*, *Phys. Lett. B* **179** (1986) 223.

[283] J. Redondo, *Solar axion flux from the axion-electron coupling*, *JCAP* **12** (2013) 008 [1310.0823].

[284] A. Serenelli, S. Basu, J.W. Ferguson and M. Asplund, *New Solar Composition: The Problem With Solar Models Revisited*, *Astrophys. J. Lett.* **705** (2009) L123 [0909.2668].

[285] Atomic Weights and Isotopic Compositions for All Elements, NIST. Website, accessed July 2022.

[286] A.M. Serenelli, S. Basu, J.W. Ferguson and M. Asplund, *New Solar Composition: The Problem With Solar Models Revisited*, *Astrophys.J.Lett.* **705** (2009) L123 [0909.2668].

[287] CAST collaboration, *Search for 14.4-keV solar axions emitted in the M1-transition of Fe-57 nuclei with CAST*, *JCAP* **12** (2009) 002 [0906.4488].

[288] F. Alessandria, R. Ardito, R.D. Artusa, F.T. Avignone, O. Azzolini, M. Balata et al., *Search for 14.4 keV solar axions from M1 transition of Fe-57 with CUORE crystals*, *JCAP* **05** (2013) 007 [1209.2800].

[289] A. Derevianko, V.A. Dzuba, V.V. Flambaum and M. Pospelov, *Axio-electric effect*, *Phys. Rev. D* **82** (2010) 065006 [1007.1833].

[290] M. Pospelov, A. Ritz and M.B. Voloshin, *Bosonic super-WIMPs as keV-scale dark matter*, *Phys. Rev. D* **78** (2008) 115012 [0807.3279].

[291] W.J. Veigele, *Photon cross sections from 0.1 keV to 1 MeV for elements Z = 1 to Z = 94*, *Atom. Data Nucl. Data Tabl.* **5** (1973) 51.

[292] C. Gao, J. Liu, L.T. Wang, X.P. Wang, W. Xue and Y.M. Zhong, *Reexamining the Solar Axion Explanation for the XENON1T Excess*, *Phys.Rev.Lett.* **125** (2020) [2006.14598].

[293] J.B. Dent, B. Dutta, J.L. Newstead and A. Thompson, *Inverse Primakoff Scattering as a Probe of Solar Axions at Liquid Xenon Direct Detection Experiments*, *Phys.Rev.Lett.* **125** (2020) [2006.15118].

[294] L. Safari, J.P. Santos, P. Amaro, K. Jänkälä and F. Fratini, *Analytical evaluation of atomic form factors: Application to Rayleigh scattering*, *Journal of Mathematical Physics* **56** (2015) 052105 [1409.0110].

[295] T. Abe, K. Hamaguchi and N. Nagata, *Atomic form factors and inverse Primakoff scattering of axion*, *Physics Letters B* **815** (2021) 136174.

[296] COSME collaboration, *Particle dark matter and solar axion searches with a small germanium detector at the Canfranc Underground Laboratory*, *Astropart. Phys.* **16** (2002) 325 [hep-ex/0101037].

[297] W. Buchmuller and F. Hoogeveen, *Coherent Production of Light Scalar Particles in Bragg Scattering*, *Phys. Lett. B* **237** (1990) 278.

[298] J.H. Hubbell, W.J. Veigele, E.A. Briggs, R.T. Brown and D.T. Cromer, *Atomic form factors, incoherent scattering functions, and photon scattering cross sections*, Tech. Rep. (1975).

[299] F.T. Avignone, D. Abriola, R.L. Brodzinski, J.I. Collar, R.J. Creswick, D.E. Di Gregorio et al., *Experimental Search for Solar Axions via Coherent Primakoff Conversion in a Germanium Spectrometer*, *Phys. Rev. Lett.* **81** (1998) 5068.

[300] Z. Ahmed, D.S. Akerib, S. Arrenberg, C.N. Bailey, D. Balakishiyeva, L. Baudis et al., *Search for axions with the CDMS experiment*, *Phys. Rev. Lett.* **103** (2009) 141802 [0902.4693].

[301] A. Morales, F.T. Avignone, R.L. Brodzinski, S. Cebrián, E. García, D. González et al., *Particle dark matter and solar axion searches with a small germanium detector at the Canfranc Underground Laboratory*, *Astropart. Phys.* **16** (2002) 325.

[302] C. Arnaboldi, F.T. Avignone, J. Beeman, M. Barucci, M. Balata, C. Brofferio et al., *Physics potential and prospects for the CUORICINO and CUORE experiments*, *Astropart. Phys.* **20** (2003) 91 [0302021].

[303] E. Armengaud, Q. Arnaud, C. Augier, A. Benoit, A. Benoit, L. Bergé et al., *Axion searches with the EDELWEISS-II experiment*, *J. Cosmol. Astropart. Phys.* **2013** (2013) 067 [1307.1488].

[304] G.J. Feldman and R.D. Cousins, *A Unified Approach to the Classical Statistical Analysis of Small Signals Typeset using REVT E X 1*, .

[305] J. Eschle, A. Puig Navarro, R. Silva Coutinho and N. Serra, *zfit: Scalable pythonic fitting*, *SoftwareX* **11** (2020) 100508 [1910.13429].

[306] G. Cowan, K. Cranmer, E. Gross and O. Vitells, *Asymptotic formulae for likelihood-based tests of new physics*, *Eur. Phys. J. C* **71** (2011) .

[307] R.G. Gratton, E. Carretta, A. Bragaglia, S. Lucatello and V. D'Orazi, *The second and third parameters of the Horizontal Branch in Globular Clusters*, *Astron. Astrophys.* **517** (2010) [1004.3862v2].

[308] N. Vinyoles, A. Serenelli, F.L. Villante, S. Basu, J. Redondo and J. Isern, *New axion and hidden photon constraints from a solar data global fit*, *J. Cosmol. Astropart. Phys.* **2015** (2015) [1501.01639v2].

[309] LUX collaboration, *First Searches for Axions and Axion-Like Particles with the LUX Experiment*, *Phys. Rev. Lett.* **118** (2017) [1704.02297v2].

[310] M. Salaris, M. Riello, S. Cassisi and G. Piotto, *The initial helium abundance of the Galactic globular cluster system*, *Astron. Astrophys.* **420** (2004) 911 [0403600].

[311] A. Ayala, I. Domínguez, M. Giannotti, A. Mirizzi and O. Straniero, *Revisiting the bound on axion-photon coupling from Globular Clusters*, *Phys.Rev.Lett.* **113** (2014) [1406.6053].

[312] M. Tanabashi, K. Hagiwara, K. Hikasa, K. Nakamura, Y. Sumino, F. Takahashi et al., *Review of Particle Physics*, *Phys. Rev. D* **98** (2018) 030001.

[313] A.M. Serenelli and S. Basu, *Determining the initial helium abundance in the Sun*, *Astrophys. J.* **719** (2010) 865.

[314] M. Buschmann, C. Dessert, J.W. Foster, A.J. Long and B.R. Safdi, *Upper Limit on the QCD Axion Mass from Isolated Neutron Star Cooling*, *Phys. Rev. Lett.* **128** (2021) [2111.09892v1].

[315] P. Carenza, T. Fischer, M. Giannotti, G. Guo, G. Martinez-Pinedo and A. Mirizzi, *Improved axion emissivity from a supernova via nucleon-nucleon bremsstrahlung*, *J. Cosmol. Astropart. Phys.* **2019** (2019) [1906.11844v3].

[316] L. Baudis, Y. Biondi, M. Galloway, F. Girard, A. Manfredini, N. McFadden et al., *Design and construction of Xenoscope — a full-scale vertical demonstrator for the DARWIN observatory*, *JINST* **16** (2021) P08052 [2105.13829].

[317] E. Aprile and T. Doke, *Liquid Xenon Detectors for Particle Physics and Astrophysics*, *Rev. Mod. Phys.* **82** (2010) 2053 [0910.4956].

[318] F. Girard, *Design and Construction of Xenoscope and Photosensor Characterisation for the DARWIN Observatory*, Ph.D. thesis, Zurich U., Projected: 2022.

[319] T. Haruyama, K. Kasami, Y. Matsubara, K. Giboni, E. Aprile, T. Nishitani et al., *High-power pulse tube cryocooler for liquid xenon particle detectors*, 4, 2004.

[320] K.L. Giboni, E. Aprile, B. Choi, T. Haruyama, R.F. Lang, K.E. Lim et al., *Xenon recirculation-purification with a heat exchanger*, *J. Instrum.* **6** (2011) P03002 [1103.0986].

[321] PS4-MT Series Rare Gas Purifier, 100 slpm, SAES. Datasheet, accessed July 2022.

[322] HIGH VOLTAGE PNC-Series, Heinzinger. Datasheet, accessed July 2022.

[323] C. Cantini et al., *First test of a high voltage feedthrough for liquid Argon TPCs connected to a 300 kV power supply*, *JINST* **12** (2017) P03021 [1611.02085].

[324] XENON collaboration, *The XENON1T Dark Matter Experiment*, *Eur. Phys. J. C* **77** (2017) 881 [1708.07051].

[325] DUNE collaboration, *The Single-Phase ProtoDUNE Technical Design Report*, 1706.07081.

[326] B.J. Mount et al., *LUX-ZEPLIN (LZ) Technical Design Report*, 1703.09144.

[327] PAI Material Properties, Curbell Plastics. Datasheet.

[328] COMSOL Inc. Website, accessed July 2022.

[329] D.Y. Akimov et al., *Measurement of single-electron noise in a liquid-xenon emission detector*, *Instrum. Exp. Tech.* **55** (2012) 423.

[330] T. Shimizu, Y. Kawahara, S. Akasaka and Y. Kogami, *Complex Permittivity Measurements of a PTFE Substrate in W Band by the Cut-off Circular Waveguide Method*, Tech. Rep. (2011).

[331] R. Peres, *Contributions to the xenon dark matter experiment: simulations of detector response to calibration sources and electric field optimization, master thesis*, 2018.

[332] LZ collaboration, *The LUX-ZEPLIN (LZ) Experiment*, *Nucl. Instrum. Meth. A* **953** (2020) 163047 [1910.09124].

[333] S. Horikawa, A. Badertscher, L. Kaufmann, M. Laffranchi, A. Marchionni, M. Messina et al., *Feasibility of high-voltage systems for a very long drift in liquid argon TPCs*, *J. Phys. Conf. Ser.* **308** (2011) 012027 [1009.4908].

[334] CeramTec. Datasheet, accessed July 2022.

[335] L. Tvrznikova, E. Bernard, S. Kravitz, K. O'Sullivan, G. Richardson, Q. Riffard et al., *Direct comparison of high voltage breakdown measurements in liquid argon and liquid xenon*, *JINST* **14** (2019) P12018 [1908.06888].

[336] L. Baudis, Y. Biondi, M. Galloway, F. Girard, S. Hochrein, S. Reichard et al., *The first dual-phase xenon TPC equipped with silicon photomultipliers and characterisation with ^{37}Ar*, *Eur. Phys. J. C* **80** (2020) 477 [2003.01731].

[337] E. Aprile et al., *The xenon100 dark matter experiment*, *Astroparticle Physics* **35** (2012) 573.

[338] F. Kuger, J. Dierle, H. Fischer, M. Schumann and F. Toschi, *Prospects of charge signal analyses in liquid xenon TPCs with proportional scintillation in the liquid phase*, *JINST* **17** (2022) P03027 [2112.11844].

[339] SolidWorks. Website, accessed July 2022.

[340] Carbagas. Website, accessed July 2022.

[341] J.P. Hobson, *Fifty years of vacuum science*, *J. Vac. Sci. Technol. A Vacuum, Surfaces, Film.* **21** (2003) S7.

[342] EXO collaboration, *A xenon gas purity monitor for EXO*, *Nucl. Instrum. Meth. A* **659** (2011) 215 [1106.1812].

[343] S. Amerio, S. Amoruso, M. Antonello, P. Aprili, M. Armenante, F. Arneodo et al., *Design, construction and tests of the ICARUS T600 detector*, *Nucl. Instruments Methods Phys. Res. Sect. A Accel. Spectrometers, Detect. Assoc. Equip.* **527** (2004) 329.

[344] M. Adamowski, B. Carls, E. Dvorak, A. Hahn, W. Jaskierny, C. Johnson et al., *The liquid argon purity demonstrator*, *J. Instrum.* **9** (2014) [1403.7236].

[345] E. Aprile et al., *Physics reach of the XENON1T dark matter experiment.*, *J. Cosmol. Astropart. Phys.* **2016** (2016) 027.

[346] G. Bakale and W.F. Schmidt, *Effect of an Electric Field on Electron Attachment to SF6 in Liquid Ethane and Propane*, Tech. Rep. 8 (1981).

[347] L7685 Xenon Lamp, Hamamatsu. Datasheet , accessed July 2022.

[348] LewVac Optic Fibres. Website, accessed July 2022.

[349] Attenuation in a solarisation resistant fibre, Thorlabs. Datasheet , accessed July 2022.

[350] Art Photonics. Website, accessed July 2022.

[351] Optic fibre feedthrough, Thorlabs. Datasheet , accessed July 2022.

[352] A. Valentini, E. Nappi and M.A. Nitti, *Influence of the substrate reflectance on the quantum efficiency of thin CsI photocathodes*, Tech. Rep. (2002).

[353] D.R. Lide, *CRC handbook of chemistry and physics*, vol. 85, CRC press (2004).

[354] P.J. Wass, D. Hollington, T.J. Sumner, F. Yang and M. Pfeil, *Effective decrease of photoelectric emission threshold from gold plated surfaces*, *Rev. Sci. Instrum.* **90** (2019) 064501 [1901.01057].

[355] Coater 150T Plus, Quorum . Datasheet , accessed July 2022.

[356] L. Manenti, L. Cremonesi, F. Arneodo, A. Basharina-Freshville, M. Campanelli, A. Holin et al., *Performance of different photocathode materials in a liquid argon purity monitor*, *J. Instrum.* **15** (2020) P09003 [2005.08187].

[357] Flatness parameter definition by Edmund Optics. Online, accessed July 2022.

[358] RGA Prima Pro, Pfeiffer. Datasheet, accessed July 2022.

[359] O. Njoya et al., *Measurements of electron transport in liquid and gas Xenon using a laser-driven photocathode*, *Nucl. Instrum. Meth. A* **972** (2020) 163965 [1911.11580].

[360] Y. Li et al., *Measurement of Longitudinal Electron Diffusion in Liquid Argon*, *Nucl. Instrum. Meth. A* **816** (2016) 160 [1508.07059].

[361] W. Shockley, *Currents to conductors induced by a moving point charge*, *J. Appl. Phys.* **9** (1938) 635.

[362] A. Göök, F.J. Hambsch, A. Oberstedt and S. Oberstedt, *Application of the ShockleyRamo theorem on the grid inefficiency of Frisch grid ionization chambers*, *Nucl. Instruments Methods Phys. Res. Sect. A Accel. Spectrometers, Detect. Assoc. Equip.* **664** (2012) 289.

[363] W. Blum, L. Rolandi and W. Riegler, *Particle detection with drift chambers*, Particle Acceleration and Detection, Springer Berlin Heidelberg (2008), 10.1007/978-3-540-76684-1.

[364] M. Dris and T. Alexopoulos, *Signal Formation in Various Detectors*, 1406.3217.

[365] O. Bunemann, T.E. Cranshaw and J.A. Harvey, *Design of Grid Ionization Chambers*, *Can. J. Res.* **27a** (1949) 191.

[366] Operation amplifier AD8066. Datasheet , accessed July 2022.

[367] CMT Rickenbach SA. Website, accessed July 2022.

[368] Resistors, Ohmite. Datasheet , accessed July 2022.

[369] Acidic soap A10, Elma. Product website, accessed July 2022.

[370] *Private communication with Prof. Dr. Masaki Yamashita* .

[371] A. Dhar, J. Loach, P. Barton, J. Larsen and A. Poon, *Low-background temperature sensors fabricated on parylene substrates*, *JINST* **10** (2015) P12002.

[372] Parylene, SCS. Datasheet , accessed July 2022.

[373] Waverunner9000 Teledyne, LeCroy. Datasheet , accessed July 2022.

[374] E.M. Gushchin, A.A. Kruglov and I.M. Obodovskii, *Electron dynamics in condensed argon and xenon*, *JETP* **55** (1982) 650.

[375] L. Baudis, Y. Biondi, C. Capelli, M. Galloway, S. Kazama, A. Kish et al., *A Dual-phase Xenon TPC for Scintillation and Ionisation Yield Measurements in Liquid Xenon*, *Eur. Phys. J. C* **78** (2018) 351 [1712.08607].

[376] *Electron mobilities in gaseous, critical, and liquid xenon: Density, electric field, and temperature effects: Quasilocalization*, *J. Chem. Phys.* **68** (1977) 1355.

[377] J.L. Pack, R.E. Voshall, A.V. Phelps and L.E. Kline, *Longitudinal electron diffusion coefficients in gases: Noble gases*, *J. Appl. Phys.* **71** (1992) 5363.

[378] H.L. Brooks, M.C. Cornell, J. Fletcher, I.M. Littlewood and K.J. Nygaard, *Electron drift velocities in xenon*, *J. Phys. D. Appl. Phys.* **15** (1982) 51.

[379] K. Yoshino, U. Sowada and W.F. Schmidt, *Effect of molecular solutes on the electron drift velocity in liquid Ar, Kr, and Xe*, *Phys. Rev. A* **14** (1976) 438.

[380] E. Shibamura, T. Takahashi, S. Kubota and T. Doke, *Ratio of diffusion coefficient to mobility for electrons in liquid argon*, *Phys. Rev. A* **20** (1979) 2547.

[381] P. Agnes, I.F. Albuquerque, T. Alexander, A.K. Alton, D.M. Asner, M.P. Ave et al., *Electroluminescence pulse shape and electron diffusion in liquid argon measured in a dual-phase TPC*, *Nucl. Instruments Methods Phys.* **904** (2018) 23 [1802.01427].

[382] M. Grech, R. Nuter, A. Mikaberidze, P. Di Cintio, L. Gremillet, E. Lefebvre et al., *Coulomb explosion of uniformly charged spheroids*, *Phys. Rev. E* **84** (2011) 056404 [1105.0409].

[383] LUX collaboration, *Investigation of background electron emission in the LUX detector*, *Phys. Rev. D* **102** (2020) 092004 [2004.07791].

[384] XENON collaboration, *Emission of single and few electrons in XENON1T and limits on light dark matter*, *Phys. Rev. D* **106** (2022) 022001 [2112.12116].

[385] L. Baudis, M. Galloway, A. Kish, C. Marentini and J. Wulf, *Characterisation of Silicon Photomultipliers for Liquid Xenon Detectors*, *JINST* **13** (2018) P10022 [1808.06827].

[386] G. Gallina et al., *Characterization of the Hamamatsu VUV4 MPPCs for nEXO*, *Nucl. Instrum. Meth. A* **940** (2019) 371 [1903.03663].

[387] R. Colle, J.M. Hutchinson and M.P. Unterweger, *The NIST Primary Radon-222 Measurement System*, *J. Research of the National Institute of Standards and Technology* **95** (1990) 155.

Appendix A

Table of Nuclear Decays from Background Sources

A.0.1 Uranium and Thorium decay chains

The decay products of the uranium and thorium chains are shown in Table A.1.

Table A.1: Decay series of ^{238}U and ^{232}Th

^{238}U			^{232}Th		
Nuclide	Half-Life	Decay-Mode	Nuclide	Half-Life	Decay-Mode
^{238}U	4.5×10^{9} y	α, γ	^{232}Th	1.41×10^{10} y	α
^{234}Th	24.1 d	β, γ	^{228}Ra	6.7 y	β
^{234}Pa	6.75 h	β, γ	^{228}Ac	6.13 h	β, γ
^{234}U	2.48×10^{5}y	α, γ	^{228}Th	1.91y	α
^{230}Th	8.0×10^{4} y	α, γ	^{224}Ra	3.64 d	α
^{226}Ra	1622y	α, γ	^{220}Rn	55.3 s	α
^{222}Rn	3.82 d	α	^{218}Po	0.145 s	α
^{218}Po	3.05 min	α	^{212}Pb	10.64 h	β, γ
^{214}Pb	26.8 min	β	^{212}Bi	60.6 min	α, β
^{214}Bi	19.7 min	α, β, γ	^{212}Po	3.04×10^{-7} s	α
^{214}Po	1.6×10^{-4} s	α	^{208}Th	3.10 min	β, γ
^{210}Pb	22.0y	β, γ	^{208}Pb	Stable	
^{210}Bi	5.01 d	β			
^{210}Po	138.4 d	α			
^{206}Pb	Stable				

A.0.2 ^{222}Ra decay chain

The decay chain of ^{222}Ra is shown in Table A.2.

Table A.2: Decay series from ^{222}Rn and ^{220}Rn [387].

^{222}Rn			^{220}Rn		
Nuclide	Half-Life	Decay-Mode	Nuclide	Half-Life	Decay-Mode
^{222}Rn	3.825 d	α	^{220}Rn	55 s	α, γ
^{218}Po	3.05 min	α	^{216}Po	0.15 s	α
^{214} Pb	26.8 min	β, γ	^{212} Pb	10.64 h	β, γ
^{214}Bi	19.9 min	β, γ	^{212}Bi	60.6 min	α, β, γ
^{214}Po	164μs	α	^{212}Po	304 ns	α
^{210} Pb	22.3a	β, γ	^{208}Tl	3.05 min	β, γ
^{210}Bi	5.0 d	β, γ	^{208} Pb	stable	
^{210}Po	138.4 d	α			
^{206} Pb	stable				

A.0.3 ^{60}Co decay scheme

The decay chain of ^{60}Co is shown in Figure A.1.

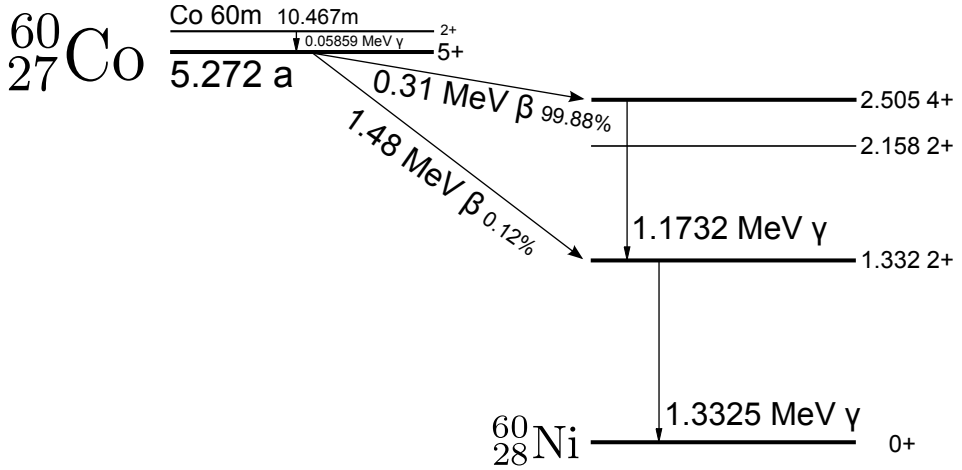

Figure A.1: Decay scheme of ^{60}Co

A.0.4 ^{40}K decay scheme

The decay chain of ^{40}K is shown in Figure A.2.

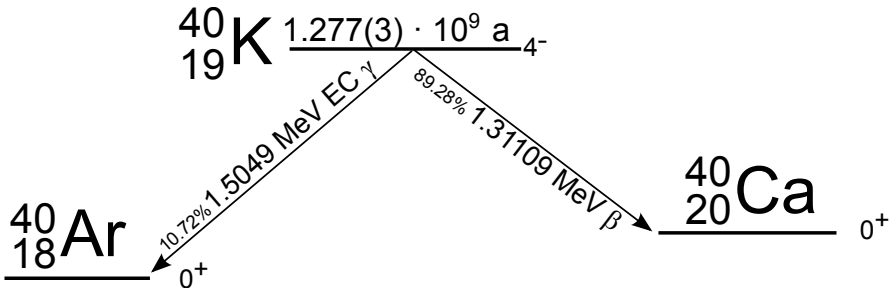

Figure A.2: Decay scheme of ^{40}K

Appendix B

Nuclear cycles in the Sun

The main cycle in the Sun is from the pp-chain:

$$p + p \rightarrow 2^1D + e^+ + v_e. \tag{B.1}$$

In this cycle, ^{7}Be is also produced, which has two decay modes that gives two different imprints in the neutrino energy:

$$\begin{aligned} ^1\mathrm{D} + p &\rightarrow ^3 He + \gamma \\ ^3\mathrm{He} + ^3\mathrm{He} &\rightarrow ^4\mathrm{He} + 2p \\ ^3\mathrm{He} + ^4\mathrm{He} &\rightarrow ^7\mathrm{Be} + \gamma \\ ^7\mathrm{Be} + e^- &\rightarrow ^7\mathrm{Li} + \nu_e \\ ^7\mathrm{Be} + \mathrm{p} &\rightarrow ^8\mathrm{Be} + \gamma \end{aligned} \tag{B.2}$$

From this cycle, ^{8}B is produced, which has the highest Q-value from the different solar neutrino components:

$$^8\mathrm{B} \rightarrow ^8\mathrm{Be}^* + \mathrm{e}^+ + \nu_\mathrm{e}. \tag{B.3}$$

The proton–electron–proton (pep) reaction by electron captures produces an electron neutrino, although in a ratio 1:400 lower than the pp cycle:

$$p + e^- + p \rightarrow 2^1\mathrm{D}^+ + v_e. \tag{B.4}$$

The CNO cycle depends on pre-existing metals in the Sun, which makes its flux dependent on the solar metallicity model assumed. The Sun converts C to N in the most central region of the core. A

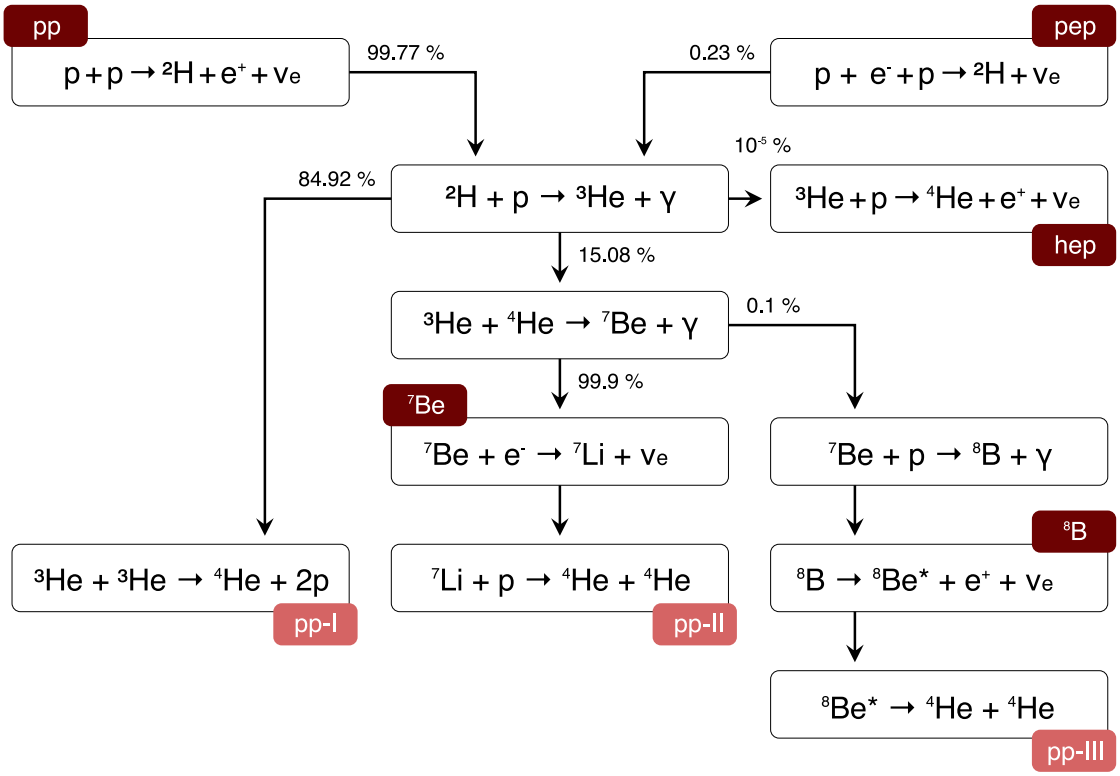

Figure B.1: Diagram of the pp-chain in the Sun.

diagram of the CNO-cycle is shown in Figure B.2.

In the cooler region of the core, pre-solar ^{12}C has been converted to ^{14}N, but little N is consumed, having a bottleneck in the proton capture reaction. Outside this core region ($T \lessapprox 10^7$K), ^{12}C lifetime is comparable to solar age. The most important reactions are:

$$\begin{aligned} {}^{13}_{7}\mathrm{N} &\rightarrow {}^{13}_{7}\mathrm{C} + \mathrm{e}^{+} + \upsilon_{\mathrm{e}} + 1.20\mathrm{MeV} \\ {}^{15}_{8}\mathrm{O} &\rightarrow {}^{15}_{7}\mathrm{N} + \mathrm{e}^{+} + \upsilon_{\mathrm{e}} + 1.73\mathrm{MeV} \end{aligned} \tag{B.5}$$

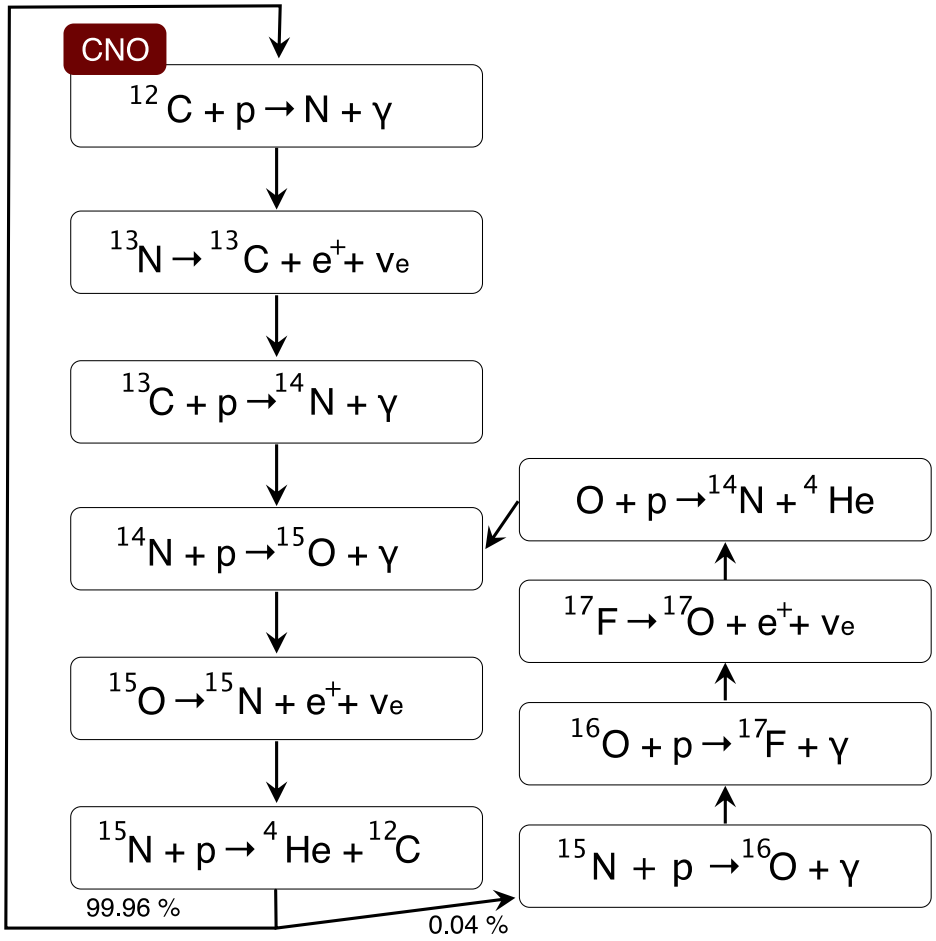

Figure B.2: Diagram of the CNO-cycle in the Sun.